Dressed Topological Insulators

Rashba Impurity, Kondo Effect, Magnetic Impurities, Proximity-Induced Superconductivity, Hybrid Systems

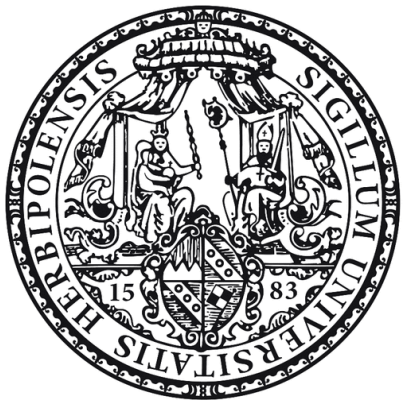

Dissertation
zur Erlangung des naturwissenschaftlichen Doktorgrades
der Julius-Maximilians-Universität Würzburg

vorgelegt von
Thore Hagen Poßke
aus Lüneburg

Würzburg 2015

Eingereicht am: 21. Juli 2015 .....
bei der Fakultät für Physik und Astronomie

1. Gutachter: Prof. Dr. Björn Trauzettel .....

2. Gutachter: Prof. Dr. Giorgio Sangiovanni .....

3. Gutachter: Prof. Dr. Matthias Vojta .....
der Dissertation

Vorsitzender: Prof. Dr. Ralph Claessen .....

1. Prüfer: Prof. Dr. Björn Trauzettel .....

2. Prüfer: Prof. Dr. Giorgio Sangiovanni .....

3. Prüfer: Prof. Dr. Hartmut Buhmann .....
im Promotionskolloqium

Tag des Promotionskolloqiums: 26. Februar 2016 .....

Doktorurkunde ausgehändigt am: .....

Abstract

Topological insulators are electronic phases that insulate in the bulk and accommodate a peculiar, metallic edge liquid with a spin-dependent dispersion. They are regarded to be of considerable future use in spintronics and for quantum computation. Besides determining the intrinsic properties of this rather novel electronic phase, considering its combination with well-known physical systems can generate genuinely new physics. In this thesis, we report on such combinations including topological insulators. Specifically, we analyze an attached Rashba impurity, a Kondo dot in the two channel setup, magnetic impurities on the surface of a strong three-dimensional topological insulator, the proximity coupling of the latter system to a superconductor, and hybrid systems consisting of a topological insulator and a semimetal. Let us summarize our primary results. Firstly, we determine an analytical formula for the Kondo cloud and describe its possible detection in current correlations far away from the Kondo region. We thereby rely on and extend the method of refermionizable points. Furthermore, we find a class of gapless topological superconductors and semimetals, which accommodate edge states that behave similarly to the ones of globally gapped topological phases. Unexpectedly, we also find edge states that change their chirality when affected by sufficiently strong disorder. We regard the presented research helpful in future classifications and applications of systems containing topological insulators, of which we propose some examples.

Preface

This thesis has been written as part of the examination to achieve the academic degree Doctor of Natural Sciences. It contains the findings accumulated during my research since the beginning of 2012 regarding the combination of topological insulators with more familiar materials and effects. This I refer to as "Dressing topological insulators" in the title. The aim was to employ the novelty of topological insulators to track interesting and themselves even newer effects in such combined systems. Of course, this strategy is not exclusive to this thesis as there are plenty of other scientists pursuing the same direction in research. Altogether, I feel that the aim has been reached and that this area of research on topological insulators has progressed due to the work presented here. I hope that the results can be used to conduct some of the indicated future projects. In regard of this, the text is, in principle, written in a way that the acquired results can be understood and, especially under consideration of the cited references, be reconstructed by a Ph.D. student or a talented master's degree candidate. I have to admit, however, that considerable dedication is required.

Something personal should be the end of this preface. During the last years, my co-authors have been from Germany, China, Israel, and Romania. Furthermore, I was working together with researchers from France, Spain, Italy, Finland, Belgium, Poland, and Russia[1]. All of them, including myself, have regarded this circumstance as completely natural. How wonderful.

I would like to thank my father, my mother, and my brother for their influence on my life, which apparently has led to something good. Subsequently, I am thankful for the warm support of my family and friends. Also, I want to thank my fiancé for her patience.

Funding and scientific acknowledgment

Regarding Chapter 5, I thank P. Simon and G. Zaránd, Jan von Delft, Jan Budich, Fabrizio Dolcini, and Michele Filippone for interesting discussions as well as the DFG (especially SPP 1666 and the DFG-JST research unit "Topotronics"), the Humboldt Foundation, and Helmholtz Foundation (VITI), as well as the ESF for financial support.

[1]The list of nations would continue for a long time if I included all persons I have had scientific conversations with during the last years.

Chapter 6 and Chapter 7 were financially supported by the DFG (German-Japanese research unit "Topotronics"; priority program SPP 1666 "Topological insulators"), the Helmholtz Foundation (VITI), and the ENB Graduate School on "Topological Insulators" from the side of Björn Trauzettel and myself. In this context, I want to thank Paolo Michetti and Chen-Hsuan Hsu for interesting discussions as well as Tim Wehling for correspondence. From the side of our coauthors Yuval Baum, Ion Cosma Fulga, and Ady Stern, the support by the European Research Council under the European Union's Seventh Framework Programme (FP7/2007-2013) / ERC Project MUNATOP, the US-Israel Binational Science Foundation, and the Minerva Foundation is gratefully acknowledged.

I want to express my gratitude to Björn Trauzettel, who has guided me excellently during my encounters with problems in solid state physics and taught me about focusing on the important tasks first. Furthermore, I want to thank Yuval Oreg and Ady Stern for their hospitality, which has made it possible for me to stay at the Weizmann Institute. Thereby I had the opportunity to benefit from truly international collaborations.

This thesis would not be the same without the numerous discussions with or influence of Jan Carl Budich, Yuval Baum, Chao-Xing Liu, Ion Cosma Fulga, Rolf Reinthaler, Dietrich Gernot Rothe, François Crépin, Florian Geißler, Pablo Burset, Moritz Fuchs, Niccolò Traverso Ziani, and Charles Gould, who I herewith want to acknowledge. Finally, I want to thank the creators of Wolfram Mathematica *[Wolfram Research, Inc., 2015]* and the LaTeX community for their software, which helped me to calculate and document my results the way I did.

Thore Posske, Würzburg, July 21, 2015

Contents

Abstract . . . iii
Preface . . . v

I. Introduction **1**

1. Introduction & motivation **2**

2. Background **4**
2.1. Topological Insulators . . . 4
2.1.1. A basic topological insulator . . . 5
2.1.2. Generalizations of and concepts beyond the presented basic model . . . 11
2.1.3. The quantum spin Hall effect . . . 15
2.1.4. Fu's model for the surface states of a three-dimensional strong topological insulator . . . 16
2.2. Magnetic and electric perturbations . . . 18
2.2.1. Zeeman terms . . . 18
2.2.2. Rashba terms . . . 18
2.2.3. Kondo physics and the Kondo cloud . . . 19
2.2.4. The RKKY approximation . . . 22
2.3. Superconductivity . . . 27

3. Methods **30**
3.1. Method of refermionizable points . . . 30
3.1.1. Bosonic-fermionic equivalence in one spatial dimension . . . 31
3.1.2. Generalized Emery-Kivelson transformations . . . 38
3.1.3. Refermionizable points of the two channel Kondo model with interacting helical leads . . . 39
3.2. Finitization of divergences generated by a local scatterer . . . 45
3.2.1. Proof by induction . . . 48
3.2.2. Continuum limit . . . 50
3.3. Multidimensional optimization and integration - The Metropolis algorithm . . . 51
3.4. Checking translationally invariant Hamiltonians for decomposability . 54

3.5. Applied transport simulations for superconductors 56

II. Results 59

4. The local Rashba scatterer 60
4.1. System 61
4.1.1. Bosonization 63
4.2. Refermionizable points 64
4.3. Exact solution at the primary refermionizable point 66
4.3.1. Orthogonality relations 68
4.3.2. Inversion of D 69
4.4. Exact transition to infinite momentum cutoff 71
4.5. Backscattering current I_B 72
4.5.1. Derivation of the refermionized form of I_B 72
4.6. Rashba energy 74
4.7. Same expectation values $\Leftrightarrow$ same Hamiltonians 75
4.8. Conclusions about the local Rashba scatterer 76

5. The local Kondo impurity 78
5.1. Exact results for the Kondo cloud of two helical liquids 79
5.1.1. Model 80
5.1.2. Method 81
5.1.3. Results 83
5.1.4. Renormalization group analysis of the crossing terms 86
5.2. The Kondo cloud in current cross correlations in helical liquids 89
5.2.1. Model 91
5.2.2. Results 92
5.2.3. Dependence of the central results on interaction strengths . . 96
5.3. Conclusion about the local Kondo impurity 99

6. Magnetically doped strong 3DTI in proximity to a superconductor 100
6.1. Magnetically doped strong 3DTI in the hexagonal warping regime . . 101
6.1.1. Model and RKKY interaction 103
6.1.2. Calculating the spin susceptibility with proper cutoffs 104
6.1.3. Engineering the position of the peaks in the RKKY interaction 105
6.1.4. Spiral ground state and its temperature stability 107
6.1.5. The electronic spectrum in the broken symmetry phase 110
6.1.6. Proximity to a conventional s-wave superconductor 111
6.2. General scheme for gapless topological superconductors 113
6.2.1. Model 115
6.2.2. Results 117

6.2.3. Intuitive model in the small Q limit . . . 120
6.2.4. Conclusions about magnetically doped 3DTI in proximity to a superconductor . . . 121

7. Hybrid systems of topological and semimetallic phases 124
7.1. The four models . . . 126
7.1.1. *Model I*: Gapped Chern insulator coupled to a 2D Dirac metal 127
7.1.2. *Model II*: Gapped Chern insulator coupled to a Chern insulator at its critical point . . . 130
7.1.3. *Model III*: Gapped Chern insulator coupled to a quantum spin Hall state at its critical point . . . 131
7.1.4. *Model IV*: Gapped quantum spin Hall phase coupled to a quantum spin Hall phase at its critical point . . . 134
7.1.5. Summary . . . 140

8. Conclusion & outlook 142

Bibliography 148

III. Appendix 165

A. Deutsche Zusammenfassung und Motivation 166
A.1. Kurze Zusammenfassung . . . 166
A.2. Deutsche Einführung und Motivation . . . 166

B. Officially required appendices 169
B.1. List of publications . . . 169

Part I.

Introduction

1. Introduction & motivation

Modern electronic phases considerably extend the phenomenology of an ordinary Fermi liquid and are hot topics in contemporary solid state physics. Examples are superconductors, Mott insulators, Wigner crystals, nematic phases, and the family of Quantum Hall effects. The latter contains first examples of topologically classified electronic phases. This topological scheme extends the Landau theory and classifies phases that are indistinguishable by spontaneously broken symmetries *[Hasan & Kane, 2010]*. Thereby it extends the understanding of electronic phases considerably. In the recent past, numerous topological insulators have been predicted and discovered *[Bernevig et al., 2006; Brüne et al., 2011; Hasan & Kane, 2010; Hasan et al., 2014; Kane & Mele, 2005a; König et al., 2007]*. These phases stand out by being insulating in their interior but conducting on their edges. The so-called edge channels conduct in a specific way that depends on the spin of the transmitted quasi particles. This unique property opens possibilities for the application of topological insulators in spintronics, having the long term goal of replacing classical electronics in computational machines, and presumably also in quantum computational approaches *[Stern & Lindner, 2013]*.

After the discovery of topological insulators, research was conducted to determine their intrinsic properties and improve the quality of the respective material systems *[Brüne et al., 2011; Hasan et al., 2014]*. This process still continues. As a next step, however, it is interesting to explore the manifold possibilities of combining topological insulators with better-known physical systems. Not at last because truly interesting effects and systems have emerged from such a procedure in the past, for instance, the Josephson junction, the diode and the transistor, and the quantum Hall effects[1].

This thesis contributes to the research about combining topological insulators with other systems. We will not give a complete survey of the vast combinatorial possibilities, a few of which are discussed in *Fu & Kane [2008]; Law et al. [2010]; Lindner et al. [2012]; Liu et al. [2009]; Ström et al. [2010]*. Instead, we focus on a few interesting examples only. To this end, we introduce the bare components in Chapter 2 by explaining what a topological insulator is (Section 2.1) and shortly explain the notions of particular electromagnetic perturbations (Section 2.2), namely the Zeeman effect and the Rashba effect, the Kondo effect (Section 2.2.3),

[1] The quantum Hall effects in their ordinary form combine two-dimensional electron gases and a strong magnetic field.

Ruderman-Kittel-Kasuya-Yosida interactions (Section 2.2.4), and superconductivity (Section 2.3). We then proceed in Chapter 3 by introducing our theoretical equipment: the theory of refermionizable points (Section 3.1), including bosonization and refermionization, a special method to treat divergences stemming from local perturbations (Section 3.2), the Metropolis algorithm (Section 3.3), and information on our transport simulations (Section 3.5). In Part II, we present the analysis of our dressed topological insulators. First, we regard a local Rashba scatterer coupled to a helical liquid with repulsive electron-electron interactions (Chapter 4), the refermionizable point of which surprisingly resembles the non-interacting limit. Next is the two channel Kondo problem for helical liquids (Chapter 5), where we resolve the Kondo cloud for certain parameter configurations exactly and propose a way of measuring it experimentally by cross current correlations. Then, we come to the RKKY interactions between magnetic impurities on a strong three-dimensional topological insulator with warping (Chapter 6). Adding superconductivity to the model generates a peculiar, two-dimensional gapless topological superconductor for which we find a general generating mechanism (Chapter 6.2). In Chapter 7, we try to synthesize a similar phase without superconductivity by coupling a two-dimensional topological insulator to a two-dimensional semimetal and find a rich phenomenology in the presence of disorder. We complete our discussions in Chapter 8 and look at possible future problems for research that base on the presented work. These range from Kondo Majorana braiding to dispersing Jackiw-Rebbi states.

Remarks on the notation and on self-quotations

During the thesis, tuples, vectors and spinors are represented by bold characters, e.g., $\boldsymbol{r} = (x_1, x_2, x_3)^T$. Their absolute value is represented by the same character but with a normal thickness $r = \sqrt{\sum_i x_i^2}$. Matrices or operators are specified in the text and not marked by a special style of the character they are represented by.

This thesis especially relies on the research published in *Posske et al. [2013]*, *Posske & Trauzettel [2014]*, *Baum et al. [2015a]*, and *Baum et al. [2015b]* (all copyrighted by the American Physical Society), which is presented in the Chapters 5, 6, and 7, respectively. These chapters largely reproduce the text of the mentioned publications and their supplemental materials. However, the publications have been restructured, revised and adapted for the presentation in this thesis. Especially, the representation of *[Baum et al., 2015b]* in Chapter 6 has been considerably restructured. Additionally, parts of the publications and their supplemental materials have been employed to introduce the respective topic in Chapter 2 and to explain the employed methods in Chapter 3 without considerable reformulation. This especially regards Section 3.5 and Section 3.2 as well as the first paragraphs of Section 2.1 and Section 2.2.3.

2. Background

2.1. Topological Insulators

The classification and realization of topological states of matter are among the main themes in modern condensed matter physics *[Kitaev, 2009; Qi & Zhang, 2011; Schnyder et al., 2008]*. Of particular interest are topological insulators and topological superconductors, which have drawn a great deal of attention over the past few years *[Bernevig et al., 2006; Chen et al., 2009; Fu & Kane, 2008; Fu et al., 2007; Haldane, 1988; Hasan & Kane, 2010; Hsieh et al., 2009a,b; Kane & Mele, 2005b; König et al., 2007; Moore & Balents, 2007]*. Topological insulators are bulk insulators accommodating metallic edge states that are protected, e.g., by time reversal symmetry or chirality, against the opening of a gap, backscattering, and localization *[Bernevig et al., 2006; Chen et al., 2009; Fu & Kane, 2008; Fu et al., 2007; Hasan & Kane, 2010; Hsieh et al., 2009a,b; Kane & Mele, 2005b; Kitaev, 2009; König et al., 2007; Moore & Balents, 2007; Qi & Zhang, 2011; Schnyder et al., 2008]*. Research regarding topological insulators has been exceedingly active in the past decade regarding both theoretical and experimental physics. Recently, the pursuit of new topological phases of matter has led to the discovery of novel quantum states and exotic excitations in systems that rely on topological insulators *[Fu & Kane, 2008; Hasan & Kane, 2010; Stern, 2010]*. But what is topology and what does topological mean?

Topology is said to be described by Edward Witten with the words: "Topology is the property of something that doesn't change when you bend it or stretch it as long as you don't break anything." *[Lowen, 2015]*. The mathematical theory that abstracts this fundamental understanding of topology has developed to one of the major branches of mathematics. In short, topology is the theory of continuity. As such, it is not surprising that topology can be applied to address numerous physical problems. Some prominent examples are the Aharonov-Bohm effect, twisted space times in general relativity and actions in quantum field theory *[Nash, 1999]*, adiabatic evolution *[Kato, 1950]*, anyons *[Dowker, 1972; Laidlaw & DeWitt, 1971; Leinaas & Myrheim, 1977]*, and many more *[Nash, 1999]*. Nevertheless, the observation *[König et al., 2007]* and description *[Bernevig et al., 2006; Kane & Mele, 2005a; Wu et al., 2006]* of topological insulators have contributed significantly to spread the notions of topology in solid state physics[1]. There are two main ap-

[1] An influential earlier application of topology in solid state physics was the theoretical explanation

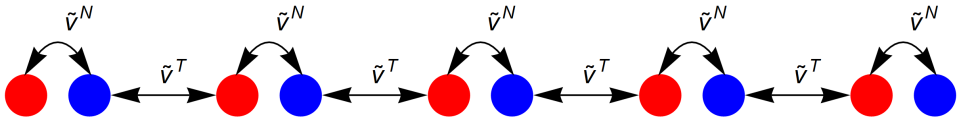

Figure 2.1.: A one-dimensional chain of atoms with a two-atomic unit cell (red and blue). If interactions between sites of the same color are forbidden, the system is described by the family of Hamiltonians in Eq. (2.1) and constitutes a very basic model to exemplify topological order. One possibility to neglect intra species coupling is the limitation to the nearest neighbor interaction, depicted as black arrows.

proaches to topological insulators. One is the more experimentally orientated idea of defining a topological insulator by a gapless bulk and the occurrence and character of its metallic edge channels, which are non-coincidental and to a certain degree protected[2]. The other, more theoretically orientated idea, embarks on a topological strategy to separate topologically trivial and non-trivial phases. The edge states then occur as a consequence of the bulk boundary correspondence *[Hasan & Kane, 2010]*. In the course of this work, we employ both approaches. If possible, we rely on the latter approach, and also introduce the topic of topological insulators in this manner. However, in Chapter 6 and Chapter 7, we introduce gapless topological phases. These special phases lack a well-defined global topological invariant[3]. We therefore then rely on the experimentally motivated definition of a topological phase.

In the following, we want to line out how topology can be applied to classify band insulators, and discuss prominent physical properties of topological insulators, especially their localized edge states. To this end, we first exemplify the most basic concepts by a toy model in Section 2.1.1. We then turn on to describe some of the physically more relevant but methodologically more involved models for topological insulators and their edge states that are encountered in actual research. The first such model describes the quantum spin Hall insulator and the second one describes the surface states of a three-dimensional topological insulator.

2.1.1. A basic topological insulator

In this section, we want to discuss a basic example of a topological insulator to establish the philosophy of applying topological methods to characterize band insulators. Albeit the example is a toy model, it shows the main aspects of a typical

of the quantum Hall effect *[Kohmoto, 1985; Thouless et al., 1982]*.

[2]In case of the quantum spin Hall effect in HgCdTe quantum wells, we have heard Laurens Molenkamp holding this view in several talks during the last years.

[3]The notion of a topological invariant is explained in the remainder of this section.

topological insulator including: topological invariants, the formation of edge states at the boundary of two topologically different systems by the bulk boundary correspondence, the dependence of the edge state localization on the bulk energy gap, and the finite size splitting of the mid-gap modes.

Let us consider periodic chains of atoms with a two-atomic unit cell as shown in Fig. 2.1. Within these systems, we label each atom of the unit cell by a different pseudo spin index and forbid interactions between sites of the same pseudo spin. If we describe the chains in the tight binding approximation, each of them is represented by a Hamiltonian of the form

$$\mathcal{H} = t \int_{k\in \mathrm{BZ}} dk\ \boldsymbol{c}^\dagger(k) H(k) \boldsymbol{c}(k), \tag{2.1}$$

$$H(k) = \left(v_x(k), v_y(k)\right) \left(\sigma_x, \sigma_y\right)^T, \tag{2.2}$$

with the unit of energy t, the annihilation operators $\boldsymbol{c}(k) = \left(c_1(k), c_2(k)\right)^T$ in momentum space, the real functions $v_x(k), v_y(k) : \mathrm{BZ} \to \mathbb{R}$, and the Pauli matrices σ_λ. Here, the Brillouin zone (BZ), is a circle of circumference $\frac{2\pi}{a}$, where a is the lattice constant[4]. The eigenvalues of Eq. (2.1) are

$$\epsilon(k) = \pm t \sqrt{v_x^2(k) + v_y^2(k)}. \tag{2.3}$$

Eventually, we want to detect traces of quantum phase transitions between insulators within the given family of Hamiltonians. To this end, we employ the following definition of an insulating topological phase:

Definition 1 (Topological insulator)**.** *Consider a family of Hamiltonians $\mathcal{H}$. If it is impossible to continuously tune the parameters from one representative insulating Hamiltonian to another one without crossing a metallic phase and without leaving $\mathcal{H}$, the representatives reside in different topological phases[5].*

For a concrete analysis, consider the two Hamiltonians

$$H^T(k) = \left(\sin(ka), -\cos(ka)\right) \left(\sigma_x, \sigma_y\right)^T, \tag{2.4}$$

$$H^N(k) = (0, 1) \left(\sigma_x, \sigma_y\right)^T. \tag{2.5}$$

Evidently, both Hamiltonians share the same spectrum, cf. Eq. (2.3), and therefore, superficially, look alike. A substantial difference between them is revealed by the

[4] The same considerations would apply to infinite systems, where $k \in \mathbb{R}$, if the class of Hamiltonians allows a proper compactification of $\mathbb{R}$. We limit ourselves on periodic systems to keep the discussion as simple and concrete as possible.

[5] At this point, the physical picture behind the definition is only that insulating regions of the parameter space that are thoroughly separated from each other by a metallic region should be different to some degree. That the above definition results in fact in a measurable difference between the two phases is a consequence of the bulk boundary correspondence as introduced below.

application of topological methods, for which we have to describe some general observations. First, our family of Hamiltonians introduced in Eq. (2.1) contains two real degrees of freedom at each point in momentum space, namely v_x and v_y. In order to classify the insulating phases, we first exclude all semimetallic phases, which, analyzing Eq. (2.3), only excludes the case in which there is a $k \in \mathrm{BZ}$ with $v_x(k) = v_y(k) = 0$. A particular insulating Hamiltonian can therefore be interpreted as a mapping from the circle S^1, reflecting the circular Brillouin zone, to the punctured plane $\mathbb{R}^2\backslash(0,0)$, reflecting the v_x-v_y plane without its origin. This mapping is continuous if we reasonably assume that the tight binding model only takes a finite number of neighbors for each unit cell into account. At this point we arrive at the interface between solid state physics and topology. Let us briefly give some remarks to the mathematically interested reader before we come back to a more physical point of view. In the context of topology, two representatives of our family of Hamiltonians belong to different phases if their associated mappings are not homotopic *[Jänich, 2006]*. The required classification of continuous mappings from the circle S^1 to the punctured plane $\mathbb{R}^2\backslash(0,0)$ is a problem considered by mathematicians a long time before the dawn of topological insulators in solid state physics[6]. The object of interest here is the so-called fundamental group π_1 of the punctured plane, which is isomorphic to $\mathbb{Z}$. The problem of characterizing the insulating phases of our toy model is therefore already solved from the mathematical point of view.

However, for not introducing unnecessary abstractness, we want to stay on the physical side to understand the topological classification. The situation is made more transparent by Fig. 2.2. Here, the mappings that are represented by the Hamiltonians H^N and H^T, respectively, are embedded in 3 dimensions. The cyclic Brillouin zone is represented by a tube, whose end points have to be thought of as being identified with each other. Each point of the tube has an attached fiber, which is $\mathbb{R}^2$. We align the origin, $(0,0)$, of each fiber reside on the tube. The attached fiber is now used to plot $v(k)$ at each point $k \in \mathrm{BZ}$. Thereby, the whole Hamiltonian is represented by a string consisting of the graph of $\boldsymbol{v}(k) = (v_x(k), v_y(k))^T$. While the string of H^N (left panel of Fig. 2.2) corresponds to a straight line, the one of H^T (right panel) circles around the tube at $\boldsymbol{v}(k) = \mathbf{0}$ in the form of a spiral. Transforming the latter Hamiltonian continuously into the other amounts to physically dragging and bending the string from the position it occupies in the depiction of H^T to its position in the depiction of H^N[7]. As the respective strings of H^N and H^T wind around the tube a different number of times, it becomes intuitively clear that it is impossible to continuously deform one of the strings into the other without

[6] For an introduction to topology, we can recommend *Jänich [2006]*.

[7] During this procedure, the identification of the starting and end point of the tube has to be kept in mind. Also, the string must not be bent backwards because then the analogy to a mapping $S^1 \to \mathbb{R}\backslash(0,0)$ would be broken.

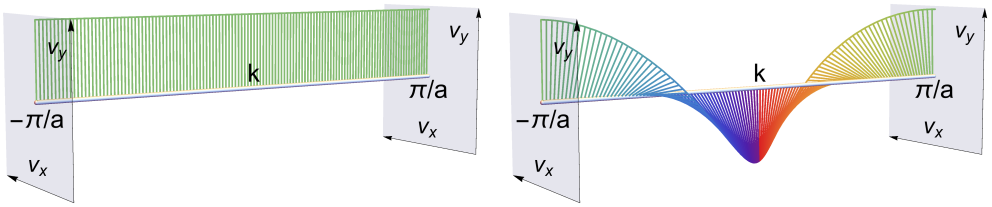

(a) H^N **(b)** H^T

Figure 2.2.: Depiction of the two models in Eq. (2.4) as mappings from S^1 to $\mathbb{R}\backslash(0,0)$ embedded in three dimensions. The Hamiltonians are represented by a string that winds a different number of times around the tube at $\boldsymbol{v}(k) = 0$. Therefore it is impossible to transform H^T and H^N continuously into each other without closing the spectral gap.

letting it cross the tube[8]. The spectral gap closes at this point of the transformation and therefore, regarding our above definition, both Hamiltonians belong to different topological phases. In fact, for our simple example, the classification by this so-called winding number is complete in a sense that all systems of the same winding number are deformable into each other according to the rules, while systems of different winding numbers are not.

2.1.1.1. The bulk boundary correspondence and edge states

Until now, the scheme of topological classification does not result in a distinguishable experimental signature between the different phases it helps to separate[9]. This signature is established by the so-called bulk boundary correspondence: if two systems of a different topological phase are coupled, mid-gap modes develop at the boundary *[Hasan & Kane, 2010]*. An intuitive explanation of the bulk boundary correspondence is given in *Hasan & Kane [2010]*. Consider two systems in a different topological phase that are coupled by a long junction. And consider that the junction deforms the Hamiltonians of the systems continuously into each other. We then know by the above definition of topological phases that the spectral gap closes somewhere within the junction. If we now shrink the junction further and further, the closure of the gap persists until we have shrunken the junction down to a point. The mid-gap states that remain are localized at the junction. The analogy even

[8] This intuition is strengthened by the following experiment. Take two strings. Make a circle out of one (this represents the tube). Wind the remaining string once around the circle (this represents $v(\boldsymbol{k})$ in H^T) and afterwards connect the ends. The construction is impossible to tare apart (which represents the topologically trivial configuration of H^N) without breaking anything.

[9] We assume here that the experimental ability of transforming between the Hamiltonians is not given or at least hard to achieve.

holds when a topologically non-trivial system is coupled to the trivial vacuum. The resulting mid-gap states are called edge states.

We can control the validity of the bulk boundary correspondence in our basic model. By transforming the Hamiltonians of Eq. (2.4) into real space, we obtain

$$\mathcal{H}^T = t \sum_{j=1}^{N} \boldsymbol{c}_j^\dagger \begin{pmatrix} 0 & \mathrm{i} \\ 0 & 0 \end{pmatrix} \boldsymbol{c}_{j+1} + H.c., \tag{2.6}$$

$$\mathcal{H}^N = t \sum_{j=1}^{N} \boldsymbol{c}_j^\dagger \sigma^y \boldsymbol{c}_j \tag{2.7}$$

where $\boldsymbol{c}_j = (c_{j,1}, c_{j,2})^T$ with $\boldsymbol{c}_{N+1} = \boldsymbol{c}_1$ are the real space annihilation operators, and N is the number of lattice sites. At this point, a similarity of our model with the one of *Kitaev [2001]* becomes apparent, which is depicted in Fig. 2.1 by labeling the nearest neighbor interactions with $\tilde{v}^N$ and $\tilde{v}^T$ respectively. While H^N couples the two atoms within one unit cell, which leaves all sites of a finite chain with partners, H^T only couples adjacent atoms of different unit cells. Necessarily, the latter procedure leaves an unpaired atom at each end of the chain. The terminal atoms therefore completely decouple from the Hamiltonian and constitute the mid-gap edge states.

In general, the edge states have a number of interesting physical properties, some of which are named in the introduction of Section 2.1. Here, we want to close this section by elaborating on one seemingly generic feature, namely, that the edge states are exponentially localized at the edge of the system, whereby the localization length is inversely proportional to the bulk energy gap. To this end, we introduce the interpolating Hamiltonian

$$\mathcal{H}^I(\lambda) = \lambda \mathcal{H}^N + (1 - \lambda)\, \mathcal{H}^T. \tag{2.8}$$

The bulk gap of $\mathcal{H}^I(\lambda)$ closes for $\lambda = 1/2$, which is at the phase boundary of a topologically trivial phase for $\lambda > 1/2$ and a non-trivial phase for $\lambda < 1/2$. By realizing $\mathcal{H}^I$ on a finite lattice, we can numerically calculate the density of states and the wave functions of the edge states. The densities of states for a topologically non-trivial system $\mathcal{H}^I(0.4)$ and a trivial system $\mathcal{H}^I(0.6)$ are depicted in Fig. 2.3. As expected, the non-trivial system exhibits mid-gap states that are absent in the trivial system. We can now interpolate linearly between the topologically nontrivial and the topologically trivial system and analyze the localization of the edge states. As shown in Fig. 2.4a, in a semi-logarithmic plot, the edge states are exponentially localized to the boundary of the chain. Furthermore, we calculate their localization length by $l = \sum_{j=1}^{N/2} |\Psi_j|^2 j / \sum_{j=1}^{N/2} |\Psi_j|^2$, where Ψ_j is the single particle wave function of an edge state in spatial representation. Note that we exclude the right edge of the system. The result is shown in Fig. 2.4b, where it can be seen that the localization length depends inversely proportionally on the bulk gap. As we will find out, this property is not obligatory in topological insulators. However, it is

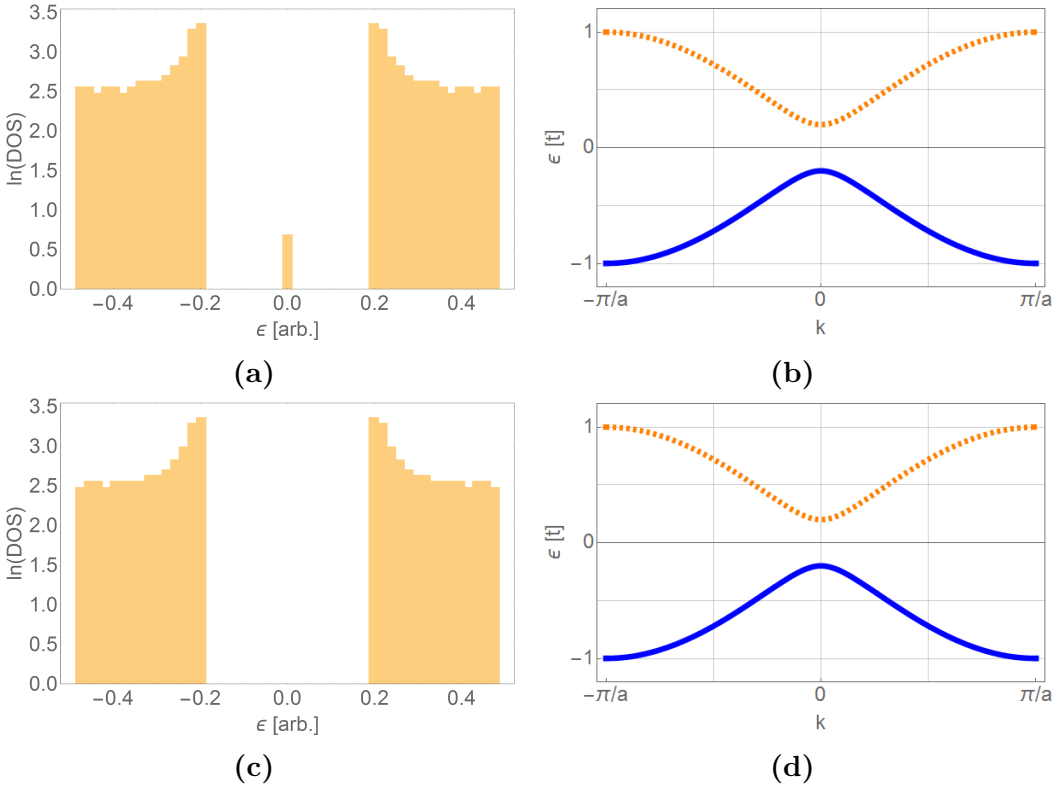

Figure 2.3.: The density of states (DOS) for a finite system and the spectrum for an infinite system of the topologically nontrivial system $\mathcal{H}^I(0.4)$, top panels, and the topologically trivial system $\mathcal{H}^I(0.6)$, bottom panels. The nontrivial system possesses mid-gap zero modes that are localized close to the edges of the system, which are absent in the trivial phase although the depicted spectra coincide. For the numerical simulation regarding the density of states, we took a system consisting of 800 sites and collected the eigenenergies in 101 equally large energy intervals.

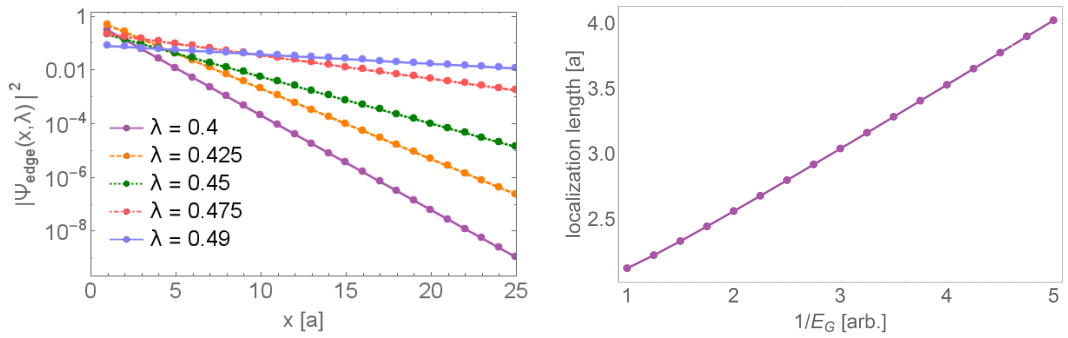

(a) The probability density of the edge states of the topologically nontrivial system.

(b) The localization length, as defined in the text, is approximately proportional to the inverse spectral gap $1/E_G$.

Figure 2.4.: The localization of the edge states for Eq. (2.8). The states are localized close to the boundaries of the 800 sites long system. The edge states get delocalized if the bulk gap closes. For $\lambda = 0.5$, the gap of the bulk is closed and the edge states are completely delocalized[10].

phenomenologically ubiquitous *[Haldane, 1988; Kane & Mele, 2005a; Kitaev, 2001; Qi et al., 2006]*, such that our findings described in Chapter 6 and Chapter 7, where we separate the localization length from the bulk gap energy, come to us as a surprise.

2.1.2. Generalizations of and concepts beyond the presented basic model

The toy model of Section 2.1.1 already introduces a number of basic concepts in the classification of topological matter. If the complexity and the dimensionality of the system rises, the methodology gets more complex as well. We cannot review the vast topic of topological insulators or, even more general, of topological state of matter here. However, we want to indicate the generalizations and introduce the concepts that are specifically needed for the understanding of Part II. For a more complete overview, we refer to *Altland & Zirnbauer [1997]; Budich & Trauzettel [2013]; Chiu et al. [2015]; Hasan & Kane [2010]; Ryu et al. [2010]; Schnyder et al. [2008]*.

Besides the introduced winding number of Section 2.1.1, there is a multitude of

[10] Please note that we add up the contributions of both edge states in Fig. 2.4 to account for numerical instabilities that occur at vanishingly small finite size splitting of the zero modes. Physically, this splitting can be explained by the interaction of the edge states through the finitely sized bulk, which lets them hybridize to a binding and an anti-binding state of negative and positive energy respectively.

different available topological invariants, the importance and applicability of which depend on the system and the question to be addressed. Examples are the homotopy and homology groups and also the Chern classes. An important topological invariant for applications is the Chern number. It is defined for discrete translationally invariant, nondegenerate[11] band insulators of infinite extent as the integral of the Berry flux over the Brillouin zone. The following definition of the Chern number is along the lines of *Hasan & Kane [2010]*. We first assign a Chern number n_m to each band m, where the bands are sorted by their energy eigenvalues:

$$n_m = \frac{1}{2\pi} \int d^2\mathbf{k}\ \mathcal{F}_m(\mathbf{k}), \tag{2.9}$$

with the Berry flux $\mathcal{F} = \nabla_{\mathbf{k}} \times \mathcal{A}_m$, where $\mathcal{A}_m$ is the Berry curvature. If we denote the m^{th} eigenvector – i.e., the eigenvector belonging to the m^{th} eigenvalue – with $|u_m(k)\rangle$, where we choose the eigenvectors to be continuous in $\mathbf{k}$ for the whole Brillouin zone, then the Berry phase is defined by $\mathcal{A}_m = \mathrm{i}\langle u_m(k)|\nabla_{\mathbf{k}}|u_m(k)\rangle$[12]. The Chern number of the system is then defined to be

$$n = \sum_m n_m, \tag{2.10}$$

where the sum runs over all occupied bands. It can be shown that, in analogy to the topological invariant of our basic model in Section 2.1.1, there are no insulators of a different Chern number that are connected by a continuous transformation without closing the bulk gap. The Chern number does not come without physical significance. Calculating the transverse electrical conductance σ_{xy} for a two-dimensional system up to first order in the applied voltage yields *[Hasan & Kane, 2010]*

$$\sigma_{xy} = n\frac{e^2}{h}. \tag{2.11}$$

In fact, the emerging current in a finite system is completely transported by edge channels[13]. Considering that each channel has a perfect conductance of $\frac{e^2}{h}$, the Chern number therefore exactly reflects the number of edge states. A for solid state physics pioneering encounter of a Chern number is described in *Thouless et al.*

[11] The definition of a Chern number is also possible for degenerate bands as long as there is a continuous function depending on the momentum that never touches a band. At the points where bands are degenerate, the later defined eigenvectors have to be chosen to depend continuously on the momentum. This is always possible. However, we do not want to go into detail on this procedure.

[12] By the occurrence of the Berry phase *[Berry, 1984]*, which could be called Kato phase regarding *Kato [1950]*, the topological insulators classified by a Chern number become intrinsically connected to the field of adiabatic dynamics, which puts them into the vicinity of adiabatic and topological quantum computing as well *[Stern & Lindner, 2013]*.

[13] For an interesting approach of explaining why the formulas for the infinitely extended system describe the finite system so well, we would like to mention *Rothe [2015]*.

[1982], which helped in understanding the perfectly quantized Hall conductance of the integer quantum Hall effect. Regarding the present work, we employ the concept of Chern numbers to understand the gapless topological superconductors that we introduce in Chapter 6. Also, we apply this method to analyze the hybrid systems in Chapter 7.

If we invert the arrow of time[14], the edge channels invert their dispersion as well and the Chern number reverses its sign *[Hasan & Kane, 2010]*. Hence, time reversal symmetric systems possess the Chern number $n = 0$. However, there is another invariant that can be non-zero for time reversal symmetric systems: the so-called $\mathbb{Z}_2$ invariant, cf., e.g. *Hasan & Kane [2010]* for a proper definition. This invariant is important for the time reversal protected quantum spin Hall insulator as described in the following Section 2.1.3 and the formation of counter-propagating spin polarized edge channels – the so-called helical liquid.

We infer that the occurrence of additional symmetries alter the usefulness of the topological invariant. This is only natural, as the definition of a topological phase in Definition 1 depends on the considered family of Hamiltonians[15].

A primary classification of Hamiltonians without unitary symmetries is achievable by considering the time reversal $\mathcal{T}$ and the particle-hole conjugation $\mathcal{P}$ together with the resulting unitary chirality $\mathcal{C} = \mathcal{T}\mathcal{P}$. The primary references about this topic are *Altland & Zirnbauer [1997]; Schnyder et al. [2008]*, but the following discussion is based on *Budich & Trauzettel [2013]*. The time reversal is an antiunitary operator that commutes with the Hamiltonian, while the particle-hole conjugation is an antiunitary operator that anticommutes with the Hamiltonian. They obtain their names from the fact that the original, physical time reversal and particle-hole conjugation (in superconductors, cf. Section 2.3) are represented by antiunitary operators of the just described kind. Furthermore, if such an operator exists, it is unique *[Schnyder et al., 2008]*. As the time reversal and the particle-hole conjugation operator each either squares to 1, -1, or is absent, the classification distinguishes 10 symmetry classes. The ten classes are shown in Tab. 2.1, and each is named by a Cartan label *[Cartan, 1926, 1927]*[16]. We rely on them in Chapter 6 and Chapter 7.

[14] Time inversion results, among other effects, in the inversion of momentum and a spin-flip.

[15] Imposing constraints on the family of Hamiltonians often amounts to reducing its dimensionality. The fact that a reduced dimensionality can lead to additional topological richness can be understood by an analogy. Imagine a duck that is surrounded by a fence. The duck can fly above the fence and thereby connect the exterior and the interior. However, if we impose a constraint to the duck by trimming its wings, and thereby reduce the dimensionality of the problem, the duck is trapped inside of the fence. This holds at least "as long as you don't break anything", referring to the quotation of Witten on p. 4. Of course, it does not count that we have already broken the wings of the imaginary duck.

The fence in this analogy represents the region of gap closure, while the available space describes the family of Hamiltonians.

[16] Cartan split the article. The second part explicitly mentions the Cartan labels starting from p.126. Interesting additional information about Cartan and his work can be deduced from

	A	AIII	AI	BDI	D	DIII	AII	CII	C	CI
$\mathcal{T}^2$	0	0	1	1	0	-1	-1	-1	0	1
$\mathcal{P}^2$	0	0	0	1	1	1	0	-1	-1	-1
$\mathcal{C}^2$	0	1	0	1	0	1	0	1	0	1

Table 2.1.: The squares of the antiunitary time reversal $\mathcal{T}$ and particle-hole conjugation $\mathcal{P}$ as well as the chirality $\mathcal{C} = \mathcal{T}\mathcal{P}$ (1, -1, and 0 for an absent symmetry) declare the 10 Cartan-Altland-Zirnbauer classes. Data taken from *Ryu et al. [2010]*.

Simplistically, the classes containing a particle-hole symmetry can be thought of as superconductors, cf. Section 2.3, while the other systems represent normal insulating phases. The possibly apparent time reversal symmetry in these systems can usually be broken by the application of a magnetic field.

The complete topological classification of band insulators and superconductors without unitary symmetries[17] has been carried out in *Ryu et al. [2010]; Schnyder et al. [2008]*. Classifications respecting additional unitary symmetries are treated in *[Chiu et al., 2015]*. For a band insulator of spatial dimension d this is achieved by labeling different topological phases by different elements of the d^{th} homotopy group of a specially constructed topological space $T_{\mathcal{H}}$ that depend on the constrained family of Hamiltonians $\mathcal{H}$ under consideration. This classifies the so-called strong topological insulators. The so-called weak topological insulators are labeled by the homotopy classes of the continuous maps of the d-dimensional torus to $T_{\mathcal{H}}$. *Budich & Trauzettel [2013]* summarize the procedure in greater detail. Regarding this work, we are only interested in strong topological insulators.

In fact, also gapless matter can be classified topologically by employing a different classification scheme, for instance, by local topological invariants that are integrals over the Berry phase along loops in momentum space. Among these systems are Weyl semimetals and nodal superconductors *[Matsuura et al., 2013; Queiroz & Schnyder, 2014]*, which possess topologically stable Fermi points and nodal lines, respectively. These systems have to be regarded in connection with Chapter 6 and Chapter 7.

It remains to be emphasized that the presented discussion is limited to the single particle picture of noninteracting electrons. Current research attempts to extend the application of topological methods to interacting electrons *[Amaricci et al., 2015; Dzero et al., 2010]*.

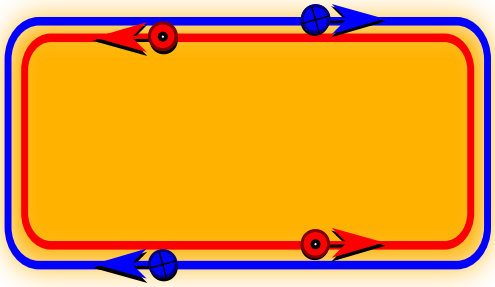

Figure 2.5.: Schematics of the quantum Spin Hall effect. The characteristic features of this topological two-dimensional electronic phase is an insulating bulk (orange) and metallic, time reversal protected edge states. The edge excitations with spin up (blue) circulate clockwise while the spin down (red) excitations circulate conversely.

2.1.3. The quantum spin Hall effect

The quantum spin Hall effect is a two-dimensional electronic quantum phase that can be understood as the spinful brother of the integer quantum Hall effect. Its insulating bulk is encircled by metallic edge states, the helical liquid. The time reversal symmetry protects the helical liquid from elastic backscattering, which leads to a robustly quantized conductance of $G = e^2/h$. The unique feature of the helical liquid is the locking between the direction of motion and the spin of its excitations. Excitations with spin down traverse the edges clockwise, while excitations with spin up propagate conversely. Fig. 2.5 depicts the quantum spin Hall insulator schematically. The effect was predicted to be potentially present in materials with a honeycomb lattice structure *[Kane & Mele, 2005a]*. However, the required spin-orbit coupling is too weak in existing materials, e.g., graphene *[Geim & Novoselov, 2007]*, that the effect of temperature or impurities can be overcome. Instead it has been observed in HgCdTe quantum wells *[König et al., 2007]* and theoretically described *[Bernevig et al., 2006; Kane & Mele, 2005a; Wu et al., 2006]* as a time reversal symmetric topological insulator in the way introduced in Section 2.1.2. Throughout this work, we model the helical edge liquid by a so-called Tomonaga-Luttinger Hamiltonian of the form

$$\mathcal{H} = \sum_{\sigma\in\pm\equiv\{\downarrow,\uparrow\}} \int dx \left[-\mathrm{i}v_F\sigma\left(\Psi_\sigma\Psi'_\sigma\right) + \frac{g_4}{2}\rho_\sigma^2 + \frac{g_2}{2}\rho_\sigma\rho_{-\sigma}\right](x), \tag{2.12}$$

with the fermionic operators Ψ, their spatial density ρ, the Fermi velocity v_F and the interaction parameters g_2 and g_4 *[von Delft & Schoeller, 1998]*. Note that the neglect

Chern & Chevalley [1952].

[17] That means the momentum space Hamiltonians fall apart into the classes of Tab. 2.1 and are not preliminary reducible by additional unitary symmetries.

of a backscattering interaction here is exact as this type of interaction would break the required time reversal symmetry. The Hamiltonian is conveniently diagonalized in its bosonized form, as introduced in Section 3.1 and performed in Section 3.1.3. The same Hamiltonian is employed by a number of authors to describe the edge states of a quantum spin Hall insulator, cf. *Budich et al. [2012]; Law et al. [2010]; Maciejko et al. [2009]; Tanaka et al. [2011]* just to name a few of them. However, the helical liquid, as a surface effect, is intrinsically connected to the two-dimensional bulk it is generated from, which result in subtleties regarding the interpretation of the results and the applicability of the model, especially for strong interactions *[Hohenadler & Assaad, 2012]*.

2.1.4. Fu's model for the surface states of a three-dimensional strong topological insulator

Three-dimensional strong topological insulators, in contrast to their two-dimensional counterparts, are reported to be experimentally observed in a number of experimental systems. Examples are Bi_xSb_{1-x}, Bi_2Se_3, Bi_2Te_3, Sb_2Te_3, Bi_2Te_2Se, $GeBi_2Te_4$ and strained HgTe *[Brüne et al., 2011; Hasan & Kane, 2010; Hasan et al., 2014; Miyamoto et al., 2012; Neupane et al., 2012; Sato et al., 2010]*. The surface states of all besides the latter material are remarkably well observable with angle resolved photo emission spectroscopy. But as a drawback, the currently achievable purity of the samples is not high enough to extract genuine surface transport. An exception is strained HgTe, where it was possible to observe the quantum Hall effect in the surface liquids *[Brüne et al., 2011]*.

The superficial electronic spectra of three-dimensional topological insulators possess a Dirac node at the Γ point that obeys a specific form of spin momentum locking *[Fu, 2009]* and the Fermi surface becomes anisotropic for chemical potentials away from the Dirac node *[Hasan et al., 2014; Miyamoto et al., 2012; Neupane et al., 2012; Sato et al., 2010]*. Here, the rotational symmetry of the Dirac node is broken down to a C_6 symmetry[18]. This so-called warping renders the Fermi surface nearly hexagonal[19] for a broad range of chemical potentials.

The surface liquid of strong three-dimensional topological insulators are for a wide class of systems well described by the low energy Hamiltonian of *Fu [2009]*

$$\mathcal{H}_0 = \int d^2\mathbf{k}\, \mathbf{c}_\mathbf{k}^\dagger \left(v_0 \left(k_x\sigma_y - k_y\sigma_x\right) + \gamma w(\mathbf{k})\sigma_z\right) \mathbf{c}_\mathbf{k}. \tag{2.13}$$

Here, $\sigma^{x,y,z}$ are the Pauli matrices in spin space, $w(\mathbf{k}) = (k_+^3 + k_-^3)/2$ with $k_\pm = k_x \pm \mathrm{i}k_y$, v_0 is the electron velocity near the Dirac point, which originates from

[18] The discrete rotational symmetries are denoted by C_i where i is the number of times the object is mapped to itself within a full rotation of 2π.

[19] Although the Hamiltonian is only C_3 symmetric, the Fermi surface follows a C_6 symmetry.

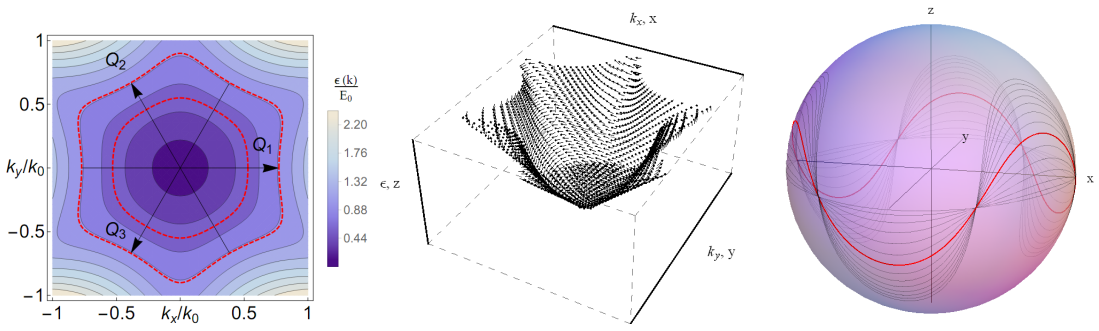

(a) **(b)** **(c)**

Figure 2.6.: The spectrum and eigenvectors of $\mathcal{H}_0$ in Eq. (2.13). Departing from the Γ point, the initially circular Fermi surface becomes hexagonal with the nesting vectors $\pm(Q_i)_{i=1}^3$. **(a)** Fermi surfaces for various chemical potentials. The hexagonal regime is marked off by red, dashed lines. Figure reprinted with permission from *Baum et al. [2015b]*. Copyright (2015) by the American Physical Society. **(b)** Three-dimensional depiction. Exemplary eigenvalues are equipped with their eigenvector represented on the Bloch sphere. **(c)** The nontrivial spin texture of the model. Each shown line on the Bloch sphere is the image of the Fermi surface for a given chemical potential under the function that maps a momentum to the corresponding eigenvector of $\mathcal{H}_0$.

Rashba spin orbit coupling[20], and γ is the warping parameter, which describes the cubic Dresselhaus spin-orbit coupling of the bulk. Furthermore, $\mathbf{c_k} = (c_{\mathbf{k},\uparrow}, c_{\mathbf{k},\downarrow})^T$ with $c_{\mathbf{k},\sigma}$ being a fermionic annihilation operator for excitations with momentum $\mathbf{k}$ and spin σ. We will rely on this model in Chapter 6, where we use it to describe the surface excitations of our strong topological insulator.

In the following, we set the unit of energy to $E_0 = |v_0^3\gamma^{-1}|^{1/2}$, the unit of momentum to $k_0 = |v_0\gamma^{-1}|^{1/2}$ and $\hbar = 1$. Also, for simplicity, the energy of the Dirac point is taken to be the energy of reference compared to which all energies are measured relatively. The warping is depicted in Fig. 2.6. Starting from a circular Fermi surface at the Γ point, the Fermi surface gets hexagonal and afterwards develops a 'snowflake' shape with increasing chemical potential. Of special importance is the hexagonal regime, which corresponds to chemical potentials in the energy range of $0.55E_0$ to $0.9E_0$ *[Baum & Stern, 2012b]*.

[20] We will explain Rashba terms in Section 2.2.2.

2.2. Magnetic and electric perturbations

2.2.1. Zeeman terms

The Zeeman effect *[Zeeman, 1897]* originally denotes the linear splitting of atomic spectral lines due to the application of a small, static magnetic field. It is explained by the direct coupling of the electron's magnetic moment to the magnetic field. Here, the total magnetic moment of the electron is generated by its angular momentum $\mathbf{J}$, which results from both the orbital and the spin contribution[21]. The effect is readily implemented by the Hamiltonian

$$\mathcal{H}_Z = \sum_{j,j'} \int \mathbf{dx}\ \Psi_j^\dagger(\mathbf{x}) m^z J^z_{j,j'} \Psi_{j'}(\mathbf{x}), \tag{2.14}$$

where Ψ_j is the annihilation operator of the electrons under consideration with the magnetic quantum number $j \in \{-J, -J+1, \ldots, J\}/\hbar$, the Zeeman field $\mathbf{m}$, which includes the g factor and is proportional to the effective magnetic field in the solid, and $\mathbf{J}$, which describes the angular momentum matrices of the respective total angular momentum. Here, we have chosen $\mathbf{m}$ to point into the z direction without loss of generality.

Terms of the form of $\mathcal{H}_Z$ (Eq. (2.14)) that appear in an effective low energy Hamiltonian are still called Zeeman terms, irrespective of their origin. Interestingly, the original Zeeman term itself can also be seen as an effective term derived from the Dirac Hamiltonian as it appears in the nonrelativistic Pauli Hamiltonian, compare, for instance, *Bárðason [2008]; Winkler [2003a]*. The effective Zeeman terms may in fact be much larger than the original one *[Reinthaler et al., 2015; Winkler, 2003a]* and can be of surprising origin. For instance, in the effective model for the conduction and valence band in semiconductors with zincblende lattice structure, the Zeeman term originates solely from the included spin-orbit coupling[22] *[Winkler, 2003a]*.

We will introduce Zeeman terms into our models in Chapter 6 and Chapter 7 to conveniently open spectral gaps.

2.2.2. Rashba terms

The Pauli Hamiltonian, derived as an effective theory from the Dirac Hamiltonian, does not only contain the Zeeman term (cf. Section 2.2.1), it also contains the spin

[21] The spin orbit coupling is assumed to be of Russel-Saunders type.
[22] In the sense that the Zeeman term vanishes as soon as we neglect the spin-orbit coupling.

orbit interaction *[Winkler, 2003a]*[23]

$$\mathcal{H}_{\mathrm{SO}} = \boldsymbol{\sigma}\,(\boldsymbol{k} \times \boldsymbol{E})\,. \tag{2.15}$$

Here, $\boldsymbol{\sigma}$ is the vector containing the Pauli spin matrices, $\boldsymbol{p}$ is the momentum operator, and $\boldsymbol{E}$ is proportional to the external magnetic field. As in Section 2.2.1 about the Zeeman term, the prefactors are included in the effective field $\boldsymbol{E}$ as not the term itself but rather its general structure is important here. Regarding equivalent formulations, we want to emphasize that $\boldsymbol{A}\cdot(\boldsymbol{B}\times\boldsymbol{C}) = (\boldsymbol{A}\times\boldsymbol{B})\cdot\boldsymbol{C}$, which renders Eq. (2.15) ambiguous and may lead to initial confusion when comparing it within the literature.

Due to Rashba's contributions of considering Eq. (2.15) in effective solid state theories *[Bychkov & Rashba, 1984]*, terms of the form of Eq. (2.15) are called Rashba terms or Rashba spin orbit coupling. In lower-dimensional systems, $\mathbf{E}$ is typically regarded to be aligned perpendicularly to the plane or line of motion of the electronic excitations. Here, the quantity $\mathbf{E}$ is not necessarily representing an external electric field. For instance, in two-dimensional systems, Rashba terms can be generated by bulk inversion asymmetry[24], which constitutes an intrinsic Rashba interaction *[Winkler, 2003b]*. Additionally, Rashba terms are generated by breaking the structural inversion symmetry, which describes the spatial inversion symmetry of the system along the direction of $\mathbf{E}$. A structural inversion asymmetry may in fact but does not need to be caused by a physical electric field *[Rothe et al., 2010; Winkler, 2003b]*. It is common to slightly abuse the term Rashba effect for spin splitting induced by structural inversion asymmetry in general according to *Winkler [2003c]* instead of limiting the name to terms of the structure given in Eq. (2.15).

In Chapter 4, we will consider a local Rashba scatterer attached to a helical liquid, which can, in regard to this section, be induced by a locally applied electric field that is aligned perpendicularly to the one-dimensional system.

2.2.3. Kondo physics and the Kondo cloud

Kondo physics *[Hewson, 1997; Kondo, 1964]* is a term describing the emerging physics of systems that consist of a localized spin degree of freedom coupled to one or multiple spin baths[25]. Therefore, the Kondo setup is one of the most basic assemblages of quantum mechanical systems with spin. Yet its description has attracted the attention of theoretical as well as experimental physicists already for

[23] Additionally, the Pauli Hamiltonian contains the so-called Darwin term and terms of higher order in the momentum, the electromagnetic potential, or both together *[Winkler, 2003a]*, which are of no importance here.

[24] Bulk inversion symmetry is the symmetry of the unit cell under point reflection.

[25] The name affix Kondo is also used with reference to multiple localized magnetic moments (as opposed to a single one) as reflected by the terms Kondo lattice *[Tsunetsugu et al., 1997]* and Kondo insulator *[Coleman, 2007]*.

many decades *[de Haas et al., 1934; Hewson, 1997; Kondo, 1964]*. In recent years, peculiarities relating to a plethora of realizations of the spin bath have been investigated *[Furusaki & Nagaosa, 1994; Leggett et al., 1987; Maciejko et al., 2009; Martinek et al., 2003; Müller-Hartmann & Zittartz, 1971]*. The spin bath is usually, but not necessarily, considered to be fermionic.

A comprehensive introduction to the main aspects of the topic is given by *Hewson [1997]*, and *Kouwenhoven & Glazman [2001]* supplies an overview on its history until recently. We want to summarize and extend the therein mentioned historical milestones that are of particular importance for this thesis. The first observation of Kondo physics happened accidentally and was reported in 1934 by *de Haas et al. [1934]*. In low temperature experiments, the conductance of several metals was measured. In contrast to the general expectancy, built up by the at that time recent experiments that led to the discovery of superconductors *[van Delft & Kes, 2010]*, the conductance did not increase in temperature for all samples but instead decreased for the magnetically contaminated ones. In 1964, Jun Kondo published a theoretical derivation of this effect derived from first principles *[Kondo, 1964]*. His success has until now coined the name of the whole field. Numerous theorists improved the theory of Kondo physics in subsequent years. In the frame of this work, the quest for exact solutions of Kondo models are of particular interest. The first steps into this direction were gone by Toulouse as described in *Toulouse [1969]*. The spirit of his idea was to transform the Kondo model unitarily so that the Hamiltonian becomes quadratic for a particular configuration of the parameters, the so-called Toulouse point. Toulouse only applied his method to the original one channel Kondo model, where a magnetic moment belonging to a spin of $\hbar/2$ is coupled to one lead. The work of *Emery & Kivelson [1992]*, followed by the work of *Schiller & Hershfield [1998]* and *von Delft et al. [1998]; Zaránd & von Delft [2000]* extended the underlying idea to the two channel Kondo model. For this work, a Kondo model is referred to as having two channels if the attached two leads couple independently to the magnetic moment[26]. This is not easily achievable experimentally *[Nozieres & Blandin, 1980]*, but can be observed with some effort *[Potok et al., 2007]*. There are proposals *[Béri & Cooper, 2012; Fabrizio & Gogolin, 1995; Law et al., 2010; Oreg & Goldhaber-Gordon, 2004]* employing electron-electron interactions in the leads and, more exotic, Majorana fermions to increase the experimental accessibility of the two channel regime. Coming back to *Emery & Kivelson [1992]*, the one exactly solvable Toulouse point was extended in this context to become an Emery-Kivelson line, reflecting that one real degree of freedom could be chosen arbitrarily without departing the set of exactly solvable parameter configurations. For the one channel Kondo model, the exact solubility went even further. Here, a modified Bethe ansatz *[Bethe, 1931; Karbach & Muller, 1998]* was found by *Andrei [1980]* and *Wiegmann*

[26] An independent coupling especially excludes electron transfer processes from one lead to the other.

[1981] that delivers exact results for the whole parameter space.

The interest in the Kondo effect increased again especially in the last decades, where it became possible to engineer quantum dots that act as Kondo impurities *[Kouwenhoven & Glazman, 2001]*. Consequently, many of the theoretical predictions could be verified in experiments. For instance, the zero-bias anomaly in the conductance and the Kondo resonance in the density of states *[Hewson, 1997]*. But there still remain puzzling details. One of the archetypal phenomena in Kondo physics that is still a subject of active research is the characteristic screening of the local spin, which occurs at temperatures smaller than the Kondo temperature: while theorists predict the excitations of the fermionic bath to orientate their spin to screen the magnetic moment on a macroscopic scale, experimental confirmation of this unique correlation is still lacking *[Affleck, 2010; Affleck & Simon, 2001; Borda, 2007; Müller-Hartmann, 1969; Park et al., 2013; Simonin, 2007]*. This considerably long-ranged screening "cloud" of excitations has been termed the Kondo cloud[27].

A concrete observable that quantifies the presence of the Kondo cloud at a given position in the fermionic bath is the equal time correlator between the spatially dependent spin density in the bath $\boldsymbol{S}(x)$ and the spin of the magnetic moment $\boldsymbol{\tau}$ *[Müller-Hartmann, 1969; Nagaoka, 1965]*. As the Kondo cloud is expected to reflect the rotationally invariance of a spin singlet, we regard only the z components of the respective quantities, i.e.,

$$\chi^z(x) = \langle \delta S^z(x) \delta \tau^z \rangle, \tag{2.16}$$

where $\delta C = C - \langle C \rangle$ and $\langle \dots \rangle$ denotes the expectation value of a given operator in a given system. In fact, we are going to use the correlator of Eq. (2.16) as a synonym for the Kondo cloud throughout this thesis.

Problems related to the direct detection of the Kondo cloud are the high frequency at which the local spin is flipping and the fundamental inability to directly measure correlations between the local spin and the lead-spin without decisively perturbing the tunneling region.

For instance, there appear diverse technical and conceptual problems if it is attempted to directly measure the Kondo cloud with two spin-sensitive scanning tunneling microscopy (STM) tips *[Borda, 2007]*. Conceivably, the most conceptually problematic aspect in this case is that the coupling of a spin sensitive STM tip to the magnetic moment is likely to influence the Kondo effect and hence the Kondo cloud itself.

[27] That screening arises is not surprising. In many cases, if a bath of fermions is coupled to an impurity, the bath tries to screen the effect of the impurity on itself. Almost as if the bath identifies an intruder and wants to keep it out. For instance, bringing additional charge Q close to a fermionic bath, the excitations screen the excess charge by accumulating a total amount of charge $-Q$ around the impurity *[Mahan, 2000]*. Similarly, the spin of the Kondo impurity is screened by a collective behavior of the excitations in the leads.

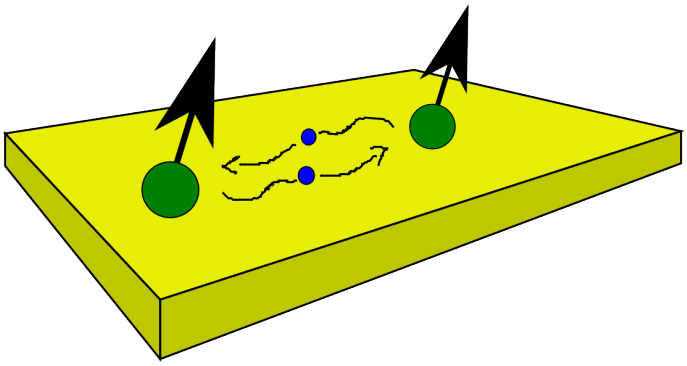

Figure 2.7.: Sketch of the idea behind the RKKY interaction: An effective spin-spin interaction is mediated by itinerant particles.

In this regard, a more promising experiment to measure the Kondo cloud should employ an indirect measurement that does not affect the close vicinity of the magnetic moment *[Affleck, 2010]*. Along these lines, recent suggestions propose to first find an observable that alters its behavior decisively upon reaching the Kondo length *[Affleck & Simon, 2001; Park et al., 2013; Pereira et al., 2008]*. Notably, *Patton et al. [2009]* mention a visible signature of the Kondo cloud in conductance fluctuations close to the magnetic moment.

New light on the Kondo cloud can be shed by means of the recently discovered quantum spin Hall insulator *[Bernevig et al., 2006; Kane & Mele, 2005a; König et al., 2007]*. Systems, where a magnetic moment is coupled to helical liquid leads, have already been analyzed *[Law et al., 2010; Maciejko, 2012; Maciejko et al., 2009]*. However, the focus never lay on the Kondo cloud. We have closed this gap in *Posske et al. [2013]; Posske & Trauzettel [2014]*, which we also present in Chapter 5. Not only do we give a method to analytically calculate the Kondo cloud in a two channel Kondo setup – a method which is readily applicable to the single channel case as well – we also discover a one to one correspondence of the Kondo cloud to current correlations far away from the Kondo region and thereby propose a minimally invasive way of detecting the Kondo cloud in helical liquids.

2.2.4. The RKKY approximation

The direct possibilities of two spins to influence each other are via the exchange interaction, if they stem from two indistinguishable particles, or via the interaction of their magnetic moments. However, they are able to interact indirectly as well, if both spins are coupled to a common reservoir of particles, using the itinerant excitations of the reservoir as mediators of the interaction. In general, this kind of interaction is time delayed – as the particles require time to travel from one spin to the other – and depends on the spin texture of the mediating particles.

However, if the motion of the particles is considerably faster than the resulting motion of the spins, an effective model is physically reasonable that only consists of the spins themselves and a direct spin-spin interaction. This idea was applied first by *Ruderman & Kittel [1954]* to describe a long ranged interaction between nuclear spins embedded in an electron gas. Due to the additional contributions of *Kasuya [1956]*, and *Yosida [1957]*, the effective interaction became known as the RKKY interaction. Despite its origin, the idea is not limited to nuclear spins but can be applied to, e.g., magnetic dopants, adatoms, quantum dots or nano magnets in solid state systems as well. Motivated by its simple picture, the RKKY interaction only depends on the properties of the itinerant particles and therefore, instinctively, mostly on properties of the reservoir close to the Fermi energy. This property will be important for the underlying idea of Chapter 6, which uses nesting to significantly increase the strength of the RKKY interactions. Furthermore, the Kondo effect, which screens the magnetic moment of the attached spin by building the Kondo cloud out of the itinerant fermions, is competing with the RKKY interaction. The validity of the RKKY approximation is therefore intuitively limited to inter-spin distances that do not exceed the Kondo length scale.

Imagine spinful electrons that are coupled to a set of magnetic impurities. The Hamiltonian is

$$\mathcal{H} = \mathcal{H}_0 + \mathcal{H}_0^s + \sum_i \sum_{\lambda\in\{x,y,z\}} J^\lambda \mathbf{c}^\dagger(\boldsymbol{r_i})\sigma^\lambda \mathbf{c}(\boldsymbol{r_i}) S_i^\lambda. \tag{2.17}$$

Here, $\mathcal{H}_0$ describes the spinful fermions, which are represented by the fermionic annihilation spinors in real space $\mathbf{c}(\boldsymbol{r}) = (c_\uparrow(\boldsymbol{r}), c_\downarrow(\boldsymbol{r}))^T$, the spins are represented by the spin operators S_i^λ with $\lambda \in \{x, y, z\}$, $i \in I$ with the index set I that labels the spatial positions of the magnetic impurities. Additionally, J^λ are real coupling constants and σ^λ are the Pauli matrices.

The question about the effective spin-spin Hamiltonian that describes Eq. (2.17) best can be approached in various ways. Here, we want to derive an effective Hamiltonian that does not take multiple interactions of the itinerant fermions with the spins into account. This effect was originally considered by Ruderman and Kittel. Higher orders can be included by the Lloyd formula *[Lloyd, 1967]*. If we want to find a Hamiltonian that corresponds to Eq. (2.17), consisting only of the spin degrees of freedom, it has to have the same expectation values up to second order in the spin-fermion interaction regarding all operators A that only consist of spin operators. If we write down the expectation value of A up to second order using the Keldysh

formalism *[Rammer, 2007]*, we obtain

$$\begin{aligned}\langle A\rangle =& \langle \mathcal{T}A\rangle_0 - \mathrm{i}\int_c d\tau \sum_{i\in I}\sum_{\lambda\in\{x,y,z\}} J^\lambda \underbrace{\langle \mathcal{T}\boldsymbol{c}^\dagger(\boldsymbol{r_i},\tau)\sigma^\lambda \boldsymbol{c}(\boldsymbol{r_i},\tau)\rangle_0}_{:=m_i^\lambda=0 \text{ (magnetization of } \mathcal{H}_0)} \left\langle \mathcal{T}S_i^\lambda(\tau)A(t)\right\rangle_0 \\ &- \int_c d\tau d\tau' \sum_{i,j}\sum_{\lambda,\lambda'} J^\lambda J^{\lambda'} \left\langle \mathcal{T}\left(\boldsymbol{c}^\dagger(\boldsymbol{r_i},\tau)\sigma^\lambda \boldsymbol{c}(\boldsymbol{r_i},\tau)\right)\left(\boldsymbol{c}^\dagger(\boldsymbol{r_j},\tau')\sigma^{\lambda'} \boldsymbol{c}(\boldsymbol{r_j},\tau')\right)\right\rangle_0 \\ &\times \left\langle \mathcal{T}S_i^\lambda(\tau)S_j^{\lambda'}(\tau')A(t)\right\rangle_0 + \mathcal{O}(J^3) \\ =&\langle A\rangle_0 + \mathrm{i}\int_c d\tau d\Delta\tau \sum_{i,j}\sum_{\lambda,\lambda'} J^\lambda J^{\lambda'}\chi_{i,j}^{\lambda,\lambda'}(\Delta\tau)\left\langle \mathcal{T}S_i^\lambda(\tau)S_j^{\lambda'}(\tau-\Delta\tau)A\right\rangle_0 + \mathcal{O}(J^3),\end{aligned} \tag{2.18}$$

where $\langle \dots \rangle$ denotes the expectation value with respect to $\mathcal{H}$, $\langle \dots \rangle_0$ the expectation value with respect to $\mathcal{H}_0$, and $\int_c d\tau \dots$ is the integral over the Keldysh contour. Here, $m_i^\lambda = \langle \mathcal{T}\boldsymbol{c}^\dagger(\boldsymbol{r_i},0)\sigma^\lambda \boldsymbol{c}(\boldsymbol{r_i},0)\rangle_0$ is the magnetization of the fermions, which we assume to vanish[28], and

$$\chi_{i,j}^{\lambda,\lambda'}(\tau-\tau') = \mathrm{i}\langle \mathcal{T}\left(\boldsymbol{c}^\dagger(\boldsymbol{r_i},0)\sigma^\lambda \boldsymbol{c}(\boldsymbol{r_i},0)\right)\left(\boldsymbol{c}^\dagger(\boldsymbol{r_j},\tau'-\tau)\sigma^{\lambda'} \boldsymbol{c}(\boldsymbol{r_j},\tau'-\tau)\right)\rangle_0 \tag{2.19}$$

is the time and space dependent spin-spin correlation. We now apply the approximation of an instantaneously transmitted interaction between the spins, which we implement by neglecting $\Delta\tau$ in the argument of the spin expectation value $\left\langle \mathcal{T}S_i^\lambda(\tau)S_j^{\lambda'}(\tau-\Delta\tau)A\right\rangle_0$[29]. The physical motivation behind this is that for sufficiently fast dynamics of the fermions, their spin-spin correlation $\chi_{i,j}^{\lambda,\lambda'}$ decays to zero before the spins have substantially changed their orientation. Note that this approximation is not valid for systems with temporally stable spin-spin correlations of the itinerant particles, like ferro- or antiferromagnetic models. We have already excluded those systems by assuming a vanishing magnetization of the reservoir. Thereby, we obtain

$$\langle A\rangle = \langle A\rangle_0 - \mathrm{i}\int_c d\tau\ \langle \mathcal{T}\left(\mathcal{H}_{\mathrm{RKKY}}(\tau)\, A\right)\rangle_0 + \mathcal{O}(J^3). \tag{2.20}$$

with the RKKY Hamiltonian

$$\mathcal{H}_{\mathrm{RKKY}} = -\sum_{i,j}\sum_{\lambda,\lambda'} J^\lambda J^{\lambda'}\chi_{i,j}^{\lambda,\lambda'} S_i^\lambda(\tau) S_j^{\lambda'} \tag{2.21}$$

[28] Note that effects of a steady magnetization of the electrons would result in a first order (in J) effect on the spins. The expected effects would therefore dominate the RKKY interaction, which is a second order effect.

[29] This effectively amounts to setting $\chi_{i,j}^{\lambda,\lambda'}(\Delta\tau) = \delta_c(\Delta\tau)\int_c d\tilde{\tau}\chi_{i,j}^{\lambda,\lambda'}(\tilde{\tau})$ with the contour delta function δ_b.

and the spin susceptibility

$$\chi_{i,j}^{\lambda,\lambda'} = \int_c d\tilde{\tau}\ \chi_{i,j}^{\lambda,\lambda'}(\tilde{\tau}). \tag{2.22}$$

As we see, under the assumptions of (i) a dynamics of the itinerant particles that is considerably faster than the dynamics of the spins and (ii) the valid exclusion of a static magnetization within the fermionic system, all observables of the spin system that are calculated in perturbation theory up to second order in the spin-fermion coupling J are the same as calculated by the first order approximation using the RKKY Hamiltonian of Eq. (2.21) instead. We have thereby arrived at an effective model that (up to first order in J) solely describes the spin degrees of freedom.

The application of the perturbative expansion indicates that we assume the Hamiltonian of the bath to be quadratic. If we furthermore assume that only one spinful particle species couples to the spins and that their Hamiltonian is translationally invariant, i.e., that it is describable by a Hamiltonian in momentum space that we call $H_0(\boldsymbol{k})$, the spin susceptibility χ can be expressed in a more suitable form for calculations. We restrict ourselves to the two-dimensional case and two dimensional Hamiltonians H_0 although the given formulas can readily be generalized to higher dimensions:

$$\chi_{\boldsymbol{r},\boldsymbol{r'}}^{\lambda,\lambda'} = \int_{-\infty}^{\infty} d^2\mathbf{q}\ \frac{e^{-\mathrm{i}\mathbf{q}\cdot(\boldsymbol{r}-\boldsymbol{r'})}}{(2\pi)^2}\chi_{\boldsymbol{q}}^{\lambda,\lambda'}, \tag{2.23}$$

$$\chi_{\boldsymbol{q}}^{\lambda,\lambda'} = \lim_{\eta\to 0}{}^{30} \int_{-\infty}^{\infty} d^2\boldsymbol{k} \sum_{\tau,\rho=\pm} \frac{f_{\beta,\mu}(\epsilon_k^\tau) - f_{\beta,\mu}(\epsilon_{\boldsymbol{k}+\boldsymbol{q}}^\rho)}{\epsilon_{\boldsymbol{k}}^\tau - \epsilon_{\boldsymbol{k}+\boldsymbol{q}}^\rho - \mathrm{i}\eta} Y_{\tau,\rho}^{\lambda,\lambda'}(\boldsymbol{k},\boldsymbol{k}+\boldsymbol{q})\theta_{\boldsymbol{k},\boldsymbol{q},\Lambda_-,\Lambda_+}^{\tau,\rho}, \tag{2.24}$$

where $\epsilon_{\boldsymbol{k}}^\alpha$ with $\alpha \in \{+,-\}$ describes the two eigenvalues of $H_0(\boldsymbol{k})$, $f_{\beta,\mu}$ is the Fermi Dirac distribution function at the inverse temperature β and the chemical potential μ, and

$$Y_{\tau,\rho}^{\lambda,\lambda'}(\boldsymbol{k},\boldsymbol{k}+\boldsymbol{q}) = s_{\tau,\rho}^{\lambda}(\boldsymbol{k},\boldsymbol{q})\left(s_{\tau,\rho}^{\lambda'}(\boldsymbol{k},\boldsymbol{k}+\boldsymbol{q})\right)^*, \tag{2.25}$$

with

$$s^\lambda(\boldsymbol{k},\boldsymbol{k'}) = U^\dagger(\boldsymbol{k})\sigma^\lambda U(\boldsymbol{k'}). \tag{2.26}$$

Here $U(\boldsymbol{k})$ denotes a matrix that diagonalized $H_0(\boldsymbol{k})$. The last symbol of Eq. (2.23) explicitly takes the possibly existing energy cutoffs Λ_+ and Λ_- of the model H_0 into

[30] Here, η is a quantity that regularizes the integrand and stems from switching the orders of a contour time and a momentum integration in our derivation. This quantity has been omitted by *Ruderman & Kittel [1954]* and instead, the principal value of the integral was taken to render it well defined (the principal value is hidden behind the $\beta \to \infty$ limit in *Ruderman & Kittel [1954]*). We can, however, not find any difference between the results of the integral of our method and the method of *Ruderman & Kittel [1954]* in any dimension, such that taking the principal value integral seems to be an equivalent regularization in this case.

account and thereby ensures that its validity regime is not left. We define

$$\theta^{\tau,\rho}_{\mathbf{k},\mathbf{q},\Lambda_-,\Lambda_+} = \begin{cases} 1 \text{ if } \epsilon^\tau(\mathbf{k}), \epsilon^\rho(\boldsymbol{k}+\boldsymbol{q}) \in (\Lambda_-, \Lambda_+) \\ 0 \text{ else.} \end{cases} \tag{2.27}$$

In this equation, Λ_- denotes the lower energy cutoff and Λ_+ the upper cutoff. Given the analytical structure of the RKKY interaction in Eq. (2.23) we can now infer its sensitivity to nesting in a more rigorous way. For this reason, we regard the appearing fraction $\frac{f_{\beta,\mu}(\epsilon^\tau_k) - f_{\beta,\mu}(\epsilon^\rho_{\mathbf{k}+\mathbf{q}})}{\epsilon^\tau_{\mathbf{k}} - \epsilon^\rho_{\mathbf{k}+\mathbf{q}} - \mathrm{i}\eta}$, which becomes large for $\epsilon^\tau_{\boldsymbol{k}} \approx \epsilon^\rho_{\boldsymbol{k}+\boldsymbol{q}}$ as a cause of divergence of the denominator, and the numerator ensures that this divergence only appears at the Fermi level. Now, if the Fermi surface of the system exhibits nesting, there is (by definition of the term nesting) a fixed vector $\boldsymbol{Q}$ of which we know that for all $\boldsymbol{k}$ lying on the Fermi surface, the considered fraction becomes arbitrarily large. These contributions add up to strongly enhance the integral, thereby the spin susceptibility, and consequently also the RKKY interaction.

The specific RKKY interaction for a spinful, spin-degenerate, quadratically dispersing fermions has been calculated by *Ruderman & Kittel [1954]* (for three-dimensional systems). Recent developments in spintronics and in particular in the field of topological insulators increase the need for a formula that takes into account non-trivial spin textures in the reservoir. This will in particular be employed in Chapter 6. Therefore, we consider a Hamiltonian of the form

$$H_0(\boldsymbol{k}) = \sum_{\lambda \in \{x,y,z\}} v^\lambda(\boldsymbol{k}) \sigma^\lambda, \tag{2.28}$$

where σ^λ are the Pauli matrices and $v^\lambda(\boldsymbol{k})$ are real functions. After some basic but tedious algebra, we arrive at an analytically simplified formula for Y, which is

$$\begin{aligned} Y^{\lambda,\lambda'}_{\tau,\rho}(\boldsymbol{k},\boldsymbol{k'}) =& \frac{1}{2}\Big(\delta_{\lambda,\lambda'}\left[1 - \gamma^T_\tau(\boldsymbol{k})\gamma_\rho(\boldsymbol{k'})\right] \\ &+ \gamma^T_\tau(\boldsymbol{k}) B^{\lambda,\lambda'} \gamma_\rho(\boldsymbol{k'}) + \mathrm{i}\epsilon_{\lambda,\lambda',\nu}\left[\gamma_\tau(\boldsymbol{k}) - \gamma_\rho(\boldsymbol{k'})\right]_\nu\Big), \end{aligned} \tag{2.29}$$

where

$$\gamma_\rho(\boldsymbol{k}) = (v^x, v^y, v^z)^T / \epsilon^\rho(\boldsymbol{k}), \tag{2.30}$$

$$B^{\lambda,\lambda'}_{a,b} = \delta_{\lambda,a}\delta_{\lambda',b} + \delta_{\lambda,b}\delta_{\lambda',a}. \tag{2.31}$$

Here, $\epsilon_{i,j,k}$ is the Levi-Civita symbol, and matrix multiplication as well as the Einstein sum convention are implicit. An interesting remark is that γ is a unit vector.

2.3. Superconductivity

We want to deliver a brief introduction and access to the literature on the formalism that allows us to describe superconductors by an effective quadratic fermionic Hamiltonian. This enables us to classify topological superconductors on the same footings as introduced for band insulators in Section 2.1. The mechanism also serves as an example of how the topological classification can be, in a first, simplistic way, extended to interacting phases. Whenever the theory under consideration is well approximated by a quadratic band model, the classification of Section 2.1 can be applied. Examples for such phases, besides the mean field superconductors, are, for instance, Kondo insulators *[Dzero et al., 2010]*, Floquet insulators *[Cayssol et al., 2013; Dehghani et al., 2014]*, and dissipative insulators *[Bardyn et al., 2013; Budich et al., 2015]*.

Superconductors are systems that, among other effects, conduct electricity almost perfectly. They are a standard part of nowadays curricula and an exhaustive representation of them and their history is accessible via various literature, for instance by *De Gennes [1999]; Schrieffer [1983]; Tinkham [2004]; van Delft & Kes [2010]*. Superconductivity is known for many systems to originate from an effective attractive interaction between the fermionic quasi particles of a solid. This effective interaction can stem from the interaction of the quasi particles with phonons *[Bardeen et al., 1957]*, magnons *[Chen & Goddard, 1988]* or from other mechanisms. For instance, an effective superconducting behavior can be induced in normally conducting materials by the close proximity to a superconductor. This effect is called proximity-induced superconductivity and is known for almost a century *[Holm & Meissner, 1932]* and treatable within the framework introduced here, cf., e.g., *Fu & Kane [2008]*. However, the microscopic mechanisms causing superconductivity, especially high-temperature superconductivity, are not fully understood and a subject of current research.

To give a concrete example, the two particle spin-singlet pairing Hamiltonian *[Tinkham, 2004]* describing conventional superconductivity is

$$\mathcal{H}_{\mathrm{BCS}} = \int_{\mathrm{BZ}} \boldsymbol{dk}\ \epsilon(\boldsymbol{k}) \boldsymbol{c}_{\boldsymbol{k}}^{\dagger} \boldsymbol{c}_{\boldsymbol{k}} + \int_{\mathrm{BZ}} \boldsymbol{dk}\ \boldsymbol{dp}\ V_{\boldsymbol{k},\boldsymbol{p}} c_{\uparrow,\boldsymbol{k}}^{\dagger} c_{\downarrow,-\boldsymbol{k}}^{\dagger} c_{\downarrow,-\boldsymbol{p}} c_{\uparrow,\boldsymbol{p}}, \tag{2.32}$$

where $\boldsymbol{c}_{\boldsymbol{k}} = (c_{\uparrow,\boldsymbol{k}}, c_{\downarrow,\boldsymbol{k}})^T$ is the spinor of the fermionic annihilation operators, wherein $\boldsymbol{k}$ is the momentum in the Brillouin zone BZ, ϵ describes the dispersion, and V describes the strength of the particle-particle interaction that pairs excitations of opposite spin and opposite momentum, i.e., spin-singlet or, as commonly called, s-wave pairing. Approximating $\mathcal{H}_{\mathrm{BCS}}$ by a mean field theory *[Tinkham, 2004]* results in an effective quadratic Hamiltonian of the form

$$\mathcal{H}_{\mathrm{BCS}}^{\mathrm{MF}} = \int \boldsymbol{dk}\ \epsilon(\boldsymbol{k}) \boldsymbol{c}_{\boldsymbol{k}}^{\dagger} \boldsymbol{c}_{\boldsymbol{k}} + \left(\Delta_{\boldsymbol{k}} c_{\uparrow,\boldsymbol{k}}^{\dagger} c_{\downarrow,-\boldsymbol{k}}^{\dagger} + H.c. \right) + E \tag{2.33}$$

with the mean field parameter, also called gap function, $\Delta_{\boldsymbol{k}} = \int_{\mathrm{BZ}} \boldsymbol{dp}\, V_{\boldsymbol{k},\boldsymbol{p}} \langle c_{\downarrow,-\boldsymbol{p}} \boldsymbol{c}_{\uparrow,\boldsymbol{p}} \rangle_0$ and the energy offset $E = -\int_{\mathrm{BZ}} \boldsymbol{dk}\ \boldsymbol{dp}\ V_{\boldsymbol{k},\boldsymbol{p}} \langle c_{\downarrow,-\boldsymbol{k}} c_{\uparrow,\boldsymbol{k}} \rangle_0^* \langle c_{\downarrow,-\boldsymbol{p}} c_{\uparrow,\boldsymbol{p}} \rangle_0$, which have to be adjusted self consistently. Here, $\langle \dots \rangle_0$ denotes the expectation value with respect to the quadratic part of the Hamiltonian. The diagonalization of the Hamiltonian in Eq. (2.33) can be achieved by a Bogoliubov transformation. We give an example for such a transformation in Section 3.1.3 and, albeit somewhat hiddenly, in Section 4.3. This Bogoliubov transformation can be taken out prosaically, for instance by a mere ansatz, see, e.g., *von Delft & Schoeller [1998]*, or, still prosaically, on a more rigorous mathematical footing as shown in *Araki [1968]*. However, rewriting the Hamiltonian using the Nambu notation *[Schrieffer, 1983]* generates additional physical insight and an algorithmic simplification. To this purpose, we define the Nambu spinor $\boldsymbol{\Psi}_{\boldsymbol{k}}^\dagger = \left(c_{\uparrow,\boldsymbol{k}}^\dagger, c_{\downarrow,\boldsymbol{k}}^\dagger, c_{\downarrow,-\boldsymbol{k}}, -c_{\uparrow,-\boldsymbol{k}}\right)$[31] and express Eq. (2.33) as

$$\mathcal{H}_{\mathrm{BCS}}^{\mathrm{MF}} = \int_{\mathrm{BZ}/2} \boldsymbol{dk}\ \boldsymbol{\Psi}_{\boldsymbol{k}}^\dagger H_{\mathrm{BdG}} \boldsymbol{\Psi}_{\boldsymbol{k}} + E_G, \tag{2.34}$$

$$H_{\mathrm{BdG}} = \begin{pmatrix} \epsilon(\boldsymbol{k}) \mathbb{1}_{2\times 2} & \begin{pmatrix} \Delta_{\boldsymbol{k}} & 0 \\ 0 & \Delta_{-\boldsymbol{k}} \end{pmatrix} \\ \begin{pmatrix} \Delta_{\boldsymbol{k}}^* & 0 \\ 0 & \Delta_{-\boldsymbol{k}}^* \end{pmatrix} & -\epsilon(-\boldsymbol{k}) \mathbb{1}_{2\times 2} \end{pmatrix}. \tag{2.35}$$

Here[32], $\mathbb{1}_{2\times 2}$ is the unit matrix in two dimensions, E_G is an appropriately chosen real constant, and the additional brackets are introduced to improve the overview.

The advantage of the Nambu notation here is twofold. First, the Bogoliubov-de Gennes Hamiltonian H_{BdG} is able to deliver some intuitive understanding of the features of the Hamiltonian in terms of particles (represented by the upper left block) and holes (lower right block). Secondly, the potentially cumbersome Bogoliubov transformation of $\mathcal{H}_{\mathrm{BCS}}^{\mathrm{MF}}$ is achieved by a unitary diagonalization of H_{BdG}. In this way, considerations regarding spectral and eigenvalue properties of normal

[31] The Nambu spinor can be chosen with the considerable freedom of a unitary transformation, which is the reason why different choices for the Nambu spinor are circulating. Also, we do not need to employ the full Nambu spinor here, which would have eight components, because the present Hamiltonian does not assume the most general form. For instance, it would be impossible to denote the term $c_{\uparrow,\boldsymbol{k}} c_{\uparrow,\boldsymbol{k}}$ with the reduced, four-component Nambu spinor. The full Nambu spinor introduces an ambiguity into the Bogoliubov-de Gennes Hamiltonian, which is resolved by demanding an intrinsic particle-hole symmetry. This symmetry is needed to represent the Bogoliubov transformation as a unitary transformation, see Section 4.3 for an example. Note that some of the Cartan-Altland-Zirnbauer symmetry classes, as discussed in Section 2.1, cannot be realized by superconductors because of this intrinsic particle-hole symmetry of H_{BdG}. For the reduced Nambu spinor, the Bogoliubov-de Gennes Hamiltonian usually still exhibits a particle-hole symmetry. However, this symmetry is not a rigorous mathematical consequence but rather a physical one.

[32] Note that Eq. (2.34) would not be equivalent to Eq. (2.33) if the integral was replaced by a sum, the index set of which contains a $\boldsymbol{k}$ being in the center or at the boundary of the Brillouin zone. This would be the case for periodic systems of finite size.

band insulators can directly be translated to the Bogoliubov-de Gennes Hamiltonian of superconductors. Most important in the context of this thesis is the thereby extended application of the topological classification along the lines of Section 2.1.

3. Methods

3.1. Method of refermionizable points

There is a multitude of Hamiltonians that are known to be simplifiable to quadratic models for a special choice of the involved parameters employing a specific scheme, which we call "Method of refermionizable points". Examples are given by models for the Kondo effect *[Emery & Kivelson, 1992; Hewson, 1997; Posske et al., 2013; von Delft et al., 1998]*, a backscatterer in a Tomonaga-Luttinger liquid *[von Delft & Schoeller, 1998]*, the dissipative two-state system and the spin-boson model *[Leggett et al., 1987]*. Regarding the Kondo problem, the idea was – up to our knowledge – first indicated by Gérard Toulouse *[Toulouse, 1969]*, who showed that there should be a mapping between the s-d model *[Hewson, 1997]* and a resonant level model for a special point in parameter space, the Toulouse point. The concrete mapping was established later by applying bosonization and refermionization. *Emery & Kivelson [1992]* subsequently found a unitary transformation that allowed them to expand the applicability of Toulouse's idea to the two channel Kondo model. Slightly generalizing, the method follows a clear schematic:

1. consider Hamiltonians that include bosonic vertex operators, i.e., operators of the form $e^{\mathrm{i}\lambda\phi}$, where ϕ is a bosonic field depending on a spatial variable.[1]

2. Find a unitary transformation that alters the form of the vertex operators to $e^{\mathrm{i}\phi}$. We call this transformation generalized Emery-Kivelson transformation.

3. Refermionize.

The bottleneck of this scheme lies in the necessary unitary transformation that allows the subsequent application of refermionization in a sensible way. The aim of this section is to explain this scheme with its strengths and drawbacks in detail. We therefore first introduce bosonization and refermionization. Subsequently, we concentrate on the determination of a suitable Emery-Kivelson transformation. The theory introduced in this section is the base of the results of Chapter 4 and Chapter 5. To exemplify its application, we detailedly calculate the refermionizable points of the two channel Kondo model in Section 3.1.3, which leads to the results of Chapter 5.

[1] Such Hamiltonians may well represent the bosonized form of a fermionic system.

3.1.1. Bosonic-fermionic equivalence in one spatial dimension

For one-dimensional systems, there is the remarkable possibility to switch back and forth between a fermionic description and a bosonic description of the model at hand under the assumption that the physical system consists of a finite number of excitations. The advantage of this freedom to choose the character of the description is that some Hamiltonians have a simple form, e.g., being quadratic, in one representation although they look exceedingly involved in the other one. This in turn can strongly facilitate predictions regarding the model under consideration. The process of switching the representations is called bosonization or refermionization[2], respectively. A more natural denotation for the latter seems to be "fermionization", in order to emphasize the emancipated status of the two procedures. However, the nomenclature has to be viewed in the historical context. Systems of interacting fermions could first be solved exactly by mapping them to noninteracting bosons. From that point of view, bosonization is much more valuable than its formally coequal brother "fermionization", such that the latter is equipped with a prefix. The historical development also explains the misleading name "abelian bosonization", the essence of which is rather the establishment of the bosonic-fermionic equivalence and not only mere bosonization *[von Delft & Schoeller, 1998]*.

In Section 3.1.1.1, we will first discuss on the subtlety of restricting our considerations to systems composed of a finite number of excitations, which has led to confusion in this context at a very fundamental level of the theory *[Luttinger, 1963; Mattis & Lieb, 1965]*. Afterwards, in Section 3.1.1.3, we introduce the equivalence between the fermionic and bosonic language, following the scheme of abelian bosonization given in *von Delft & Schoeller [1998]*.

3.1.1.1. Foundations and historical excerpts of bosonization

It is appreciable for physicists to be able to describe fermions obeying a linear dispersion relation. Especially prominent in solid state physics is the linear approximation of the dispersion relation around the Fermi energy of one-dimensional solids. Naively, the Hamiltonian acting on the Fock space $\mathcal{F}$ that is taken to describe such fermions is

$$\mathcal{H}_0 = \sum_{k\in K} k c_k^\dagger c_k, \tag{3.1}$$

where the fermionic annihilaton operators c_k obey the anticommutation relations

$$\{c_k^\dagger, c_{k'}\} = \delta_{k,k'}, \tag{3.2}$$
$$\{c_k, c_{k'}\} = 0 \tag{3.3}$$

[2]Another name for refermionization is debosonization, as used by *Matveev [1995]*.

for all $k \in K = \{\Delta_K z \mid z \in \mathbb{Z}\}$, where $\Delta_K = \frac{2\pi}{L}$ with L being the length of the system in real space, which we assume to obey periodic boundary conditions. However, there is an issue regarding the physical correctness of this approach: Since K is not bounded from below in this model, the Hamiltonian of Eq. (3.1) possesses no ground state that accommodates a finite number of particles. In principle, this shortcoming excludes the Hamiltonian for physically sensible applications, as, put simply, there are only finitely many particles in the universe. It is unavoidable to mention the concept of the Dirac sea in this context, i.e., taking into consideration states with infinitely many fermions filling the states below the Fermi energy. This concept is especially appealing to solid state physicists, as we can think of the Dirac sea representing the inert, energetically low lying, filled states of the valence bands. The drawbacks of Dirac's idea, however, are not to be ignored *[Weinberg, 1996]*: there is the infinite density of electrons, which, besides conceptual problems, introduces various divergences of observables and in particular begins to matter when a coupling to, e.g., the electro-magnetic theory is considered. Finally, the Dirac model becomes absurd when considering bosons obeying a linear dispersion relation because of the missing Pauli exclusion principle. *Weinberg [1996]* discusses more shortcomings of the Dirac sea and puts it into the historical context.

Instead, we want to introduce the more general approach of normal ordering. Here, we want to present an in our eyes particularly pleasant interpretation of this concept, which emphasizes the necessity of restricting the considerations to a finite number of particles in Fock space. The concept is based on previous definitions of normal order as described by, for instance, *Luttinger [1963]*, *Mattis & Lieb [1965]*, and *von Delft & Schoeller [1998]*. With regard to this, consider as a starting point the model Hamiltonian for fermions with linear dispersion relation using particles and holes,

$$\mathcal{H}_0' = \sum_{k \in K^+} k p_k^\dagger p_k + k h_k^\dagger h_k, \tag{3.4}$$

with the particles p_k and holes h_k, which both obey fermionic anticommutation relations. As the positrons and electrons in the Dirac equation, the particles and holes here are interpreted as two emancipated species. The original fermions of the model c_k can be expressed in particle and hole operators as

$$c_k = \begin{cases} p_k \text{ for } k \geq 0 \\ h_{-k}^\dagger \text{for } k < 0, \end{cases} \tag{3.5}$$

which results in a Hamiltonian similar to Eq. (3.1), namely

$$\mathcal{H}_0' = \sum_{k \in K^+} k c_k^\dagger c_k - \sum_{k \in K^-} k c_k c_k^\dagger. \tag{3.6}$$

The formal difference to Eq. (3.1) only lies in an, albeit diverging, constant. However, the conceptual difference is huge. In contrast to Eq. (3.1), Eq. (3.4) has a

well defined ground state in terms of a finite number of particles and holes, namely zero particles and zero holes. Applying the decomposition into particles and holes, reasonable effective Hamiltonians of linearly dispersing fermions and bosons can be derived, which have non-diverging vacuum expectation values. In principle, these Hamiltonians have to be derived anew. However, there is a short track and a short-hand notation called normal ordering. The fermionic normal order of a string of creation and annihilation operators h, $h^\dagger$, p, and $p^\dagger$ is defined here by anticommuting all creation operators to the left and all annihilation operators to the right, where for each anticommutation that occurs in this process, the anticommutator is taken to be 1 instead of its actual value. The bosonic normal order is very similar, but regards commutations instead of anticommutations. We denote a normal ordered string S of operators by ${}^*_*S^*_*$. By the definition of normal order, we are allowed to anticommute, or, respectively, commute, within S at will. For instance, we have

$${}^*_*p_1p_2p_3{}^*_* = -{}^*_*p_2p_1p_3{}^*_* = {}^*_*p_3p_2p_1{}^*_*. \tag{3.7}$$

It is important to keep in mind that for us, normal ordering is nothing but a short hand notation. One has to be extremely careful in employing this short hand notation and take care of what it means in the specific context. An example of subtle mistakes that can arise relates to simplifications and replacements within a string of operators and the assumption that normal ordering behaves as a linear operator. On the one hand, consider

$${}^*_*p_1^\dagger p_2^\dagger p_2 p_1{}^*_* = {}^*_* - p_1^\dagger p_2 p_2^\dagger p_1 + p_1^\dagger p_1{}^*_* = p_1^\dagger p_2^\dagger p_2 p_1 + p_1^\dagger p_1. \tag{3.8}$$

On the other hand, consider

$${}^*_*p_1^\dagger p_2^\dagger p_2 p_1{}^*_* = p_1^\dagger p_2^\dagger p_2 p_1. \tag{3.9}$$

The mistake here is that the middle of Eq. (3.8) is not defined a priori. However, for convenience of notation, we, as many more authors *[Altland & Simons, 2006a; Rammer, 2007; von Delft & Schoeller, 1998]*, will assume the normal order of a sum to be the sum of the respective normal orders. Thereby, we have to be very careful that mistakes of the type described in Eq. (3.8) do not occur. By Eq. (3.5), we are allowed to apply normal order directly onto strings of c and $c^\dagger$. Note that for momenta k smaller than the Fermi momentum k_F, this has the effect that creation operators $c_k^\dagger$ appear to the right and annihilation operators c to the left. Exactly opposite as for operators with momenta larger than k_F. As an example for employing normal order, we want to state that the naively constructed Hamiltonian of Eq. (3.1) is connected to the particle-hole representation, cf. Eq. (3.4), by

$${}^*_*\mathcal{H}_0{}^*_* = \sum_{k\in K} k^*_* c_k^\dagger c_k{}^*_* = \sum_{k\in K^+} k c_k^\dagger c_k - \sum_{k\in K^-} k c_k c_k^\dagger = \mathcal{H}_0'. \tag{3.10}$$

3.1.1.2. Commutator relations of the Fourier transformed density operator

One of the essential observations that led to the theory of bosonization is the non-vanishing commutator of the density operator in momentum space

$$\rho_k = \sum_p c^\dagger_{p+k} c_p. \tag{3.11}$$

It is an ironic circumstance that Luttinger himself, whose name will be bound to the physics of 1D fermionic systems for eternity – considering the name Tomonaga-Luttinger liquid – calculated the commutator incorrectly when he re-invented bosonization *[Luttinger, 1963]*. His mistake was corrected later by *Mattis & Lieb [1965]*. However, Tomonaga derived the correlator completely correctly many years earlier than Luttinger *[Tomonaga, 1950]* and humbly attributed the origin of the idea to Bloch *[Bloch, 1933, 1934]*.

Nevertheless, there still appear to remain misconceptions about the origin of non-vanishing density commutators as *Mattis & Lieb [1965]* and later publications, also *von Delft & Schoeller [1998]* partially have not passed down as rigorous an argumentation as introduced by *Tomonaga [1950]*, whose concept we are going to follow. The reason why there is subtlety in computing the commutators of interest is that the result is different for different subspaces of the Fock space $\mathcal{F}$. On the subspace consisting of the states with an infinite number of holes (ordered in the form of a Dirac sea) and a finite number of particles the commutator vanishes, while for the subspace of a finite number of particles and holes, which is the physically relevant subspace, the commutator reaches its familiar form. We want to derive the commutator in detail.

$$\begin{aligned}[\rho_k, \rho_{k'}] &= \sum_{p,p' \in K} \left[c^\dagger_{k+p} c_p, c^\dagger_{k'+p'} c_{p'} \right] = \sum_{p,p' \in K} c^\dagger_{k+p} c_{p'} \delta_{p,k'+p'} - c^\dagger_{k'+p'} c_p \delta_{k+p,p'} \\ &= \sum_{p \in K} c^\dagger_{k+p} c_{p-k'} - c^\dagger_{k'+k+p} c_p. \end{aligned} \tag{3.12}$$

For any state $|a\rangle$ with a finite number of particles and for finite k and k' there is an $s_u > 0 \in K$ with

$$c_{m_u} |a\rangle = 0 \ \forall m_u > s_u - |k| - |k'|. \tag{3.13}$$

As an example: for $|k| = |k'| = 0$, the quantity s_u describes the particle in $|a\rangle$ that has the largest momentum. If $|a\rangle$ has a finite number of holes as well, there is an $s_\mathrm{t} \geq 0 \in K$ with

$$c^\dagger_{-m_\mathrm{t}} |a\rangle = 0 \ \forall m_\mathrm{t} > s_\mathrm{t} - |k| - |k'|, \tag{3.14}$$

in contrast if $|a\rangle$ has an infinite number of holes in the form of a Dirac sea, there is an $s_\mathrm{t} \in K$ with

$$c_{-m_\mathrm{t}} |a\rangle = 0 \ \forall m_\mathrm{t} > s_\mathrm{t} - |k| - |k'|. \tag{3.15}$$

This gives

$$[\rho_k, \rho_{k'}]\,|a\rangle = \left(\sum_{p=-s_\mathrm{t}}^{s_u} c^\dagger_{p+k}c_{p-k'} - \sum_{p=-s_\mathrm{t}+k'}^{s_u+k'} c^\dagger_{k+p}c_{p-k'}\right)|a\rangle$$
$$= \mathrm{sgn}(k')\left(\sum_{p\in A(-s_\mathrm{t},k')} - \sum_{p\in B(s_\mathrm{u},k')}\right) c^\dagger_{p+k}c_{p-k'}|a\rangle, \tag{3.16}$$

with

$$\begin{aligned} A(-s_\mathrm{t},k') =& \{\min(-s_\mathrm{t}, -s_\mathrm{t}+k'), \ldots, \max(-s_\mathrm{t}, -s_\mathrm{t}+k') - \Delta_K\} \\ B(s_\mathrm{u},k') =& \{\min(s_\mathrm{u}, s_\mathrm{u}+k') + \Delta_K, \ldots, \max(s_\mathrm{u}, s_\mathrm{u}+k')\} \end{aligned} \tag{3.17}$$

and $(\sum_{k\in A} + \sum_{k\in B})\, f(k)$ being a symbolic notation for $\sum_{k\in A} f(k) + \sum_{k\in B} f(k)$. The sum over B vanishes due to the choice of s_u – which annihilates the state $|a\rangle$ for the appearing operators – and the sum over A gives

$$\mathrm{sgn}(k') \sum_{p\in B(s_\mathrm{t},k')} \left(\delta_{k,-k'} - c_{p-k'}c^\dagger_{k+p}\right)|a\rangle = |a\rangle \begin{cases} \delta_{k,-k'}\frac{k'}{\Delta_K} & \text{(i)}, \\ 0 & \text{(ii)}, \end{cases} \tag{3.18}$$

where the cases denote: (i) $|a\rangle$ possesses a finite number of holes, (ii) $|a\rangle$ possesses an infinite number of holes in the form of a Dirac sea. We observe that the result does not depend on any additional structure of $|a\rangle$. We therefore conclude the following operator identity on the subspaces of states with infinitely and finitely many holes respectively

$$[\rho_k, \rho_{k'}] = \begin{cases} -\delta_{k,-k'}\frac{k}{\Delta_K} & \text{(i)}, \\ 0 & \text{(ii)}. \end{cases} \tag{3.19}$$

This equation resembles the famous starting point of abelian bosonization. Whenever the commutator identity of Eq. (3.19) and therefore also the bosonization identity is used as an operator identity, it has to be kept in mind that these are only valid on the subspace of a finite number of particles and holes. However, as the states containing a finite number of particles and holes are in most cases the only physical ones and other states have no impact on the system as they lie energetically too far away from the Fermi level, bosonization can often be employed without the knowledge of this subtlety.

3.1.1.3. Abelian bosonization

There are many comprehensive and exhaustive texts on abelian bosonization, e.g., *Giamarchi [2003]; Haldane [1981]; Schönhammer [1997]; von Delft & Schoeller [1998]*, just to mention a few of them. We concentrate here on the representation

of the most important part, the equivalence between the fermionic and the bosonic description in one dimension. Our explanations stay close to the approach of *von Delft & Schoeller [1998]*, besides some signs that we alter for convenience, and we refer to this reference for all proofs omitted in this section. Hence, our presentation is in no way meant to be original. Additionally to the abelian approach, there is a field theoretical approach to bosonization, for instance sketched in *Altland & Simons [2006a]*, which we are not going to follow here.

Consider the subspace $\mathcal{F}$ of the Fock space that only contains a finite number of particles and holes – as introduced in Section 3.1.1.1 – describing one-dimensional fermions confined to the segment $\{-L/2, L/2\}$. Then the set of fermionic creation and annihilation operators in momentum space $c_k^\dagger$ and c_k, obeying $\{c_k, c_p\} = \delta_{k,p}$, together with the vacuum state $|0\rangle \in \mathcal{F}$ span $\mathcal{F}$. This vacuum state is defined as the state in $\mathcal{F}$ that has the properties[3]

$$\begin{aligned} c_k|0\rangle &= 0 \text{ for } k \geq 0, \\ c_k^\dagger|0\rangle &= 0 \text{ for } k < 0. \end{aligned} \tag{3.20}$$

The backbone of abelian bosonization is the fact that there is a set of (mostly) bosonic operators that also spans $\mathcal{F}$. In this respect, it only remains a matter of taste if the bosonic or the fermionic algebra is used to describe problems of one-dimensional particles. In the following passage, we introduce the bosonic operators spanning $\mathcal{F}$ and afterwards, we establish the isomorphism between them and the fermionic operators.

In Section 3.1.1.2, we introduced the commutation relations of the density operator in momentum space as the heart of bosonization. In fact, regarding Eq. (3.19), we can define bosons[4] in momentum space by

$$b_k^\dagger = -\mathrm{i}\sqrt{\frac{\Delta_K}{k}}\rho_k = -\mathrm{i}\sqrt{\frac{\Delta_K}{k}}\sum_p c_{p+k}^\dagger c_p \tag{3.21}$$

for all $k > 0$ $k \in \{n\Delta_K \mid n \in \mathbb{N}\} =: K$ that fulfill

$$\left[b_k, b_{k'}^\dagger\right] = \delta_{k,k'}, \tag{3.22}$$

$$[b_k, b_{k'}] = 0. \tag{3.23}$$

It is important to note here, that the bosons are only defined for positive momenta. Otherwise, there would be a dependence between bosons by $b_k^\dagger = b_{-k}$. In the following, we will, however, use Eq. (3.21) extended to positive and negative k, having this obstacle in the back of our minds. Departing from Eq. (3.21), real space

[3] In fact, the vacuum state is only unique up to a phase.

[4] The definition of Eq. (3.21) differs from the one in *von Delft & Schoeller [1998]* by a sign to let Eq. (3.24) look more natural.

bosons are therefore defined not by an ordinary Fourier transform of Eq. (3.21) but by

$$\Phi(x) = \sum_{k \in K \setminus \{0\}} \frac{e^{\mathrm{i}kx - a|k|/2}}{\sqrt{|k|/\Delta_k}} b_k^\dagger. \tag{3.24}$$

Here, $a \in \mathbb{R}^+$ is regularizing the sum. In the limit $a \to 0$ the bosonic commutation relation

$$[\Phi(x), \partial_{x'} \Phi(x')] = 2\pi\mathrm{i}\delta(x - x') - \frac{2\pi\mathrm{i}}{L} \tag{3.25}$$

is obtained. It is also notable that the real space bosonic fields are self-adjoint. The physical picture behind these bosons is that they describe the bosonic density fluctuations of the fermionic liquid. As this intuition suggests, it can be shown, cf., e.g., *von Delft & Schoeller [1998]*, that the bosons $b_k^\dagger$ span the equal particle subspaces of $\mathcal{F}$, i.e., the subspaces with a constant number $N = p - h$, where p is the number of particles and h the number of holes. The only ingredient remaining for fully spanning $\mathcal{F}$ is a ladder operator that connects the equal particle subspaces. To obtain such an operator, consider the usual occupation number basis of $\mathcal{F}$, given by products of fermionic creation operators in momentum space acting on the vacuum

$$|\boldsymbol{w}\rangle = \prod_{i \geq 0} \left(c_i^\dagger\right)^{w_i} \prod_{i > 0} \left(c_{-i}\right)^{(1 - w_{-i})} |0\rangle, \tag{3.26}$$

where $\boldsymbol{w}$ is a binary vector with $w_i = \langle w | c_i^\dagger c_i | w \rangle$ for $i \in \Delta_k \mathbb{Z}$. We now define $\boldsymbol{w}^{\ll}$ as $(w^{\ll})_i := w_{i-1}$. With this notation[5], a convenient choice of the aforementioned ladder operator is

$$F^\dagger |\boldsymbol{w}\rangle := |\boldsymbol{w}^{\ll}\rangle, \tag{3.27}$$

where we define this linear operator $F^\dagger$ by determining its action on the basis under consideration[6]. The operator of Eq. (3.27) is called Klein factor. As can be seen by

$$\langle v | F F^\dagger | w \rangle = \sum_i v_{i-1} w_{i-1} = \sum_i v_i w_i = \langle v | w \rangle, \tag{3.28}$$

the Klein factor is unitary. With the definition of the Klein factor, we have established a complete set of operators, namely $\left\{F^\dagger, F\right\} \cup \left\{b_k^\dagger \mid k \in \Delta_k \mathbb{Z} \setminus \{0\}\right\}$ that span $\mathcal{F}$ and are mostly of bosonic nature. Already with the definition of the bosonic fields in Eq. (3.21) and Eq. (3.24), many one-dimensional fermionic Hamiltonians, for instance, the one of locally interacting fermions, can be written solely in bosonic

[5] The notation is adapted from informatics, where $\ll$ denotes the bit shift operator to the left.
[6] This determines all matrix elements $\langle v | F | w \rangle = \langle v | w^{\ll} \rangle = \sum_i v_i w_{i-1}$.

degrees of freedom. However, the true power of bosonization is revealed by the so-called bosonization identity[7]

$$\Psi^\dagger(x) = \frac{F^\dagger}{\sqrt{2\pi a}} e^{\mathrm{i}\Delta_k N x} e^{\mathrm{i}\Phi(x)}. \tag{3.29}$$

where $N := \rho_0$ is the number operator. Together with the momentum representation of $\{\Psi(x) \mid x \in \{-L/2, L/2\}\}$ by $\{c_k \mid k \in \Delta_k\mathbb{Z}\}$, the definition of the bosonic fields in Eq. (3.21), the definition of the Klein factors in Eq. (3.27), this bosonization identity completes the isomorphism between the fermionic operators $\{c_k \mid k \in \Delta_k\mathbb{Z}\}$ and the (mostly) bosonic operators $\left\{F^\dagger, F, N\right\} \cup \left\{b_k^\dagger \mid k \in \Delta_k\mathbb{Z}\backslash\{0\}\right\}$.

3.1.2. Generalized Emery-Kivelson transformations

Many Hamiltonians that we are going to discuss, include vertex operators of the form

$$e^{\mathrm{i}(\lambda_+\phi_+(0)+\lambda_-\phi_-(0))}, \tag{3.30}$$

where ϕ_+ and ϕ_- are bosonic fields. If $\lambda_+ = 1$ and $\lambda_- = 0$, the vertex operator would readily be refermionizable by Eq. (3.29). Otherwise, a sensible refermionization seems to be out of reach. The generalized Emery-Kivelson transformation rotates a bosonic field into the exponential of the vertex operator and thereby renders it refermionizable. The origin and name of the transformation lies in its application to the Kondo problem as conducted by *Emery & Kivelson [1992]*, which we slightly extend here to be applicable to more general situations. Consider a theory with two bosonic degrees of freedom ϕ_+ and ϕ_- and the term

$$e^{\mathrm{i}(\lambda_+\phi_+(0)+\lambda_-\phi_-(0))} A, \tag{3.31}$$

with a linear operator A, two real numbers λ_+ and λ_-, and the bosonic fields ϕ_+ and ϕ_-. Now, we consider a unitary operator

$$U = e^{\mathrm{i}B}, \tag{3.32}$$

with a hermitian operator B that fulfills the following requirements

$$\begin{aligned} [B, \phi_+(0)] &= 0 \\ [B, \phi_-(0)] &= 0 \\ [B, A] &= (a_+\phi_+(0) + a_-\phi_-(0))\, A, \end{aligned} \tag{3.33}$$

with real a_+ and a_-. With this transformation, we have

$$UAU^\dagger = e^{\mathrm{i}[B,\cdot]} A = e^{\mathrm{i}(a_+\phi_+(0)+a_-\phi_-(0))} A, \tag{3.34}$$

[7] We refer to *von Delft & Schoeller [1998]* for a proof of the bosonization identity.

using the Hadamard lemma[8]

$$e^{\mathrm{i}B}Ae^{-\mathrm{i}B} = A + \mathrm{i}(BA - AB) + \cdots = e^{\mathrm{i}[B,\cdot]}A. \tag{3.35}$$

The vertex operator commutes with U since B commutes with U. We therefore obtain

$$Ue^{\mathrm{i}(\lambda_+\phi_+(0)+\lambda_-\phi_-(0))}AU^\dagger = e^{\mathrm{i}((\lambda_++a_+)\phi_++(\lambda_-+a_-)\phi_-)(0)}A. \tag{3.36}$$

We can now attempt to find two new bosonic fields

$$\begin{pmatrix} \nu_1 \\ \nu_2 \end{pmatrix} = M \begin{pmatrix} \phi_+ \\ \phi_- \end{pmatrix} \tag{3.37}$$

with the orthogonal matrix

$$M = \frac{1}{\sqrt{(\lambda_+ + a_+)^2 + (\lambda_- + a_-)^2}} \begin{pmatrix} \lambda_+ + a_+ & \lambda_- + a_- \\ \lambda_- + a_- & -(\lambda_+ + a_+) \end{pmatrix}. \tag{3.38}$$

This matrix can only be orthogonal in case there are real numbers, a_+ and a_-, such that

$$(\lambda_+ + a_+)^2 + (\lambda_- + a_-)^2 = 1. \tag{3.39}$$

If this condition can be met, the considered term is transformed to

$$Ue^{\mathrm{i}(\lambda_+\phi_++\lambda_-\phi_-)}AU^\dagger = e^{\mathrm{i}\nu_1}A, \tag{3.40}$$

and hence sensibly refermionizable. A drawback of the generalized Emery-Kivelson transformation is the possibly increasing complexity of the remaining parts of the Hamiltonian and of A in its fermionic representation. We employ the generalized Emery-Kivelson transformation as the basis of the results of Chapter 4 and Chapter 5. An illustrative application of a generalized Emery-Kivelson transformation is given in Section 3.1.3, where the details of the diagonalization of the two channel Kondo Hamiltonian of Chapter 5 are derived.

3.1.3. Refermionizable points of the two channel Kondo model with interacting helical leads

The aim of this section is to deliver an instructive example of the theory introduced in Section 3.1.2 by finding the refermionizable points of the two channel Kondo

[8] Here, $[B,\cdot]$ is a symbolic notation, which is read as: insert the string to the right in place of the dot, e.g., $[B,\cdot]C = [B,C]$. Additionally, $e^{\mathrm{i}[B,\cdot]}$ is the short notation for the series $\sum_{n=0}^{\infty} \frac{1}{n!} \left(\mathrm{i}\,[B,\cdot]\right)^n$.

Hamiltonian with interacting, helical leads[9]. Due to the history of the Kondo model's refermionizable points, we will call these points Toulouse points *[Emery & Kivelson, 1992; Posske et al., 2013; Toulouse, 1969; Zaránd & von Delft, 2000]*. They are points in the parameter space for which there is a mapping of the respective two-particle Hamiltonian to a quadratic one, following the scheme of Section 3.1:

1. bosonize,
2. apply a generalized Emery-Kivelson transformation,
3. refermionize.

This technique has also been employed to analyze the Kondo problem for a single helical liquid by *Maciejko [2012]*. The modeling Hamiltonian is

$$\mathcal{H} = \sum_{a\in\{\mathrm{t,b}\}} \mathcal{H}_a + \mathcal{H}^{\pm}_{K,a} + \mathcal{H}^{z}_{K,a}, \tag{3.41}$$

$$\mathcal{H}_a = \sum_{\sigma\in\pm\equiv\{\downarrow,\uparrow\}} \int dx \left[-\mathrm{i}v_{a,F}\sigma\left(\tilde{\Psi}_{a,\sigma}\tilde{\Psi}'_{a,\sigma}\right) + \frac{g_{a,4}}{2}\tilde{\rho}^2_{a,\sigma} + \frac{g_{a,2}}{2}\tilde{\rho}_{a,\sigma}\tilde{\rho}_{a,-\sigma}\right](x), \tag{3.42}$$

$$\mathcal{H}^{\pm}_{K,a} = J^{\perp}_a \tilde{\Psi}^{\dagger}_{a,\uparrow}(0)\tilde{\Psi}_{a,\downarrow}\tau^{-} + H.c., \tag{3.43}$$

$$\mathcal{H}^{z}_{K,a} = \frac{1}{2}J^{z}_a\left(\tilde{\rho}_{a,\uparrow} - \tilde{\rho}_{a,\downarrow}\right)\tau^{z}. \tag{3.44}$$

The helical Tomonaga-Luttinger Hamiltonians $\mathcal{H}_a$, with $a \in \{\mathrm{t,b}\}$, are bosonized with the bosonization identity, see Eq. (3.29) and Section 3.1.1.3, where we only consider the limit of large systems, i.e. $\Delta_k \to 0$:

$$\tilde{\Psi}^{\dagger}_{a,\sigma}(\sigma x) = \frac{F^{\dagger}}{\sqrt{2\pi a}} e^{\mathrm{i}\tilde{\varphi}_{a,\sigma}(x)}. \tag{3.45}$$

The helical Hamiltonians are subsequently diagonalized by a Bogoliubov transformation in momentum space, cf. *von Delft & Schoeller [1998]* for details, which leads to the new bosonic fields[10]

$$\begin{aligned}\varphi_{a,\sigma}(x) =& \frac{1}{\sqrt{8}}\Big[\left(g_a^{-1/2} + g_a^{1/2}\right)\left(\tilde{\varphi}_{a,\uparrow}(x) - \sigma\tilde{\varphi}_{a,\downarrow}(x)\right) \\ &+ \left(g_a^{-1/2} - g_a^{1/2}\right)\left(\sigma\tilde{\varphi}_{a,\uparrow}(-x) - \tilde{\varphi}_{a,\downarrow}(-x)\right)\Big].\end{aligned} \tag{3.46}$$

[9] This Hamiltonian is detailedly described in Chapter 5 and the physics is explained in Section 2.2.3.

[10] The notation employed here differs to the one of *von Delft & Schoeller [1998]* slightly: (i) opposite sign in the definition of the Fourier transform, (ii) opposite sign in the definition of the bosonization procedure for left moving fields. This leads to apparently different formulations, which turn out to be equivalent taking a closer look.

Here, the so-called Luttinger parameter

$$g_a = \sqrt{\frac{v_{a,F} + 2\pi g_{a,4} - 2\pi g_{a,2}}{v_{a,F} + 2\pi g_{a,4} + 2\pi g_{a,2}}}, \tag{3.47}$$

appears, which describes the strength of interactions in the system. For $x = 0$, Eq. (3.46) reduces to

$$\varphi_{a,\sigma}(0) = \frac{1}{\sqrt{2}} g^{-\sigma/2} \left(\tilde{\varphi}_{a,\uparrow}(0) - \sigma \tilde{\varphi}_{a,\downarrow}(0)\right). \tag{3.48}$$

Note, however, that for the derivative at $x = 0$, the full formula of Eq. (3.46) has to be employed, which effectively changes $g \to \frac{1}{g}$. This reveals

$$\varphi'_{a,\sigma}(0) = \frac{1}{\sqrt{2}} g^{\sigma/2} \left(\varphi'_{a\uparrow}(0) - \sigma \varphi'_{a\downarrow}(0)\right). \tag{3.49}$$

Employing Eq. (3.48) and Eq. (3.49) leads to the bosonized form of the two channel Kondo Hamiltonian

$$\mathcal{H}_a = \int dx \; \frac{v_a}{2} \sum_\sigma \left(\varphi'_{a,\sigma}\right)^2 (x), \tag{3.50}$$

$$\mathcal{H}^{\perp}_{K,a} = \frac{\tau^-}{4\pi} J^{\perp}_a F^{\dagger}_{a\uparrow} F_{a\downarrow} \exp\left(\mathrm{i}\sqrt{2g_a}\varphi_{a,+}(0)\right) + H.c., \tag{3.51}$$

$$\mathcal{H}^{z}_{K,a} = \frac{J^z_a}{4\pi} \sqrt{\frac{2}{g_a}} \varphi'_{a+}(0) \tau^z, \tag{3.52}$$

where

$$v_a = \sqrt{(v_{a,F} + 2\pi g_{a,4} - 2\pi g_{a,2})(v_{a,F} + 2\pi g_{a,4} + 2\pi g_{a,2})}. \tag{3.53}$$

The generalized Emery-Kivelson rotation, as introduced in Section 3.1.2 is given by the unitary transformation

$$U = \exp(\mathrm{i} \sum_{a,\sigma} \lambda_{a,\sigma} \varphi_{a,\sigma}(0) \tau^z). \tag{3.54}$$

Applying this transformation to Eq. (3.50) and Eq. (3.52) results in

$$U \mathcal{H}_a U^\dagger = \mathcal{H}_a - \sum_\sigma v_a \lambda_{a,\sigma} \partial_x \varphi_{a,\sigma}(x) \mid_{x=0} \tau^z, \tag{3.55}$$

$$U \mathcal{H}^z_{K,a} U^\dagger = \mathcal{H}^z_{K,a} + \text{const.}, \tag{3.56}$$

exploiting

$$\left[(\varphi'_j(x))^2, \varphi_{j'}(x)\right] = -2\mathrm{i}\delta_{j,j'} \varphi'_j(x) \left(\delta(x) - \frac{1}{L}\right).^{11} \tag{3.57}$$

These Hamiltonians, $U\mathcal{H}U^\dagger$ and $U\mathcal{H}_zU^\dagger$, contain τ^z, which can be expressed as a single particle term in a fermionic representation of the spin degree of freedom. Therefore, $U\mathcal{H}U^\dagger$ and $U\mathcal{H}_zU^\dagger$ effectively contain multiple particle terms which we want to exclude. In order to cancel these two particle terms, we demand the condition

$$\sum_{a,\sigma} v_a \lambda_{a,\sigma} \partial_x \varphi_{a,\sigma}(x) \mid_{x=0} \tau^z = \sum_{a,\sigma} \delta_{\sigma,+} \frac{J_a}{4\pi} \sqrt{\frac{2}{g_a}} \partial_x \varphi_{a,\sigma}(x) \mid_{x=0} \tau^z, \tag{3.58}$$

which is equivalent to

$$\lambda_{a,-} = 0 \text{ and } J_a^z = \sqrt{8g_a}\lambda_{a,+}\pi v_a \tag{3.59}$$

by comparing coefficients. The generalized Emery-Kivelson rotation of $\mathcal{H}_{K,\pm}$ reveals

$$\begin{aligned} U\mathcal{H}_{K,\pm}U^\dagger =& \frac{\tau^-}{4\pi}\Big(J_{\mathrm{t}}^\perp F_{\mathrm{t},\uparrow}^\dagger F_{\mathrm{t},\downarrow} e^{(\mathrm{i}(\sqrt{2g_{\mathrm{t}}}-\lambda_{\mathrm{t},+})\varphi_{\mathrm{t},+}(0)-\lambda_{\mathrm{b},+}\varphi_{\mathrm{b},+}(0))} \\ &+ J_{\mathrm{b}}^\perp F_{\mathrm{b},\uparrow}^\dagger F_{\mathrm{b},\downarrow} e^{(\mathrm{i}(\sqrt{2g_{\mathrm{b}}}-\lambda_{\mathrm{b},+})\varphi_{\mathrm{b},+}(0)-\lambda_{\mathrm{t},+}\varphi_{\mathrm{t},+}(0))}\Big) + H.c.. \end{aligned} \tag{3.60}$$

To be able to simplify the Hamiltonian by refermionization, the vertex operators of Eq. (3.60) are now, according to Section 3.1.2, taken to be of the form $e^{\pm \mathrm{i}\nu_j(0)}$ with $\nu_j(x) = \sum_j M_{j',j}\varphi_j(x)$ being four new bosonic fields and M being an orthogonal matrix. The remaining task is to find such transformations M that, as an additional constraint, do not complicate the remainder of the Hamiltonian. If M mixes fields from the left and the right side, then $U\mathcal{H}_0U^\dagger$ has off-diagonal elements for the case of unequal quasi particle velocities on both sides, i.e., $v_{\mathrm{t}} \neq v_{\mathrm{b}}$. As M necessarily mixes fields from both sides (except for the trivial $M = \mathbb{1}$), we impose $v_{\mathrm{t}} = v_{\mathrm{b}} := v$ as a first constraint to the Toulouse points. Furthermore, we note that only two vertex operators appear in Eq. (3.60). Although M is generally a four times four matrix, we can therefore assume without loss of generality that M only mixes two bosonic fields, which we choose to be ν_1 and ν_2. The remaining bosonic fields are assumed to remain unchanged. Finally, we are left with a last unmentioned degree of freedom. Either, we choose the boson ν_2 to decouple from the Hamiltonian or not. This leads to two generic cases

3.1.3.1. Case A: only ν_1 appears in the exponents

We assume that the first vertex operator of Eq. (3.60) equals $e^{-\mathrm{i}\nu_1(0)}$ and the second one equals $e^{\pm\mathrm{i}\nu_1(0)}$. This yields

$$\sqrt{2g_a} - \lambda_{a,+} = \pm\lambda_{a,+} \tag{3.61}$$

[11] The term $\frac{1}{L}$ appearing on the right hand side of Eq. (3.57) is not negligible in this case as the commutator is inserted within an integral over the full space, cf. Eq. (3.50).

for $a \in \{\mathrm{t}, \mathrm{b}\}$, which leads to the solutions

$$g_a = 0 \text{ or } \lambda_a = \sqrt{g_a/2}. \tag{3.62}$$

The solution with one $g_a = 0$ is of less interest, as it describes the rather unphysical, infinitely strong interacting limit of the Tomonaga-Luttinger liquid. We therefore restrict ourselves to the case of $\lambda_a = \sqrt{g_a/2}$, where the condition of orthogonality of M gives

$$g_\mathrm{t} + g_\mathrm{b} = 2. \tag{3.63}$$

Therefore, there is a sensible representation of g_a in terms of

$$g_\mathrm{t} = 2\sin^2(\alpha) \text{ and } g_\mathrm{b} = 2\cos^2(\alpha), \tag{3.64}$$

with $\alpha \in \left[0, \frac{\pi}{2}\right)$. By Eq. (3.37), we obtain

$$\begin{pmatrix} \nu_1(x) \\ \nu_2(x) \end{pmatrix} = \frac{1}{\sqrt{2}} \begin{pmatrix} \sqrt{g_\mathrm{t}} & -\sqrt{g_\mathrm{b}} \\ \sqrt{g_\mathrm{b}} & \sqrt{g_\mathrm{t}} \end{pmatrix} \begin{pmatrix} \varphi_{\mathrm{t},+}(x) \\ \varphi_{\mathrm{b},+}(x) \end{pmatrix}. \tag{3.65}$$

Inserting λ_a into Eq. (3.59) results in

$$J_a^z = 2\pi v g_a. \tag{3.66}$$

Employing this representation, the Toulouse points of case A are summarized by

$$\begin{aligned} A &= \{v_\mathrm{t}, g_\mathrm{t}, J_\mathrm{t}^z, v_\mathrm{b}, g_\mathrm{b}, J_\mathrm{b}^z\} \\ &= \{v, 2\sin^2(\alpha), 4\pi v_a \sin^2(\alpha), 2\cos^2(\alpha), 4\pi v \cos^2(\alpha) \mid v \in \mathbb{R},\ \alpha \in [0, \frac{\pi}{2})\}. \end{aligned} \tag{3.67}$$

3.1.3.2. Case B: ν_1 appears in the top-lead exponent, ν_2 in the bottom-lead exponent

Let us repeat the exponents of interest in Eq. (3.60) and call them $ExpI$ and $ExpII$ respectively:

$$ExpI := \mathrm{i}\left[(\sqrt{2g_\mathrm{t}} - \lambda_{\mathrm{t},+})\varphi_{\mathrm{t},+}(0) - \lambda_{\mathrm{b},+}\varphi_{\mathrm{b},+}(0)\right], \tag{3.68}$$

$$ExpII := \mathrm{i}\left[(\sqrt{2g_\mathrm{b}} - \lambda_{\mathrm{b},+})\varphi_{\mathrm{b},+}(0) - \lambda_{\mathrm{t},+}\varphi_{\mathrm{t},+}(0)\right]. \tag{3.69}$$

We now demand $ExpI$ to equal $\mathrm{i}\nu_1(0)$ and $ExpII$ to equal $\mathrm{i}\nu_2(0)$. In this case, the orthogonality of the transformation matrix M introduces the following constraints to g_a and λ_a:

$$1 - \left(\sqrt{2g_\mathrm{t}} - \lambda_{\mathrm{t},+}\right)^2 = \lambda_{\mathrm{b},+}^2, \tag{3.70}$$

$$1 - \lambda_{\mathrm{t},+}^2 = \left(\sqrt{2g_\mathrm{b}} - \lambda_{\mathrm{b},+}\right)^2, \tag{3.71}$$

$$-\left(\sqrt{2g_\mathrm{t}} - \lambda_{\mathrm{t},+}\right)\lambda_{\mathrm{t},+} = \left(\sqrt{2g_\mathrm{b}} - \lambda_{\mathrm{b},+}\right)\lambda_{\mathrm{b},+}, \tag{3.72}$$

where the first two constraints stem from the normality of the row vectors of M and the third constraint from their orthogonality. Adding $(Eq.\ (3.70)) + (Eq.\ (3.71)) + 2 \times (Eq.\ (3.72))$ reveals the characteristic

$$g_\mathrm{t} + g_\mathrm{b} = 1. \tag{3.73}$$

Note that this is different to case A, where the relation of Eq. (3.63) holds. In case B a sensible representation of g_t and g_b is given by

$$g_\mathrm{t} = \sin^2(\beta) \text{ and } g_\mathrm{b} = \cos^2(\beta) \tag{3.74}$$

with $\beta \in [0, \frac{\pi}{2})$. The variables $\lambda_{\mathrm{t},+}$, and $\lambda_{\mathrm{b},+}$ that fulfill Eqs. (3.70)-(3.72) are found by eliminating $\lambda_{\mathrm{b},+}$ using $\Big(Eq.\ (3.70)) \times Eq.\ (3.71) - (Eq.\ (3.71))^2\Big)$. This reveals $\lambda_{\mathrm{t},+}$. The quantity $\lambda_{\mathrm{b},+}$ can subsequently be found by symmetry arguments. There is a pair of solutions that is distinguished by the additional parameter $s \in \{-1, 1\}$. The solutions read

$$\lambda_{\mathrm{t},+} = \frac{1}{\sqrt{2}}(\sqrt{g_\mathrm{t}} + s\sqrt{g_\mathrm{b}}), \tag{3.75}$$

$$\lambda_{\mathrm{b},+} = \frac{1}{\sqrt{2}}(\sqrt{g_\mathrm{b}} + s\sqrt{g_\mathrm{t}}) = s\lambda_{\mathrm{t},+}. \tag{3.76}$$

This results in

$$\begin{pmatrix} \nu_1(x) \\ \nu_2(x) \end{pmatrix} = \frac{1}{\sqrt{2}} \begin{pmatrix} \sqrt{g_t} - s\sqrt{g_b} & -s\sqrt{g_t} - \sqrt{g_b} \\ -\sqrt{g_t} - s\sqrt{g_b} & \sqrt{g_b} - s\sqrt{g_t} \end{pmatrix} \begin{pmatrix} \varphi_{t,+}(x) \\ \varphi_{b,+}(x) \end{pmatrix} \tag{3.77}$$

and

$$J^z_\mathrm{t} = 2\pi v\,(g_\mathrm{t} + s\sqrt{g_\mathrm{b} g_\mathrm{t}}) = \pi v(1 - \cos(2\beta) + s\sin(2\beta)) \tag{3.78}$$

$$J^z_\mathrm{b} = 2\pi v\,(g_\mathrm{b} + s\sqrt{g_\mathrm{t} g_\mathrm{b}}) = \pi v(1 + \cos(2\beta) + s\sin(2\beta)). \tag{3.79}$$

The obtained solutions can readily be verified to fulfill Eqs. (3.70)-(3.72)[12]. To be concrete, the Toulouse points of case B are represented by

$$\begin{aligned} B =& \{v_\mathrm{t}, g_\mathrm{t}, J^z_\mathrm{t}, v_\mathrm{b}, g_\mathrm{b}, J^z_\mathrm{b}\} \\ =& \{v, \sin^2(\beta), \pi v(1 - \cos(2\beta) + s\sin(2\beta), \cos^2(\beta), \\ & \pi v(1 + \cos(2\beta) + s\sin(2\beta)) \mid v \in \mathbb{R},\ \beta \in [0, \frac{\pi}{2}),\ s \in \{-1, 1\}\}. \end{aligned} \tag{3.80}$$

[12]In fact, the validity of the solution *must* be verified regarding the use of non-equivalence transformations in the course of the derivation.

3.1.3.3. Summary

In summary, we find that the set of Toulouse points for the two channel Kondo model with helical leads separates into two subsets that we call A and B. The Toulouse points of subset A fulfill the relation $g_\mathrm{t} + g_\mathrm{b} = 2$, which means that for repulsive interactions on one lead, the other lead exhibits attractive interactions[13]. A special Toulouse point in this class is the non-interacting limit with $g_\mathrm{t} = g_\mathrm{b} = 1$. The subset B contains Toulouse points that obey $g_\mathrm{t} + g_\mathrm{b} = 1$, which includes the prominent case $g_\mathrm{t} = g_\mathrm{b} = 1/2$. The physics of the system at these points will turn out to be decisively different from the one experienced by systems with parameters in A, which, as we explain in Chapter 5 results from that fact that there appear no anomalous terms, i.e., products of two creation operators, in the refermionized Hamiltonian of case B.

3.2. Finitization of divergences generated by a local scatterer

This section is a revised version of the appendix of *Posske & Trauzettel [2014]*, copyrighted by the American Physical Society. Also regard the remarks on page 3.

In this section, we explain the method that we use in Section 5.2 to backpropagate the density operator for the two channel Kondo model of helical liquids at $g = \frac{1}{2}$ in time. The time evolution can, as a consequence of our method, be carried out exactly, even if we depart from the Toulouse points in a specific way. We consider the method to be generalizable to diverse systems consisting of one-dimensional channels that are coupled to a zero dimensional scatterer. These systems intrinsically suffer from the fact that the time evolution of the moving particles is not well-defined at the point of the zero-dimensional scatterer. The solution that we propose to the problem is to regularize the size of the scatterer to be finite in extent. To facilitate further research regarding the aforementioned generalization, we especially explain the technical details of the procedure in this section.

Let us consider the Hamiltonian that is more detailedly explained in Section 5.2,

[13] The Toulouse points A would be physically relevant in a scenario where one of the leads is proximity-coupled to a superconductor. Additionally, the Toulouse points A are of interest because they contain the non-interacting limit.

Eq. (5.27):

$$\begin{aligned}\mathcal{H}^0 &= \sum_{a\in\{\mathrm{t,b}\}} \int dx\ \Psi^\dagger(x)_a(-\mathrm{i}\partial_x)\Psi(x)_a,\\ \mathcal{H}_K^\perp &= j_\mathrm{t}^\perp \Psi_\mathrm{t}^\dagger(0)\tau^- + j_\mathrm{b}^\perp \Psi_\mathrm{b}^\dagger(0)\tau^- + H.c.,\\ \mathcal{H}_K^z &= j_\mathrm{t}^z \Psi_\mathrm{t}^\dagger(0)\Psi_\mathrm{t}(0)\tau^z + j_\mathrm{b}^z \Psi_\mathrm{b}^\dagger(0)\Psi_\mathrm{b}(0)\tau^z.\end{aligned} \tag{3.81}$$

where Ψ describes a fermionic species, τ a spin $\frac{1}{2}$ degree of freedom, the appearing j are real coupling constants, and the indices t and b describe the bottom and the top lead. Note that this Hamiltonian is the refermionized two channel Kondo model for interacting helical leads close to the set of Toulouse points B, cf. Section 3.1.3. However, directly at the Toulouse points, $\mathcal{H}_K^z$ vanishes. Hence, we are treating a Hamiltonian that is not analytically solvable by standard means. In the following, we focus on evolving the density operator $\rho_a(x) := \Psi_a^\dagger(x)\Psi_a(x)$ with $x > 0$ backwards in time to shortly before it has interacted with the impurity. For this reason, we introduce the time dependence of all operators in the Heisenberg picture to be denoted as the second argument of the operator.

$$\Psi(x,t) = e^{\mathrm{i}\mathcal{H}t}\Psi(x,t=0)e^{-\mathrm{i}\mathcal{H}t}, \tag{3.82}$$

where we abandon the index of the lead now and in the following as the calculation is valid for either lead. To compute the time evolution, we look at the time derivative of Ψ at $t = 0$. For spatial arguments that are not equal to zero, the time evolution just becomes the linear propagation in space because the interaction with the magnetic moment is localized at $x = 0$. A technical problem in this procedure appears directly at $x = 0$, where we would have to evaluate the commutator $[\Psi(0,0), H]$ which is not well defined. The reason for this "divergence" of the derivative of the fermionic field is, physically speaking, the vanishing size of the impurity. To avoid this type of divergence, we introduce the smeared delta function $\delta_d^y(x)$ that is centered at $y \in \mathbb{R}$. The exact shape of this function is unimportant. Of importance are the following properties that are going to be used at a later stage:

$$\lim_{d\to 0}\int_{I\subset\mathbb{R}} dx\ \delta_d^y P(x) = \begin{cases} P(y) \text{ if } y \in \mathring{I} \subset \mathbb{R},\\ \frac{1}{2}P(y) \text{ if } y \in \partial I \subset \mathbb{R},\\ 0 \text{ else,}\end{cases} \tag{3.83}$$

for P being a sum of products of the fields τ^+, τ^-, Ψ, and $\Psi^\dagger$ in the Heisenberg picture, where x can appear in the time argument as well; $\mathring{I}$ denotes the interior of I and ∂I denotes the boundary of I. Furthermore, the following identity has to hold for multidimensional integrals

$$\begin{aligned}&\lim_{d\to 0}\int dx_1\ldots dx_n\ \delta_d^{y_1}(x_1)\ldots\delta_d^{y_n}(x_n)P(\vec{x})\\ &\quad= \lim_{d_1\to 0}\ldots\lim_{d_n\to 0}\int dx_1\ldots dx_n\ \delta_{d_1}^{y_1}(x_1)\ldots\delta_{d_n}^{y_n}(x_n)P(\vec{x}).\end{aligned} \tag{3.84}$$

A concrete example of the smeared delta function is the Lorentzian

$$\delta_d^y(x) = \frac{d}{\pi(d^2 + (x-y)^2)}. \tag{3.85}$$

In this context, the length scale d can be interpreted as the size of the impurity. The interaction Hamiltonians with a broadened impurity become

$$\begin{aligned}\mathcal{H}^{K,\perp} &= \sum_{a\in\{\mathrm{t,b}\}} j_a^\perp \int dx\ \delta_d^0(x)\Psi_a^\dagger(x)\tau^- \ + H.c.,\\ \mathcal{H}^{K,z} &= \sum_{a\in\{\mathrm{t,b}\}} j_a^z \int dx\ \delta_d^0(x)\Psi_a^\dagger(x)\Psi_a(x)\tau^z.\end{aligned} \tag{3.86}$$

The time derivative of $\Psi(x)$ is then given by

$$\partial_t\Psi(x,t)|_{t=0} = \mathrm{i}\left[\Psi(x,0),\mathcal{H}\right] = \partial_x\Psi(x) + \mathrm{i}j^\perp\delta_d^x(0)\Psi(x)\tau^+ + \mathrm{i}j^z\delta_d^x(0)\Psi(x)\tau^z. \tag{3.87}$$

We now solve the time evolution for the operator Ψ exactly by cutting the time into infinitesimally small slices, solving the evolution of a time slice exactly, and iterate. This technique shows similarities to an approach taken in the derivation of the path integral for quantum mechanics as presented in *Altland & Simons [2006a]*. Let us consider the field $\Psi(\epsilon, t=0)$ for $\epsilon \in \mathbb{R}^+$, which we want to backpropagate 2ϵ in time, where the units of time and space coincide because we have chosen the velocity of the particles to be unitless. We define $\epsilon \gg d$ [14], which means that we start sufficiently far away from the impurity to collect all its effects on the time evolution. Then, we obtain

$$\Psi(\epsilon,-2\epsilon) = e^{-\mathrm{i}\mathcal{H}2\epsilon}\Psi(\epsilon,0)e^{\mathrm{i}\mathcal{H}2\epsilon} = \lim_{N\to\infty}\left(1-\mathrm{i}\mathcal{H}\eta\right)^N\Psi(\epsilon,0)\left(1+\mathrm{i}\mathcal{H}\eta\right)^N, \tag{3.88}$$

with $\eta = \frac{2\epsilon}{N}$, where the convergence of the right hand side towards the left hand side is proven by comparing all orders in ϵ. Denoting

$$\Psi^k(\epsilon,0) := \left(1-\mathcal{H}\eta\right)^k\Psi(\epsilon,0)\left(1+\mathrm{i}\mathcal{H}\eta\right)^k, \tag{3.89}$$

we look at the first time slice

$$\begin{aligned}\Psi^1(\epsilon,0) &= \Psi(\epsilon,0) - \mathrm{i}\eta\left[\mathcal{H},\Psi(\epsilon,0)\right] + \mathcal{O}(\eta^2)\\ &= \Psi(\epsilon,0) - \eta\partial_x\Psi_a(\epsilon) - \mathrm{i}j_a^\perp\delta_d^\epsilon(0)\tau^-(0) - \mathrm{i}j_a^z\delta_d^\epsilon(0)\tau^z(0)\Psi(0,0) + \mathcal{O}(\eta^2)\\ &= \Psi(\epsilon-\eta,0) - \mathrm{i}j_a^\perp\delta_d^\epsilon(0)\tau^-(0) - \mathrm{i}j_a^z\delta_d^\epsilon(0)\Psi_a(0)\tau^z(0) + \mathcal{O}(\eta^2),\end{aligned} \tag{3.90}$$

[14] It is unusual for a parameter to be called ϵ that is taken larger than another variable. However, the naming stems from the fact that we are going to take ϵ to be small compared to the Kondo length scale at the end of the calculation.

where we use $[\Psi, \tau^z] = 0$. Since we take $\eta \to 0$ at the end of our calculations, we henceforth neglect terms of an order larger than or equal to η^2. This is justified by the identity

$$\lim_{N\to\infty} \left(1 + \frac{x}{N} + \mathcal{O}(\eta^2)\right)^N = e^x = \lim_{N\to\infty} \left(1 + \frac{x}{N}\right)^N. \tag{3.91}$$

The general formula for an arbitrary number of time steps is given by

$$\begin{aligned}\Psi^k = \; & \Psi(\epsilon - \eta k) + \sum_{n=1}^{\infty} (-\mathrm{i} j^z \eta)^n \sum_{(l_i)_{i=1}^n > 0}^{\sum_{i=1}^n l_i \leq k-n} \delta_d^\epsilon(\eta l_1) \left[\prod_{j=2}^{n} \delta_d^0(\eta l_j)\right] \\ & \times \left[\prod_{j=1}^{n} \tau^z \left(\eta \left(n - k - j + \sum_{i=1}^{n-j} l_i\right)\right)\right] \\ & \times \left(\frac{j^\perp}{j^z}\tau^-(\eta\kappa) + \tau^z(\eta\kappa)\Psi(\eta\kappa, 0)\right)\Bigg|_{\kappa = n-k+\sum_{i=1}^n l_i}.\end{aligned} \tag{3.92}$$

Here, $(l_i)_{i=1}^n > 0$ denotes all n-tuples of integers, each of which is larger than 0, and the product assumes an ordering of its factors from the left to the right with increasing index, i.e., $\prod_{j=1}^n a_j = a_1 \times \ldots \times a_n$. Eq. (3.92) can be proven by complete induction over k.

3.2.1. Proof by induction

In the following, we use the shorthand notation

$$\gamma \equiv -\mathrm{i} j_a^z, \tag{3.93}$$

$$\alpha_k \equiv \frac{j_a^\perp}{j_a^z} c(\eta k) + \tau^z(\eta k)\Psi(\eta k, 0), \tag{3.94}$$

$$\beta_k \equiv \tau^z(\eta k). \tag{3.95}$$

Then, Eq. (3.90) reads

$$\Psi^1 = \Psi(\epsilon - \eta) + \gamma\eta\delta_a^\epsilon(0)\alpha_0. \tag{3.96}$$

For α_k, the evolution of one time step is readily obtained by Eq. (3.90):

$$(1 - \mathrm{i}\mathcal{H}\eta)\,\alpha_k\,(1 + \mathrm{i}\mathcal{H}\eta) = \alpha_{k-1} + \gamma\eta\delta_a^0(-\eta k)\beta_{\eta(k-1)}\alpha_0. \tag{3.97}$$

Because the next step is very technical, it may be of interest to the reader to gain intuition about the iteration of time slices by regarding the following equations.

$$
\begin{aligned}
\Psi^2 &= \Psi(\epsilon-2\eta)+\gamma\eta\sum_{l_1=0}^{1}\delta_a^\epsilon(\eta l_1)\alpha_{-1+l_1}+(\gamma\eta)^2\delta_a^\epsilon(0)\delta_a^0(0)\beta_{-1}\alpha_0,\\
\Psi^3 &= \Psi(\epsilon-3\eta)+\gamma\eta\sum_{l_1=0}^{2}\delta_a^\epsilon(\eta l_1)\alpha_{-2+l_1}+(\gamma\eta)^2\sum_{l_1=0}^{1}\sum_{l_2=0}^{1-l_1}\delta_a^\epsilon(\eta l_1)\beta_{-2+l_1}\alpha_{-1+l_1+l_2}\\
&\quad+(\gamma\eta)^3\delta_a^\epsilon(0)\delta_a^0(0)\delta_a^0(0)\alpha_0\beta_{-1}\beta_{-2},\\
\Psi^4 &= \Psi(\epsilon-4\eta)+\gamma\eta\sum_{l_1=0}^{3}\delta_a^\epsilon(\eta l_1)\alpha_{-3+l_1}+(\gamma\eta)^2\sum_{l_1=0}^{2}\sum_{l_2=0}^{2-l_1}\delta_a^\epsilon(\eta l_1)\beta_{-3+l_1}\alpha_{-2+l_1+l_2}\\
&\quad+(\gamma\eta)^3\sum_{l_1=0}^{1}\sum_{l_2=0}^{1-l_1}\sum_{l_3=0}^{1-(l_1+l_2)}\delta_a^\epsilon(\eta l_1)\delta_a^0(\eta l_2)\delta_a^0(\eta l_3)\beta_{-2+l_1+l_2}\beta_{-3+l_1}\alpha_{-1+l_1+l_2+l_3}\\
&\quad+(\gamma\eta)^4\delta_a^\epsilon(0)\delta_a^0(0)\delta_a^0(0)\delta_a^0(0)\beta_{-a}\beta_{-2}\beta_{-3}\alpha_0.
\end{aligned}
$$

Let us proceed with the proof. The start of the induction is already obtained for $k=1$ in Eq. (3.96). The step is given as follows:

$$
\begin{aligned}
\Psi^{k+1} &= (1-\mathrm{i}\mathcal{H}\eta)\,\Psi^k\,(1+\mathrm{i}\mathcal{H}\eta)\\
&= \Psi(\epsilon-\eta(k+1))+\underbrace{\gamma\eta\delta_a^\epsilon(k\eta)\alpha_0}_{\text{in next step's sum}}\\
&\quad+\sum_{n=1}^{\infty}(\gamma\eta)^n\sum_{(l_i)_{i=1}^n>0}^{\sum_{i=1}^n l_i\le k-n}\delta_a^\epsilon(\eta l_1)\left[\prod_{j=2}^{n}\delta_a^0(\eta l_j)\right]\times\left[\prod_{j=1}^{n}\beta_{-1-n-k-j+\sum_{i=1}^{n-j}l_i}\right]\\
&\quad\times\left[\alpha_{n-(k+1)+\sum_{i=1}^n l_i}+\underbrace{\gamma\eta\delta_a^0(\eta(k-n-\sum_{i=1}^{n}l_i))\beta_{n-(k+1)+\sum_{i=1}^{n-j}\alpha_0}}_{\text{shift index to next step}}\right],
\end{aligned}
\tag{3.98}
$$

such that

$$\begin{aligned}\Psi^{k+1} =&\Psi(\epsilon-\eta(k+1))+\sum_{n=1}^{\infty}(\gamma\eta)^n\left\{\sum_{(l_i)_{i=1}^n>0}^{\sum_{i=1}^n l_i\leq k-n}\delta_a^\epsilon(\eta l_1)\left[\prod_{j=2}^{n}\delta_a^0(\eta l_j)\right]\right.\\ &\times\left[\prod_{j=1}^{n}\beta_{-1-n-k-j+\sum_{i=1}^{n-j}l_i}\right]\alpha_{n-(k+1)+\sum_{i=1}^n l_i}\\ &+\sum_{(l_i)_{i=1}^{n-1}>0}^{\sum_{i=1}^{n-1}l_i\leq(k+1)-n}\delta_a^\epsilon(\eta l_1)\left[\prod_{j=2}^{n-1}\delta_a^0(\eta l_j)\right]\\ &\left.\times\delta_a^0((k+1)-n-\sum_{i=1}^{n-1}l_i)\left[\prod_{j=1}^{n}\beta_{-2-n-k-j+1+\sum_{i=1}^{n-j}l_i}\right]\beta_{-1+n-(k+1)+\sum_{i=1}^{n-1}l_i}\alpha_0\right\}.\end{aligned} \tag{3.99}$$

We now focus on the second summand in the large braces and introduce a dummy variable $l_n=(k+1)-n-\sum_{i=1}^{n-1}$. The sum $\sum_{(l_i)_{i=1}^{n-1}>0}^{\sum_{i=1}^{n-1}\leq(k+1)-n}\dots$ then has the same effect as $\sum_{(l_i)_{i=1}^{n}>0}^{\sum_{i=1}^{n}=(k+1)-n}\dots$, since l_n represents the missing amount from $\sum_{i=1}^{n-1}l_i$ to $(k+1)-n$. The second summand in the large braces therefore transforms to

$$\begin{aligned}&\sum_{(l_i)_{i=1}^{n}>0}^{\sum_{i=1}^{n}l_i=(k+1)-n}\delta_a^\epsilon(\eta l_1)\left[\prod_{j=2}^{n-1}\delta_a^0(\eta l_j)\right]\delta^0(\eta l_n)\\ &\quad\times\left[\prod_{j=2}^{n-1}\beta_{n-(k+1)-j=\sum_{i=1}^{n-j}l_i}\right]\beta_{n-(k+1)-1+\sum_{i=1}^{n-1}l_i}\alpha_{n-(k+1)+\sum_{i=1}^{n}l_i}\\ &=\sum_{(l_i)_{i=1}^{n}>0}^{\sum_{i=1}^{n}l_i=(k+1)-n}\delta_a^\epsilon(\eta l_1)\left[\prod_{j=2}^{n}\delta_a^0(\eta l_j)\right]\alpha_{n-(k+1)+\sum_{i=1}^{n}l_i}\left[\prod_{j=1}^{n}\beta_{-1-n-k-j+\sum_{i=1}^{n-j}l_i}\right].\end{aligned} \tag{3.100}$$

Hence, the two summands in the large braces of Eq. (3.99) simplify to

$$\sum_{(l_i)_{i=1}^{n}>0}^{\sum_{i=1}^{n}l_i\leq(k+1)-n}\delta_a^\epsilon(\eta l_1)\left[\prod_{j=2}^{n}\delta_a^0(\eta l_j)\right]\times\left[\prod_{j=1}^{n}\beta_{n-(k+1)-j+\sum_{i=1}^{n-j}l_i}\right]\alpha_{n-(k+1)+\sum_{i=1}^{n}l_i}, \tag{3.101}$$

which concludes the proof.

3.2.2. Continuum limit

To obtain the continuum limit in time and hence the time evolution, we let N go to infinity, which is equivalent to $\eta\to 0$. In doing so, we replace $\eta N\to 2\epsilon$ and set all

products of the form $\eta \times c$ to zero if c is a fixed and hence finite number. Furthermore, sums of the form $\sum_{l=1}^{N} \eta f(\eta l)$ become integrals for non diverging functions and operators f. This procedure yields

$$\begin{aligned}\Psi(\epsilon,-2\epsilon) = \; & \Psi(-\epsilon,0) \\ & + \sum_{n=1}^{\infty}(-\mathrm{i}j_a^z)^n \int_0^{2\epsilon} dl_1 \int_0^{2\epsilon-l_1} dl_2 \ldots \int_0^{2\epsilon-(\sum_{i=1}^{n} l_i)} dl_n \delta_d^{\epsilon}(l_1) \left[\prod_{j=2}^{n} \delta_d^0(l_j)\right] \\ & \times \left[\prod_{j=1}^{n} \tau^z(-2\epsilon + \sum_{i=1}^{n-j} l_i)\right] \\ & \times \left(\frac{j^{\perp}}{j^z}\tau^-(-2\epsilon + \sum_{i=1}^{n} l_i) + \tau^z(-2\epsilon + \sum_{i=1}^{n} l_i)\Psi(-2\epsilon + \sum_{i=1}^{n} l_i, 0)\right).\end{aligned} \tag{3.102}$$

For a particular shape of the impurity (encoded in δ_d), the integrals in general do not simplify further. But by taking the limit $d \to 0$, belonging to the case that the size of the impurity is considerably smaller than the resolution of the possible measurements, we can exploit the properties of the representation of the smeared delta function postulated in Eq. (3.83) and Eq. (3.84) to obtain

$$\Psi(\epsilon,-2\epsilon) = \Psi(-\epsilon,0)\frac{1-(\frac{j^z}{4})^2}{1+(\frac{j^z}{4})^2} - \tau^-(-\epsilon)\frac{\mathrm{i}j^{\perp}}{1+\mathrm{i}\frac{j^z}{4}} - \tau^z(-\epsilon)\Psi(-\epsilon,0)\frac{\mathrm{i}j^z}{1+(\frac{j^z}{4})^2}. \tag{3.103}$$

In this derivation, the property $(\tau^z)^2 = \frac{1}{4}$, and the identity $\sum_{n=0}^{\infty}(\mathrm{i}\frac{j^z}{4})^n = \frac{1}{1-\mathrm{i}\frac{j^z}{4}}$ for $|j^z| < 4$ have been exploited. Starting from Eq. (3.103), the evolution in time for the density operator becomes

$$\begin{aligned}\rho(\epsilon,-2\epsilon) &= \Psi^{\dagger}\Psi(\epsilon,-2\epsilon) \\ &= \rho(-\epsilon,0) \\ &\quad + \frac{\left(j^{\perp}\right)^2}{1+(\frac{j^z}{4})^2}\left(\tau^z(-\epsilon)+1/2\right) + \left(\mathrm{i}j^{\perp}\frac{1+\mathrm{i}\frac{j^z}{4}}{(1-\mathrm{i}\frac{j^z}{4})^2}\tau^+(-\epsilon)\Psi(-\epsilon,0) + H.c.\right).\end{aligned} \tag{3.104}$$

Notably, the term containing the two-particle operator $\Psi^{\dagger}(-\epsilon,0)\tau^z(-\epsilon)\Psi(-\epsilon,0)$ vanishes because its prefactor is zero.

3.3. Multidimensional optimization and integration - The Metropolis algorithm

Being able to optimize objects regarding certain properties is highly desirable. In practical problems, the optimality of systems can often be represented as a real

valued function that acts on a set of real parameters. The optimal system is found by determining the global maximum [15] of this function. In general, the parameter space is too large to sample it sufficiently to yield a satisfactory accuracy. This resulted in the creation of numerous numerical algorithms and strategies dedicated to optimization problems with widely spread applications from physics over engineering to market analysis *[Lemaréchal, 2001; Nocedal & Wright, 2006]*. Of particular interest here are so-called Monte Carlo algorithms as we employ the Metropolis algorithm, a Markov Chain Monte Carlo algorithm *[Kruschke, 2011; Müller-Gronbach et al., 2012]*, in Chapter 6 to determine the ground state and the thermal behavior of magnetic impurities on the surface of a three-dimensional topological insulator. Monte Carlo algorithms employ randomness to, for instance, determine the ground state or calculate multi-dimensional integrals like expectation values in solid state systems *[Müller-Gronbach et al., 2012]*. Consider the classical expectation value of a property A in a canonical ensemble

$$\langle A \rangle = \frac{1}{Z} \sum_{\omega \in \Omega} e^{-\beta E_\omega} A_\omega, \tag{3.105}$$

where β is the inverse temperature, Z is the partition function, E is the energy and Ω is the phase space of the system under consideration, which we take to be discrete for reasons of simplicity. Numerically sampling over the full phase space uniformly randomly and summing up the obtained contributions will in general yield poor results for the convergence to the actual result of the expectation value. The reason behind this is that, for sufficiently large β, the largest contribution to the sum is given by the energetically low lying states. However, these states are rare in the phase space, such that it is unlikely they will be chosen by the method in an adequate number *[Metropolis et al., 1953]*. *Metropolis et al. [1953]* therefore introduced an ingenious idea: instead of sampling states from the phase space uniformly randomly and weighting its contribution with the Boltzmann factor, they generate states according to the Boltzmann distribution and average uniformly over them. We want to explain this so-called Metropolis algorithm in greater detail and explain why it works. In doing so, we stay close to the original explanation of *Metropolis et al. [1953]*. The algorithm is short:

1. generate an initial state of the system,
2. iterate the following sufficiently often:
   i) propose a random change of the state,
   ii) accept the change with the probability $\min\left(1, e^{-\beta \Delta E}\right)$.

   Here, $\Delta E = E_2 - E_1$, wherein E_1 is the energy of the current state and E_2 is the energy of the proposed state.

[15] Of course, determining the global minimum instead is a pure matter of taste.

3. Average the desired quantity uniformly over the tuple of states obtained by the iterations of 2.

The proposed random change in 2i) has to be ergodic, and unbiased, i.e., the random changes are in principle able to sample the whole phase space and the probability $P_{\omega,\xi}$ of changing the state ω to the state ξ is equal to the probability $P_{\xi,\omega}$ of the inverse process. Let us explain why the Metropolis algorithm succeeds in generating a Boltzmann distribution of the states characterized by

$$p_\omega/p_\xi = e^{-\beta\left(E_\omega - E_\xi\right)}. \tag{3.106}$$

To this end, we describe the system by a rate equation for the probabilities p_ω that the system resides in state ω. The rate equation is

$$\begin{aligned} p_\omega(t+1) - p_\omega(t) = &\underbrace{\sum_{\xi^<} P_{\xi^<,\omega} e^{-\beta\left(E_\omega - E_{\xi^<}\right)} p_{\xi^<}(t)}_{\text{arriving from smaller energy}} - \underbrace{\sum_{\xi^<} P_{\omega,\xi^<} p_\omega(t)}_{\text{departing to smaller energy}} \\ &+ \underbrace{\sum_{\xi^>} P_{\xi^>,\omega} p_{\xi^>}(t)}_{\text{arriving from larger energy}} - \underbrace{\sum_{\xi^>} P_{\omega,\xi^>} e^{-\beta\left(E_{\xi^<} - E_\omega\right)} p_\omega(t)}_{\text{departing to larger energy}}, \end{aligned} \tag{3.107}$$

where $\xi^>$ runs over the states of larger energy than ω while $\xi^<$ runs over the states of less or equal energy. Now, let us consider any two states of the system, ω and ξ, with a finite transition probability $P_{\xi,\omega} = P_{\omega,\xi}$. We consider ξ to have a smaller energy than ω without loss of generality. The probability current from ω to ξ is

$$j_{\omega,\xi}(t) = P_{\omega,\xi} p_\omega(t) - P_{\xi,\omega} e^{-\beta\left(E_\omega - E_\xi\right)} p_\xi(t). \tag{3.108}$$

Hence,

$$\operatorname{sgn}\left\{j_{\omega,\xi}(t)\right\} = \operatorname{sgn}\left\{p_\omega(t) - e^{-\beta(E_\omega - E_\xi)} p_\xi(t)\right\}. \tag{3.109}$$

Therefore, the probability flows from ω to ξ if the ratio $\frac{p_\omega(t)}{p_\xi(t)}$ exceeds the Boltzmann ratio $e^{-\beta(E_\omega - E_\xi)}$ but instead flows from ξ to ω if $\frac{p_\omega(t)}{p_\xi(t)}$ is smaller than the Boltzmann ratio. In the course of iteration, $\frac{p_\omega(t)}{p_\xi(t)}$ will therefore be equilibrated to $e^{-\beta(E_\omega - E_\xi)}$, where all probability currents vanish and the system reaches detailed balance. This process of equilibration is also called thermalization. In practice, the size of the random step in 2i) has to be chosen according to the energetic landscape. If the step is too small, the state will not change enough to sample a sufficient region of the phase space. If it is too large, the acceptance rate will be very low, resulting in a mostly unchanged state as well. The Metropolis algorithm can also be used – as it will be done in Chapter 6 – to find the ground state of systems by taking the

limit $\beta \to \infty$. However, care has to be taken to avoid local minima, to which the algorithm would immediately stick if β is chosen too large from the start. Instead, a successive increase of β has turned out to be useful. Following this so-called annealing protocol[16], the algorithm can avoid local minima. Still, one has to keep in mind that achieving fast thermalization and efficient annealing protocols is more an art than an exact science[17] *[Kruschke, 2011]* and strongly depends on the problem to be solved.

3.4. Checking translationally invariant Hamiltonians for decomposability

In Chapter 7, we will design gapless topological insulators by coupling a gapped topological phase to a gapless semimetallic phase. Thereby, an interesting phase, the gapless topological system, is created. It is important to find out, whether the resulting system is intrinsically original or if it can be decomposed into two or more non-interacting systems by globally changing the frame of reference, where globally means momentum independently. We call such systems that fall apart into two non-interacting systems decomposable. Imagine a translation invariant Hamiltonian of the form

$$\mathcal{H} = \bigoplus_{k \in \mathrm{BZ}} h(k), \tag{3.110}$$

where $h(k)$ is the Hamiltonian in momentum space and k lies within the Brillouin zone (BZ). Here, we take $h(k)$ to be an n-dimensional, complex hermitian matrix that continuously depends on k. The Hamiltonian is said to be decomposable if there is a unitary transformation U with the property that $Uh(k)U^\dagger$ is, up to re-indexing, the direct sum of two lower-dimensional matrices for all $k \in \mathrm{BZ}$ and the structure of the blocks and the re-indexing does not change depending on k[18]. We say about such a unitary transformation U that it decomposes $\mathcal{H}$. In the following, we want to present a numerical[19] check for decomposability, which can be applied to the

[16] Although the terminology of the Metropolis algorithm strongly employs terms from thermodynamics (thermalization, annealing), the process of iterating the Metropolis algorithm starting from a random initial position is not to be confused with the proper, physical thermalization and the annealing protocol must not be confused with the proper dynamics of the system.

[17] Giorgio Sangiovanni, 2014, private communication.

[18] Some brief remark on the choice of the wording: our definition of decomposability is similar to the definition of decomposability of linear representations of groups, which must not be confused with the definition of reducibility *[Dresselhaus et al., 2008]*. Note, however, that $\{h(k) \mid k \in \mathrm{BZ}\}$ is not a group. Using the word reducible would in this context therefore be confusing. The wording could also be confused with the reducibility by a unitary transformation in the context of Cartan-Altland-Zirnbauer classes as mentioned in Chapter 7.

[19] The method can also be employed analytically for sufficiently simple systems.

systems in Chapter 7. The test is also applicable to general translationally invariant Hamiltonians. While the upcoming proof is of technical nature, the underlying idea is short: (i) diagonalize $h(p)$ at one point p in momentum space where $h(p)$ is non-degenerate. By this, the system at one point in momentum space, namely p, is maximally decomposed. (ii) The full system, for all momenta, is then either also decomposed by the transformation utilized in *(i)* or not. In the first case, we have found a decomposing transformation. In the second case, it turns out that the full system is not decomposable at all. In this respect, we formulate

Theorem 1 (Check for decomposability)**.** *For a given Hamiltonian $\mathcal{H}$ according to Eq. (3.110), choose a $p \in BZ$ and let U_p be a unitary operator that diagonalizes $h(p)$. The Hamiltonian is decomposable if and only if the operator U_p decomposes $\mathcal{H}$.*

Proof. We fix a $p \in \mathrm{BZ}$ and a U_p such that $h(p)$ is nondegenerate and diagonalized by U_p. Let us assume that $\mathcal{H}$ is decomposable[20]. Then, by the definition of decomposability above, there exists a unitary operator U' such that $U'h(k)U'^{\dagger}$ is the direct sum of two lower-dimensional matrices for all $k \in \mathrm{BZ}$. This is in particular true for $k = p$. Let $m \geq 2$ denote the number of different blocks into which the Hamiltonian is decomposed by U'. By lemma 1 – that we give below – there are unitary operators u_i with $i \in \{1 \dots m\} =: I$ that can be interpreted to act exclusively on the i-th block such that

$$U_p = \mathcal{P}\left(\bigoplus_{i\in I} u_i\right) U', \tag{3.111}$$

with an appropriate permutation of the row vectors $\mathcal{P}$. By direct application of Eq. (3.111), it follows that

$$U_p h(k) U_p^{\dagger} = \mathcal{P}\left(\bigoplus_{i\in I} u_i\right) U'h(k)U'^{\dagger} \left(\bigoplus_{i\in I} u_i\right)^{\dagger} \mathcal{P}^{\dagger} \tag{3.112}$$

for all $k \in \mathrm{BZ}$. If we regard the right hand side, then $U'h(k)U'^{\dagger}$ is block diagonal with m blocks by definition and the subsequent transformation by $\bigoplus_{i\in I} u_i$ conserves this property as the u_i only act on the i-th block. Therefore $U_p h(k) U_p^{\dagger}$ is block diagonal up to k-independent re-indexing and expressible as the direct sum of two lower-dimensional matrices (up to re-indexing). Hence, $\mathcal{H}$ is decomposable by definition. □

Lemma 1. *Let h be a nondegenerate, n-dimensional hermitian matrix and U a unitary operator that diagonalizes h. Furthermore, let U' be a unitary operator that block diagonalizes h into m blocks. Then there are unitary operators u_i with*

[20] To be complete: if U_p decomposes $\mathcal{H}$, then the Hamiltonian is decomposable. This is a trivial statement. The proof is only concerned about the inverse direction.

$i \in \{1 \dots n\}$ that only act on the i-th block and a permutation of the row vectors $\mathcal{P}$ such that

$$U = \mathcal{P}(\bigoplus_{i \in I} u_i)U'. \tag{3.113}$$

Proof. Each block of $U'hU'^{\dagger}$ is hermitian, hence, there is a unitary operator, which we call v_i, that diagonalizes the i-th block. The operator $V = (\bigoplus_{i \in I} v_i)U'$ then diagonalizes h by virtue of its definition. Therefore, both U and V diagonalize h. But the diagonalizing operator of a nondegenerate matrix is unique up to permutations of its column vectors and a unitary factor per column vector. This is the case because the column vectors are set as normed eigenvectors of the one-dimensional eigenspaces. Hence, there is a permutation $\mathcal{P}$ and phases $e^{\mathrm{i}\phi_j}$ with $\phi_j \in [0, 2\pi)$ and $j \in \{1, \dots n\}$ such that $U = \mathcal{P}D\left(\left(e^{\mathrm{i}\phi_j}\right)_{j=1}^{n}\right)V$, where $D(\dots)$ denotes the diagonal matrix with the diagonal entries specified in the brackets. Let s_i and $f_i \in \{1, \dots, n\}$ denote the starting and the end index of the i-th block in $U'hU'^{\dagger}$ respectively. We then define $u_i = D\left(\left(e^{\mathrm{i}\phi_j}\right)_{j=s_i}^{f_i}\right)v_i$ and Eq. (3.113) follows. □

3.5. Applied transport simulations for superconductors

This section is a revised version of a part of the supplemental material of *Baum et al. [2015a]*, copyrighted by the American Physical Society. Also regard the remarks on page 3.

It is important for Chapter 6 to be able to have a signature in transport that distinguishes between gapped and gapless superconductors, where the gap refers to the spectral gap of the Bogoliubov-De Gennes Hamiltonian of the bulk. While both gapped and gapless superconductors are perfect conductors of charge, their thermal conductance is markedly different. The transport calculations that yield the results of Chapter 6 are performed by connecting the system to disorder free leads at temperatures T_0 and $T_0 + \delta T$, and computing the scattering matrix,

$$S_{\mathrm{ab}} = \begin{pmatrix} r_{\mathrm{ab}} & t_{\mathrm{ab}} \\ t'_{\mathrm{ab}} & r'_{\mathrm{ab}} \end{pmatrix}, \tag{3.114}$$

between any two leads, a and b. This enables us to determine the thermal conductance in the low-temperature, linear response regime, $G_{\mathrm{ab}} = G_0 \mathrm{Tr}\,(t_{\mathrm{ab}} t_{\mathrm{ab}}^{\dagger})$ where $G_0 = \pi^2 k_{\mathrm{B}}^2 T_0/(6h)$ is the quantum of thermal conductance for superconductors, which is half the value of the ordinary quantum of thermal conductance *[Dahlhaus et al., 2010; Kane & Fisher, 1996; Rego & Kirczenow, 1999; Schwab et al., 2000]*. All transport simulations are performed using the Kwant code *[Groth et al., 2014]*.

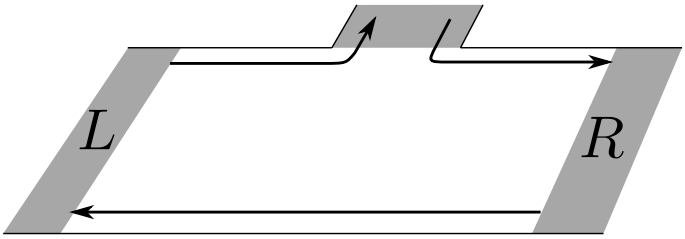

Figure 3.1.: Sketch of the three-terminal geometry used in transport simulations. The edge states (arrows) give the only chiral contribution to transport. Figure reprinted with permission from *Baum et al. [2015a]* (supplemental material). Copyright (2015) by the American Physical Society.

Conventional topological superconductors have a gapped bulk, such that the thermal conductance is only generated by edge state transport. In contrast, gapless topological superconductors have both bulk and edge excitations at the Fermi level, hence, both contribute to the conductance. In order to separate the bulk and edge contributions, we perform transport simulations in a three-terminal setup, as shown in Fig. 3.1. By subtracting the conductance between any two leads from the one of the reverse direction ($G_{LR} - G_{RL}$, for instance), we obtain the chiral contribution to transport, which, in the model of Chapter 6, exists only due to the edge states.

Transport through the bulk and edge may also be determined by comparing the conductance of a system when changing from hard-wall to periodic boundary conditions, as it is done in Chapter 7. In the model of Chapter 6, however, different lattice terminations independently change the chirality of the edge states, and result in the formation of a spurious conducting channel when periodic boundary conditions are applied. Hence, for a typical termination, the difference in conductance between systems with hard-wall and periodic boundary conditions contains contributions from both the edge and the bulk. Therefore, this setup can not be used for all possible terminations. The three-terminal setup of Fig. 3.1 overcomes this problem, while being less prone to finite-size effects, since the boundary conditions are kept fixed. Additionally, unlike the periodic boundary conditions technique, it has the advantage of modeling an experimentally accessible scenario.

Part II.

Results

4. The local Rashba scatterer

One of the dominant contributions to the popularity of the quantum spin Hall state is the insensibility of its edge states to time reversal preserving elastic backscattering. The canonical question arises which perturbations at all are capable of altering their perfect conductance. This answer is of experimental importance as well by indicating which perturbations should be avoided to reduce the observed decrease in conductance for larger samples *[König, 2008]*. The theoretical research into this direction covered numerous scenarios which, for instance, describe the influence of magnetic impurities *[Maciejko et al., 2009; Tanaka et al., 2011]*[1]; flux trapping loops *[Delplace et al., 2012]*; the combined effects of disorder, a magnetic field, spin-orbit interactions, and charge puddles *[Essert et al., 2015; Essert & Richter, 2015; Väyrynen et al., 2013]*; Rashba scatterers *[Budich et al., 2012; Geissler et al., 2014; Ström et al., 2010]*; or even the interplay of some of these ingredients *[Kimme et al., 2015]*. Here, Rashba scatterers play a particularly interesting role because realizations of topological insulators intrinsically rely on the effect of strong spin-orbit coupling. While the Rashba interaction alone is elastic and therefore cannot induce backscattering, its interplay with intrinsic interactions is able to generate multi-particle backscattering processes. Along this line, *Geissler et al. [2014]* and *Crépin et al. [2012]* have a look at the interplay between electron-electron interactions and a single, localized scatterer or randomly distributed scatterers respectively. Their analysis shows that the interaction strength described by a Luttinger parameter of $g = \frac{1}{2}$ represents a very peculiar case. On the one hand, the Rashba disorder and the two particle backscattering become relevant, in the renormalization group context, for $g < \frac{1}{2}$ while being irrelevant for $g > \frac{1}{2}$. On the other hand, the system possesses a line of fixed points at $g = \frac{1}{2}$. Additionally, for the case of a single rashba scatterer, $g = \frac{1}{2}$ marks the point of crossover between two different scaling behaviors of the conductance correction in dependence on temperature *[Crépin et al., 2012]*[2]. In fact, there is no sign that two-particle backscattering is at all generated for the peculiar interaction strength $g = \frac{1}{2}$ up to fourth order in perturbation theory[3] and first order in a renormalization group analysis *[Crépin et al., 2012]*. The description of the physics around $g = \frac{1}{2}$ therefore is of particular interest and can lead to a

[1] Chapter 5 goes into detail about the effects induced by a magnetic Kondo impurity.

[2] For a random Rashba potential, in contrast, the crossover of the scaling behavior shifts to $g = \frac{1}{4}$ *[Geissler et al., 2014]*

[3] Based on notes of Florian Geissler, April 2015. There is going to be a manuscript on the perturbational treatment of the local Rashba scatterer on arxiv.org soon.

better understanding what fundamentally distinguishes the regimes of $g > \frac{1}{2}$ and $g < \frac{1}{2}$.

In this chapter, the Hamiltonian of a helical liquid coupled to a localized Rashba scatterer is bosonized and a certain set of its refermionizable points is determined. To achieve this, we employ the generalized Emery Kivelson transformation of Section 3.1.2, which renders it possible to refermionize the Hamiltonian for all interaction strengths $g < 1/2$. The absence of such a simplifying refermionization for $g > \frac{1}{2}$ underlines the fundamental difference to the regime $g < \frac{1}{2}$. The refermionized Hamiltonian resembles the one of free fermions that interact in a peculiar manner at the origin. It also contains unusual summands that consist of a product of an odd number of fermionic operators.

For the special case of $g = 1/2$, the full Hamiltonian is directly simplifiable by refermionization and maps to a quadratic model. The quadratic model is subsequently exactly diagonalized by the scheme of *von Delft & Schoeller [1998]* that was applied to an ordinary backscatterer. There are important differences between the Rashba scatterer at the refermionizable point and the ordinary backscatterer:

1. ultra-violet integral divergences appear that are treated by a momentum cutoff Λ,

2. if the limit $\Lambda \to \infty$ is taken carelessly, the eigenparticles of the Rashba Hamiltonian are the same as if there was no Rashba scatterer.

Because of 2., numerous observables, especially transport properties, do not depend on the strength of the Rashba scatterer α_R. In particular, they remain unaltered compared to the bare Luttinger liquid without Rashba impurity. This mechanism is the mathematical explanation for the absence of the generation of two-particle backscattering at $g = \frac{1}{2}$. To illustrate this, we analytically show the extinction of the backscattering current for an arbitrarily large applied voltages at arbitrary temperatures.

Nonetheless, there are properties of the system that are affected by the Rashba scatterer. For instance, we show that the expectation value of the Rashba energy is one of them and additionally construct an observable with this feature, namely $\frac{e^{\mathcal{H}(\alpha_R=0)}}{Z(\alpha_R=0)} - \frac{e^{\mathcal{H}(\alpha_R=\alpha_f)}}{Z(\alpha_R=\alpha_f)}$, where Z is the partition function, $\mathcal{H}$ the Hamiltonian of the system, and α_f is an arbitrary non-zero complex constant. Although this hermitian operator does not immediately deliver an experimentally available observable, its existence demonstrates that the Rashba impurity at $g = 1/2$ has an effect on the system at all.

4.1. System

Fig. 4.1 illustrates the schematic setup of a local Rashba scatterer, c.f. Section 2.2.2, coupled to a helical liquid at the edge of a quantum spin Hall insulator, c.f. Sec-

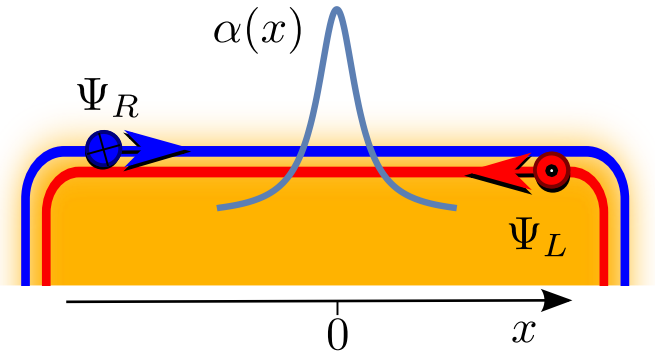

Figure 4.1.: A local Rashba scatterer coupled to a helical liquid at the edge of a quantum spin Hall insulator. The Rashba scatterer is illustrated by the gray line, which represents the spatial profile of the structural inversion symmetry $\alpha(x)$. This could be generated by an electric field. The helical liquid is described by the left mover Ψ_L with spin up and the right mover Ψ_R with spin down.

tion 2.1.3. The Hamiltonian that is the base to describe this system is

$$\mathcal{H} = \mathcal{H}_0 + \mathcal{H}_{\text{int}} + \mathcal{H}_R. \tag{4.1}$$

Here, $\mathcal{H}_0$ and $\mathcal{H}_{\text{int}}$ denote an interacting, helical Tomonaga-Luttinger liquid with the Luttinger parameters g and v, where we set $v = 1$ for convenience. Their explicit form is given in Section 3.1.3, Eq. (3.42). Furthermore, the Rashba Hamiltonian is

$$\mathcal{H}_R = \int_{-L/2}^{L/2} dx\ \alpha(x) \left(\Psi_R^{\dagger\prime} \Psi_L - \Psi_R^\dagger \Psi_L' \right)(x) + H.c. \tag{4.2}$$

with the real space fermionic operators Ψ_L (for the left moving fields), and Ψ_R (for the right moving fields), which we conveniently demand to obey periodic boundary conditions. The Hamiltonian is essentially the same as in *Crépin et al. [2012]*.

If we introduce the Fourier transform

$$\Psi_{L/R}(x) = \sum_{k \in \frac{2\pi}{L}\mathbb{Z}} \frac{e^{\mp ikx}}{\sqrt{L}} c_{L/R,k}, \tag{4.3}$$

the Hamiltonian above is represented by

$$\begin{aligned}
\mathcal{H}_0 =& \sum_{s\in\{L,R\}} \sum_{k\in\frac{2\pi}{L}\mathbb{Z}} k c^\dagger_{s,k} c_{s,k},\\
\mathcal{H}_R =& -\mathrm{i}\sum_{k_1,k_2} \frac{\alpha(x)}{L}\left(e^{-\mathrm{i}x(k_1+k_2)} k_1 c^\dagger_{R,k_1} c_{L,k_2} - e^{-\mathrm{i}x(k_1+k_2)} k_2 c^\dagger_{R,k_1} c_{L,k_2}\right) + H.c.\\
=& \sum_{k_1,k_2} \tilde{\alpha}(k_1,k_2) c^\dagger_{R,k_1} c_{L,k_2} + H.c.,\\
\tilde{\alpha}(k_1,k_2) =& \int_{-L/2}^{L/2} dx\ \alpha(x) \frac{\mathrm{i}(k_2-k_1)e^{-\mathrm{i}x(k_1+k_2)}}{L},\\
\mathcal{H}_{\mathrm{int}} =& g\sum_{k_1,k_2,k_3} c^\dagger_{R,k_1} c^\dagger_{L,k_2} c_{R,k_3+k_1} c_{L,k_3+k_2}.
\end{aligned} \tag{4.4}$$

Note that the momentum index k that labels the operators $c_{L,k}$ and $c^\dagger_{L,k}$ is not the physical momentum but the negative momentum in this convention.

4.1.1. Bosonization

Instead of introducing different conventions for left and right moving fields, it is more convenient, from our point of view, to first convert all fields to right moving fields. We denote these right moving fields with an additional tilde,

$$\tilde{\Psi}_\uparrow(x) = \Psi_L(-x), \tag{4.5}$$

$$\tilde{\Psi}_\downarrow(x) = \Psi_R(x). \tag{4.6}$$

This rewriting facilitates the application of bosonization along the lines of Section 3.1.1. Applying the bosonization identity subsequently, which reads

$$\tilde{\Psi}_\sigma = \frac{F}{\sqrt{2\pi a}} e^{-\mathrm{i}\tilde{\varphi}_\sigma(x)} \quad \text{for } \sigma\in\{\uparrow,\downarrow\}, \tag{4.7}$$

the full Hamiltonian of the local Rashba scatterer, i.e., $\alpha(x)=\delta(x)\alpha$, is expressed as

$$\mathcal{H}_0 = \sum_\sigma \int dx \frac{v}{2}\left(\varphi'_\sigma(x)\right)^2 \tag{4.8}$$

$$\begin{aligned}
\mathcal{H}_R =& \alpha\left(\Psi^\dagger_L \Psi'_R - \Psi^{\dagger\prime}_L \Psi_R\right)(0) + H.c.\\
=& \alpha\left(\tilde{\Psi}^{\dagger\prime}_\uparrow \tilde{\Psi}_\downarrow + \tilde{\Psi}_\uparrow{}^\dagger \tilde{\Psi}'_\downarrow\right)(0) + H.c.\\
=& \alpha\frac{F^\dagger_\downarrow F_\uparrow}{2\pi a}\left[e^{\mathrm{i}\tilde{\varphi}_\downarrow(0)}\mathrm{i}\tilde{\varphi}'_R(0) e^{-\mathrm{i}\tilde{\varphi}_\uparrow(0)} + e^{\mathrm{i}\left(\tilde{\varphi}_\downarrow(0)-\tilde{\varphi}_\uparrow(0)\right)}\left(-\mathrm{i}\tilde{\varphi}'_\uparrow(0)\right)\right] + H.c.\\
=& -\alpha\frac{\mathrm{i}}{2\pi a} F^\dagger_\downarrow F_\uparrow e^{\mathrm{i}\left(\tilde{\varphi}_\downarrow(0)-\tilde{\varphi}_\uparrow(0)\right)}\left(-\tilde{\varphi}'_\downarrow(0)+\tilde{\varphi}'_\uparrow(0)\right) + H.c.\\
=& \alpha\frac{-1}{\sqrt{2g}\pi a} F^\dagger_\downarrow F_\uparrow e^{-\mathrm{i}\sqrt{2g}\tilde{\varphi}_+(0)}\tilde{\varphi}'_+(0) + H.c..
\end{aligned} \tag{4.9}$$

Here, we employ the bosonic field ϕ_+ as introduced in Eq. (3.46) - Eq. (3.49) (in Section 3.1.3) and have to keep in mind that $[\tilde{\varphi}_\downarrow(x), \tilde{\varphi}_\uparrow(x')] = 0$.

4.2. Refermionizable points

The given form of the transformed Rashba Hamiltonian implies a particularly simple form of the full Hamiltonian in the limit $g \to 1/2$, namely

$$\mathcal{H}_R = \frac{-1}{\sqrt{g\pi a}} \left(\alpha \Psi_+{}' + \alpha^* \Psi_+^\dagger{}' \right) \tag{4.10}$$

employing the refermionization, cf. Section 3.1.1,

$$\Psi_+(x) = \frac{1}{\sqrt{2\pi a}} F_\downarrow^\dagger F_\uparrow e^{-\mathrm{i}\varphi_+(x)}. \tag{4.11}$$

Note that $F_\uparrow^\dagger F_\downarrow$ fulfills the algebra of a Klein factor. It may be interesting to mention that it is physically intuitive that the Rashba Hamiltonian of Eq. (4.10) increases its relevance for decreasing g. This reflects the fact that the particle-particle interaction, encoded in g, facilitates the backscattering that is caused by the locally induced spin-orbit coupling.

We want to remark that the Hamiltonian is additionally refermionizable for a wider range of g. To this end, we employ the generalized Emery Kivelson transformation of Section 3.1.2

$$U = e^{\mathrm{i}B}, \tag{4.12}$$

to refermionize the term in Eq. (4.8) that contains a vertex operator of the form

$$e^{\mathrm{i}\lambda\phi_+(0)} A. \tag{4.13}$$

Comparing the general scheme with the problem at hand, we have

$$A = F_\downarrow^\dagger F_\uparrow \phi_+'(0), \quad \lambda_+ = -\sqrt{2g}, \quad \lambda_- = 0. \tag{4.14}$$

A possible choice for B that fulfills the requirements of Eq. (3.33) is

$$\begin{aligned} B &= a_- \mathcal{N} \phi_-(0), \\ \mathcal{N} &= \frac{1}{a_R + a_L} \left(a_R \mathcal{N}_R - a_L \mathcal{N}_L \right), \end{aligned} \tag{4.15}$$

with arbitrary real constants a_L and a_R. The checks employ the identities[4]

$$\left[F_a^\dagger, \mathcal{N}_{a'} \right] = -\delta_{a,a'} F^\dagger, \tag{4.16}$$

$$[F_a, \mathcal{N}_{a'}] = \delta_{a,a'} F. \tag{4.17}$$

[4] Note that the ansatz of Eq. (4.12) is also useful to refermionize the Hamiltonian of *von Delft & Schoeller [1998]* describing a normal backscattering impurity coupled to a spinless Tomonaga-Luttinger liquid. A suitable choice would be $U = e^{\mathrm{i}\mathcal{N}_+\phi_+(0)}$.

Since we have $\lambda_+ = -\sqrt{2g}$, together with the constraint $\lambda_+^2 + a_-^2 = 1$, as derived in Eq. (3.39), this transformation is limited to simplify Hamiltonians with an interaction strength $g \leq \frac{1}{2}$. If we refermionize the transformed bosons ν_i according to

$$\Psi_i = \frac{F_\uparrow^\dagger F_\downarrow}{\sqrt{2\pi a}} e^{-\mathrm{i}\nu_i}, \tag{4.18}$$

the Rashba Hamiltonian reduces to a model of locally interacting fermions

$$\mathcal{H}_R \propto \Psi_1^{\dagger\prime} \left(\lambda_+ + a_- \Psi_2^\dagger(0)\Psi_2(0)\right). \tag{4.19}$$

A drawback of the generalized Emery Kivelson transformation is the increasing complexity of the bare Hamiltonian $\mathcal{H}_0 = \sum_\sigma \frac{1}{2} \int dx \ \left(\phi'_\sigma(x)\right)^2$. Here, we have

$$\begin{aligned}
[B, \mathcal{H}_0] =& a_- \mathcal{N} \int dx \ 2\phi'_-(x) \underbrace{\left[\phi_-(0), \phi'_-(x)\right]}_{2\pi\mathrm{i}\delta(x) - \frac{1}{L}} \\
=& 4\pi\mathrm{i} a_- \mathcal{N} \left(\phi'_-(0) - \underbrace{\int dx \ \frac{\phi'_-(x)}{L}}_{=0} \right) \\
=& 4\pi\mathrm{i} a_- \mathcal{N} \phi'_-(0) =: C \qquad (4.20) \\
[B, C] =& -8\pi^2 a_-^2 \mathcal{N}^2 \delta(0) + \mathcal{O}\left(1/L\right). \qquad (4.21)
\end{aligned}$$

This results in

$$\begin{aligned}
U\mathcal{H}_0 U^\dagger =& \mathcal{H}_0 - 4\pi a_- \mathcal{N} \phi'_-(0) + 4\pi^2 a_-^2 \mathcal{N}^2 \frac{1}{a} \\
=& \mathcal{H}_0 - 4\pi a_- \mathcal{N} \left(a_- \Psi_1^\dagger(0)\Psi_1(0) - \lambda_+ \Psi_2^\dagger(0)\Psi_2(0)\right) + \frac{4\pi^2 a_-^2}{a} \mathcal{N}^2, \qquad (4.22)
\end{aligned}$$

where we have to take care not to conduct the limit $a \to 0$ incautiously in order to avoid the undefined object $\delta(0)$. The advantage of the fermionic description in Eq. (4.22) over the bosonic one is, in principle, the improved accessibility of perturbation theory. An example of how involved the perturbative treatment of the bosonic form can be will become available soon[5].

[5] Based on notes of Florian Geissler, April 2015. Cf. the respective footnote on p. 60.

4.3. Exact solution at the primary refermionizable point

After refermionization at $g = \frac{1}{2}$, cf. Eq. (4.10), and Fourier transforming, we reach at

$$\mathcal{H} = \sum_{k \in \frac{2\pi}{L}\mathbb{Z}} \epsilon_k c_k^\dagger c_k + \mathrm{i}kt \left(c_k^\dagger - c_k \right), \tag{4.23}$$

with the real constant $t = \frac{|\alpha|}{\sqrt{g\pi a}}$, where we have included the phase of α into the definition of c_k. An explicit scheme how to diagonalize this kind of Hamiltonian is given in *von Delft & Schoeller [1998]*, which we will follow closely here. First, we transform by

$$U = e^{\mathrm{i}\frac{\pi}{2}\mathcal{N}^2}, \tag{4.24}$$

where $\mathcal{N} = \sum_k c_k^\dagger c_k$. Employing the Hadamard lemma of Eq. (3.35) and

$$\begin{aligned}
\left[\mathcal{N}^2, c_k^\dagger\right] =& \mathcal{N}^2 c_k^\dagger - c_k^\dagger \mathcal{N}^2 = \begin{cases} 0 & \text{acting on } |1\rangle \\ 1|1\rangle & \text{acting on } |0\rangle \end{cases} = c_k^\dagger, \\
\left[\mathcal{N}^2, c_k\right] =& \mathcal{N}^2 c_k - c_k \mathcal{N}^2 = \begin{cases} -1|0\rangle & \text{acting on } |1\rangle \\ 0 & \text{acting on } |0\rangle \end{cases} = -c_k
\end{aligned} \tag{4.25}$$

this yields

$$\begin{aligned}
U c_k U^\dagger =& e^{\mathrm{i}\frac{\pi}{2}\left[\mathcal{N}^2, \cdot\right]} c_k = c_k - \mathrm{i}\frac{\pi}{2} c_k + \frac{\left(-\mathrm{i}\frac{\pi}{2}\right)^2}{2} c_k + \ldots, \\
=& e^{-\mathrm{i}\frac{\pi}{2}} c_k = c_k e^{-\mathrm{i}\pi\left(\mathcal{N} - \frac{1}{2}\right)} = \mathrm{i} c_k \alpha_D \\
U c_k^\dagger U^\dagger =& \left(U c_k U^\dagger \right)^\dagger = \mathrm{i} c_k^\dagger \alpha_D.
\end{aligned} \tag{4.26}$$

Here,

$$\alpha_D = e^{-\mathrm{i}\pi\mathcal{N}} \tag{4.27}$$

is a Majorana fermion which anticommutes with all c_k and $c_k^\dagger$. The fermion can also be called Matveev trick fermion due to its introduction in *Matveev [1995]*; although Matveev gives *Guinea [1985]* as his source of inspiration. However, it should be kept in mind that this Majorana fermion does not constitute an additional degree of freedom as it is an operator that is formed out of the c_k themselves, which already are a complete[6] set of operators. This is an important issue for perturbative approaches because α_D generally should have non-vanishing contractions with

[6] A complete set of operators means that the Hilbert space is spanned by sums of products of these operators acting on a specified vacuum state.

the lead fermions in order to render perturbation theory sensibly applicable. The transformed Hamiltonian then reads

$$U\mathcal{H}U^\dagger = \sum_k \left(\epsilon_k + \mu\right) c_k^\dagger c_k + kt\left(c_k - c_k^\dagger\right)\alpha_D. \tag{4.28}$$

Note that the zero momentum mode c_0 decouples from the Hamiltonian, due to the prefactor kt, and is henceforth excluded. Now, the Bogoliubov-ansatz is utilized:

$$\mathcal{H} = \sum_{\epsilon\in\mathcal{E}^+} \epsilon d_\epsilon^\dagger d_\epsilon + E_g, \tag{4.29}$$

with $\mathcal{E}^+$ being an appropriate index set for the eigenenergies, which are all taken to be real numbers larger or equal to zero[7]. The fermion d_ϵ is

$$d_\epsilon = \sum_k D^1_{\epsilon,k} c_k + \sum_k D^2_{\epsilon,k} c_k^\dagger + D_{\epsilon,D}\alpha_D = \sum_{i\in I} D_i c_i, \tag{4.30}$$

where

$$I = \left(\left(\frac{2\pi}{L}\mathbb{Z}\backslash\{0\}\right)\times\{1,2\}\right)\bigcup\{D\} \tag{4.31}$$

and

$$c_i = \begin{cases} c_k & \text{if } i = (k,1), \\ c_k^\dagger & \text{if } i = (k,2), \\ \alpha_D & \text{if } i = D. \end{cases} \tag{4.32}$$

We then obtain

$$\begin{aligned}
[d_\epsilon, \mathcal{H}] =& \epsilon d_\epsilon = \epsilon \sum_i D_i c_i \\
=& \left[\sum_i D_i c_i, \sum_k \left(k+\mu\right) c_k^\dagger c_k - kt\left(c_k^\dagger - c_k\right)\alpha_D\right] \\
=& \left(k+\mu\right)\left(D^1_{\epsilon,k} c_k - D^2_{\epsilon,k} c_k^\dagger\right) + \sum_k \left[tk\alpha_D\left(-D^1_{\epsilon,k} + D^2_{\epsilon,k}\right)\right] + D_{\epsilon,D} kt\left(c_k^\dagger - c_k\right),
\end{aligned} \tag{4.33}$$

and comparing coefficients results in

$$D^1_{\epsilon,k} = \frac{kt}{k+\mu-\epsilon} D_{\epsilon,D}, \tag{4.34}$$

$$D^2_{\epsilon,k} = \frac{kt}{k+\mu+\epsilon} D_{\epsilon,D}, \tag{4.35}$$

$$\epsilon D_{\epsilon,D} = \sum_k kt\left(D^2_{\epsilon,k} - D^1_{\epsilon,k}\right). \tag{4.36}$$

[7]The sign of the eigenenergies is not predetermined because of possible particle $\leftrightarrow$ hole transformations.

From these equations, we can determine the possible ϵ and the coefficients D_i. Firstly, there is a solution for $\epsilon = 0$: choose D^1 and D^2 according to Eq. (4.34) and Eq. (4.34), respectively, then Eq. (4.36) is automatically fulfilled. From the later mentioned orthogonality condition for D, Eq. (4.40), we obtain

$$D_{0,D} = e^{\mathrm{i}\phi_0} \left[1 + 2\sum_k \left(\frac{kt}{k+\mu}\right)^2\right]^{-1/2}, \tag{4.37}$$

where ϕ_0 is an arbitrary phase[8]. Secondly, we can determine the possible $\epsilon \neq 0$ by replacing D^1 and D^2 in Eq. (4.36). This results in the transcendent formula

$$\sum_k \frac{2\,(tk)^2}{\epsilon^2 - (k+\mu)^2} = 1. \tag{4.38}$$

The sum on the left hand side of Eq. (4.38) diverges for large k for any real ϵ. To solve the underlying issue, we introduce a momentum cutoff Λ and let all sums over k from now on run implicitly within the range of $[-\Lambda, \Lambda]$. In a physical system, the cutoff would signify the onset of bulk bands of the topological insulator or the validity regime of the linear approximation of one dimensional channels.

4.3.1. Orthogonality relations

The fermionic conditions

$$\begin{aligned} \left\{d_\epsilon, d^\dagger_{\epsilon'}\right\} &= \delta_{\epsilon,\epsilon'}, \\ \{d_\epsilon, d_{\epsilon'}\} &= 0 \end{aligned} \tag{4.39}$$

result in unitarity conditions for the coefficients D that read

$$\sum_{i\in I} D_{\epsilon,i} D^*_{\epsilon',i} = \delta_{\epsilon,\epsilon'}, \tag{4.40}$$

$$\sum_{i\in I} D_{\epsilon,i} D_{\epsilon',\bar{i}} = 0, \tag{4.41}$$

where the bar over the index, e.g., $\bar{i}$, signifies $(k,1) \mapsto (k,2)$, $(k,2) \mapsto (k,1)$, and $D \mapsto D$. For Eq. (4.40) with $\epsilon = \epsilon'$ and under consideration of Eq. (4.34) and Eq. (4.35) follows

$$D_{\epsilon,D} = e^{\mathrm{i}\phi_\epsilon} \left[1 + \sum_k \left(\frac{kt}{k+\mu-\epsilon}\right)^2 + \left(\frac{kt}{k+\mu+\epsilon}\right)^2\right]^{-1/2}, \tag{4.42}$$

[8] Later, it will be shown that the phase necessarily vanishes.

where ϕ_ϵ is a phase to be determined later. The expression can be simplified, using Eq. (4.38), to

$$D_{\epsilon,D} = e^{\mathrm{i}\phi_\epsilon} \left[\sum_k \left(\frac{2kt\epsilon}{(k+\mu)^2 - \epsilon^2} \right)^2 \right]^{-1/2} \tag{4.43}$$

because

$$\left(\frac{1}{k+\mu-\epsilon} \right)^2 + \left(\frac{1}{k+\mu+\epsilon} \right)^2 - \frac{-2}{-\epsilon^2 + (k+\mu)^2} = \left(\frac{1}{k+\mu-\epsilon} - \frac{1}{k+\mu-\epsilon} \right)^2 . \tag{4.44}$$

In summary, we have, until now, derived a necessary condition for all eigenenergies ϵ, stated in Eq. (4.38), and formulas for the corresponding coefficients by Eq. (4.34), Eq. (4.35), Eq. (4.37), and Eq. (4.42). Thereby, the Hamiltonian is already diagonalized exactly. For the practical, analytical calculation of observables that are given in terms of the fermionic fields c, however, we have to invert the transformation matrix D and evaluate the appearing sums that run over the momentum space. This is achieved in the following sections.

4.3.2. Inversion of D

We have already found that the set of fermions d is expressible as a linear combination of the fermions c of Eq. (4.32), i.e.,

$$d_\epsilon = \sum_i D_{\epsilon,i} c_i . \tag{4.45}$$

The inverse relation is given by

$$c_i = \sum_{\epsilon \in \mathcal{E}} \left(D^*_{\epsilon,i} d_\epsilon + D_{\epsilon,\bar{i}} d^\dagger_\epsilon \right) \left(1 - \frac{1}{2} \delta_{\epsilon,0} \right) . \tag{4.46}$$

If we introduce for each $\epsilon \in \mathcal{E}$ its negative partner to form the set $\mathcal{E}^\pm = \mathcal{E} \cup (-\mathcal{E})$ and define

$$D_{-\epsilon,i} = D^*_{\epsilon,\bar{i}}, \tag{4.47}$$

we can write Eq. (4.46) more compactly as

$$c_i = \sum_{\epsilon \in \mathcal{E}^\pm} D^*_{\epsilon,i} d_\epsilon . \tag{4.48}$$

The proof that Eq. (4.48) holds is, from our point of view, more involving than described by, for instance, *von Delft & Schoeller [1998]* and *Zaránd & von Delft*

[2000] within their approach to diagonalize the two channel Kondo model for Fermi liquid leads exactly. The proof relies on the fact that D is a unitary matrix, which transforms between the index sets I and $\mathcal{E}^{\pm}$. If we accept this statement, Eq. (4.48) becomes derivable by acting with $D^{\dagger}$ on Eq. (4.45). There are, however, some subtleties in this procedure, which we would like to comment on. The main issue regards a proper bijection between the index sets I and $\mathcal{E}^{\pm}$. Especially for finite momentum cutoffs, where the sets are countable, it becomes apparent that the index sets $\mathcal{E}$ and I do not have the same cardinality. And hence, without completion to $\mathcal{E}^{\pm}$, no linear transformation between the corresponding vector spaces can be an isomorphism (and hence D could not be an invertible matrix). However, if a proper bijection between $\mathcal{E}$ and I is found, we can assert that D is in the group of matrices connecting I and $\mathcal{E}^{\pm}$. We can subsequently apply the very general statement that for any group G, we have $aa^{-1} = a^{-1}a$ for all elements $a \in G$. Therefore, we can indeed infer Eq. (4.48) from Eq. (4.45) in the way the mentioned references indicate. In order to construct the necessary bijection between $\mathcal{E}^{\pm}$ and I, we continuously tune t from zero to its desired value, where for $t = 0$ the identity $\mathcal{E}^{\pm} = I$ is fixed[9].

By virtue of Eq. (4.47), we obtain the constraint $\mathrm{Im}\{D_{0,D}\} = 0$, which leads to

$$\phi_0 = 0. \tag{4.49}$$

Regarding the c fermions, we specifically have

$$c_k = c_{(k,1)} = \sum_{\epsilon \in \mathcal{E}^{\pm}} D^{*}_{\epsilon,(k,1)} d_{\epsilon}, \tag{4.50}$$

$$c_k^{\dagger} = c_{(k,2)} = \sum_{\epsilon \in \mathcal{E}^{\pm}} D^{*}_{\epsilon,(k,2)} d_{\epsilon} = \sum_{\epsilon \in \mathcal{E}^{\pm}} D_{\epsilon,(k,1)} d_{\epsilon}^{\dagger}, \tag{4.51}$$

$$\alpha_D = c_D = \sum_{\epsilon \in \mathcal{E}^{\pm}} D^{*}_{\epsilon,(k,D)} d_{\epsilon}.w \tag{4.52}$$

4.3.2.1. Confirmation of the unitarity of D

The unitarity of D, which is demanded by Eq. (4.39) can be checked to verify the findings for the coefficients as given in Eq. (4.34), Eq. (4.35), Eq. (4.37), and Eq. (4.42). This is done by showing that

$$\sum_i D_{\epsilon_i} D^{*}_{\epsilon',i} = \delta_{\epsilon,\epsilon'} \tag{4.53}$$

[9]Note that we already excluded the fermion of zero momentum c_0.

for all $\epsilon, \epsilon' \in \mathcal{E}^{\pm}$. For $\epsilon = \epsilon'$, Eq. (4.53) is valid as a direct consequence of inserting Eq. (4.42). For $\epsilon \neq \epsilon'$ we can employ partial fraction decomposition to yield

$$\begin{aligned}\sum_i D_{\epsilon,i} D^*_{\epsilon',i} &= \left[\sum_k (kt)^2 \left(\frac{1}{(k+\mu-\epsilon)(k+\mu-\epsilon')}\right) + 1\right] D_{\epsilon,D} D^*_{\epsilon',D} \\ &= \sum_k \frac{(kt)^2}{\epsilon-\epsilon'} \left(\underbrace{\frac{1}{k+\mu-\epsilon} - \frac{1}{k+\mu+\epsilon}}_{=\frac{2\epsilon}{(k+\mu)^2-\epsilon^2} \Rightarrow \sum_k (kt)^2 \cdots = -\epsilon} - \left[\frac{1}{k+\mu-\epsilon'} - \frac{1}{k+\mu+\epsilon'}\right] \right) + 1 \\ &= \frac{-\epsilon+\epsilon'}{\epsilon-\epsilon'} + 1 = 0, \end{aligned} \tag{4.54}$$

which needed to be shown.

4.4. Exact transition to infinite momentum cutoff

The eigenparticles of the Rashba Hamiltonian have been derived in Section 4.3. There is a peculiarity to these particles, namely that they do not differ from the original particles c in the limit $\Lambda \to \infty$. This apparent paradox is resolved by taking the order of the limits properly. It is a good example that the limit $\Lambda \to \infty$ should only be executed after having evaluated the observables for an arbitrary cutoff. If the limit is done the other way around, the Rashba impurity is found to leave the system completely unaltered. There is a nice proof that this is impossible and that the Rashba scatterer has to have some influence on the system. We give this proof in Section 4.7. It shows that two Hamiltonians that have the same observables for a finite, non-zero temperature only differ by a constant. Therefore, as the Rashba Hamiltonian is not just a constant, there have to be observables that depend on the strength of the Rashba scatterer.

In the following we calculate the transformation matrix D in the limit $\Lambda \to \infty$. First, we find the solutions for ϵ. For large cutoffs Λ, the transcendental equation for ϵ, Eq. (4.38),

$$1 = \sum_k \frac{2\,(kt)^2}{\epsilon^2 - (k+\mu)^2}, \tag{4.55}$$

has a large negative ultraviolet contribution. To compensate for that and fulfill the equation, ϵ^2 has to be just above $(k_\epsilon + \mu)^2$. Here, we label $k_\epsilon \in \frac{2\pi}{L}\mathbb{Z}$ with the index ϵ. As we only regard positive ϵ participating in the creation of the d fermions, cf. Eq. (4.30), we have the solution

$$\epsilon = |k_\epsilon + \mu| + \delta > 0, \tag{4.56}$$

where δ is a small parameter that vanishes for $\Lambda \to \infty$. We now calculate the transformation matrix D. By virtue of Eq. (4.56), we have

$$D_{\epsilon,D} = e^{\mathrm{i}\phi_\epsilon} \left[\sum_k \left(\frac{2\epsilon k t}{(k+\mu)^2 - \epsilon} \right)^2 \right]^{-1/2} \approx -e^{\mathrm{i}\phi_\epsilon} \frac{\delta}{k_\epsilon t} \to 0, \tag{4.57}$$

where $\approx$ means asymptotically for $\Lambda \to \infty$. Additionally, it is

$$D_{\epsilon,(k,1)} = e^{\mathrm{i}\phi_\epsilon} \frac{kt}{k+\mu-(k_\epsilon+\mu+\delta)} \frac{\delta}{k_\epsilon t} \to -e^{\mathrm{i}\phi_\epsilon} \delta_{k,k_\epsilon} \tag{4.58}$$

$$D_{\epsilon,(k,2)} \to -e^{\mathrm{i}\phi_\epsilon} \delta_{k,-k_\epsilon} \delta_{\mu,0}. \tag{4.59}$$

This means that for $\mu \neq 0$ and $\phi_\epsilon = \pi$, we have

$$d_\epsilon = c_{k_\epsilon}. \tag{4.60}$$

We observe that the case $\mu = 0$ is special in this regard, as it reveals $d_\epsilon \propto c_{k_\epsilon} + c^\dagger_{k_\epsilon}$. However, the case is also special in the sense that the fermions $\frac{1}{\sqrt{2}} \left(c_k - c_k^\dagger \right)$ decouple from the Hamiltonian and have exactly the same energy as $\frac{1}{\sqrt{2}} \left(c_k + c_k^\dagger \right)$. Therefore, even in this case, we can rotate the d fermions to obtain eigenparticles that do not differ from the c fermions.

We want to mention that the obtained transformation represented by D explicitly also holds for a finite cutoff and has been numerically checked for small systems to deliver correct results.

4.5. Backscattering current I_B

4.5.1. Derivation of the refermionized form of I_B

The operator describing the backscattering current I_{bs} is determined by

$$\begin{aligned}
\mathrm{i}I_{bs} =& \left[H_R, \frac{1}{2} \left(N_L - N_R \right) \right] \\
=& \frac{-1}{2} \int dx' dx \left[\alpha(x') \left(\Psi_R^{\dagger\prime} \Psi_L - \Psi_R^\dagger \Psi_L' \right)(x') + H.c., \left(\Psi_R^\dagger \Psi_R - \Psi_L^\dagger \Psi_L \right)(x) \right] \\
=& \frac{-1}{2} \int dx' dx \; \alpha(x') \Big(- \left\{ \Psi_R^{\dagger\prime}(x'), \Psi_R(x) \right\} \Psi_R^\dagger(x) \Psi_L(x') \\
& - \Psi_R^{\dagger\prime}(x') \left\{ \Psi_L(x'), \Psi_L^\dagger(x) \right\} \Psi_L(x) + \Psi_R^\dagger(x) \left\{ \Psi_R^\dagger(x'), \Psi_R(x) \right\} \Psi_L'(x') \\
& + \Psi^\dagger(x')_R \left\{ \Psi_L'(x') \Psi_L^\dagger(x) \right\} \Psi_L(x) \Big) - H.c..
\end{aligned} \tag{4.61}$$

Here, the $-H.c.$ originates from $[A,B]^\dagger = -\left[A^\dagger, B^\dagger\right]$ and

$$[AB, CD] = A \{B, C\} D - AC \{B, D\} + \{A, C\} DB - C \{A, D\} B \tag{4.62}$$

was used. Furthermore, employing

$$\left\{\Psi^\dagger(x')', \Psi(x)\right\} = \left\{\Psi^\dagger(x'), \Psi(x)'\right\} = \delta'(x'-x) \tag{4.63}$$

and $\int dx\ \delta'(x)f(x) = -f'(0)$, we obtain

$$\begin{aligned}
\mathrm{i}I_{bs} =& \frac{-1}{2}\int dx'dx\ \alpha(x')\left(-\delta'(x'-x)\Psi_R^\dagger(x)\Psi_L(x') - \Psi_R^\dagger(x')\delta(x'-x)\Psi_L(x)\right.\\
&\left.+\Psi_R^\dagger(x)\delta(x'-x)\Psi_L'(x') + \Psi_R^\dagger(x')\delta'(x'-x)\Psi_L(x)\right) - H.c.\\
=& \frac{-1}{2}\int dx\ \alpha(x)\left(+\Psi_R^\dagger\Psi_L' - \Psi^{\dagger\prime}{}_R\Psi_L + \Psi_R^\dagger\Psi_L' - \Psi^{\dagger\prime}{}_R\Psi_L\right)(x) - H.c.\\
=& \int dx\ \alpha(x)\left(\Psi_R^{\dagger\prime}\Psi_L - \Psi_R^\dagger\Psi_L'\right)(x) - H.c..
\end{aligned} \tag{4.64}$$

It is convenient to define

$$A = \int dx\ \alpha(x)\left(\Psi_R^{\dagger\prime}\Psi_L - \Psi_R^\dagger\Psi_L'\right)(x), \tag{4.65}$$

and we observe by comparison to Eq. (4.2) that

$$\mathcal{H}_R = A + A^\dagger, \tag{4.66}$$

$$\mathrm{i}I_{bs} = A - A^\dagger. \tag{4.67}$$

Hence, the backscattering current is intimately connected to the Rashba Hamiltonian. We can now facilitate the further transformation of the backscattering current by referring to the reformulation of the Rashba Hamiltonian. The transformations of $\mathcal{H}_R$ that lead to its description in the fields d_ϵ are described in Section 4.3. If we focus on $\alpha(x) = \alpha_R\delta(x)$, we get

$$A = \alpha_R\left(\Psi_R^{\dagger\prime}\Psi_L - \Psi_R^\dagger\Psi_L'\right)(0) = \alpha_R\sqrt{\frac{g}{2\pi a}}\Psi_+'(0) = t\Psi_+'(0) \tag{4.68}$$

by Eq. (4.8) with $t = |\alpha_R|\frac{1}{\sqrt{g\pi a}}$. Due to Eq. (4.26), we furthermore have

$$\begin{aligned}
U\Psi'(0)U^\dagger &= \mathrm{i}\Psi'(0)\alpha_D,\\
U\Psi^{\dagger\prime}(0)U^\dagger &= \mathrm{i}\Psi^{\dagger\prime}(0)\alpha_D,
\end{aligned} \tag{4.69}$$

where the unitary transformation U is given by Eq. (4.24). Therefore, the Fourier space formulation of I_{bs} is

$$I_{bs} = \mathrm{i}\left(A^\dagger - A\right) = -\mathrm{i}t\sum_k \mathrm{i}\left(\mathrm{i}kc_k - (-\mathrm{i}k)\,c_k^\dagger\right)\alpha_D = \mathrm{i}t\sum_k k\left(c_k + c_k^\dagger\right)\alpha_D. \tag{4.70}$$

Employing the results of Section 4.3, Eq. (4.50), the expectation value of the backscattering current becomes

$$\begin{aligned}\langle I_{\mathrm{bs}}\rangle &= \sum_{k,\epsilon,\epsilon'} k\left[D_{\epsilon,(k,1)} + D^*_{\epsilon,(k,2)}\right] D^*_{\epsilon,D}\langle d_\epsilon d_{\epsilon'}\rangle \\ &= \sum_{k,\epsilon} k\left[\overbrace{D^*_{-\epsilon,(k,1)}D^*_{\epsilon,D}}^{D^*_{\epsilon,(k,2)}D^*_{-\epsilon,D}}\underbrace{\langle d_{-\epsilon}d_\epsilon\rangle}_{n_\epsilon} + D^*_{\epsilon,(k,2)}D^*_{\epsilon,D}\underbrace{\langle d_\epsilon d_\epsilon\rangle}_{n_{-\epsilon}}\right] \\ &= \sum_{k,\epsilon} k\left[D^*_{\epsilon,(k,2)}D^*_{\epsilon,D}\left(n_\epsilon + n_{-\epsilon}\right)\right] = \sum_{k,\epsilon} D^*_{\epsilon,(k,2)}D^*_{\epsilon,D} = 0. \end{aligned} \tag{4.71}$$

with the Fermi distribution function $n_\epsilon = \frac{1}{1+e^{\beta\epsilon}}$ that implicitly depends on temperature. Note that

$$\langle d_{-\epsilon}d_\epsilon\rangle = \begin{cases} n_\epsilon & \text{for } \epsilon \geq 0 \\ 1 - n_{-\epsilon} = n_\epsilon & \text{for } \epsilon \leq 0 \end{cases} = n_\epsilon. \tag{4.72}$$

The last equality of Eq. (4.71) holds because of the unitarity of D[10]. In this regard, the backscattering current vanishes for an arbitrary applied voltage and an arbitrary temperature. It also does not depend on whether the limit $\Lambda \to \infty$ is considered or not. This is in particular remarking, as the system at $g = \frac{1}{2}$, which we describe here at its primary refermionizable point, combines the local Rashba scatterer with a considerably strong particle-particle interaction. This interplay should in principle generate two-particle backscattering and hence a measurable backscattering current. The disappearance of the backscattering current is a surprising property caused by the special nature of the refermionizable point.

4.6. Rashba energy

An observable that should, by physical intuition, depend on the strength of the Rashba coupling, is the Rashba Hamiltonian $\mathcal{H}_R$ itself. The exact calculation for $g = \frac{1}{2}$ reveals

$$\mathcal{H}_R = t\sum_{k,\epsilon} k D^*_{\epsilon,(k,2)}D^*_{\epsilon,D}\left(n_{-\epsilon} - n_\epsilon\right), \tag{4.73}$$

which was derived in complete analogy to Eq. (4.71). This quantity does not vanish and is proportional to the Rashba coupling. If the limit $\Lambda \to \infty$ is taken, the quantity becomes independent of temperature.

It is interesting, in this context, to mention that the expectation value of the squared Rashba energy is also independent of the temperature. This explicitly stays true for finite cutoffs. Additionally, we find that the squared Rashba energy is independent of the Rashba coupling and exhibits an ultra-violet divergence.

[10] Note the sum over ϵ

4.7. Same expectation values ⇔ same Hamiltonians

In this section, we rigorously show that two operators that have the same expectation values, effectively are the same, i.e., they only differ by a constant. This especially helps us in demonstrating that the local Rashba scatterer, as it is represented in the model by a nontrivial operator, has some influence on the physics even if the quasi-particles coincide with the free system if limit of an infinite momentum cutoff is taken.

Let H and H' be hermitian operators acting on the same Hilbert space V and let all hermitian operators A on V have the property

$$\langle A\rangle_H = \langle A\rangle_{H'} \;\Leftrightarrow\; \frac{\mathrm{Tr}\left\{e^{-\beta H}A\right\}}{\mathrm{Tr}\left\{e^{-\beta H}\right\}} = \frac{\mathrm{Tr}\left\{e^{-\beta H'}A\right\}}{\mathrm{Tr}\left\{e^{-\beta H'}\right\}} \tag{4.74}$$

for one positive, real number β. Furthermore call $\rho(') = \frac{e^{-\beta H(')}}{\mathrm{Tr}\left\{e^{-\beta H(')}\right\}}$. This leads to

$$\mathrm{Tr}\{(\rho-\rho')A\} = 0. \tag{4.75}$$

Choose $A = \rho - \rho'$ and an arbitrary orthonormal basis of V, which is denoted by $\{|n\rangle | n \in I\}$, where I is an appropriate index set. Then it is

$$\mathrm{Tr}\{AA\} = \sum_{n,m\in I}\langle n|A|m\rangle\langle m|A|n\rangle = \sum_{n,m\in I}|\langle n|A|m\rangle|^2 = 0 \tag{4.76}$$

because A is hermitian and the last equality holds because of Eq. (4.75). Since $|\langle n|A|m\rangle|^2 \geq 0$, we have $|\langle n|A|m\rangle| = 0$ for all $n, m \in I$ and equivalently

$$A = \rho - \rho' = 0 \tag{4.77}$$

$$\frac{1}{Z}e^{-\beta H} = \frac{1}{Z'}e^{-\beta H'} \tag{4.78}$$

$$H - H' = \frac{1}{\beta}\left[\ln\left(\frac{Z'}{Z}\right) + U\right], \tag{4.79}$$

where U is an arbitrary operator fulfilling $e^U = 1$. Note that we took the logarithm in the step from Eq. (4.78) to Eq. (4.79). This is possible because it is independently taken on both sides and the Baker Campbell Hausdorff formula is omitted. We now differentiate both sides of Eq. (4.79) with respect to β and obtain

$$0 = -\frac{1}{\beta}\underbrace{\left(\frac{1}{\beta}\left[\ln(Z') - \ln(Z) + U\right]\right)}_{=H-H' \text{ by Eq. (4.79)}} + \frac{1}{\beta}\left[-\langle H'\rangle + \langle H\rangle\right)] \tag{4.80}$$

$$H - H' = \langle H\rangle - \langle H'\rangle \tag{4.81}$$

because

$$\partial_\beta \ln(Z) = \partial_\beta \ln\left(\mathrm{Tr}\left\{e^{-\beta H}\right\}\right) = -\frac{1}{Z}\,\mathrm{Tr}\left\{e^{-\beta H} H\right\} = -\langle H\rangle. \tag{4.82}$$

The operators H and H' therefore only differ by a constant. The inverse is also true: if the operators only differ by a constant, then Eq. (4.74) is fulfilled as can be seen by direct calculation. Finally, we want to note that if two Hamiltonians H and H' are given which do not only differ by a constant, the operator $\rho - \rho'$ represents an observable that lets their different behavior become apparent.

Applied to the problem of the local Rashba scatterer, we can therefore conclude that

$$A = \frac{e^{\mathcal{H}(\alpha_R=0)}}{Z(\alpha_R=0)} - \frac{e^{\mathcal{H}(\alpha_R=\alpha_f)}}{Z(\alpha_R=\alpha_f)}, \tag{4.83}$$

with a nonvanishing complex number α_f is a hermitian operator, and therefore an observable, that has an expectation value that depends on the strength of the local Rashba scatterer. It has to be mentioned that the quantity A is of rather abstract nature and can, presumably, not be observed in experiments. We still consider this proof of principle useful for theoretical purposes and for finding more meaningful physical properties that distinguish two seemingly equal Hamiltonians. In fact, by examining the exponents appearing in A, we can already speculate that the expectation value of the Rashba Hamiltonian itself - the Rashba energy - should depend on the strength of the Rashba coupling. That this in fact is the case is shown in Section 4.6.

4.8. Conclusions about the local Rashba scatterer

In this chapter, we gain considerable insight into the refermionizable points of the local Rashba scatterer. At the Luttinger parameter of $g = \frac{1}{2}$, the system is diagonalizable without an additional Emery-Kivelson transformation. At this special point, the system behaves at first sight as if the Rashba scatterer is completely transparent. We demonstrate this by diagonalizing the Hamiltonian exactly and show that a large fraction of observables behaves as if the Rashba scatterer was absent. A particular important example of this phenomenon is given by the backscattering current I_B, which vanishes for arbitrary temperature, arbitrary strength of the Rashba scatterer, and an arbitrary momentum cutoff. However, by constructing the observable $\frac{e^{\mathcal{H}(\alpha_R=0)}}{Z(\alpha_R=0)} - \frac{e^{\mathcal{H}(\alpha_R=\alpha_f)}}{Z(\alpha_R=\alpha_f)}$, we prove that there exists a clear signature of the Rashba scatterer also at $g = \frac{1}{2}$. Another example for such an observable is the Rashba energy itself. Finally, we want to remark that the presented diagonalization at the primary refermionizable point enables the computation of almost arbitrary

observables. Hence, the Hamiltonian of a local Rashba scatterer attached to a helical liquid lead at the specific interaction strength of $g = \frac{1}{2}$ can be considered as solved.

The mechanism that allows the Rashba impurity to backscatter the quasi-particles of the attached helical liquid is the joint action of the particle-particle interaction and the local spin-orbit coupling. In the next chapter, we abandon the necessity of particle-particle interactions and instead allow backscattering by storing the excess spin that is generated by a single backscattering process. This storage is conveniently achieved by a local magnetic quantum dot, the local Kondo impurity.

5. The local Kondo impurity

A magnetic quantum dot, i.e., a Kondo dot (Section 2.2.3, that is coupled to helical liquids is one of the simplest nontrivial perturbations which allow elastic backscattering. In such systems, the backscattering is assisted by a spin flip of the Kondo dot. Along these lines, former publications *[Maciejko et al., 2009; Tanaka et al., 2011]* have mainly focused on the effect of a magnetic impurity on the conductance of the helical liquid and not on the screening of the localized spin, cf. Section 2.2.3. However, attaching helical liquids to a Kondo dot also offers unique opportunities to investigate spin-dependent scattering off the Kondo dot: by carrying away spin resolved information about the Kondo dot in distinct directions, correlations become measurable away from the Kondo region, avoiding the usual experimental necessity of locally perturbing the direct vicinity of the Kondo dot. This property is unique to helical liquids because of the unique correlation of motion and spin of their elementary excitations. The following two sections elaborate on the possibility to employ this particular feature to resolve the Kondo cloud in a setup where a Kondo dot with spin $\frac{1}{2}$ is coupled to two helical liquids at the edges of a quantum spin Hall insulator. Section 5.1 considers the Toulouse points, cf. Section 3.1, at which the Hamiltonian is mapped to a quadratic one. The Toulouse points separate into two qualitatively different sets as derived in Section 3.1.3. The first set is related to the known Toulouse points of the non-interacting case. The second set appears exclusively in the case of interactions. We employ the Toulouse points to determine the local screening and the Kondo screening cloud analytically and calculate the signature of applied voltages. Section 5.2 concludes the topic by proving a generic connection between the Kondo cloud and the space- and time-resolved current cross correlations in the setup at hand for a regime of parameters that even exceeds the Toulouse points. For the case of two helical liquid leads with Luttinger parameters $g_\mathrm{t} = g_\mathrm{b} = 1/2$, the relation is a direct proportionality up to first order in the z spin coupling if the measurement is taking place sufficiently far away from the magnetic moment. This requirement is a merit rather than a restriction, because a distant manipulation of the system is incapable of directly affecting the magnetic moment. Furthermore, we discuss disturbances away from the preferred point $g_\mathrm{t} = g_\mathrm{b} = \frac{1}{2}$ and show how to restore the proportionality.

As a consequence of the presented results, probing the current cross correlations describes a tool to directly detect the Kondo cloud and even resolve it spatially. The associated measurements are conceptually more promising than a direct measurement of the correlation between the magnetic moment and the spin density in the

leads because the magnetic moment is in no manner directly perturbed.

5.1. Exact results for the Kondo cloud of two helical liquids

This section is a revised version of *Posske et al. [2013]* and its supplemental material, copyrighted by the American Physical Society. Also regard the remarks on page 3.

In this section, we analyze the screening of a magnetic quantum dot (QD) with spin $\frac{\hbar}{2}$ coupled to two helical liquids in a two channel Kondo model *[Nozieres & Blandin, 1980; Potok et al., 2007]*. Interestingly, we find two qualitatively distinct sets A and B of Toulouse points by the explained extension of the method of Emery and Kivelson, cf. Section 3.1, in particular Section 3.1.2, and Section 3.1.3. Set A contains the Toulouse point of the two channel Kondo model for noninteracting leads *[Emery & Kivelson, 1992]*, while set B resembles a one channel Toulouse point at both Luttinger parameters $g = \frac{1}{2}$ *[Tanaka et al., 2011]*. We subsequently solve the model exactly for all Toulouse points. This enables us to provide exact results for the temperature and voltage dependent Kondo screening cloud. Determining the local screening and the spatially extended Kondo screening cloud, we are able to demonstrate a different phenomenology for the novel interacting set of Toulouse points. For case A, the magnetic field of the QD is always "perfectly screened" *[Zaránd & von Delft, 2000]* locally. However, the interacting case B provides, for example, no screening and overscreening. The Kondo cloud obeys an asymptotic decay for large x that is quadratic at zero temperature[1]. At finite temperature $T = 1/(k_B\beta)$, the decay becomes exponential after a length scale $\xi_T \approx \hbar v\beta$, which was also predicted by *[Borda, 2007]* for the one channel Kondo model. In contrast to the noninteracting one channel case, we find a $\ln^2(x)$ instead of an x^{-1} divergence for small x. Furthermore, we observe that an applied spin flavor voltage $\mu_x = \tilde{\mu}_\mathrm{t} + \tilde{\mu}_\mathrm{b}$, whereby "flavor" denotes top(t) or bottom(b) (see Fig. 5.1), and a spin voltage $\mu_s = \tilde{\mu}_\mathrm{t} - \tilde{\mu}_\mathrm{b}$ have distinct effects on the Kondo cloud. While the former acts as an artificial magnetic field which decreases the extent of the Kondo cloud significantly, the latter induces spatial oscillations of the Kondo cloud. Such a spin voltage can be conveniently applied by a charge bias in a four-terminal helical liquid setup, which hence generates the possibility of manipulating the Kondo cloud easily. A schematic setup is drawn in Fig. 5.1 where the magnetic QD is realized by a properly gated anti-dot.

[1] Here, x denotes the distance to the QD as depicted in Fig. 5.1.

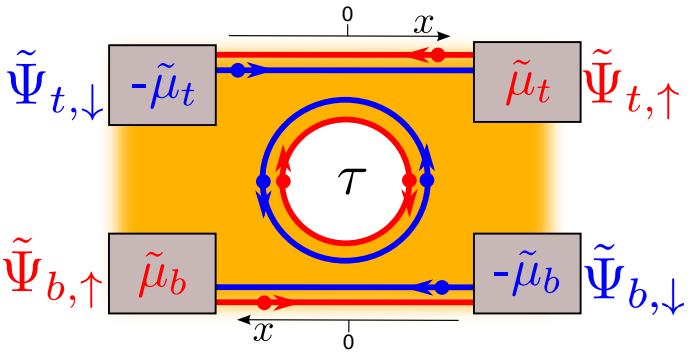

Figure 5.1.: Two helical liquids of a quantum spin Hall insulator are coupled via an anti-dot. Properly gated, the dot resembles a magnetic impurity with $S = \frac{1}{2}$. Each side is brought out of equilibrium by an applied voltage. Figure reprinted with permission from *Posske et al. [2013]*. Copyright (2013) by the American Physical Society.

5.1.1. Model

The setup is modeled by a two channel Kondo Hamiltonian, as discussed in *Law et al. [2010]; Posske et al. [2013]; Schiller & Hershfield [1998]*, with

$$\begin{aligned}\tilde{\mathcal{H}}_a &= \sum_{\sigma\in\{\uparrow,\downarrow\}} \int dx \left(v_{F,a}\tilde{\Psi}^\dagger_{a,\sigma}(x)(\sigma \mathrm{i}\partial_x)\tilde{\Psi}_{a,\sigma}(x) + \frac{g_{4,a}}{2}\tilde{\rho}^2_{a,\sigma}(x) + g_{2,a}\tilde{\rho}_{a,\downarrow}(x)\tilde{\rho}_{a,\uparrow}(x)\right), \\ \tilde{\mathcal{H}}^K_a &= \sum_{\lambda\in\{x,y,z\}} J^\lambda \tilde{S}^\lambda_a(0)\tau^\lambda. \end{aligned} \tag{5.1}$$

for each lead $a \in \{\mathrm{t}, \mathrm{b}\}$. Here, $\tilde{\mathcal{H}}_a$ describes the helical liquid of lead a with the fermionic fields $\tilde{\Psi}_{a,\sigma}$ of spin σ. Note that the direction of space in the top lead is inverse to the one of the bottom lead as depicted in Fig. 5.1. The real constants are the Fermi velocity $v_{F,a}$ and $g_{2/4,a}$, the interaction strengths in the leads. It is convenient to introduce the Luttinger parameters $g_a = \sqrt{v_{J,a}/v_{N,a}}$ and $v_a = \sqrt{v_{J,a}v_{N,a}}$ instead, where $v_{N/J,a} = v_{F,a} + \frac{g_{4,a}\pm g_{2,a}}{2\pi\hbar}$ *[Schönhammer, 1997]*. The interaction of lead a with the magnetic moment τ is given by $\mathcal{H}^K_a$. Further, $\tilde{S}^\lambda_a = \frac{\hbar}{2}\sum_{\sigma,\sigma'}\tilde{\Psi}^\dagger_{a,\sigma}\sigma^\lambda_{\sigma,\sigma'}\tilde{\Psi}_{a,\sigma'}$ denotes the spatially resolved spin density in lead a with σ^λ being the λ-th Pauli matrix. By considering isotropic interactions in the x and y directions, i.e., $J^x_a = J^y_a =: J^\perp_a$, which is equivalent to conserve the total z spin, the Kondo coupling of lead a is written as the sum of

$$\begin{aligned}\mathcal{H}^\perp_{K,a} &= J^\perp_a \tilde{\Psi}^\dagger_{a,\uparrow}(0)\tilde{\Psi}_{a,\downarrow}(0)\tau^- + H.c., \\ \mathcal{H}^z_{K,a} &= \frac{1}{2}J^z_a\left(\tilde{\rho}_{a,\uparrow}(0) - \tilde{\rho}_{a,\downarrow}(0)\right)\tau^z, \end{aligned} \tag{5.2}$$

with $\tau^\pm = \frac{1}{2}\left(\tau^x \pm \mathrm{i}\tau^y\right)$ and $S^\pm = \frac{1}{2}\left(S^x \pm \mathrm{i}S^y\right)$. Following Section 3.1.1 and *von Delft & Schoeller [1998]*, the helical liquids are bosonized and diagonalized by introducing

the fields $\varphi_{a,\pm}(x)$, cf. Eq. (3.46). This leads to

$$\begin{aligned}\mathcal{H}_a &= \int dx\ \frac{v_a}{2}\sum_\sigma \left(\partial_x\varphi_{a,\sigma}(x)\right)^2,\\ \mathcal{H}^\perp_{K,a} &= \frac{1}{4\pi a_c}J^\perp_a F^\dagger_{a\uparrow}F_{a\downarrow}e^{\left(\mathrm{i}\sqrt{2g_a}\varphi_{a,+}(0)\right)}\tau^- + H.c.,\\ \mathcal{H}^z_{K,a} &= \frac{J^z_a}{4\pi}\sqrt{\frac{2}{g_a}}\partial_x\varphi_{a,+}(0)\tau^z.\end{aligned} \tag{5.3}$$

We furthermore include the chemical potentials $\tilde{\mu}_a$ similarly to *Schiller & Hershfield [1998]; Tanaka et al. [2011]* by the nonequilibrium operator[2]

$$\mathcal{Y} = \sum_{a\in\{\mathrm{t,b}\}}\tilde{\mu}_a\left(\tilde{\mathcal{N}}_{a,\uparrow}-\tilde{\mathcal{N}}_{a,\downarrow}\right), \tag{5.4}$$

where $\tilde{\mathcal{N}}_{a,\sigma}$ is the total number operator of the fermion $\tilde{\Psi}_{a,\sigma}$. In principle, independent chemical potentials at each terminal depicted in Fig. 5.1 could be considered. However, as the Kondo interaction is a spin interaction, two of the four potential configurations, namely the ones that are only able to alter charge properties, decouple from the quantum dot. Therefore, we do not consider them explicitly.

5.1.2. Method

We obtain all Toulouse points by restricting J^z_a to the value such that $\mathcal{H}^z_{K,a}$ cancels the Emery-Kivelson rotation, $U = \exp(\mathrm{i}\sum_a \lambda_{a,+}\varphi_{a,+}(0)\tau^z)$, of $\mathcal{H}_a$ and applying an orthogonal transformation to the bosonic fields. We find two different classes of Toulouse points, A and B, which we derive detailedly in Section 3.1.3. To connect to the historical notation *[Emery & Kivelson, 1992]*, we rename the fields that are introduced in Section 3.1.3 to $\nu_1 =: \varphi_4$ and $\nu_2 =: \varphi_2$. Within the set of Toulouse points A, the vertex operator of $\mathcal{H}^\perp_{K,t}$ and the one of $\mathcal{H}^\perp_{K,t}$ in Eq. (5.3) take the form $e^{\pm\mathrm{i}\phi_4(0)}$. Therefore, we obtain $\lambda_{a,+} = \sqrt{g_a/2}$. For case B, the form of the vertex operator in $\mathcal{H}^\perp_{K,b}$ instead assumes $e^{\pm\mathrm{i}\phi_2(0)}$, where ϕ_2 and ϕ_4 are linearly independent bosonic fields. We then find

$$\lambda_{t,+} = \frac{1}{\sqrt{2}}(\sqrt{g_t}+s\sqrt{g_b}), \tag{5.5}$$

$$\lambda_{b,+} = s\lambda_{t,+} = \frac{1}{\sqrt{2}}(\sqrt{g_b}+s\sqrt{g_t}). \tag{5.6}$$

Here, $s\in\{-1,1\}$ is introduced to describe the two branches the Toulouse points of case B are falling apart into. A representation of the resulting coupling constants for all Toulouse points is given in Tab. 5.1. Case A is characterized by $g_\mathrm{t}+g_\mathrm{b}=2$

[2] This operator is explicitly employed in Eq. (5.7).

	A	B
$v_\mathrm{t}, v_\mathrm{b}$	v	
g_t	$2\sin^2(q)$	$\sin^2(q)$
g_b	$2\cos^2(q)$	$\cos^2(q)$
$g_\mathrm{t}+g_\mathrm{b}$	2	1
J^z_t	$2\pi v g_\mathrm{t}$	$\pi v(1-\cos(2q)+s\sin 2q)$
J^z_b	$2\pi v g_\mathrm{b}$	$\pi v(1+\cos(2q)+s\sin 2q)$

Table 5.1.: Toulouse points of the two channel Kondo model for helical liquids. There are two disconnected sets A and B of Toulouse points whereby B possesses two branches, distinguished by $s=\{-1,1\}$. The parametrization uses $v\in(0,\infty)$ and $q\in(0,\pi/2)$.

and contains the noninteracting case. In contrast, the novel case B obeys $g_\mathrm{t}+g_\mathrm{b}=1$ and intrinsically relies on interactions. In particular, it contains $g_\mathrm{t}=g_\mathrm{b}=\frac{1}{2}$, for which refermionization is known to be a promising method in similar models *[Tanaka et al., 2011; von Delft & Schoeller, 1998]*, and possesses two solvable values of $J^z_{\mathrm{t/b}}$ for each solvable configuration of $g_{\mathrm{t/b}}$.

The grand canonical operators of the resulting resonant level models after refermionization to the fermionic fields $\Psi_j(x)=\frac{1}{\sqrt{2\pi a_c}}G_j e^{-\mathrm{i}\phi_j(x)}$ are *[Emery & Kivelson, 1992]*

$$\mathcal{H}_A=-\mu_x\mathcal{N}_2-\mu_s\mathcal{N}_4+\mathcal{H}_0+\frac{1}{2\sqrt{2\pi a_c}}\left(J^\perp_\mathrm{t}\Psi^\dagger_4(0)c+J^\perp_\mathrm{b}\Psi_4(0)c+H.c.\right), \tag{5.7}$$

with the local pseudofermion $c=G_2^\dagger\tau^-$, for case A, where we exploited the extended treatment of Klein factors and number operators in *Zaránd & von Delft [2000]*, and

$$\begin{aligned}\mathcal{H}_B=&-(\mu_x-\mu_s)\mathcal{N}_2-(\mu_x+\mu_s)\mathcal{N}_4+\mathcal{H}_0\\&+\frac{1}{2\sqrt{2\pi a_c}}\left(J^\perp_\mathrm{t}\Psi^\dagger_4(0)c+J^\perp_\mathrm{b}\Psi^\dagger_2(0)c+H.c.\right)\end{aligned} \tag{5.8}$$

for case B with $c=\tau^-$, $\mathcal{N}_{2/4}=\frac{1}{2}(\tilde{\mathcal{N}}_{t/b,\uparrow}-\tilde{\mathcal{N}}_{t/b,\downarrow})$ and $G_{2/4}=F^\dagger_{t/b,\downarrow}F_{t/b,\uparrow}$ similarly to *von Delft & Schoeller [1998]*. In both cases, the noninteracting Hamiltonian is given by

$$\mathcal{H}_0=v\sum_j\int dx\ \Psi_j(x)(\mathrm{i}\partial_x)\Psi_j(x). \tag{5.9}$$

Note that, opposed to the Hamiltonian of case A, there are no terms within the Hamiltonian for case B that combine two fermionic annihilation operators. The Hamiltonians of Eqs. (5.7) and (5.8) are solvable via a variety of techniques, see,

e.g., *Schiller & Hershfield [1998]* and *Zaránd & von Delft [2000]*. The following results are based on infinite order perturbation theory in the Keldysh formalism as explained in *Posske [2012]*.

5.1.3. Results

We first focus on the z-screening of the spin τ of the QD. The contributions to this quantity are the local screening at $x = 0$, determined by the locally bound spin in the leads, and the spatially extended Kondo cloud. The local screening $S_0^z = \sum_a \int_{-\epsilon}^{\epsilon} dx\ \langle \tilde{S}_a^z(x) \rangle$, with $\tilde{S}_a^z(x) = \frac{1}{2}(\tilde{\rho}_{a,\uparrow} - \tilde{\rho}_{a,\downarrow})$ and $\epsilon = 0^+$, is given by

$$S_0^z = -\langle \tau^z \rangle \sum_a \frac{J_a^z}{4\pi v g_a}. \tag{5.10}$$

Following Tab. 5.1, this reveals $S_0^z = -\langle \tau^z \rangle$ for case A and the magnetic field of the QD is locally screened. For case B however, this results in $S_0^z = -\langle \tau^z \rangle \left(1 + \frac{s}{2\sqrt{g_\mathrm{t} g_\mathrm{b}}}\right)$, whereat $s = \pm$ corresponds to the two possible branches of Toulouse points in case B. Hence, for an arbitrary large interaction in one of the helical liquids, the locally accumulated spin gets arbitrarily large as well. This interaction induced phenomenon clearly distinguishes Fermi liquid leads from helical liquid leads.

The Kondo screening cloud $\chi_a^z(x)$ is represented by, cf. Section 2.2.3,

$$\chi_a^z(x, g_\mathrm{t}, g_\mathrm{b}) = \langle \delta \tilde{S}_a^z(x) \delta \tau^z \rangle, \tag{5.11}$$

with $\delta C = C - \langle C \rangle$. We find that for case A, the Kondo cloud does not depend on the interaction parameters $g_{\mathrm{t/b}}$. For convenience, we therefore denote the Kondo cloud of case A by $\chi_a^z(x, 1)$ later. Furthermore, the sum of the Kondo clouds on both sides vanishes, i.e.,

$$\sum_a \chi_a^z(x, g_\mathrm{t}, g_\mathrm{b}) = 0. \tag{5.12}$$

Interestingly, Eq. (5.12) also implies that the Kondo correlations of different sides have different signs. Thereby, the side of positive correlations is determined by the weaker in-plane coupling $|J_\mathrm{a}^\perp|$. If the in-plane coupling of both sides is equal, however, the development of a Kondo cloud is forbidden by this symmetry. Physically, this phenomenon can be interpreted as a competition between the two leads for the possibility to screen the impurity. This would be desirable for both leads – if we remind ourselves of the one channel Kondo model – but only the stronger coupled lead wins and participates in the desired singlet. The weaker coupled lead is forced into a triplet configuration.

For case B, the Kondo cloud at a specific choice of g_L, g_R, and s is derivable from a generic Kondo cloud, which is the one for the Toulouse point with $g_\mathrm{t} = g_\mathrm{b} = \frac{1}{2}$

and $s = -1$. We denote it by $\chi^z_a(x, \frac{1}{2})$. For arbitrary interaction parameters, the other Kondo clouds are then given by[3]

$$\chi^z_a(x, g_\mathrm{t}, g_\mathrm{b}) = \frac{1}{2} \sum_{a'} \left(aa' - s\sqrt{\frac{g_{-a}}{g_a}} \right) \chi^z_{a'}(x, \tfrac{1}{2}), \tag{5.13}$$

with $a, a' \in \{\mathrm{t} \equiv +, \mathrm{b} \equiv -\}$. A direct consequence of Eq. (5.13) is a simple dependence of the total Kondo cloud on the interaction parameters

$$\sum_a \chi^z_a(x, g_\mathrm{t}, g_\mathrm{b}) = \frac{-s}{2\sqrt{g_\mathrm{t} g_\mathrm{b}}} \sum_a \chi^z_a(x, \tfrac{1}{2}). \tag{5.14}$$

In equilibrium, i.e., for vanishing voltages, the analytical expressions for the Kondo clouds read

$$\chi^z_\mathrm{t}(x, 1) = \mathrm{sgn}\,(J^\perp_\mathrm{b} - J^\perp_\mathrm{t}) \frac{k_B \sqrt{T^K_1 T^K_2}}{4\pi^2 v} e^{-\frac{2\pi|x|}{\hbar v \beta}} \tilde{\Phi}\left(|x|, \beta, T^K_1\right) \tilde{\Phi}\left(|x|, \beta, T^K_2\right), \tag{5.15}$$

$$\chi^z_\mathrm{t}(x, \tfrac{1}{2}) = \frac{k_B T^K_\mathrm{t}}{2\pi^2 v} e^{-\frac{2\pi|x|}{\hbar v \beta}} \tilde{\Phi}^2\left(|x|, \beta, T^K_1 + T^K_2\right), \tag{5.16}$$

where $\tilde{\Phi}(|x|, \beta, T^K) = \Phi(e^{-\frac{2\pi|x|}{\hbar v\beta}}, 1, \frac{1}{2} + \frac{1}{2\pi}\beta k_B T^K)$ with the Hurwitz-Lerch transcendent $\Phi(z, s, \alpha) = \sum_{n=0}^\infty \frac{z^n}{(n+\alpha)^s}$, and the Kondo temperatures $T^K_{1/2} = \frac{(J^\perp_\mathrm{t} \mp J^\perp_\mathrm{b})^2 \hbar}{16\pi a_c k_B v}$ *[Schiller & Hershfield, 1998]* and $T^K_\mathrm{t} = \frac{(J^\perp_\mathrm{t})^2 \hbar}{16\pi a_c k_B v}$. The equilibrium Kondo cloud is shown in Fig. 5.2. Concerning case A, given in Fig. 5.2a, we choose $T^K_A = \sqrt{T^K_1 T^K_2}$ to be the temperature of reference. Both Kondo length scales $\xi^K_{1/2} = \hbar v/(k_B T^K_{1/2})$ appear in the shape of the Kondo cloud by inducing a crossover to different asymptotic behaviors. The leading divergence for small x is $\ln^2(x)$ and the asymptotic behavior for large x is a quadratic decay. For finite temperature, the Kondo cloud decays exponentially in x after a length scale $\xi_T \approx \hbar v \beta$. Here, the behavior for small x at $g_L = g_R = 1$ has to be contrasted with the case of a single lead as described by *Borda [2007]*. In that reference, the author argues for a x^{-1} divergence at small x, while the large x behavior and the temperature dependence coincides with our findings for two leads.

For case B (Fig. 5.2b), the temperature of reference is conveniently chosen to be $T^K_B = T^K_1 + T^K_2$. Rescaled by T^K_t, the generic Kondo cloud of side t is a universal curve for all coupling parameters. In contrast to case A, the only relevant length scale is determined by $\xi^K_B = \hbar v/(k_B T^K_B)$.

Applied voltages $\mu_x = \tilde{\mu}_\mathrm{t} + \tilde{\mu}_\mathrm{b}$ and $\mu_s = \tilde{\mu}_\mathrm{t} - \tilde{\mu}_\mathrm{b}$, cf. Fig. 5.1, alter the Kondo cloud distinctly. The spin flavor voltage μ_x acts as a magnetic field, see also *Tanaka et al. [2011]*, and strongly shrinks the Kondo cloud in both classes of Toulouse points.

[3] Please note that the version of this formula published in *Posske et al. [2013]* contains a sign error, which can be seen from the limit $g_t = g_b$ and $s = -1$.

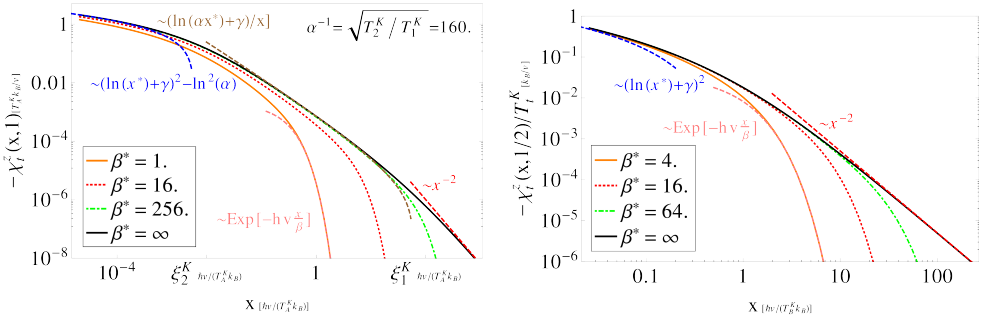

(a) **(b)**

Figure 5.2.: The decay of the generic Kondo clouds in equilibrium for different inverse temperatures $\beta^* = k_B T^K_{A/B}\beta$ on a double-logarithmic scale. The relevant limits of the clouds are depicted as dashed curves, γ is the Euler-Mascheroni constant. **(a)** Noninteracting Kondo cloud. The temperature of reference is T^K_A. Both Kondo temperatures $T^K_{1/2}$ determine crossover length scales of the cloud at $\xi^K_{1/2} = \hbar v/(k_B T^K_{1/2})$. **(b)** Interacting Kondo cloud rescaled by T^K_{t}. The temperature of reference is T^K_B. The curve is universal for all $J^\perp_{\mathrm{a}}$ and only the length scale determined by T^K_B is relevant. Figure reprinted with permission from *Posske et al. [2013]*. Copyright (2013) by the American Physical Society.

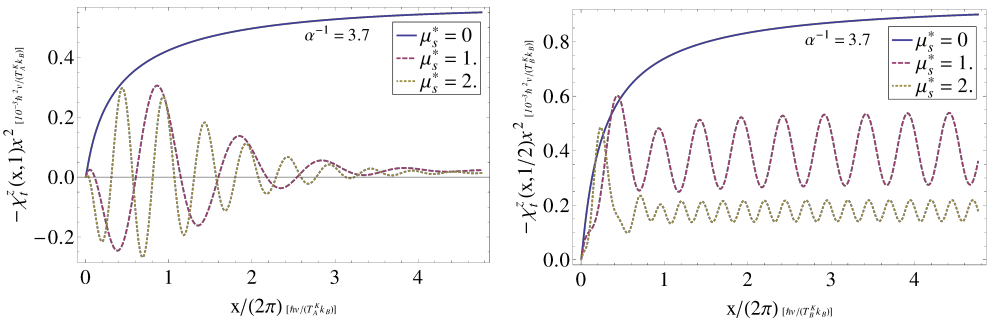

(a) **(b)**

Figure 5.3.: The generic Kondo clouds rescaled by x^2 at zero temperature in nonequilibrium. **(a)** Noninteracting Kondo cloud. An applied spin voltage $\mu_s = k_B T^K_{A/B}\mu^*_s$ induces exponentially decaying oscillations of the frequency $\mu_s/(\hbar v)$ in the Kondo cloud and locally changes its sign. **(b)** Interacting Kondo cloud. Additional permanent oscillations of the frequency $2\mu_s/(\hbar v)$ appear. Figure reprinted with permission from *Posske et al. [2013]*. Copyright (2013) by the American Physical Society.

This reflects the sensitivity of Kondo physics to unhindered spin flips of the QD. An increasing μ_s instead induces oscillations in the Kondo cloud depicted in Fig. 5.3. For case A, an oscillation of the frequency $\mu_s/(\hbar v)$ changes the sign of the Kondo cloud locally. This oscillation decays exponentially and the Kondo cloud becomes monotonic again for large x. For case B, the universality of the Kondo cloud at a specific T_B^K is destroyed in nonequilibrium. In addition to the oscillations of case A, case B shows oscillations of the frequency $2\mu_s/(\hbar v)$, which decay quadratically in x. Nevertheless, the Kondo cloud never changes signs for all x. The oscillations can be interpreted as the impact of Friedel oscillations on the Kondo cloud. While Friedel oscillations in helical liquids are suppressed in the presence of ordinary scatterers, the spin-flip scattering off the magnetic QD to the oppositely moving channel generates an interference of the wave functions in both channels.

5.1.4. Renormalization group analysis of the crossing terms

To complete the analysis of the model in Section 5.1.1, we calculate in this section the scaling dimensions of the so-called crossing terms which have been excluded up to now. To this end, we repeat the calculations of *Law et al. [2010]* in the weak limit of the xy-coupling as well as for finite z-coupling and extend them to arbitrary interaction strengths on both sides of the quantum spin Hall system. We find that the crossing terms become irrelevant for the majority of Toulouse points, which underlines the experimental relevance of our model.

Additionally to the considered two channel Kondo Hamiltonian of Eq. (5.2), the crossing terms

$$\mathcal{H}_{\text{cross}} = \sum_{\lambda\in\{x,y,z\}} J^z \tilde{\Psi}^\dagger_{\text{t},\sigma}(0)\sigma^\lambda_{\sigma,\sigma'}\tilde{\Psi}_{\text{b},\sigma'}(0) + H.c. \tag{5.17}$$

appear in models which assume a one channel contribution. This is, for instance, the case for the effective model of an Anderson impurity in the Kondo limit *[Hewson, 1997; Law et al., 2010; Schrieffer & Wolff, 1966]*. Because Anderson models are in many cases the physically correct models to describe Kondo behavior *[Nozieres & Blandin, 1980]*, it is an experimentally important question if the crossing terms can be neglected or not. Normally, they can not, which is one of the reasons why two channel Kondo physics is not easily observed. The situation changes when interactions become important. This can be understood on the basis of the following intuitive picture. Imagine a system of two leads attached to an Anderson impurity that is occupied by one particle almost all of the time. If the particle from the impurity tunnels into lead 1, the Coulomb interaction facilitates a subsequent tunneling from lead 1 back to the impurity. Additionally, when a particle from lead 1 tunnels to the impurity, the lower electron density facilitates the subsequent tunneling of a particle back to lead 1. Thereby, the exchange of particles between lead 1 and lead 2 becomes suppressed, which is equivalent to the crossing terms losing their relevance.

This concept is proven for many setups. The most important reference for our purposes is *Law et al. [2010]*, which discusses the scaling dimensions of the crossing terms for our setup but does not consider different interaction strengths for the two helical liquids. To discuss our case, which crucially relies on the interaction strengths being different, we henceforth extend the calculations of *Law et al. [2010]* to allow for different interaction strengths. On this basis, we determine the ranges of interaction strengths for which the crossing terms are irrelevant.

Assuming $J^x_{\text{cross}} = J^y_{\text{cross}} \equiv J^\perp_{\text{cross}}$, i.e., conservation of the z component of the total spin, as it has been assumed for the other tunneling events, the Hamiltonian of the system reads

$$\mathcal{H} = \sum_{a\in \text{t,b}} \left(\mathcal{H}_{0,a} + \mathcal{H}^\perp_{K,a} + \mathcal{H}^z_{K,a}\right) + \mathcal{H}^\perp_{\text{cross}} + \mathcal{H}^z_{\text{cross}}, \tag{5.18}$$

$$\mathcal{H}_{0,a} = \sum_\sigma \int dx \frac{v}{2} (\partial_x \varphi_{a,\sigma}(x))^2, \tag{5.19}$$

$$\mathcal{H}^\perp_{K,a} = \frac{J^\perp_a}{4\pi a_c} F^\dagger_{a,\uparrow} F_{a,\downarrow} e^{\left(\mathrm{i}\sqrt{2g_a}\varphi_{a,+}(0)\right)} \tau^- + H.c., \tag{5.20}$$

$$\mathcal{H}^z_{K,a} = \frac{J^z_a}{4\pi} \sqrt{\frac{2}{g_a}} \varphi_{a,+}(0) \tau^z, \tag{5.21}$$

$$\begin{aligned}\mathcal{H}^\perp_{\text{cross}} = \frac{J^\perp_2}{4\pi a_c} \Bigg(& F^\dagger_{\text{t},\uparrow} F_{\text{b},\downarrow} e^{\frac{\mathrm{i}}{\sqrt{2}}\left(\sqrt{g_\text{b}}\varphi_{b,+}(0) + \sqrt{g_\text{t}}\varphi_{t,+}(0) + \frac{1}{\sqrt{g_t}}\varphi_{\text{t},-}(0) - \frac{1}{\sqrt{g_\text{b}}}\varphi_{\text{b},-}(0)\right)} \\ & + F^\dagger_{\text{b},\uparrow} F_{\text{t},\downarrow} e^{\frac{\mathrm{i}}{\sqrt{2}}\left(\sqrt{g_\text{b}}\varphi_{b,+}(0) + \sqrt{g_\text{t}}\varphi_{t,+}(0) - \frac{1}{\sqrt{g_t}}\varphi_{\text{t},-}(0) + \frac{1}{\sqrt{g_\text{b}}}\varphi_{\text{b},-}(0)\right)} \Bigg) \tau^- + H.c.,\end{aligned} \tag{5.22}$$

$$\begin{aligned}\mathcal{H}^z_{\text{cross}} = \frac{J^z_2}{4\pi a_c} \Bigg(& F^\dagger_{\text{b},\uparrow} F_{\text{t},\uparrow} e^{\frac{\mathrm{i}}{\sqrt{2}}\left(-\sqrt{g_\text{t}}\varphi_{\text{t},+}(0) - \frac{1}{\sqrt{g_\text{t}}}\varphi_{\text{t},-}(0) + \sqrt{g_\text{b}}\varphi_{\text{b},+}(0) + \frac{1}{\sqrt{g_\text{b}}}\varphi_{\text{b},-}(0)\right)} \\ & + F^\dagger_{\text{b},\downarrow} F_{\text{t},\downarrow} e^{\frac{\mathrm{i}}{\sqrt{2}}\left(\sqrt{g_\text{t}}\varphi_{\text{t},+}(0) - \frac{1}{\sqrt{g_\text{t}}}\varphi_{\text{t},-}(0) - \sqrt{g_\text{b}}\varphi_{\text{b},+}(0) + \frac{1}{\sqrt{g_\text{b}}}\varphi_{\text{b},-}(0)\right)} \Bigg) + H.c.\,.\end{aligned} \tag{5.23}$$

To determine whether the crossing terms in $\mathcal{H}^\perp_{\text{cross}}$ and $\mathcal{H}^z_{\text{cross}}$ are important, we calculate their scaling dimension for a given parameter configuration. We could use the bare Hamiltonians $\mathcal{H}_{0,a}$ of each side a as fixed point Hamiltonians and calculate the scaling dimensions for all coupling parameters (other than $g_{\text{t/b}}$) being small. With a bare Hamiltonian of $\sum_a \mathcal{H}_{0,a}$ we could, namely, exploit a useful shortcut to calculate the scaling dimension of vertex operators: *With a bare Hamiltonian* $\mathcal{H}_0 = \frac{v}{2}\sum_a \int dx (\partial_x \varphi_a(x))^2$*, the scaling dimension* s *of a vertex operator* $V = e^{\sum_a \alpha_a \varphi_a(0)}$ *is* $s = \frac{1}{2}\sum_a \alpha_a^2$ *in the weak coupling limit.* With this, we could read off the scaling dimensions for the weak coupling fixed point directly.

However, taking $\sum_a \mathcal{H}_{a,0}$ as fixed point Hamiltonian has the drawback of yielding poor results for the scaling dimensions at some of the J's being finite. A more accurate approach is to allow for as many finite coupling constants as possible. As

Op.\FPs	FP general	FP weak
$J_a^\perp$	$g_a - \frac{J_a^z}{2\pi v_a} + \frac{1}{16\pi^2}\sum_{a'} \frac{(J_{a'}^z)^2}{g_{a'}\pi^2 v_{a'}^2}$	$\frac{1}{2}(g_\mathrm{t} + g_\mathrm{b})$
J_2^z	$\frac{1}{4}(g_\mathrm{t} + \frac{1}{g_\mathrm{t}} + g_\mathrm{b} + \frac{1}{g_\mathrm{b}}) > 1$	$\frac{1}{4}(g_\mathrm{t} + \frac{1}{g_\mathrm{t}} + g_\mathrm{b} + \frac{1}{g_\mathrm{b}}) > 1$
$J_2^\perp$	$\frac{1}{4}\sum_{a'}(g_{a'} + \frac{1}{g_{a'}} - \frac{J_{a'}^z}{\pi v_{a'}} + \frac{(J_{a'}^z)^2}{4g_{a'}\pi^2 v_{a'}^2})$	$\frac{1}{4}(g_\mathrm{t} + \frac{1}{g_\mathrm{t}} + g_\mathrm{b} + \frac{1}{g_\mathrm{b}}) > 1$

Op.\FPs	FP A	FP B
$J_a^\perp$	$\frac{1}{4}(g_\mathrm{t} + g_\mathrm{b}) = \frac{1}{2}$	$\frac{1}{2}(g_\mathrm{t} + g_\mathrm{t}) = \frac{1}{2}$
J_2^z	$\frac{1}{4}(g_\mathrm{t} + \frac{1}{g_\mathrm{t}} + g_\mathrm{b} + \frac{1}{g_\mathrm{b}}) > 1$	$\frac{1}{4}(g_\mathrm{t} + \frac{1}{g_\mathrm{t}} + g_\mathrm{b} + \frac{1}{g_\mathrm{b}}) > 1$
$J_2^\perp$	$\frac{1}{4}(\frac{1}{g_\mathrm{t}} + \frac{1}{g_\mathrm{b}}) > \frac{1}{2}$	$\frac{1}{4}(g_\mathrm{t} + \frac{1}{g_\mathrm{t}} + g_\mathrm{b} + \frac{1}{g_\mathrm{b}}) > 1$

Table 5.2.: Table of scaling dimensions for the setup in Fig. 5.1 following *Law et al. [2010]* and extending their method to different interaction strengths within the leads. FPs stands for "fixed points". "FP general" is the fixed point for arbitrary interaction strength on both sides, finite J^z's and small $J^\perp$'s. "FP weak" is the fixed point of all J's being small. "FP A" and "FP B" are the special Toulouse points for which the scaling dimensions are calculated by plugging the particular parameters of Tab. 5.1 into the formulas for the general case.

indicated by *Emery & Kivelson [1992]*, the model at hand allows an exact solution for all J_a^z being finite and all other J's vanishing. To this end, the unitary Emery-Kivelson rotation

$$\mathcal{H} \to U\mathcal{H}U^\dagger = \mathcal{H}', \tag{5.24}$$

$$U = e^{\mathrm{i}\sum_a \lambda_a \varphi_{a,+}(0)\tau^z},\ \lambda_a = \frac{J_a^z}{\sqrt{8g_a}\pi v_a} \tag{5.25}$$

is performed. This absorbs $\mathcal{H}_a^z$ into $\mathcal{H}_{0,a}$ and transforms

$$(\tau^-)' = U\tau^- U^\dagger = \tau^- e^{-\mathrm{i}\sum_a \lambda_a \varphi_{a,+}(0)}. \tag{5.26}$$

All other parts of the Hamiltonian remain unchanged as they commute with U or only give a constant as an additional contribution. Effectively, the transformation changes the exponents of the vertex operators in $\mathcal{H}_a^\perp$ and $\mathcal{H}_\mathrm{cross}^\perp$ and thereby its first order scaling dimensions. This allows a direct determination of the scaling dimensions with the fixed point Hamiltonian $\sum_a \mathcal{H}_{a,0} + \mathcal{H}_{K,a}^z$. An overview is given in Tab. 5.2 where the scaling dimensions of the crossing terms in the general case and at the special Toulouse points are listed. The values for the Toulouse points are obtained by accounting for the special values of J_a^z as described in Tab. 5.1. As can be seen, the crossing terms normalize to zero for the weakly coupled impurity and for the Toulouse points of case B. For the Toulouse points of case A, the situation

is more complex. While the z-crossing term is irrelevant for the whole parameter range, the $\perp$-crossing term becomes relevant if $1 - \sqrt{1/2} \leq g_\mathrm{t} \leq 1 + \sqrt{1/2}$. For this regime, we derive from Tab. 5.2 that the scaling dimension of the $\perp$-crossing term is greater than the scaling dimension of the term that couples to $J_a^\perp$ (which was also emphasized in *Law et al. [2010]*). This indicates that, following the RG flow, the coupling of the $\perp$-crossing term grows slower than $J_a^\perp$. Therefore, starting at approximately equal strength of both coupling constants, we expect the $J_a^\perp$ term to dominate the crossing term for sufficiently low temperature and applied voltage. Regarding this fact, we still expect our model to be physically meaningful within the range of interactions for which the $\perp$-crossing terms become relevant.

The situation is summarized in Fig. 5.4 where the dashed line represents the Toulouse points, the yellow regions the case where the crossing terms are relevant but less relevant than the considered terms, and the red regions the case where the crossing terms become the most relevant terms. In conclusion, the coupling of the crossing terms are normalized to zero in the following cases:

- the weak coupling limit;
- all Toulouse points of case B;
- the Toulouse points of case A for g_t or g_b smaller than $1 - \sqrt{1/2}$;

and we consider the most relevant terms in our model within the critical parameter region $1 - \sqrt{1/2} \leq g_\mathrm{t} \leq 1 + \sqrt{1/2}$ for the Toulouse points of case A.

5.2. Direct proportionality between the Kondo cloud and current cross correlations in helical liquids

Due to the special spin-orbit locking of helical liquids, the information about interaction processes with a magnetic moment is carried away from the scattering region in a spin resolved fashion. It sounds reasonable to conjecture that a finite frequency current noise measurement between different reservoirs (in the four-terminal setup of Section 5.1) allows an indirect detection of the Kondo cloud. If the noise frequency matches the frequency corresponding to the Kondo temperature, the current fluctuations should be most sensitive to the Kondo correlations that give rise to the Kondo cloud. This conjecture establishes the foundation of this section, where we show indeed a one-to-one correspondence between the time- and space-resolved current cross correlations (Fig. 5.5) and the Kondo cloud. This one-to-one correspondence even

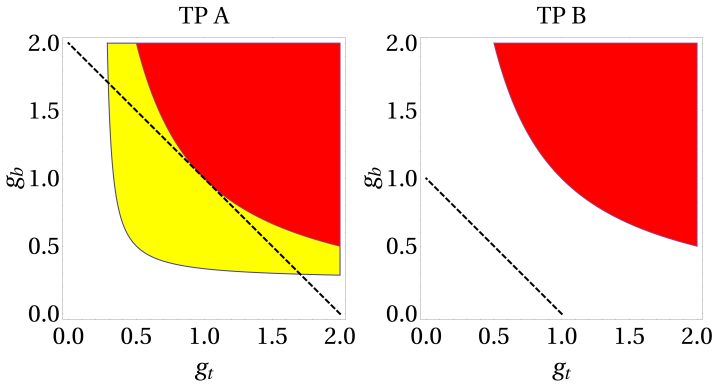

(a) Toulouse points A **(b)** Toulouse points B

Figure 5.4.: The relevance of the crossing terms, Eq. (5.23). The dashed lines represent the parameter constraints of the Toulouse points. Within the white region, the crossing terms are irrelevant. Within the yellow region they are relevant but less relevant than the considered terms and in the red region they are the most relevant terms. The color of the regions is calculated by taking the formulas of Tab. 5.1 for the remaining parameters.

exceeds the sets of Toulouse points in certain degrees of freedom[4]. findings are in particular remarkable as they establish an exact mapping between both observables although their analytic structures themselves are unknown. With this we mean that we can exactly relate the expectation values on the base of operator identities.

From the experimental side, the theoretical findings substantially improve upon existing suggestions of probing the Kondo cloud, especially in connection to the explained difficulties, cf. Section 2.2.3, of measuring the Kondo cloud at its cradle. In contrast to the Kondo cloud itself, the current cross correlations are present far away from the magnetic moment. Regarding the here established scheme, the measuring distance should be larger than the Kondo length and is, in theory, not limited from above. In practice, the purity of the sample, temperature, etc. give an upper bound. Therefore, we propose a direct way to detect the Kondo cloud in the least invasive manner since the current cross correlations are measurable far away from the magnetic moment.

The concrete suggestion is illustrated in Fig. 5.5. The setup is similar to Fig. 5.1 but is equipped with a device to detect current correlations instead of leads of a different chemical potential. By propagating the density operator backwards in time, as detailedly described in Section 3.2, we relate the current cross correlations to the Kondo cloud in an exact manner for a broad range of the Kondo parameters. In first order of the z-couplings, this relation is a direct proportionality. As a concrete

[4]The couplings J^z_{t} and J^z_{b} do not have to assume their Toulouse values.

example, we give the explicit analytical form of both quantities for vanishing z-couplings and emphasize the necessity to measure the current cross correlations in the time domain.

For reasons of clarity, we first constrain ourselves to the particular choice of interaction parameters $g_\mathrm{t} = g_\mathrm{b} = \frac{1}{2}$. The main reason is the direct and unperturbed appearance of the Kondo cloud in the current cross correlations for this case. Eventually, we depart from this particular value on the line $g_\mathrm{t} + g_\mathrm{b} = 1$, and discuss that the signature of the Kondo cloud remains in principle visible in the current cross correlations by simple post-processing of the data.

The section is organized as follows. In Section 5.2.1, we introduce our model and transform the Hamiltonian to an interacting resonant level model. Afterwards, in Section 5.2.2, we derive the proportionality relation between the Kondo cloud and the current cross correlations and present the Fourier transforms of both quantities. Finally, we discuss how the proportionality is affected by a change of the Luttinger parameters in Section 5.2.3.

5.2.1. Model

We consider a magnetic moment of spin $\hbar/2$ that is coupled to two helical liquids as shown in Fig. 5.5. In contrast to the setup of Section 5.1, the applied chemical potentials are abandoned in favor of contacts at the top and the bottom lead that allow us to measure the space- and time-resolved current cross correlations $\langle \delta I_\mathrm{t}(x,0)\delta I_\mathrm{b}(y,t)\rangle$ between the positions x and y with the time delay t.

For reasons which will become clear in Section 5.2.2, x and y should be of the order of or larger than the Kondo length scale ξ^K and t of the order of or larger than the Kondo time scale τ^K. Both scales are canonically derived from the Kondo temperature T^K by $\xi^K = v\tau^K = \frac{v\hbar}{k_B T^K}$; v is the Luttinger parameter of the leads that describes the velocity of their excitations. Additionally, to resolve the structure of the Kondo cloud spatially, it is essential that either the time delay t is tunable or one of the contacts is movable.

The setup is modeled by the same two channel Kondo Hamiltonian as discussed in Section 5.1.1. As we focus on the special case of $g_\mathrm{t} = g_\mathrm{b} = \frac{1}{2}$ and $v_\mathrm{t} = v_\mathrm{b} := v$, the Hamiltonian is simplified directly by the application of bosonization and refermionization without an intermediate Emery Kivelson transformation, as introduced in Section 3.1.1. The refermionized Hamiltonian then becomes an interacting resonant level model

$$\begin{aligned}
\mathcal{H}^0 &= \sum_{j\in\{\mathrm{t},\hat{\mathrm{t}},\mathrm{b},\hat{\mathrm{b}}\}} \int dx\ \hbar v\ \Psi^\dagger(x)_j(-\mathrm{i}\partial_x)\Psi(x)_j,\\
\mathcal{H}_K^\perp &= j_\mathrm{t}^\perp \Psi_\mathrm{t}^\dagger(0)\tau^- + j_\mathrm{b}^\perp \Psi_\mathrm{b}^\dagger(0)\tau^- + H.c.,\\
\mathcal{H}_K^z &= j_\mathrm{t}^z \Psi_\mathrm{t}^\dagger(0)\Psi_\mathrm{t}(0)\tau^z + j_\mathrm{b}^z \Psi_\mathrm{b}^\dagger(0)\Psi_\mathrm{b}(0)\tau^z. \qquad (5.27)
\end{aligned}$$

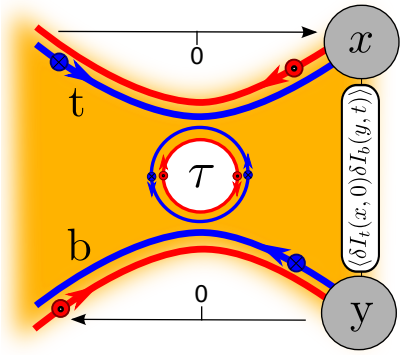

Figure 5.5.: Two helical liquids are coupled to a magnetic moment τ of spin $\hbar/2$. The blue (red) lines indicate edge channels with spin down (up) moving clockwise (counterclockwise) at the outer edge of the system. Contacts at x and y allow to measure the space- and time-resolved current cross correlations. Figure reprinted with permission from *Posske & Trauzettel [2014]*. Copyright (2014) by the American Physical Society.

Notable simplifications compared to the physical Hamiltonian in its original form are that two of the former four fermionic fields decouple and the only two-particle term appears in $\mathcal{H}_K^z$. In Eq. (5.27), the fermionic fields Ψ are non-linear combinations of the physical ones $\tilde{\Psi}$, but the relation that is important here is the linear dependence of the transformed densities

$$\rho_a(x) = \frac{1}{4}(3,1,-1,-3) \times (\tilde{\rho}_{a,\uparrow}(x), \tilde{\rho}_{a,\downarrow}(x), \tilde{\rho}_{a,\uparrow}(-x), \tilde{\rho}_{a,\downarrow}(-x))^T \tag{5.28}$$

on the physical ones. The coupling constants are $j^{\perp}_{\mathrm{t/b}} = \frac{J^{\perp}_{\mathrm{t/b}}\hbar v}{2\sqrt{2\pi a_c}}$, where a_c is the cutoff length scale of the bosonization procedure, and $j^z_{\mathrm{t/b}} = \hbar J^z_{\mathrm{t/b}}$. For $j^z_{\mathrm{t}} = j^z_{\mathrm{b}} = 0$, the Hamiltonian reaches a Toulouse point *[Emery & Kivelson, 1992; Posske et al., 2013; Schiller & Hershfield, 1998; Toulouse, 1969]* where many observables can be calculated analytically. It is interesting in this context that the interacting resonant level model has recently attracted new attention because of the development of exact methods at finite temperature and out of equilibrium *[Andergassen et al., 2011; Boulat & Saleur, 2008; Doyon, 2007; Mehta & Andrei, 2006]* to solve it. Applied to our setup, these methods could extend the range of exactly solvable parameter configurations considerably.

5.2.2. Results

The Kondo cloud on side a is, cf. Section 2.2.3, defined as the spatially resolved correlation of the z spin density in lead a and the z component of the magnetic

moment. Specifically, it takes the form

$$\chi_a^z(x) = \langle \delta\tilde{S}_a^z(x)\delta\tau^z\rangle. \tag{5.29}$$

In the following, an additional argument of the operators denotes the time in the Heisenberg picture. If no additional argument is given, we imply that it is equal to zero. The space- and time-resolved current cross correlations are, in this notation, given by

$$\chi^{cc}(x,y,t) = \langle \delta I_{\mathrm{t}}(x)\delta I_{\mathrm{b}}(y,t)\rangle = (2ev)^2\langle \delta\tilde{S}_{\mathrm{t}}^z(x)\delta\tilde{S}_{\mathrm{b}}^z(y,t)\rangle. \tag{5.30}$$

It is here where the very special attribute of the helical liquid, namely that the spin density is proportional to the current, initially connects the two quantities of Eqs. (5.29) and (5.30).

Next, we express the current cross correlations in the fields of the simplified Hamiltonian in Eq. (5.27), and exploit its symmetry under simultaneous time reversal and space inversion[5]. For the Kondo cloud, we obtain

$$\chi_a^z(x) = \langle \delta\rho_a(-|x|)\delta\tau^z\rangle, \tag{5.31}$$

and the current cross correlations become

$$\chi^{cc}(x,y,t) = (ev)^2\sum_{\sigma=\pm}\langle \delta\rho_{\mathrm{t}}(\sigma|x|,0)\delta\rho_{\mathrm{b}}(-\sigma|y|,t)\rangle. \tag{5.32}$$

It is crucial for the derivation of Eq. (5.32) that

$$\langle \rho_{\mathrm{t}}(|x|)\rho_{\mathrm{b}}(|y|,t)\rangle = \langle \rho_{\mathrm{t}}(-|x|)\rho_{\mathrm{b}}(-|y|,-t)\rangle^* = 0 \tag{5.33}$$

for all times t. The physical reason for the last equality is that excitations in different leads are independent of each other before they can interact at the site of the magnetic moment.

To derive and physically motivate the close relation between the quantities of Eqs. (5.31) and (5.32), we take the density operators with positive spatial argument in the summands of the latter equation and propagate them backwards in time before they have interacted with the magnetic moment. This propagation can be done exactly due to the property $(\tau^z)^2 = \frac{\hbar^2}{4}$ although the Hamiltonian possesses two-particle terms. In order not to hide the important results behind the more technical but albeit highly insightful details, the have already been explained in Section 3.2. The result reveals

$$\begin{aligned}\rho_a\left(x,-x/v-\epsilon\right) =& \rho_a(-v\epsilon,0) + \frac{\left(j_a^\perp/v\right)^2}{\hbar\left(1+(\frac{j_a^z}{4v})^2\right)}(\tau^z(-\epsilon)+\hbar/2)\\ &+\left(\mathrm{i}\frac{j_a^\perp}{\hbar v}\frac{1+\mathrm{i}\frac{j_a^z}{4v}}{(1-\mathrm{i}\frac{j_a^z}{4v})^2}\tau^+(-\epsilon)\Psi_a(-v\epsilon,0)+H.c.\right),\end{aligned} \tag{5.34}$$

[5]The exploited symmetry of the transformed Hamiltonian in Eq. (5.27) originates from the symmetries of the physical Hamiltonian in Eq. (5.1), namely, time reversal symmetry and the symmetry under simultaneous z spin flip and space inversion.

for any positive time ϵ. It is seen here that the density at positive spatial values carries information about the magnetic moment in the term proportional to τ^z. This is the basic reason why it is possible to measure the Kondo cloud by looking at current cross correlations. Inserting Eq. (5.34) into Eq. (5.32), we encounter three types of expectation values: (i) density correlations of the form $\langle\delta\rho_{\mathrm{t}}(-v\epsilon,0)\delta\rho_{\mathrm{b}}(-|y|,t-|x|-\epsilon)\rangle$, which vanish as explained in the derivation of Eq. (5.32), (ii) terms like $\langle\delta\tau^z(-\epsilon)\delta\rho_{\mathrm{b}}(-|y'|,t-|x|-\epsilon)\rangle$ that resemble the Kondo cloud, and (iii) correlators similar to $\langle\delta(\tau^+(-\epsilon)\Psi_{\mathrm{t}}(-v\epsilon,0))\delta\rho_{-a}(-|y|,t-|x|-\epsilon)\rangle$, which vanish in first order in $j^z_{\mathrm{t/b}}$. Retaining only the first and zeroth orders in $j^z_{\mathrm{t/b}}$, we therefore obtain

$$\begin{aligned}\chi^{cc}(x,y,t) =&\frac{e^2}{\hbar}\Big((j^{\perp}_{\mathrm{t}})^2\langle\delta\rho_{\mathrm{b}}(-|y|,t-|x|/v)\delta\tau^z\rangle^*\\ &+(j^{\perp}_{\mathrm{b}})^2\langle\delta\rho_{\mathrm{t}}(-|x|,-t-|y|/v)\delta\tau^z\rangle\Big)\,.\end{aligned}\tag{5.35}$$

This expression consists of two summands each of which already resembles the Kondo cloud defined in Eq. (5.29). The aim is now to choose a time frame for which one of the summands becomes proportional to the Kondo cloud and the other one is suppressed. To reveal the Kondo cloud from the first summand, we constrain $vt-|x|-|y|<0$ and shift the time argument of the density operator into its spatial argument. The same can be done for the second summand in the case $vt+|x|+|y|>0$. For suppressing the summand that fails to be proportional to the Kondo cloud within one of the respective time frames, we argue that there is an intrinsic time scale τ^c after which $\langle\delta\rho_a(-\eta,0)\delta\tau^z(t)\rangle$ decays rapidly if $|t|>\tau^c$. Here, η is a finite but small positive position in space. This assumption is physically motivated by the fact that a scattering problem lacks periodicity and usually exhibits no infinite length correlations. We consider the required time τ^c to be of the order of the Kondo time scale τ^K because it is the largest time scale that is immediately connected to the Hamiltonian. Nevertheless, the concrete choice of this time scale τ^c is, in principle, of no significance for the following results. This argument leads us to two time frames fulfilling the demanded conditions: (i) $(|x|+|y|)/v > t > \tau^K$, where the current cross correlations are greatly dominated by the first correlator in Eq. (5.35) since $|-t-(|x|+|y|)/v|$ is more than $2\tau^K$ larger than $t+(|x|+|y|)/v$. (ii) $-\tau^K > t > -(|x|+|y|)/v$, where the current cross correlations are dominated by the second correlator in Eq. (5.35). We are now able to state the central result of this section:

$$\chi^{cc}(x,y,t)\approx\frac{2e^2vk_B}{\hbar^3}\begin{cases}T^K_{\mathrm{t}}\chi^z_{\mathrm{b}}\left(|x|+|y|-vt\right) & \text{(i)},\\ T^K_{\mathrm{b}}\chi^z_{\mathrm{t}}\left(|x|+|y|+vt\right) & \text{(ii)},\end{cases}\tag{5.36}$$

where $T^K_{\mathrm{t/b}}=\frac{\hbar(j^{\perp}_{\mathrm{t/b}})^2}{2k_bv}=\frac{\hbar(J^{\perp}_{\mathrm{t/b}})^2}{16\pi a_ck_Bv}$ is the Kondo temperature of one lead calculated as if the other one does not exist *[Schiller & Hershfield, 1998]*. The deviation of

Eq. (5.36) from an identity is suppressed arbitrarily by measuring further away from the magnetic moment, i.e., increasing $|x|+|y|$, and therefore, it vanishes for any practical purpose. Rephrased, Eq. (5.36) states that, for certain time frames, the Kondo clouds of both leads are mirrored in the current cross correlations by a direct proportionality, and the proportionality factors are determined by the Kondo temperature of the respective opposite lead.

To give a descriptive example of a manifestation of this relation, we derive the analytical formulas in the limit $j^z_{\mathrm{t/b}} \to 0$ for both the Kondo cloud and the current cross correlations, following the lines of *Posske et al. [2013]*, and compare them. Additionally, this calculation, which is done independently of the more general considerations leading to Eq. (5.36), serves as a check of the validity of Eq. (5.36) for a specific choice of parameters. For convenience, we introduce

$$\zeta(x) = \frac{1}{\pi} e^{-\frac{\pi}{\hbar v \beta} x} \Phi\left(e^{-\frac{2\pi}{\hbar v \beta} x}, 1, \frac{1}{2} + \frac{\beta k_B T^K}{2\pi}\right), \tag{5.37}$$

which depends implicitly on the inverse temperature $\beta = 1/(k_B T)$ and the Kondo temperature *[Schiller & Hershfield, 1998]*

$$T^K = T^K_{\mathrm{t}} + T^K_{\mathrm{b}}. \tag{5.38}$$

Furthermore, $\Phi(z, s, a)$ is the Hurwitz-Lerch transcendent *[Weisstein, 2013]*. For the Kondo cloud, we obtain

$$\chi^z_a(x) = -\frac{\hbar k_B T^K_a}{2v} \zeta^2(|x|), \tag{5.39}$$

and the space- and time-resolved current cross correlations are

$$\chi^{\mathrm{cc}}(x, y, t) = -\frac{e^2 k_B T^K_{\mathrm{t}} k_B T^K_{\mathrm{b}}}{\hbar^2} \left\{\zeta^2\left(|x|+|y|-vt\right)^* + \zeta^2\left(|x|+|y|+vt\right)\right\}. \tag{5.40}$$

Hence, as predicted, the analytically derived formulas satisfy the proportionality relation of Eq. (5.36), and the proportionality factor is given by the corresponding Kondo temperature.

In experiments, it is common to measure frequency-resolved current cross correlations. We want to point out that the similarity in the time domain does not simply transfer to the frequency domain. The reason is that the full range of t is taken into account in a Fourier transform and the proportionality in the time domain is limited to certain time frames. To show this explicitly, we present analytical expressions for the Fourier transforms $\hat{f}(k) = ⨍ dx\, e^{\mathrm{i}kx} f(x)$ of the Kondo cloud and the current cross correlations of Eqs. (5.39) and (5.40) at zero temperature. Here, we take the principal-value Fourier transform since the Kondo cloud diverges at the site of the magnetic moment. The result is

$$\hat{\chi}^z_a(k) = -\frac{2\hbar^2}{\pi^2} \frac{T^K_a}{T^K} \mathrm{Re}\left\{\frac{\mathrm{Li}_2\left(1 + \frac{\mathrm{i}\hbar v k}{k_B T^K}\right) + \frac{\pi^2}{12}}{2 + \frac{\mathrm{i}\hbar v k}{k_B T^K}}\right\}, \tag{5.41}$$

where Li_2 is the dilogarithm and

$$\hat{\chi}^{\mathrm{cc}}(\omega,|x|+|y|)=\Theta(-\omega)\frac{8e^2k_B}{\pi\hbar}\frac{T_{\mathrm{t}}^K T_{\mathrm{b}}^K}{T^K}\times\mathrm{Re}\left\{\frac{\mathrm{i}e^{-\mathrm{i}\frac{\omega}{v}(|x|+|y|)}\ln\left(1+\frac{\mathrm{i}\hbar\omega}{k_BT^K}\right)}{2+\frac{\mathrm{i}\hbar\omega}{k_BT^K}}\right\} \tag{5.42}$$

with Θ being the Heaviside function. Instead of depicting the Fourier transform of the Kondo cloud at zero temperature of a single side, we concentrate on the more universal total Kondo cloud $\chi^z=\chi_{\mathrm{t}}^z+\chi_{\mathrm{b}}^z$. The functional form of its Fourier transform at zero temperature is shown in Fig. 5.6a. An interesting feature is revealed by $\hat{\chi}^z(0)=-\frac{\hbar^2}{4}$, i.e., the spatial integral over the total Kondo cloud in the ground state equals the expected value for exact screening.

The Fourier transform of the current cross correlations at zero temperature in turn is illustrated in Fig. 5.6b. It is convenient to introduce the envelope function

$$\hat{\chi}_{\mathrm{max}}^{cc}=\Theta(-\omega)\frac{8e^2k_B}{\pi\hbar}\frac{T_{\mathrm{t}}^K T_{\mathrm{b}}^K}{T^K}\left|\frac{\ln\left(1+\frac{\mathrm{i}\hbar\omega}{k_BT^K}\right)}{2+\frac{\mathrm{i}\hbar\omega}{k_BT^K}}\right|. \tag{5.43}$$

For generic values of $|x|+|y|$, $\chi^{cc}(\omega,|x|+|y|)$ oscillates between $\pm\hat{\chi}_{\mathrm{max}}^{cc}$. Hence, for clarity, we choose two representative values for $|x|+|y|$ in Fig. 5.6b. First, we set $|x|+|y|$ equal to twice the Kondo length ξ^K, which is a typical value for the setup at hand in the sense that a broad range of the Kondo cloud can be spatially resolved in the time domain. Secondly, we look at $|x|+|y|=0$. Evidently, there is no obvious similarity between the Kondo cloud and the current cross correlations in the frequency domain.

5.2.3. Dependence of the central results on interaction strengths

The experimental realization of the proposed setup seems to be highly challenging. Nevertheless, we have chosen to treat the system at hand because it shows the clearest possible appearance of the Kondo cloud in the current cross correlations. This feature can be affected by altering the interaction strengths $g_{\mathrm{t/b}}$, the effects of which we are going to discuss now. Allowing for an unrestricted choice of $g_{\mathrm{t/b}}$ would exceed the scope of this work, since, following the scheme of generalized Emery Kivelson transformation, Section 3.1.2, there exists no simplifying refermionization in this case. Covered by the method at hand, however, are the two lines $g_{\mathrm{t}}+g_{\mathrm{b}}=1$ and $g_{\mathrm{t}}+g_{\mathrm{b}}=2$. In both cases, correlators of the form $\langle\Psi^\dagger\tau^-\Psi^\dagger\Psi\rangle$ appear additionally in the current cross correlations, where the fermionic fields Ψ can be of different leads, space, and time. Although these additional correlators are interesting objects themselves, they hinder the direct measurement of the Kondo cloud in principle. As the second line $g_{\mathrm{t}}+g_{\mathrm{b}}=2$ is based on a different effective Hamiltonian *[Posske et al., 2013]*, we limit ourselves here to describing the first line $g_{\mathrm{t}}+g_{\mathrm{b}}=1$ in greater

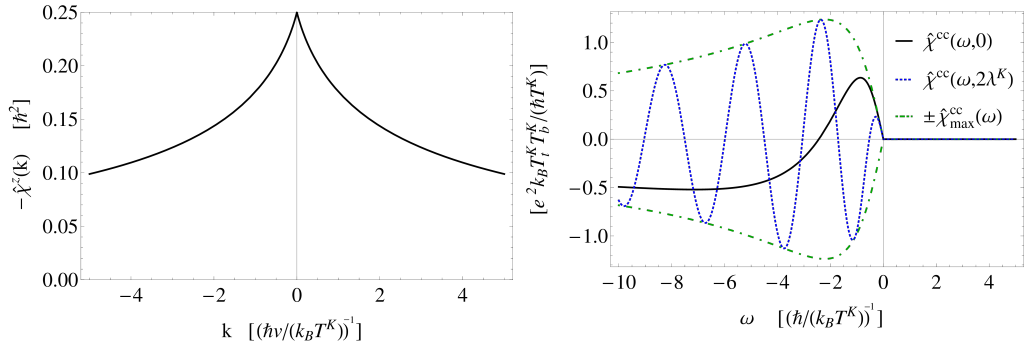

Figure 5.6.: Fourier transforms of the total Kondo cloud, **(a)**, and the current cross correlations, **(b)**, at zero temperature. The current cross correlations are depicted for the two representative values of $|x|+|y|$ equals zero and $|x|+|y|$ equals twice the Kondo length λ^K. Furthermore, we involve the envelope function $\hat{\chi}^{cc}_{\max}$. Despite the analogy of the Kondo cloud and the current cross correlations in the time domain (for certain time frames), they show no apparent similarity in the frequency domain. Figure reprinted with permission from *Posske & Trauzettel [2014]*. Copyright (2014) by the American Physical Society.

detail. If we leave $g_\mathrm{t} = g_\mathrm{b} = \frac{1}{2}$ with the constraint $g_\mathrm{t} + g_\mathrm{b} = 1$, the Hamiltonian of Eq. (5.27) slightly changes, so that all appearing fields Ψ_t are replaced by Ψ_4 and all fields Ψ_b are replaced by Ψ_2 with the relations[6]

$$\begin{pmatrix} \rho_4 \\ \rho_2 \end{pmatrix} = \frac{1}{\sqrt{2}} \begin{pmatrix} \sqrt{g_\mathrm{t}} - s\sqrt{g_\mathrm{b}} & -s\sqrt{g_\mathrm{t}} - \sqrt{g_\mathrm{b}} \\ -\sqrt{g_\mathrm{t}} - s\sqrt{g_\mathrm{b}} & -s\sqrt{g_\mathrm{t}} + \sqrt{g_\mathrm{b}} \end{pmatrix} \begin{pmatrix} \rho_\mathrm{t} \\ \rho_\mathrm{b} \end{pmatrix}, \tag{5.44}$$

where $s \in \{-1, +1\}$, cf. Section 3.1.3.2 and in particular Eq. (3.77) for the derivation. The resulting transformed Hamiltonian is

$$\begin{aligned} \mathcal{H}_K^\perp &= \hat{j}_\mathrm{t}^\perp \Psi_4^\dagger(0)\tau^- + \hat{j}_\mathrm{b}^\perp \Psi_2^\dagger(0)\tau^- + H.c., \\ \mathcal{H}_K^z &= \hat{j}_\mathrm{t}^z \Psi_4^\dagger(0)\Psi_4(0)\tau^z + \hat{j}_\mathrm{b}^z \Psi_2^\dagger(0)\Psi_2(0)\tau^z \end{aligned} \tag{5.45}$$

with $\hat{j}_a^\perp = j_a^\perp$ and

$$\hat{j}_a^z = \frac{j^z}{\sqrt{2g_a}} - \sqrt{2}\pi v(\sqrt{g_a} + s\sqrt{g_{\neg a}}). \tag{5.46}$$

[6]Please note that *Posske & Trauzettel [2014]* erroneously have the indices of the left hand side of Eq. (5.44) the other way around, which can be seen by considering the limit $g_\mathrm{t} = g_\mathrm{b} = \frac{1}{2}$ and $s - 1$, where it is $\rho_4 = \rho_\mathrm{t}$ and $\rho_2 = \rho_\mathrm{b}$.

Here, $\neg a$ denotes the opposite side of a, i.e., $\neg\mathrm{t} = \mathrm{b}$ and $\neg\mathrm{b} = \mathrm{t}$. Note that the calculations done in first order around $j_a^z = 0$ in Section 5.2.2 now hold in first order around $\hat{j}_a^z = 0$, which corresponds to $j_a^z = 2\pi v(g_a + s\sqrt{g_a g_{\neg a}})$. We want to put special emphasis on the fact that, for $s = +1$, the couplings $j_{\mathrm{t/b}}^z$ do not need to be small compared to $j_{\mathrm{t/b}}^\perp$, which could be seen as unphysical considering that the respective bare couplings should be of the same order. In fact, to assume a small ratio $j_{\mathrm{t/b}}^z/j_{\mathrm{t/b}}^\perp$ is not unphysical as the renormalization group (RG) analysis given in Section 5.1.4 shows. Since the terms coupled to $j_{\mathrm{t/b}}^\perp$ are relevant while the terms coupled to $j_{\mathrm{t/b}}^z$ are part of the free Hamiltonian in the RG calculations, $j_{\mathrm{t/b}}^\perp$ initially grows following the RG flow. Hence, starting with small bare couplings of the same order, the RG flow generates a situation with a small ratio $j_{\mathrm{t/b}}^z/j_{\mathrm{t/b}}^\perp$.

For the current cross correlations, we obtain the additional contribution

$$\chi_{AS}^{cc} = \sum_{\sigma,\sigma'\in\{\pm\}} s\frac{e^2}{\hbar}\frac{g_\mathrm{b} - g_\mathrm{t}}{4\sqrt{g_\mathrm{t} g_\mathrm{b}}} \times \langle \delta\rho_4(\sigma x)\delta\rho_4(\sigma' y,t) - \delta\rho_2(\sigma x)\delta\rho_2(\sigma' y,t)\rangle\,. \tag{5.47}$$

Terms of the form $\langle \Psi^\dagger \tau^- \Psi^\dagger \Psi\rangle$ appear here by applying Eq. (5.34) to the density operators with positive spatial argument. The quantity χ_{AS}^{cc} is anti-symmetric in both pairs of couplings $(g_\mathrm{t}, g_\mathrm{b})$ and $(\hat{j}_\mathrm{t}, \hat{j}_\mathrm{b})$. The latter is seen by considering the invariance exhibited by the Hamiltonian in Eq. (5.45) under simultaneous exchange of the fields $\Psi_4 \leftrightarrow \Psi_2$ and exchange of the couplings $\hat{j}_\mathrm{t} \leftrightarrow \hat{j}_\mathrm{b}$. In this regard, χ_{AS}^{cc} vanishes for an equal coupling to the magnetic moment $\hat{j}_\mathrm{t} = \hat{j}_\mathrm{b}$, but, in general, we encounter a perturbation of the proportionality between the Kondo cloud and the current cross correlations. However, χ_{AS}^{cc} can be eliminated under the assumption that results of the crossed current correlations for several values of the couplings $\hat{j}$ are available. A concrete example for an elimination is to add up the current cross correlations of two systems, where the second system differs from the first one only by exchanged tunnel couplings $\hat{j}_\mathrm{t} \leftrightarrow \hat{j}_\mathrm{b}$. By the above-mentioned invariance of the Hamiltonian, this exchange is equivalent to the exchange of $\rho_4 \leftrightarrow \rho_2$. The proportionality relation of Eq. (5.35) is then only slightly altered. Instead of the Kondo cloud of one lead, a linear combination of the Kondo clouds of both leads occurs. For instance, for $(|x|+|y|)/v > t > \tau^K$ and first order in $\hat{j}^z$, we obtain

$$\chi^{cc}(x,y,t) + \chi_{\hat{j}_\mathrm{t}\leftrightarrow\hat{j}_\mathrm{b}}^{cc}(x,y,t) = c_\mathrm{t}\chi_\mathrm{t}^z + c_\mathrm{b}\chi_\mathrm{b}^z \tag{5.48}$$

with

$$c_\mathrm{t} = -\frac{2e^2 v k_B}{\hbar^3}\left(s\sqrt{g_\mathrm{t} g_\mathrm{b}}T^K + g_\mathrm{t} T_M^K\right) \tag{5.49}$$

$$c_\mathrm{b} = -\frac{2e^2 v k_B}{\hbar^3}\left(s\sqrt{g_\mathrm{t} g_\mathrm{b}}T^K - g_\mathrm{b} T_M^K\right), \tag{5.50}$$

where we introduced the auxiliary temperature $T_M^K = T_\mathrm{t}^K - T_\mathrm{b}^K$.

5.3. Conclusion about the local Kondo impurity

This chapter shows that the two channel Kondo model with helical liquid leads can be solved exactly for two sets of Toulouse points that are characterized by relations between the interaction strengths of both leads, namely $g_\mathrm{t} + g_\mathrm{b} = 2$ and $g_\mathrm{t} + g_\mathrm{b} = 1$, respectively. The mysterious Kondo cloud can therefore be resolved analytically and its similarities to the ordinary Fermi liquid Kondo problem but also its different behavior in nonequilibrium can be determined and discussed. The advantage of helical liquids over Fermi liquids, however, only reveals its true strength if when we desire to measure the Kondo cloud. Ultimately due to unique charge-spin correspondence, we find a direct proportionality of the current cross correlations – within a certain time frame – to the Kondo cloud. The setup therefore has the potential to measure the Kondo cloud least invasively.

If a single magnetic impurity is able to generate the described rich phenomenology, what are multiple magnetic impurities going to achieve? In Chapter 8, we shortly play with the ideas of a one-dimensional chain of impurities and describe that we expect a fully electrically tunable transition from a ferromagnetic to an antiferromagnetic ground state. The next chapter, Chapter 6, goes a step further and promotes the dimensionalities of the considered constituents to a two-dimensional lattice of magnetic impurities on a three-dimensional topological insulator. To render the situation even more interesting, we explicitly consider a spin-anisotropic dispersion relation that exhibits nesting, cf. Section 2.1.4. Here, we expect interesting spin textures to form in the ground state.

6. Magnetically doped strong three-dimensional topological insulator (3DTI) in proximity to a superconductor

This chapter is a revised version of *Baum et al. [2015b]*, copyrighted by the American Physical Society. We have reassembled the material considerably in order to improve the presentation. Also regard the remarks on page 3.

The localization length of the edge states of a topological insulator (TI) is usually inverse to the size of the bulk energy gap. We have already exemplified this behavior for the simple model of Section 2.1.1 but there are numerous additional examples for experimentally more relevant models like the Haldane model *[Haldane, 1988]*, the Kane-Mele model *[Kane & Mele, 2005a]*, the Qi-Wu-Zhang model *[Qi et al., 2006]*, and the Kitaev chain *[Kitaev, 2001]*[1]. Closing the bulk gap therefore leads to the complete delocalization and hence distinction of the edge states[2]. Following the above mentioned evidence, we assumed that the closure of the bulk energy gap of an ordinary topological insulator is equivalent to the hybridization of the edge states with the bulk states. Much to our surprise, we discovered a system, where the edge states persist to be well localized even in the absence of a bulk energy gap. This system is the surface of a magnetically doped three-dimensional strong topological insulator, which is brought into proximity to an s-wave superconductor. In fact, the original intention of this setup was to solve for the ground state magnetic order of the impurities if the chemical potential lies within the hexagonal warping regime of the topological insulator. This part of our research is presented in Section 6.1, where the system is introduced in detail and our results regarding this topic are presented: a considerably stable spiral spin wave is formed at the surface. Bringing

[1] Although the latter is a topological superconductor, its mean field spectrum can be treated in the same fashion as a topological insulator as described in Section 2.3.

[2] There are known exceptions, where systems exhibit topological behavior also in the absence of a bulk gap *[Deng et al., 2014; Keselman & Berg, 2015]*. Among these exceptions are, e.g., Weyl semimetals and nodal superconductors *[Matsuura et al., 2013; Queiroz & Schnyder, 2014]*. However, the application of topology in these cases is profoundly different to the approach that characterizes band insulators.

the system into the proximity of an s-wave superconductor generates spectra that simultaneously possess a gapless bulk and well-localized edge states. In fact, there is a general mechanism behind the formation of this type of gapless topological phases, which is applicable to all two-dimensional spin-momentum locked phases that exhibit proximity-induced s-wave pairing and a non-ferromagnetic periodic magnetization. This mechanism is extracted and elaborated on in Section 6.2. Let us outline the important physical scheme, which is detailedly explained in Section 6.2: the periodic magnetization opens a magnetic gap at particular regions of the Fermi surface but, crucially, leaves parts of the Fermi surface ungapped. The introduction of proximity-induced superconductivity now opens a superconducting gap at these magnetically untouched regions and competes with the aforementioned magnetic gap in the other regions. If the superconducting pairing is weaker than the magnetism, the interesting situation occurs that the former Fermi surface consists of gapped parts that either have a superconducting or a magnetic domination. The gap vanishes at the points that separate these regions. In fact, the closure of the gap is deeply protected by this mechanism.

6.1. Magnetically doped strong three-dimensional topological insulators in the hexagonal warping regime

In this section, we generate complex magnetic order on the surface of three-dimensional strong topological insulators without the need for fine tuning. To obtain this effect, we consider the hexagonally warped region of chemical potentials as explained in Section 2.1.4. One possibility to induce spontaneous magnetization on the surface is the Coulomb interaction between electrons as investigated in *Baum & Stern [2012a,b]*. In particular, if the chemical potential lies within a specific range where the electronic Fermi surface is nested, a skyrmion lattice may form on the surface of these materials. Nonetheless, the analysis points out that the electron-electron interaction strength in experimentally realized topological insulators is too weak to generate the necessary instability. Another source of magnetism is delivered by magnetic dopants. Research into this direction has been put forward in *Caprara et al. [2012]; Liu et al. [2009]; Rosenberg & Franz [2012]; Schmidt et al. [2011]*, who focus on chemical potentials close to the Dirac point. Among other results, the references describe an opening of a surface gap due to surface ferromagnetism, which possesses a larger transition temperature than the bulk magnetism. Exact expressions for the Ruderman-Kittel-Kasuya-Yosida (RKKY) interaction *Kasuya [1956]; Nakamura et al. [1985]; Roth et al. [1966]; Ruderman & Kittel [1954]; Yosida [1957]* on the surface of topological insulators have been given by *Zhu et al. [2011]*, which concluded for the possibility of the formation of a complex magnetic order

on the surface. A spiral magnetic order in a one-dimensional chain of magnetic adatoms has been predicted by *Klinovaja et al. [2013]; Ye et al. [2010]. Jiang & Wu [2011]* have claimed to have predicted a helical magnetic order in the hexagonal warping regime by employing a mean field theory for systems that also exhibit electron-electron interactions.

In this section, we theoretically explore a system that is composed of classical magnetic moments aligned on a lattice on the surface of a three-dimensional strong topological insulator, the chemical potential of which is tuned to the hexagonal warping regime, cf. Section 2.1.4. The magnetic moments could be arranged on a lattice by physically dragging them into the positions employing techniques of atomic force microscopy. The occurring nesting is expected to enhance physical properties in momentum representation that originate from excitations close to the Fermi energy at the corresponding nesting vectors. Indeed, we find that the interaction among the magnetic impurities, which is mediated by the electronic states – i.e., the RKKY interaction – to be dominated by peaks in Fourier space at the nesting momenta. We then numerically determine the ground state magnetic order for a generic system and find that three spiral spin waves constitute the degenerate ground state of the system. By changing the lattice structure of the magnetic impurities or tuning the chemical potential, the peaks of the RKKY interaction can be shifted and even merged. Thereby, the spiral structures are significantly manipulable. Furthermore, we determine the stability of the spiral phase against temperature and find, that for experimentally realistic lattices and interactions of the magnetic moments with the surface states, the spiral phase stays stable up to temperatures of tens of Kelvin.

Finally, we consider the proximity coupling of the system at hand to an s-wave superconductor. The formation of the spiral wave already leads to a partial gap opening at the Fermi surface of the electronic spectrum. Coupling the considered system to an s-wave superconductor generates a gapless topological phase with peculiar properties. We abstract the underlying mechanism in Section 6.2 and thereby introduce more general gapless topological superconductors of the described kind. As a substantial advantage, the physical realization of a magnetically doped three-dimensional topological insulator in proximity to a superconductor fulfills the extracted necessary requirements without the need for fine tuning physical properties. We want to remark that *Zyuzin & Loss [2014]* consider a similar setup to the one we present here. In contrast to this section, they focus on chemical potentials close to the Dirac point, and predict the appearance of frustrated anti-ferromagnetism.

The structure of this section is as follows. In Section 6.1.1, we present the model and the RKKY interactions in dependence on the lattice structure of the magnetic impurities and the chemical potential which takes the form of several δ-peaks in momentum space. After a side remark on the calculation of the RKKY interactions with proper energy cutoffs in Section 6.1.2, we explain in Section 6.1.3 how to engineer the position of these peaks by changing the lattice structure of the magnetic impurities or the chemical potential. We then proceed to calculate the spiral ground

state configuration and its stability of the classical spins employing the Metropolis algorithm for a generic class of RKKY interactions in Section 6.1.4. We furthermore estimate the transition temperature from a spirally ordered state to an unordered state to tens of Kelvin. In Section 6.1.5, we enter the spiral surface magnetization into the Hamiltonian and determine the altered electronic spectrum. We conclude the chapter by coupling the system to an s-wave superconductor in Section 6.1.6.

6.1.1. Model and RKKY interaction

In the following, we place magnetic impurities, which are arranged on a lattice, onto the surface of a three dimensional topological insulator. Each lattice position is numbered by two integer indices, $(j_1, j_2) = \boldsymbol{j} \in \mathbb{Z}^2$. The spin of the impurity at $\boldsymbol{r_j}$ is described by the operator $S^\lambda_{\boldsymbol{j}}$. The magnetic moments couple via their spin to the spin density of the itinerant excitations $s^\lambda_{\boldsymbol{j}} = c^\dagger_{\boldsymbol{j}} \sigma^\lambda c_{\boldsymbol{j}}$ by a local exchange interaction,

$$\mathcal{H}_{int} = \sum_{\boldsymbol{j}\in\mathbb{Z}^2} \sum_{\lambda\in\{x,y,z\}} J^\lambda_{\boldsymbol{j}} S^\lambda_{\boldsymbol{j}} s^\lambda_{\boldsymbol{j}}, \tag{6.1}$$

where $J^\lambda_{\boldsymbol{j}}$ are the exchange coupling constants. For simplicity, we assume that all moments couple equally to the spin density and that J is spatially homogeneous. Hence, we replace $J^\lambda_{\boldsymbol{j}} \equiv J_0$.

If the dynamics of the electronic excitations is considerably faster than the one of the impurities, the effective impurity interaction can be deduced via linear response theory as conducted in Section 2.2.4. Assuming this condition is met, the system is well approximated by an RKKY Hamiltonian of the form

$$\mathcal{H}_{\mathrm{RKKY}} = -\sum_{\boldsymbol{i},\boldsymbol{j}} \sum_{\lambda,\lambda'\in\{x,y,z\}} J_0^2 \chi^{\lambda,\lambda'}_{\boldsymbol{r_i},\boldsymbol{r_j}} S^\lambda_{\boldsymbol{i}} S^{\lambda'}_{\boldsymbol{j}} . = \int_{\mathrm{BZ}} d^2\boldsymbol{q}\; S^\lambda_{\boldsymbol{q}} J^{\lambda,\lambda'}_{\boldsymbol{q}} S^{\lambda'}_{-\boldsymbol{q}}, \tag{6.2}$$

where $\hbar = 1$ and $\boldsymbol{S_q}$ is the Fourier transform of the magnetic impurity spin, which we treat as classical further below. Additionally it is,

$$J^{\lambda,\lambda'}_{\boldsymbol{q}} = \frac{-J_0^2}{2\pi V_{\mathrm{uc}}} \sum_{\boldsymbol{G}} \chi^{\lambda,\lambda'}_{-(\boldsymbol{q}+\boldsymbol{G})}, \tag{6.3}$$

where $\mathbf{G}$ runs over the set of reciprocal lattice vectors of the impurity lattice, and V_{uc} is the area of a unit cell. The quantity χ is the spin susceptibility of the bare surface without magnetic impurities *[Baum & Stern, 2012b; Jiang & Wu, 2011]* as introduced in Section 2.2.4 For the considered model of Fu, which we introduce in Section 2.1.4, the quantity has been numerically calculated previously *[Baum & Stern, 2012b; Jiang & Wu, 2011]*. It exhibits pronounced peaks at the six nesting vectors that are depicted in Fig. 2.6. As we refer to the spin susceptibility in the

following, we repeat its definition from page 25 in the following three formulas for completeness

$$\chi^{\lambda,\lambda'}_{\boldsymbol{r},\boldsymbol{r'}} = \int_{-\infty}^{\infty} d^2\mathbf{q}\, \frac{e^{-\mathrm{i}\mathbf{q}\cdot(\boldsymbol{r}-\boldsymbol{r'})}}{(2\pi)^2} \chi^{\lambda,\lambda'}_{\boldsymbol{q}}, \tag{6.4}$$

$$\chi^{\lambda,\lambda'}_{\boldsymbol{q}} = \lim_{\eta\to 0} \int_{-\infty}^{\infty} d^2\boldsymbol{k} \sum_{\tau,\rho=\pm} \frac{f_{\beta,\mu}(\epsilon^{\tau}_{k}) - f_{\beta,\mu}(\epsilon^{\rho}_{\boldsymbol{k}+\boldsymbol{q}})}{\epsilon^{\tau}_{\boldsymbol{k}} - \epsilon^{\rho}_{\boldsymbol{k}+\boldsymbol{q}} - \mathrm{i}\eta} Y^{\lambda,\lambda'}_{\tau,\rho}(\boldsymbol{k},\boldsymbol{k}+\boldsymbol{q}) \theta^{\tau,\rho}_{\boldsymbol{k},\boldsymbol{q},\Lambda_-,\Lambda_+}, \tag{6.5}$$

$$\theta^{\tau,\rho}_{\mathbf{k},\mathbf{q},\Lambda_-,\Lambda_+} = \begin{cases} 1 \text{ if } \epsilon^{\tau}(\mathbf{k}), \epsilon^{\rho}(\boldsymbol{k}+\boldsymbol{q}) \in (\Lambda_-,\Lambda_+), \\ 0 \text{ else.} \end{cases} \tag{6.6}$$

In the last equation, Λ_- denotes the lower momentum cutoff, given by the end of the bulk valence band, and Λ_+ the upper cutoff, given by the start of the bulk conduction band. For a further explanation of Eq. (6.4) we refer to Section 2.2.4.

6.1.2. Calculating the spin susceptibility with proper cutoffs

As seen from Eq. (6.5), the integral to be evaluated for obtaining the spin susceptibility contains a sum over four terms, which we label, according to the indices τ and ρ, as $(++)$, $(+-)$, $(-+)$, and $(--)$. The physical pictures behind the different contributions are the following: The $(++)$ contribution contains properties originating close to the Fermi energy, the $(+-)$ and $(-+)$ contributions describe high energy processes between the upper and lower branches of the Dirac cone, and the $(--)$ contribution describes processes of states that lie deep in the Fermi sea. As such, the latter does not play an important role at low temperatures. Additionally, since bulk states are neither close to the Fermi energy nor are they localized at the surface, we do not expect the a priori neglected and until now unmentioned bulk terms to contribute significantly to the RKKY interaction.

If the RKKY interaction is dominated by the properties of the system close to the Fermi energy, the $(+-)$ and $(-+)$ terms may be neglected, as done by *Jiang & Wu [2011]* , and *Baum & Stern [2012b]*. This leads to the spin susceptibility as illustrated in Fig. 6.1, where only the $(++)$ term is considered. The dominant contributions occur close to the six nesting vectors (Fig. 2.6). The data is obtained by numerically integrating Eq. (6.5) over a hexagonal lattice of 1600×1600 sites with a resolution of $100 \times 100/k_0^2$. The integrand of Eq. (6.4) is made well-defined at the boundaries of the integration region by regularizing the denominator with $\eta = 2^{-13} E_0$.

However, the mathematical structure of the physically dismissed $(+-)$ and $(-+)$ contributions does not allow to neglected them a priori. In fact, without the introduction of the cutoffs Λ_+ and Λ_-, the spin susceptibility would be dominated by these contributions. Therefore, we give numerical estimates for the range of cutoffs

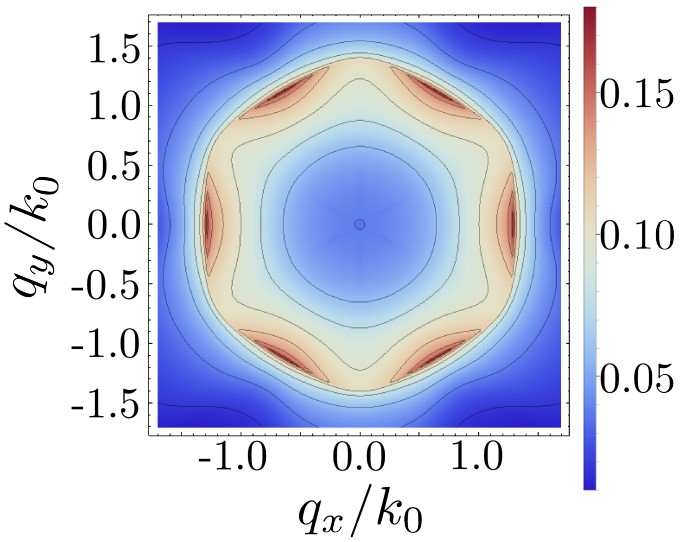

Figure 6.1.: The largest eigenvalue of the spin susceptibility χ in momentum space at zero temperature and for $\mu = 0.7E_0$. Figure reprinted with permission from *Baum et al. [2015b]*. Copyright (2015) by the American Physical Society.

in which their omission is valid. Fig. 6.2 shows the effect of an increasing cutoff, from 0 to $2E_0$, for $\Lambda = \Lambda_+ = -\Lambda_-$. The $(+-)$ and $(-+)$ terms contribute to the susceptibility at small momenta, such that keeping only the contributions close to the nesting vectors is not justified for sufficiently large Λ.

Recent experimental data *[Hasan et al., 2014; Miyamoto et al., 2012; Neupane et al., 2012; Sato et al., 2010]* shows that for most materials the upper cutoff is larger than the absolute value of the lower one[3] and that both lie within the range where the $(+-)$ and $(-+)$ contributions may be validly neglected. In Bi_2Te_2Se for instance, the lower cutoff is close to zero *[Miyamoto et al., 2012; Neupane et al., 2012]*. In $GeBi_2Te_4$ however, both cutoffs are larger than for most materials *[Neupane et al., 2012]* such that an inclusion of the $(+-)$ and $(-+)$ terms may be necessary.

6.1.3. Engineering the position of the peaks in the RKKY interaction

From Eq. (6.3) we infer that the RKKY interaction strongly depends on the lattice structure and the lattice constant of the magnetic impurities as well as on the chemical potential. The position of the peaks that dominate the RKKY interaction in momentum space can therefore be engineered taking into consideration different lat-

[3]The cutoffs Λ_- and Λ_+ are defined as the difference in energy from the Dirac point to the onset of the valence and bulk band respectively.

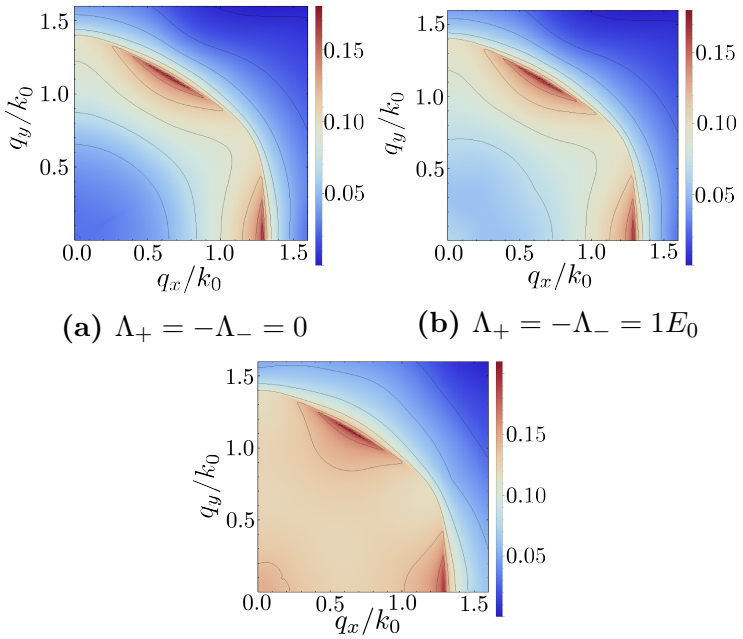

(a) $\Lambda_+ = -\Lambda_- = 0$ **(b)** $\Lambda_+ = -\Lambda_- = 1E_0$

(c) $\Lambda_+ = -\Lambda_- = 2E_0$

Figure 6.2.: The largest eigenvalue of the spin susceptibility χ for different cutoffs Λ at zero temperature and $\mu = 0.7E_0$. For large cutoffs, the concentration of χ around the nesting momenta gets reduced and the contributions at low momenta have to be taken into account. Figure reprinted with permission from *Baum et al. [2015b]*. Copyright (2015) by the American Physical Society.

tice structures, lattice constants, and chemical potentials. To exemplify the different appearing peak structures, we choose a square lattice, a hexagonal lattice with the lattice vectors $(1,0)a$ and $(1/2,\sqrt{3}/2)a$, and a by $\pi/3$ rotated hexagonal lattice. The results are assembled in Fig. 6.3, where the RKKY interaction in Fourier space is qualitatively represented by its largest eigenvalue. It can be seen that for $a < \pi Q^{-1}$, where Q is the modulus of the nesting vectors, the choice of the lattice structure has no significant effect on the RKKY interaction. It can be seen that if the lattice constant a is smaller πQ^{-1}, neither the specific size of the lattice constant nor the type of Bravais lattice alter our results. We therefore believe that our findings can be extended to randomly ordered magnetic dopants on the surface above a critical density of adatoms which still lies within the experimentally realizable range. However, below the critical density, i.e., for $a > \pi Q^{-1}$, different peaks can be brought to overlap since the nesting vectors exceed the first Brillouin zone. By this mechanism, the position of the peaks can be engineered according to the needs.

A similar effect as to change the lattice constant is achieved by tuning the chemical potential within the hexagonal range. The latter procedure has the advantage of leaving the sample unaltered in its physical structure and enabling an improved experimental accessibility. Exploiting the full hexagonal range of $\mu \in \{0.55E_0, 0.9E_0\}$, the absolute value of the nesting vectors can be changed by a factor of 1.5.

6.1.4. Spiral ground state and its temperature stability

For lattice constants smaller than $\pi|2k_F|^{-1}$, the RKKY interaction is not significantly altered by the choice of the lattice. In this generic regime, we perform an analysis employing a Metropolis algorithm *[Metropolis et al., 1953]* neglecting the contributions to J away from its peaks. For simplicity, we treat the spins classically and take them to be vectors on the unit sphere ($\hbar = 1$). The results can be rescaled to the desired size of the spins. To facilitate the numerical calculations, we specifically approximate J by its contributions close to the peaks,

$$\hat{J}_{\boldsymbol{p}}^{\lambda,\lambda'} = \sum_{q \in \pm\{Q_i\}_{i=1}^{3}} \mathrm{rect}\left(\frac{p_x - q_x}{\sqrt{A}}\right) \mathrm{rect}\left(\frac{p_y - q_y}{\sqrt{A}}\right) J_q^{\lambda,\lambda'}, \tag{6.7}$$

where A accounts for the approximated area of the peak in momentum space and rect is the rectangular function. From Fig. 6.1, we estimate $A \approx 0.1k_0^2$. We expect a broad class of systems with a J-matrix consisting of a finite number of peaks to develop spin waves as their global energetic minima. The concrete system we analyze is a 16×16 lattice of spins positioned on a hexagonal lattice with a lattice constant $a = \frac{\pi}{4}Q^{-1}$, which obeys periodic boundary conditions. We start at a random spin distribution where every configuration of the spins in the configuration space is picked equally likely and subsequently employ the Metropolis algorithm, cf. Section 3.3 and *[Metropolis et al., 1953]*, to thermalize the system. For $\beta \to \infty$, we

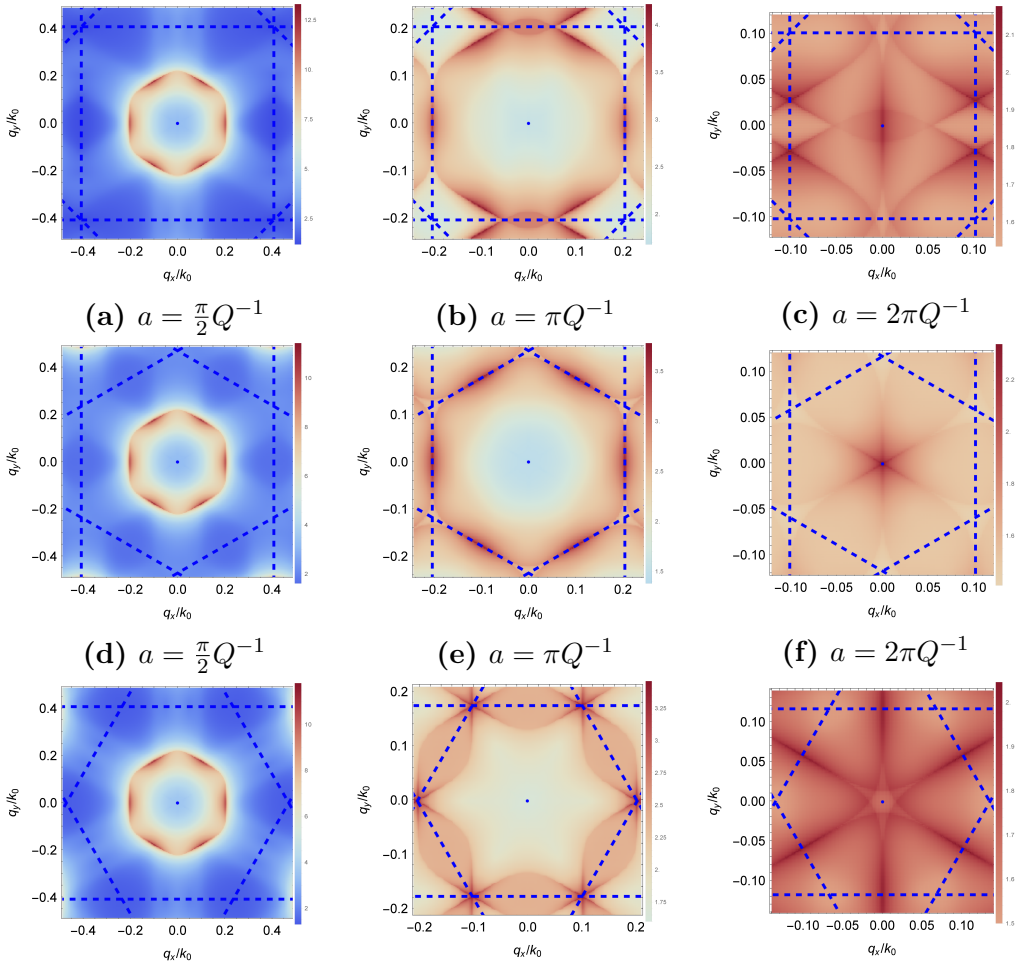

(a) $a = \frac{\pi}{2}Q^{-1}$ **(b)** $a = \pi Q^{-1}$ **(c)** $a = 2\pi Q^{-1}$

(d) $a = \frac{\pi}{2}Q^{-1}$ **(e)** $a = \pi Q^{-1}$ **(f)** $a = 2\pi Q^{-1}$

(g) $a = \frac{\pi}{2}Q^{-1}$ **(h)** $a = \frac{2\pi}{\sqrt{3}}Q^{-1}$ **(i)** $a = \frac{3\pi}{\sqrt{3}}Q^{-1}$

Figure 6.3.: The largest eigenvalue of the RKKY interaction in momentum space for different lattice structures and lattice constants a. The borders of the Brillouin zones are marked by dotted lines. **top panels**: quadratic lattice, **middle panels**: hexagonal lattice as defined in the text, **bottom panels**: by $\pi/3$ rotated hexagonal lattice. Figure reprinted with permission from *Baum et al. [2015b]*. Copyright (2015) by the American Physical Society.

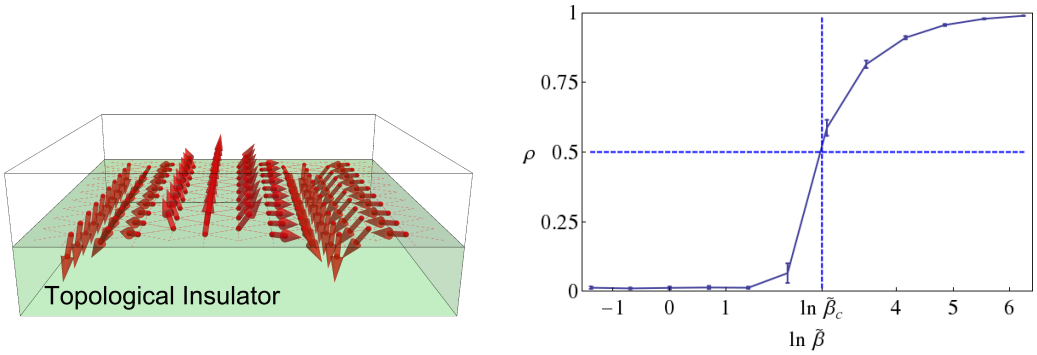

(a) Setup illustration and the spiral spin order in the ground state for an aligned hexagonal lattice of the magnetic impurities.

(b) Stability of the spiral order against normalized inverse temperature, both defined in the text. The bars signify the standard deviation induced by temperature fluctuations.

Figure 6.4.: Spatial structure and temperature stability of the spiral magnetic ground state order. Figure adapted with permission from *Baum et al. [2015b]*. Copyright (2015) by the American Physical Society.

reach local energetic minima. We find that all initial configurations relax to one of three spiral waves[4].

One manifestation of the spiral waves is illustrated in Fig. 6.4a, where we only show an excerpt of the system that encompasses exactly one magnetic unit cell into the relevant direction. The depicted spiral wave possesses the momentum Q_1. The remaining two ground state configurations are found to possess momenta Q_2 and Q_3, cf. Fig. 2.6, and are related to the depicted one by a rotation around the z axis about an angle of $\pi/3$ and $2\pi/3$ respectively. Note that each spiral wave is degenerated in phase, which is equivalent to shifting the origin of the spiral. It is important to mention that the classical superposition of the spiral spin waves does not represent a minimal energetic configuration. The reason is given by the constraint that all spins lie on spheres. A superposition of spherical vectors, however, does not generally lie on a sphere.

To determine the stability of the numerically found local minima against temperature, we start in one of the ground states and gradually decrease β. At a critical inverse temperature β_c, the thermal fluctuations destroy the spiral order. In order to depict this destruction in a simple way, we introduce the spiral order parameter $\rho = 4\pi M^{-4} \sum_{i=1}^{3} S_{Q_i}^2$, where M^2 is the number of simulated spins and Q_i are the nesting vectors. This parameter measures how much weight the three spiral ground states contribute to the total spin configuration. With regard to the constraint that

[4]We also find an amount of non-spirality in the waves which lies at around 2%. In the further discussions, we neglect this amount.

all spins lie on the unit sphere, ρ equals 1 only if the system resides in one of the spiral ground states, while it vanishes in the thermodynamic limit for an inverse temperature $\beta \to 0$. For a finite number of simulated spins, the infinite temperature value of the order parameter is $\rho = 12\pi^2/M^4$.

The dependence of ρ on the normalized inverse temperature $\tilde{\beta} = \beta J_0^2 \hbar^4 k_0^2/(V_{uc} E_0)$ is shown in Fig. 6.4b for $M = 16$. For $\tilde{\beta} \to \infty$, the system resides in one of the ground states and hence $\rho = 1$. Increasing temperature, the system gets perturbed and ρ decreases. For $\tilde{\beta}_c \approx 15$, ρ falls below, 1/2, which we define as the limit of domination of the physical properties of the system by the ground state.

We therefore identify $\beta_c = \tilde{\beta}_c V_{uc} E_0/(J_0^2 \hbar^4 k_0^2)$ as the experimentally relevant inverse temperature of a phase transition from a spirally ordered to an unordered state. Up to our knowledge, there is at the moment neither experimental nor first principles data for the magnetic couplings J_0 on the surfaces of strong topological insulators. We therefore estimate values of the exchange coupling J_0 in an order of magnitude approximation by considering an exchange energy of the order of $0.1 - 1\text{eV}$ per unit cell of the topological insulator. This yields $J_0 \approx 10 - 10^2 \text{meVnm}^2/\hbar^2$. We furthermore consider a lattice constant of $a = 1\text{nm}$, which has been achieved and even been underbid in recent experiments *[Nadj-Perge et al., 2014; Polini et al., 2013]*. Finally, we allow for k_0^2/E_0 ranging from $1.5\text{eV}^{-1}\text{nm}^{-2}$ for Bi_2Te_2Se to $3.8\text{eV}^{-1}\text{nm}^{-2}$ for Bi_2Te_3, which we take from the table in *Jiang & Wu [2011]*. With these values, the critical temperature T_c lies between $0.12K$ and $30K$.

6.1.5. The electronic spectrum in the broken symmetry phase

We now turn our attention towards the surface electrons. In order to find the electronic spectrum in the broken symmetry phase, i.e., when the magnetic impurities are arranged in their spiral ground state order, we adopt a mean field approach where we treat the spin wave as the background magnetization for the electrons. This yields the following single particle Hamiltonian for the quasi particles:

$$\begin{aligned} H =& H_0 + H_m, \\ H_m =& m \boldsymbol{S}(\boldsymbol{r}) \cdot \boldsymbol{\sigma}, \end{aligned} \tag{6.8}$$

where H_0 is given in Eq. (2.13), and $\boldsymbol{S}(\boldsymbol{r})$ is the spiral spin wave

$$\boldsymbol{S}(\boldsymbol{r}) = \boldsymbol{U} \cos(\boldsymbol{Q} \cdot \boldsymbol{r}) + \boldsymbol{V} \sin(\boldsymbol{Q} \cdot \boldsymbol{r}), \tag{6.9}$$

which is characterized by one of the nesting vectors $\boldsymbol{Q}$ and the two perpendicular unit vectors $\boldsymbol{U}$ and $\boldsymbol{V}$. For simplicity, we choose $\boldsymbol{Q}$ to be the nesting vector in the x direction, i.e., $\boldsymbol{Q} = 2k_F(1,0,0)^T$. Exploiting the periodicity in the x direction, this Hamiltonian can be solved by using Bloch's theorem, to yield the band structure. For the numerical implementation, we truncated the Hamiltonian such that the number of bands is 28. Taking further bands into account does not change the

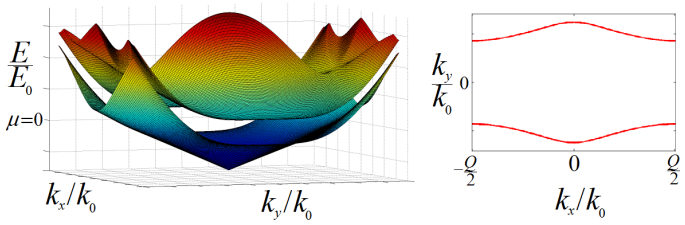

Figure 6.5.: The electronic spectrum and the Fermi surface in the broken symmetry phase. Energy and momentum are measured in units of E_0 and k_0 respectively. A magnetic gap is opened in parts of the Fermi surface. Figure printed with permission from Yuval Baum.

band structure close to the Fermi energy significantly in our simulations. The band structure near the chemical potential and the Fermi surface is shown in Fig. 6.5, where k_x is restricted to the first Brillouin zone. Clearly, a magnetic gap is opened in parts of the Fermi surface.

It is now natural to ask how the altered electronic spectrum in turn influences the RKKY interaction. In fact, the two quantities should be determined self-consistently. However, the backaction of the magnetization on the electronic spectrum already is a second order effect in the coupling between the itinerant excitations and the magnetic dopants J. If we choose J to be sufficiently small compared to the energy scales governing the electronic degrees of freedom, we expect to obtain a good approximation without taking higher orders of J into account. We still consider the self-consistent treatment an interesting branch to follow in future research, cf. Chapter 8.

6.1.6. Proximity to a conventional s-wave superconductor

In this section, we shortly describe how the proximity to a conventional s-wave superconductor alters the broken symmetry phase. The electronic Hamiltonian assumes the form

$$H = H_0 \otimes \tau_z + H_m \otimes \tau_0 + \Delta\tau_x, \tag{6.10}$$

where the symbol τ denotes the Pauli matrices in particle-hole space, cf. Section 2.3. In the limit of an infinite (or periodic) system, we can use Bloch's theorem to yield the band structure. The band structure near the chemical potential for both $\Delta < m$ and $m < \Delta$ appear in Fig. 6.6a and Fig. 6.6b.

While for $m < \Delta$ the spectrum is fully gapped, there are four Dirac-nodes in the spectrum at the edges of the first Brillouin zone for $\Delta < m$. Out of the four depicted Dirac nodes, only two are distinct, i.e., not connected by a reciprocal lattice vector. The described spectra serve a first example to demonstrate a more general mechanism that causes the creation of a gapless topological superconductor. In the following Section 6.2, we will isolate this mechanism and explain its physical

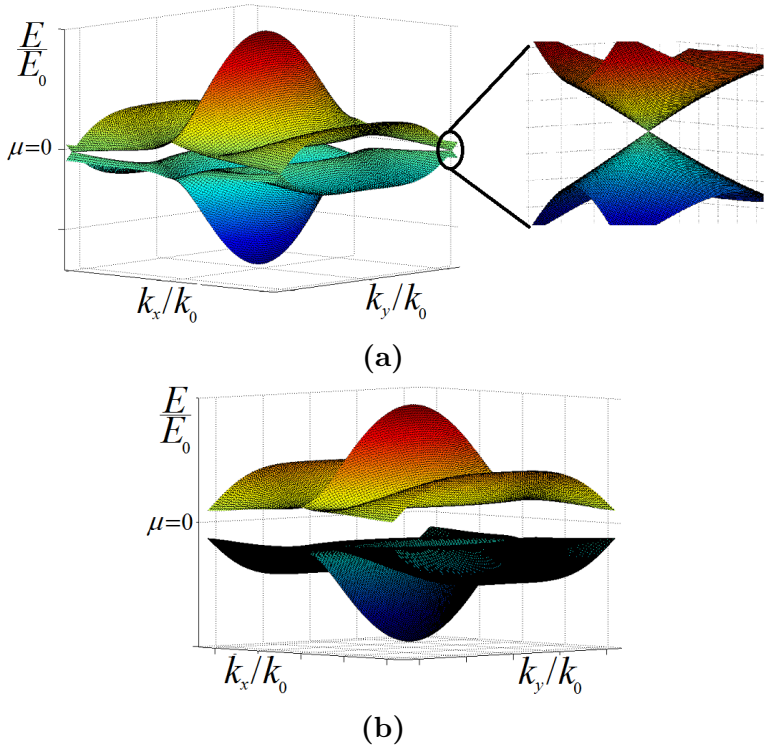

Figure 6.6.: The electronic spectrum of Eq. (6.10). The momentum k_x is restricted to the first Brillouin zone. (a) The spectrum for $\Delta < m$. The spectrum is not gapped. Two Dirac nodes appear at the edges of the Brillouin zone. (b) The spectrum for $m < \Delta$. The spectrum is fully gapped. Figure printed with permission from Yuval Baum.

consequences. We will find that the spiral magnetic order in combination with the spin-momentum locking of the itinerant excitations plays the most important role and that we can assume the superconductivity to be comparably weak.

6.2. General scheme for gapless topological superconductors

In this section, we present a scheme of generating an intrinsically gapless superconducting phase of symmetry class D *[Kitaev, 2009; Schnyder et al., 2008]*, which simultaneously hosts gapless Dirac modes in the bulk and well localized, propagating, one-dimensional modes, also known as chiral Majorana edge states *[Fu & Kane, 2008]*.

This phase is distinct from previous proposals. In addition, it is distinct from the hybrid systems that will be introduced in Chapter 7. First, it emerges from intrinsic degrees of freedom as opposed to relying on an engineered coupling between topological phases and gapless ones. Second, it may spontaneously form on the surface of three dimensional topological insulators, which provides a new experimental route for realizing and probing gapless topological phases. Finally, the chirality of its edge modes depends on disorder in an unusual manner. We suggest a concrete example of this phase: a two-dimensional electron gas (2DEG) with Rashba spin-orbit coupling in the presence of a modulated magnetization and proximity-induced s-wave superconductivity. We analyze the spectral properties and the thermal conductance of the system in the absence and presence of disorder and small Zeeman fields. More details on the method of our simulations are given in Section 3.5. It is important to emphasize that we are interested in thermal and not in charge transport properties. This is ultimately attributed to the fact that both gapped and gapless superconductors are perfect conductors of charge, while their thermal conductance is markedly different. In particular, we refer to the quantum of thermal conductance $G_0 = \pi^2 k_B^2 T_0/(6h)$, where T_0 is the temperature of the system.

The systems that are introduced in this chapter, share a couple of similarities with the hybrid systems of Chapter 7. One example is that, in the clean case, Dirac excitations in the bulk coexist with two types of edge states, depending on the edge orientation, i.e., along which angle the straight edge is aligned in the two-dimensional system. For most orientations, we identify "strong" edge states that do not hybridize with the bulk states due to energy and momentum conservation. Their wave functions remain exponentially localized near the edge despite the absence of a bulk gap. For some orientations, this is not the case, and the edge states wave functions leak into the bulk, making the edge modes "weak". Surprisingly, we find that the structure of the edge states crucially depends on the terminal orientation of the magnetization at the edge of the system. Specifically, for certain terminations,

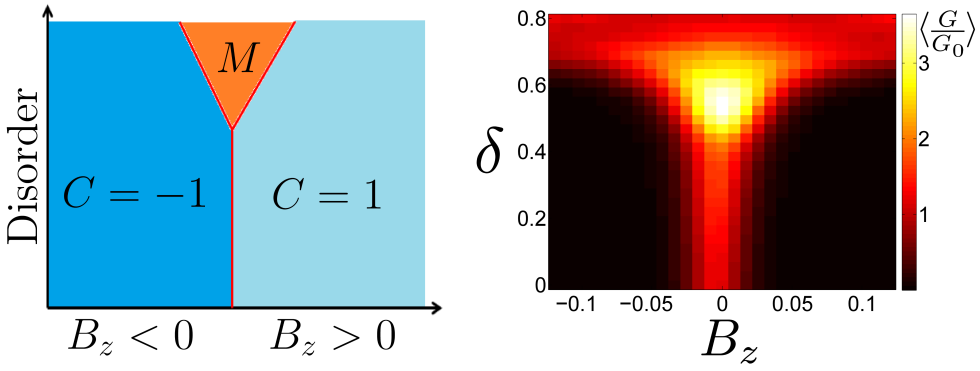

(a) **(b)**

Figure 6.7.: (a) Phase diagram as a function of Zeeman field B_z and disorder strength δ. Phase transitions are shown in red. M denotes a metallic phase which typically forms in a disordered two- dimensional superconductor *[Chalker et al., 2001]*. (b) Disorder averaged bulk thermal conductance of the model in Eq. (6.13). The calculation is done in a two-terminal setup with periodic boundary conditions. The lattice size is 80×80, and the parameters are $m = 0.2$ and $\Delta = 0.14$. Each point is obtained by averaging over 50 independent realizations of disorder. Figure reprinted with permission from *Baum et al. [2015b]*. Copyright (2015) by the American Physical Society.

the intrinsic origin of the edge states leads to a disorder induced inversion of the edge state chirality.

The inclusion of a uniform Zeeman field that is aligned perpendicularly to the 2DEG, B_z, leads to a gap opening in the bulk spectrum, and the gapped system possesses a non-trivial Chern number, cf. Section 2.1, which has the same sign as B_z. Thus, the gapless phase at $B_z = 0$ is a transition between two topologically distinct insulating phases. In the presence of disorder, the non-trivial Chern number of the system implies delocalized[5] edge states and localized bulk states. At the transition between different Chern numbers, the bulk gap must close, such that the phase diagram in the space of disorder and gap-opening perturbation contains a critical line, where the bulk states remain delocalized. The topological phase transition occurs at $B_z = 0$ also in the presence of weak on-site potential disorder, leading to the phase diagram sketched in Fig. 6.7a. Starting from the gapless point in the clean limit and increasing disorder strength, the system remains critical; the bulk states remain delocalized while the edge states disappear.

[5]Here, we refer to "localized" and "delocalized" in the sense and context of Anderson localization and not in the sense of being exponentially localized to the edge of a system. It is unfortunate, but due to the habitual use of language unavoidable, that the same word is utilized with two different meanings.

6.2.1. Model

It was originally shown by *Fu & Kane [2008]* that when a region of a 3DTI surface is proximity-coupled to a ferromagnet and another neighboring region is proximity-coupled to an s-wave superconductor, then one-dimensional gapless states must exist at the interface between these two regions. Both the ferromagnet and the superconductor induce a gap in the spectrum of the TI surface. The region in space where the gap changes its nature – from a magnetically induced gap to a superconductivity-induced gap – is the region that hosts the gapless mode. Here, we consider a momentum-space-analogous scenario in which the nature of the gap changes in the two-dimensional Brillouin zone. We show that this construction dictates the existence of gapless excitations in the two-dimensional bulk, which are localized in momentum space and extended in real space.

The scheme we consider is based on a family of two-dimensional Hamiltonians of the type,

$$H = H_0 + H_{\mathrm{m}} + H_{\mathrm{SC}}, \tag{6.11}$$

where:

1. H_0 represents a Hamiltonian of spinful electrons, where spin-orbit coupling breaks the degeneracy of the two spin directions for a given momentum. For concreteness, we take a 2DEG with Rashba spin-orbit coupling

$$H_0 = \left[t\left(2 - \cos ak_x - \cos ak_y\right) - \mu\right]\sigma_0 + \lambda\left(\sigma_x \sin ak_x - \sigma_y \sin ak_y\right), \tag{6.12}$$

   where t is the hopping amplitude, μ is the chemical potential, λ is the spin-orbit strength, a is the lattice constant, and the σ_i's are the Pauli matrices in spin space. This Hamiltonian has two circular Fermi surfaces, an inner and an outer one[6].

2. H_{m} is a Zeeman coupling to a spatially periodic magnetization, characterized by a wave-vector $\mathbf{Q}$, that opens a gap in parts of the Fermi surface. For concreteness, we take $H_{\mathrm{m}} = m\sigma_z \cos Qx$, with $Q = 2k_F$, where k_F is the Fermi momentum of the outer Fermi surface.

3. $H_{\mathrm{SC}} = \Delta\psi_{\mathbf{k},\uparrow}\psi_{-\mathbf{k},\downarrow} + \mathrm{H.c.}$ is a superconducting s-wave pairing, with $\psi_{\mathbf{k},\sigma}$ being the annihilation operator of a quasi-particle with spin σ and momentum $\mathbf{k}$, and Δ is the induced pairing potential, cf. Section 2.3.

[6] For the special chemical potential $\mu = 0$, the inner Fermi surface is only a point and is gapped by superconductivity. Therefore, we do not expect it to contribute to any of the here observed effects.

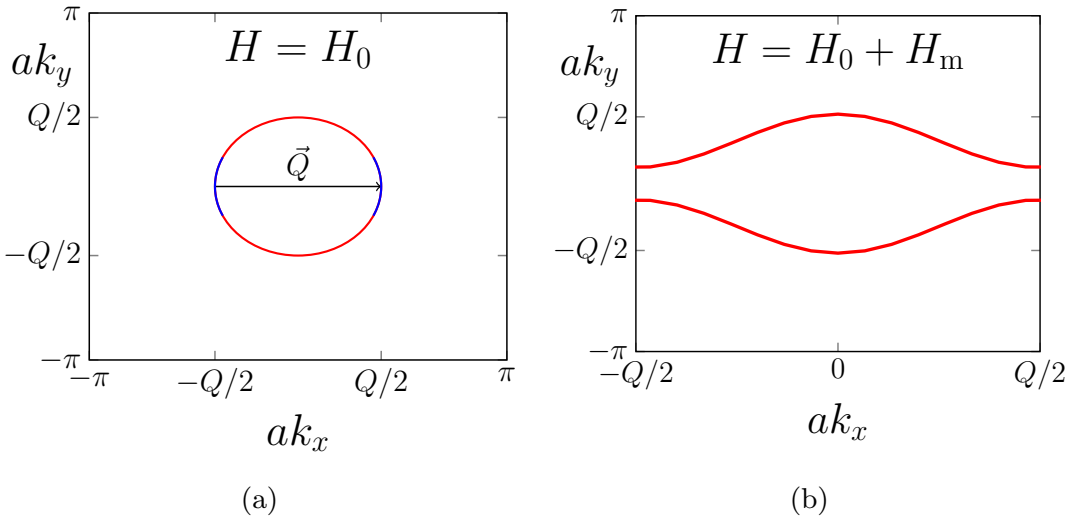

Figure 6.8.: The Fermi surface that arises from H: (a) the blue curves denote regions of the outer Fermi surface that will be gapped by the magnetization and the red curves denote regions that will be gapped by superconductivity. (b) H_m defines a new Brillouin zone and leads to an open Fermi surface. The addition of superconductivity gaps out the remaining Fermi surface except for four discrete points, as shown in Fig. 6.9a. Figure reprinted with permission from *Baum et al. [2015b]*. Copyright (2015) by the American Physical Society.

In the absence of superconductivity, the periodic magnetization, H_m, defines a Brillouin zone of size $|\mathbf{Q}|$ along the direction of $\mathbf{Q}$, and opens a gap at some of its edges[7]. For $|\mathbf{Q}|\sim 2k_F$, where k_F is the Fermi momentum, an open Fermi-surface develops. The effect of superconducting pairing, H_SC, depends on its strength. Strong pairing ($|\Delta|> |m|$) renders the entire Fermi surface superconducting, and destroys the effect of the magnetization. Weak superconductivity ($|\Delta|< |m|$), on the other hand, leads to the aforementioned situation where one part of the Fermi surface is gapped by the magnetization and the other part is gapped by superconductivity. Therefore, the nature of the gap changes along a path in momentum space that follows the original Fermi surface, and the gap is closed at the point of change. The development of the different gaps is illustrated in Fig. 6.8 to Fig. 6.9a.

By introducing the Nambu basis, $(\psi_\uparrow^\dagger, \psi_\downarrow^\dagger, \psi_\downarrow, -\psi_\uparrow)$, as in Section 2.3, the full Bogoliubov-de Gennes Hamiltonian becomes

$$H = H_0\tau_z + H_\mathrm{m}\tau_0 + \Delta\sigma_0\tau_x, \tag{6.13}$$

where the τ_i's are Pauli matrices in particle-hole space. The model obeys a particle-

[7]For the practical calculation, we assume that the magnetic periodicity is commensurate with the lattice periodicity.

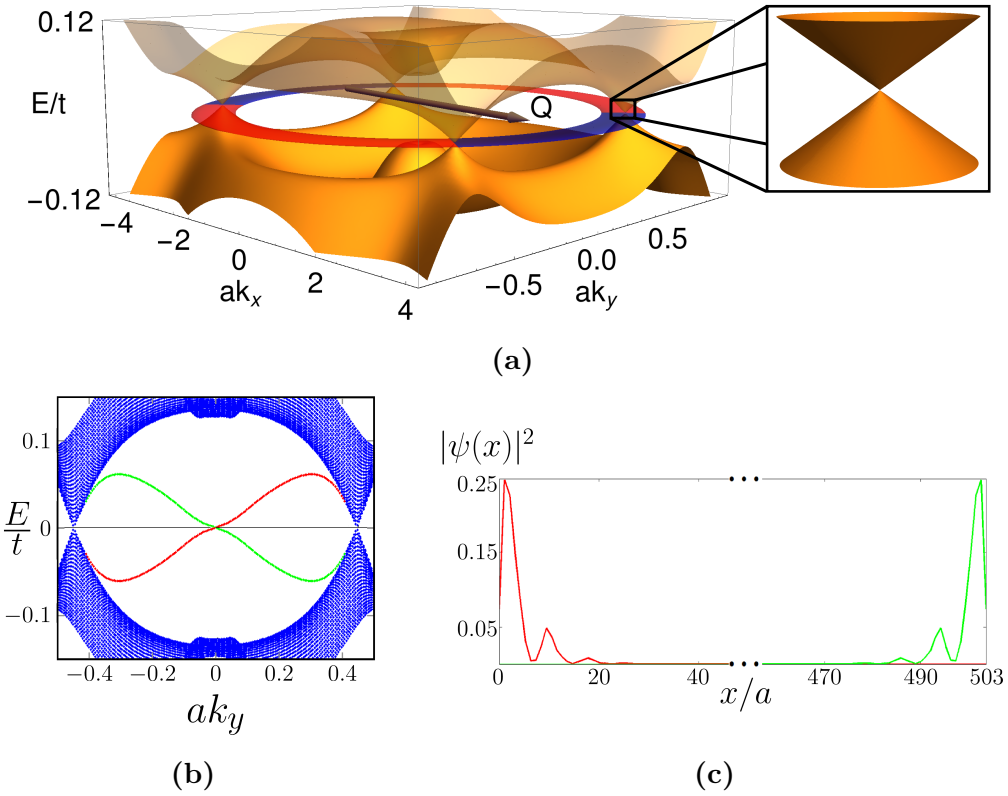

Figure 6.9.: Band structure of the Hamiltonian, Eq. (6.11), with **(a)** periodic boundary conditions. The red and blue regions are gapped by the superconductor and the magnetization, respectively, cf. Fig. 6.8. **(b)** An edge along the y direction. Gapless edge states (red, green) coexist with the bulk nodes (blue). **(c)** Typical edge state wave functions. Figure reprinted with permission from *Baum et al. [2015b]*. Copyright (2015) by the American Physical Society.

hole symmetry $\mathcal{P} = \sigma_y \tau_y \mathcal{K}$, $\mathcal{P}^2 = 1$, with $\mathcal{K}$ signifying complex conjugation, but, due to the magnetic field, no time reversal symmetry and consequently no chiral symmetry. Therefore, the model belongs to symmetry class D, cf. Section 2.1 and *[Schnyder et al., 2008]*, which has a topological classification according to $\mathbb{Z}$ in two spatial dimensions.

6.2.2. Results

In the following, we discretize the Hamiltonian of Eq. (6.13) on a square lattice of $L_x \times L_y$ sites, setting $t = a = 1$, $\mu = 0$ and $\lambda = \sqrt{2}-1$, which gives $Q = \frac{\pi}{2}$. The band structure near the Fermi level for $|\Delta| < |m|$ is shown in Fig. 6.9a. There are two distinct Dirac nodes in the spectrum at the edges of the first Brillouin zone. Adding a small uniform Zeeman field, B_z, leads to a mass gap at the two Dirac cones. The

gapped system is a class D superconductor with a Chern number $C = \mathrm{sgn}\,(B_z)$. In contrast, for $|\Delta| > |m|$, the spectrum is fully gapped (not shown), with $C = 0$ for any $|B_z| < |\Delta|$. For $B_z = 0$ and in the presence of boundaries, we find weak edge states when the boundary is along the x-direction and strong edge states for all other orientations of the edge. The spectrum of the system with boundaries along the y-direction and for $\Delta < m$ appears in Fig. 6.9b. Beside the two bulk nodes at finite k_y, there are well localized (strong) chiral edge modes.

We find that the edge mode properties are not determined uniquely by the edge's orientation. The modulated nature of the magnetization additionally leads to a dependence on the termination of the lattice. For the parameters we chose, the magnetization wave vector is $\boldsymbol{Q} = (\pi/(2a), 0)$, i.e., the magnetization is periodic along the x direction with a periodicity of four sites. Hence, there are four different ways to terminate the lattice in the x direction. We label them according to the magnetization of the last two sites: $(0,+)$, $(+,0)$, $(0,-)$ and $(-,0)$. For a different choice of magnetic periodicity, the size of the unit cell changes but the physics remains similar. The dependence of the edge states on the termination is shown in Fig. 6.10a, where the spectrum of a system with an edge along the y direction is plotted for the four different terminations. Blue points denote bulk states and the other colors denote the right edge state. The left edge state is fixed in the $(0,+)$ termination and is not shown. Both the dispersion and the chirality of the edge state change as the termination changes. Nonetheless, as long as particle-hole symmetry is preserved, the chirality remains non-zero, since the latter is determined solely by the imbalance between right and left movers that cross the line of zero energy. Notice, that for two terminations the edge states cross the Fermi level three times, once at $k_y = 0$ and twice, with an opposite velocity, close to the bulk nodes. Hence, the chirality is determined by the edge states in the vicinity of the bulk nodes.

We confirm the dependence of the edge modes' chirality and their contribution to the thermal conductance on the edge orientation and the termination of the lattice by performing transport simulations. Using a three-terminal geometry, we separate bulk and edge contributions to transport. For details about the calculations, we refer to Section 3.5. The simulations are done in the clean limit as well as in the presence of disorder, which we model as a random spatial variation of the chemical potential, which is chosen to lie within $[-\delta, \delta]$ uniformly distributed and independently for each lattice site, with δ being the disorder strength. The qualitative results do not depend on the type of disorder, as long as the disorder correlation length is much shorter than the system size and as long as particle-hole symmetry is preserved. In the presence of weak disorder, the contribution of the chiral edge states to the thermal conductance is slightly reduced due to hybridization of the edge modes with the bulk. For moderate disorder, the edge states at finite momenta hybridize strongly with the bulk nodes, as opposed to the edge states at small momenta. Therefore, beyond a certain disorder strength, the edge states around zero momentum dominate the transport, leading to a unique inversion of the edge state chirality, which is

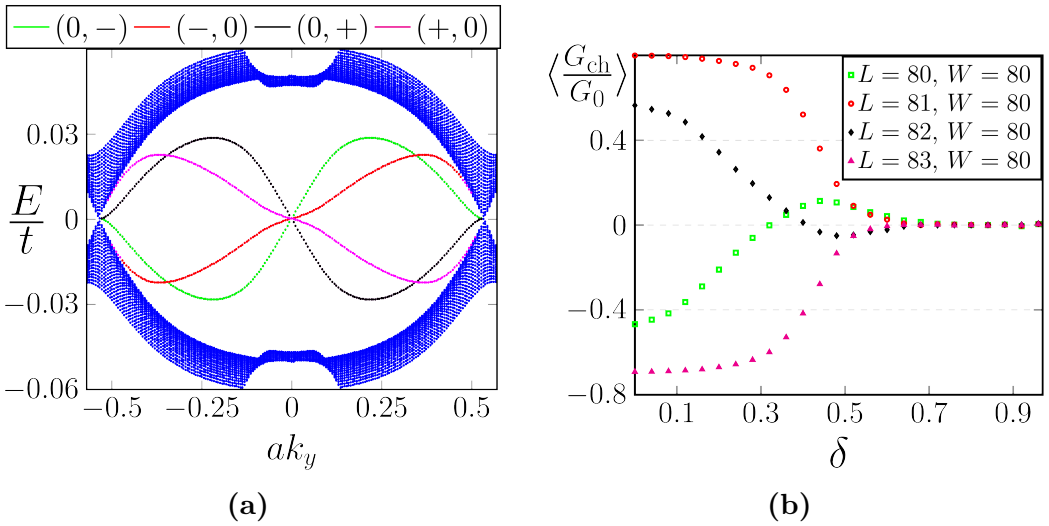

Figure 6.10.: **(a)** The spectrum of a system with an edge along the y direction for all possible terminations. The colors in the legend denote the right edge state. **(b)** Strong edge contribution, $G_{\mathrm{ch}} = G_{RL} - G_{LR}$, to the thermal conductance as a function of disorder strength δ. We use $m = 0.1$ and $\Delta = 0.05$. For $\delta = 0$, the chirality of the edge states changes in dependence on the termination and on disorder. Figure reprinted with permission from *Baum et al. [2015b]*. Copyright (2015) by the American Physical Society.

induced by disorder (see Fig. 6.10b). As the disorder strength is further increased, all contributions of the edge states to the thermal conductance vanish as the system enters a thermal metal phase.

In the thermodynamic limit and for clean systems, the contribution of the strong edge states to the thermal conductance becomes quantized as Fig. 6.11a shows. In contrast, the contribution of the weak edge states vanishes as a function of the system size, see Fig. 6.11b. There exists an intuitive explanation why the weak edge states hybridize so effectively, especially compared to the models introduced in Chapter 7: In this model, the coupling between the edge and bulk states depends on the normal and superconducting parameters of the model and therefore cannot be independently tuned. The energy scales that correspond to these parameters are large compared to the topological gap scale, $|\Delta| - |m|$, and therefore the weak edge states hybridize effectively. In the presence of a uniform Zeeman field B_z, the dependence on the termination disappears and the chirality is solely determined by the sign of B_z. We plot the bulk thermal conductance of the system as a function of B_z and the disorder strength δ in Fig. 6.7b. The calculated phase diagram agrees nicely with the theoretical expectation of Fig. 6.7a. In the following, we provide an illustrative model aiming to intuitively explain the dependence on the termination

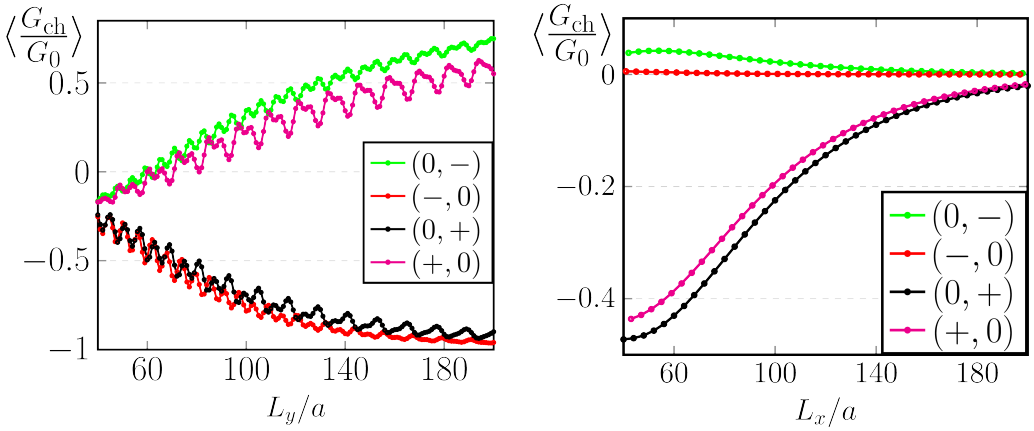

Figure 6.11.: Edge contribution, $G_{\rm ch}$, to the thermal conductance in the absence of disorder ($\delta = 0$) as a function of the system size, for the different terminations. Here, $m = 0.1$ and $\Delta = 0.05$. **(a)** Strong edge states. While their chirality depends on the termination, their contribution to the thermal conductance approaches unity. **(b)** Weak edge states. Independently of the termination, their contribution approaches zero. Figure reprinted with permission from *Baum et al. [2015b]*. Copyright (2015) by the American Physical Society.

of the lattice.

6.2.3. Intuitive model in the small Q limit

Some of the main properties of the system can be explained by an intuitive model, which is based on the limit of a slowly varying magnetization, i.e., the small Q limit. This intuitive explanation gives physical insight into the formation of strong and weak edge states. Furthermore, it indicates the observed change in chirality depending on the lattice termination. However, it should be pointed out that we provide this cartoon model solely to aid the development of intuition. Although it shows features similar to the ones of the model given in Section 6.2.1, the concrete physics can eventually not be extrapolated from the small Q limit since the here established real space picture (cf. Fig. 6.12) breaks down as Q becomes comparable to $k_{\rm F}$.

The dependence of the strong edge states on the magnetic termination may be understood intuitively from the small Q limit. It was shown by *Sau et al. [2010]* that the combination of a Rashba spin-orbit coupling, an s-wave superconducting pairing, Δ, and a uniform Zeeman field, B_z, leads to a two-dimensional class D topological superconductor with a well defined Chern number. The value of the

Chern number is sgn(B_z) for $|\Delta| < |B_z|$ and zero for $|\Delta| > |B_z|$. In the limit of small Q, the Hamiltonian of Eq. (6.11) can be locally thought of as a system subjected to a uniform Zeeman field. Thus, we can think about the system in real space as stripes of superconductors, with alternating Chern numbers, connected in series alongside their long edges. Edge states flow where the Chern numbers change. Ignoring the gapped bulk states of each stripe, we may view the system as a collection of one-dimensional chiral Majorana channels, which we illustrate in Fig. 6.12. We assume only a nearest neighbor coupling between these chiral channels, such that channels with the same chirality are coupled by t_s (symmetric coupling) and that channels with an opposite chirality are coupled by t_a (anti-symmetric coupling), and obtain the two-dimensional band structure of the system, if we assume that it is infinitely large. If the symmetric coupling is the dominant coupling, i.e., $|t_s| > |t_a|$, each two neighboring Majorana channels with similar chirality form a single fermionic chiral channel. Coupling fermionic channels with an alternating chirality through a coupling t_a leads to a gapless phase with two Dirac cones in the two-dimensional Brillouin zone. In this regard, the gapless bulk states in our original model can be understood as the band structure emerging from $|t_s| > |t_a|$. The strong edge states are then a remnant of the channels near the edge, and their nature depends periodically on the termination. Consistent to our findings in Section 6.2.2, the chirality of the edge states in this picture also depends periodically on the termination and changes sign with a period of two stripes.

Adding a uniform Zeeman field on top of this picture leads to an asymmetry between regions with different Chern numbers. Depending on the sign of the Zeeman field, the size of the regions with a given Chern number increases while the size of the regions with the opposite Chern number decreases. In the picture of the one-dimensional chiral channels, this can be thought of as dimerization of channels. Hence, a single Chern number prevails in the system.

6.2.4. Conclusions about magnetically doped 3DTI in proximity to a superconductor

We show that magnetic impurities, which are placed on a lattice on the surface of a strong three-dimensional topological insulator with warping form a magnetic spiral in the ground state of the system, which is considerably stable against the influence of temperature. The wave vector of the hereby possible spirals is engineerable according to the needs by altering the chemical potential or the lattice structure of the magnetic impurities. However, our findings indicate, that above a certain density of magnetic dopants, the developed spiral order is of a generic kind, i.e., it is independent of the lattice structure and the lattice constant of the magnetic impurities. Therefore, we assume that our findings also hold for randomly distributed magnetic surface dopants. This in turn opens realistic opportunities that the described effects can be

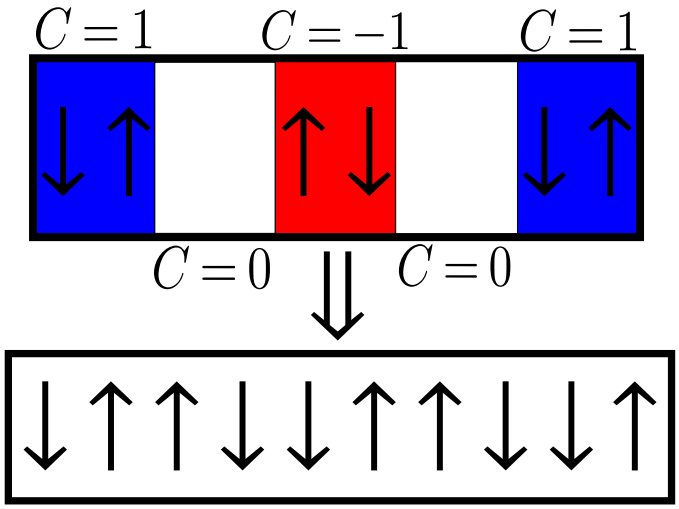

Figure 6.12.: Illustration of the connection of our findings to *Sau et al. [2010]* in the limit of small Q. Upper part: the system, in real space, is described as stripes of superconductors, with alternating Chern numbers, connected in parallel. The chiral Majorana edges states of each stripe are depicted by arrows. Lower part: the gapped bulk states of each stripe are ignored, and the system may be thought of as a collection of one-dimensional chiral channels connected in series and coupled by nearest neighbor coupling. Figure reprinted with permission from *Baum et al. [2015b]*. Copyright (2015) by the American Physical Society.

experimentally observed systems in the near future.

Subsequently, the spiral magnetization is employed to generate a peculiar gapless topological superconductor by bringing the surface into proximity to an s-wave superconductor. We extract the mechanism, which lies behind the build-up of this gapless topological superconductor, and generalize it to systems that exhibit spin-momentum locking and a spatially periodic magnetization. Thereby, we are able to describe general features of the phase in the presence of disorder. One of these features is the dependence of the edge states' chirality on the termination of the lattice.

The gapless topological superconductors unify two seemingly incompatible features of a topological system: (i) well localized edge states and (ii) a gapless bulk spectrum. However, the described systems are complex and rely on an involved interplay of nontrivial magnetism and superconductivity. Therefore, we posed ourselves the question: is it possible to generate such ambivalent systems on a simpler and more general footing, also in the absence of superconductivity? In fact, as we describe in the following Chapter 7, the basic idea of coupling a gapped topological phase to a gapless semimetal suffices to construct these interesting electronic phases.

It has to be mentioned, though, that the idea of hybrid systems is not able to give the complete foundation of the phase presented in the present Chapter 6.2. The gapless phases built by the interplay of magnetism and superconductivity emerge from intrinsic degrees of freedom as opposed to relying on an engineered coupling between two hybridized systems. Therefore, an exact mapping of the former systems to hybrid models seems to be impossible. A particular feature that remains unexplained by the approach of hybrid systems is the chirality change of the edge modes in dependence on disorder.

7. Hybrid systems of topological and semimetallic phases

This chapter is a revised version of *Baum et al. [2015a]* and its supplemental material, copyrighted by the American Physical Society. Also regard the remarks on page 3.

In this chapter, we present several examples of two-dimensional models that simultaneously host well-localized, gapless one-dimensional modes on the edge and a gapless two-dimensional bulk spectrum. Such systems may be constructed, for example, by coupling a gapped two-dimensional state of matter that carries edge states to a gapless two dimensional system in which the spectrum is composed of a number of Dirac cones. The existence of this phase is counter-intuitive and in fact defies one of the main principles of topological insulators, namely the instability of the edge states for systems with a gapless bulk spectrum. A concrete example of the generic scenario is given in Section 2.1.1, where the described simple toy model exhibits exponentially well localized edge states in the regime of a negative gap, the localization length of which is inversely proportional to the size of the gap. If the gap is closed, the localization length of the edge states consequently diverges and, for any finite sample size, hybridizes with the edge state from the opposite edge. During this process, the characteristics of a topological insulator are gradually lost. The phases that are discussed here do not suffer from this drawback. In contrast, the topological energy scale, as reflected in the localization length of the appearing edge states, is independent of the bulk gap. Furthermore, the edge states possess unique properties that distinguish them from non-topological edge states. Most notably, they are either chiral or helical and intimately related to properties of the bulk.

We find that, in the absence of disorder, the edge states can be protected even when the two systems are coupled, as a cause of momentum and energy conservation. Here, all models that we consider share similar spectral and transport characteristics, showing distinct bulk and edge contributions that do not mix. We explicitly distinguish between weak and strong edge states by the level of their mixing with the bulk. The presence of disorder unravels the difference between the presented models. In some of the models, where the bulk is localized, disorder stabilizes the edge modes and decouples them from the bulk, while in others, where the bulk remains metallic, it completely mixes the two. We analyze the conditions under which these two cases occur. Similarly, the different nature of the different models is revealed

when we introduce weak perturbations that open energy gaps in the spectrum. We provide concrete Hamiltonians for models based on coupling a gapless phase to a topological phase, for example, in a bilayer system, and analyze their spectral and transport properties. Beyond that, we propose a concrete physical realization based on a bilayer Hg(Cd)Te quantum well. Note that the systems we consider share the lack of a bulk energy gap with Weyl semimetals and nodal superconductors *[Matsuura et al., 2013; Queiroz & Schnyder, 2014]*, but are distinguished from them by being two-dimensional and by having no topological protection to the gapless nature of the bulk. Additionally, the edge states that appear in those phases, are mostly flat (Majorana) bands, especially for the nodal superconductors, and Fermi arcs. The edge states we find here, obey a linear dispersion at a touching point at a momentum different than the momenta of bulk gap closure and inherit the properties of the edge states from the topological insulator that participates in the respective hybrid system.

The edge properties in gapped topological states of matter can be studied through the local density of states (LDOS) *[Chen et al., 2009; Hasan & Kane, 2010; Hsieh et al., 2009a; Qi & Zhang, 2011]*. At energies smaller than the bulk energy gap, the LDOS is non-zero at the edge, and decreases exponentially as a function of the distance from the edge. Due to the absence of a bulk gap, this is not the case for the systems we consider, and we therefore have to employ different methods for studying the edge. For the clean case, we study a cylindrical geometry, in which the lattice momentum parallel to the edge, $k_{||}$, is a good quantum number. We find two types of edge states, which we call strong and weak. Strong edge states carry a momentum $k_{||}$ and an energy $\epsilon(k_{||})$ for which there are no bulk states. Their wave functions are exponentially localized near the edge with the localization length being inversely proportional to the bulk gap at $k_{||}$. Weak edge states occur when for all values of $k_{||}$ and energies $\epsilon(k_{||})$ for which there are states at the edge, there are also states in the bulk. The edge states then easily hybridize with the bulk states, and their wave functions are not exponentially localized. We find that the "strength" of the edge mode depends on the orientation of the edge. For the models we consider, there are only a few orientations in which the edges are weak.

The edge states are also reflected in transport *[Bernevig et al., 2006; Hasan & Kane, 2010; Hsieh et al., 2009a,b; König et al., 2007; Qi & Zhang, 2011]*. We distinguish between edge versus bulk transport by studying transport in devices of two terminals with both periodic and hard wall boundary conditions. This method is useful also in the presence of disorder, where states are not characterized by their momentum. Generally, in gapped phases with a non-trivial topological index, edge state transport is robust as long as the relevant energy scales for transport are smaller than the bulk gap. Remarkably, for the systems we consider, the bulk gap vanishes, and yet the edge state transport may still be robust. In particular, we find that disorder may even stabilize the edge state transport.

The effect of disorder on the systems we consider may be inferred from the effect

of a translationally invariant perturbation that opens a gap in the bulk spectrum. Such a perturbation makes the system acquire a well-defined topological index. When the topological index is a Chern number whose value does not depend on the perturbation that opens the gap, the gapless phase is a transition between two insulating phases with the same Chern number. Then, in the presence of disorder, the bulk states may become localized and the edge states stabilize. In contrast, when the value of the Chern number depends on the sign of the perturbation, then the gapless phase separates two topologically distinct insulating phases and the phase diagram in the space of disorder and gap-opening perturbation must contain a critical line, where the bulk states remain delocalized and the edge states disappear. Away from the critical line, the system is a well-defined Chern insulator. For cases where the topological index is not a Chern number, the localization properties of the bulk and edge states depend on the symmetries of the specific model.

7.1. The four models

We now introduce four models that share the same behavior in the absence of disorder, namely the coexistence of edge states and a gapless bulk, but strongly differ away from that point. The models we consider are based on a designed coupling between a gapped two-dimensional topological phase H_1 and a gapless two-dimensional phase H_2. The simplest example would be a bilayer system in which the two layers are described by the Hamiltonians H_1 and H_2 which are tunnel-coupled by H_c. The combined Hamiltonian can then be written as

$$H = \begin{pmatrix} H_1 & H_c \\ H_c^\dagger & H_2 \end{pmatrix}. \tag{7.1}$$

Here, the topological phase H_1 is an insulator or a superconductor with a non-trivial topological index. For simplicity, we assume that the gap of H_1 constitutes the largest appearing energy scale. The Hamiltonian H_2 is gapless, for example, having a Dirac spectrum. The coupling H_c is chosen such that the full Hamiltonian remains gapless. The different blocks should be combined such that the full Hamiltonian is irreducible, and hence belongs to a symmetry class according to *Schnyder et al. [2008]* and Section 2.1.2. In general, the symmetry class of the full Hamiltonian is given by the minimal symmetry of H_1 and H_2, although, by fine tuning parameters, the resulting Hamiltonian may accidentally obey additional symmetries.

In the first three models, H_1 describes a quantum Hall state with a non-zero Chern number, while H_2 describes three gapless phases that follow three different symmetries. As a consequence of the different symmetries, the effect of disorder on the three systems is markedly different. Models I and II show the behavior of a system where the value of the Chern number is independent or dependent on the gap-opening perturbation, respectively. Model III shows that the symmetries of

the full Hamiltonian determine its behavior, even when the building blocks H_1 and H_2 have different localization properties. The fourth model belongs to a different topological class, being characterized by a $\mathbb{Z}_2$ invariant, but has the advantage of being experimentally accessible in a Hg(Cd)Te double quantum well *[Bernevig et al., 2006; König et al., 2007; Michetti et al., 2012]*.

7.1.1. *Model I*: Gapped Chern insulator coupled to a 2D Dirac metal

For the topological part, H_1, we take the Qi-Wu-Zhang Hamiltonian *[Qi et al., 2006]* of the quantum anomalous Hall effect,

$$H_1 = \sum_{\mathbf{k}} \left[\epsilon(\mathbf{k}) - (t_0(\cos k_x + \cos k_y) - \mu)\sigma_z + v_1(\sigma_x \sin k_x + \sigma_y \sin k_y)\right], \qquad (7.2)$$

where $\epsilon(k) = t_1(1 - \cos k_x - \cos k_y)\sigma_0$ is the kinetic energy and the σ's are the Pauli matrices in spin space. Here and in the following, we set the lattice constant to $a = 1$, as well as $t_0 = 1$, expressing all other Hamiltonian parameters relative to these scales. The model belongs to symmetry class A and has a non-zero Chern number for $0 < \mu < 2$. For the gapless part, we use $H_2 = \sum_{\mathbf{k}} v_2(\sigma_x \cos k_x + \sigma_z \sin k_y)$, which contains four Dirac cones in its spectrum, at $(k_x, k_y) = (\pm\pi/2, 0)$ and $(\pm\pi/2, \pi)$. Notice that this model obeys effective time-reversal, particle-hole and chiral symmetries which all square to unity: $\mathcal{T} = \sigma_x\mathcal{K}$, $\mathcal{P} = \sigma_z\mathcal{K}$, and $\mathcal{C} = \sigma_y$, respectively, where $\mathcal{K}$ denotes the right acting operator of complex conjugation. Therefore, the Hamiltonian belongs to class BDI, cf. Tab. 2.1, which is topologically trivial in two spatial dimensions. Finally, we take $H_c = t\sum_k(\sigma_0 + \sigma_x)$ for the coupling term. In fact, for any H_c with a zero determinant, the full Hamiltonian remains gapless. Solving for its spectrum in a cylindrical geometry, we find weak edges when the boundary is along the y direction or spans an angle of $\pm\arctan(0.5)$ with the x axis. Then, bulk and edge states occur at the same momentum and energy. The strong edge states appear for all other boundary orientations.

The band structure of the system with open boundary conditions in the y direction is shown in Fig. 7.1a. The blue points denote bulk states while the red/green points denote right/left propagating edge states, whose wave functions decay exponentially into the bulk (Fig. 7.1b). The zero modes in the bulk coexist with well localized chiral edge states. In contrast, the spectrum and typical edge states of a system with open boundary conditions in the x direction are shown in Fig. 7.1c and Fig. 7.1d. Here, the red points denote edge states that hybridize with the bulk. We find numerically that the local density of states near the edge is larger than in the bulk (not shown), but the latter does not decay to zero at large distances from the edge.

Adding a mass term $m\sigma_y$ to H_2 opens a bulk gap. This term breaks both the $\mathcal{P}$ and $\mathcal{C}$ symmetries of H_2, but leaves $\mathcal{T}$ intact. Hence, the gapped version of H_2 belongs to class AI in the tenfold classification *[Kitaev, 2009; Schnyder et al., 2008]*,

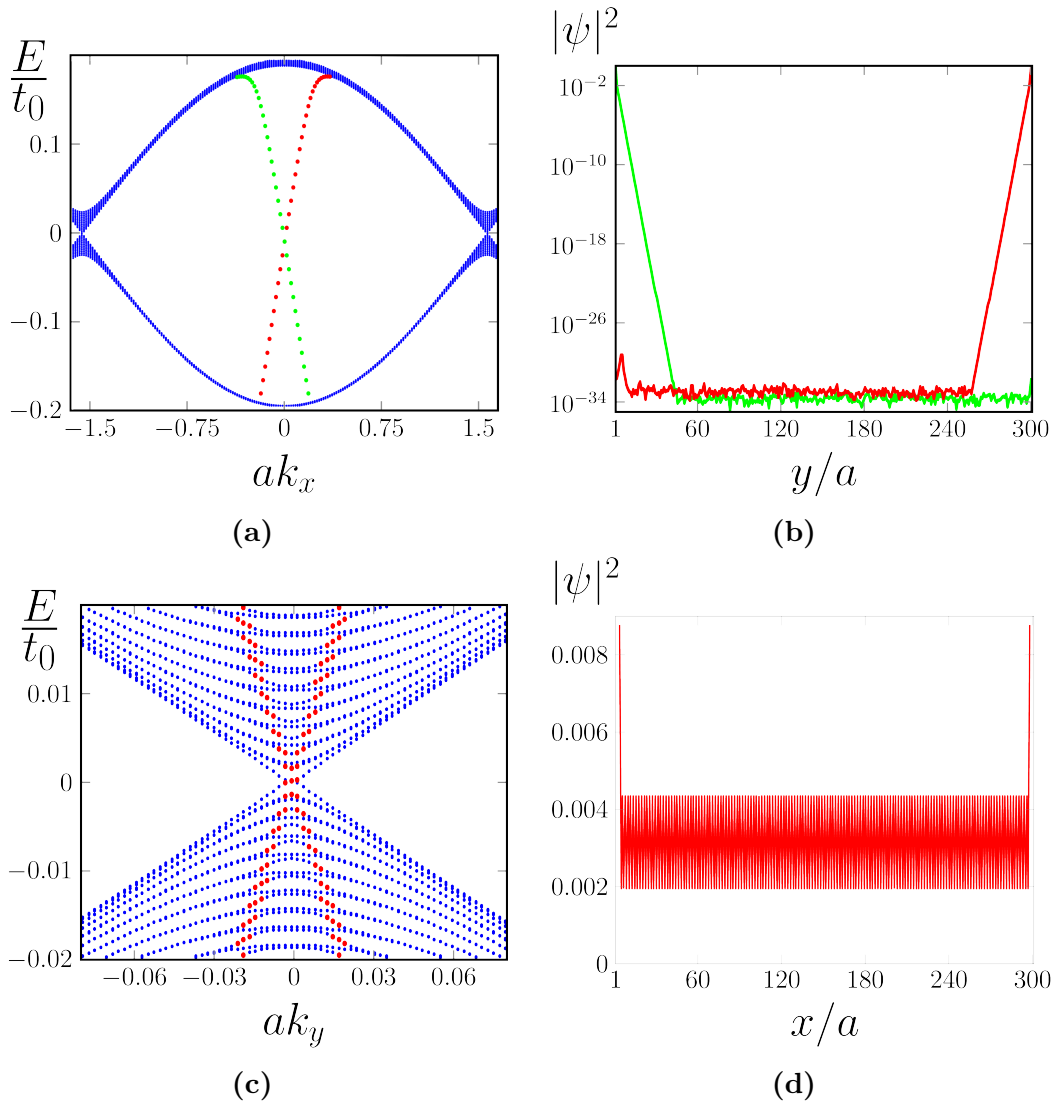

Figure 7.1.: Band structure and edge state wave functions of *model I* for different edge orientations. Edges along the y direction in **(a)** and **(b)**: Well-localized states on the two edges (red, green) coexist with zero modes in the bulk (blue). Edges along the x direction in **(c)** and **(d)**: Due to energy and momentum overlap, hybridized edge states (red) coexist with the bulk states. Figure reprinted with permission from *Baum et al. [2015a]*. Copyright (2015) by the American Physical Society.

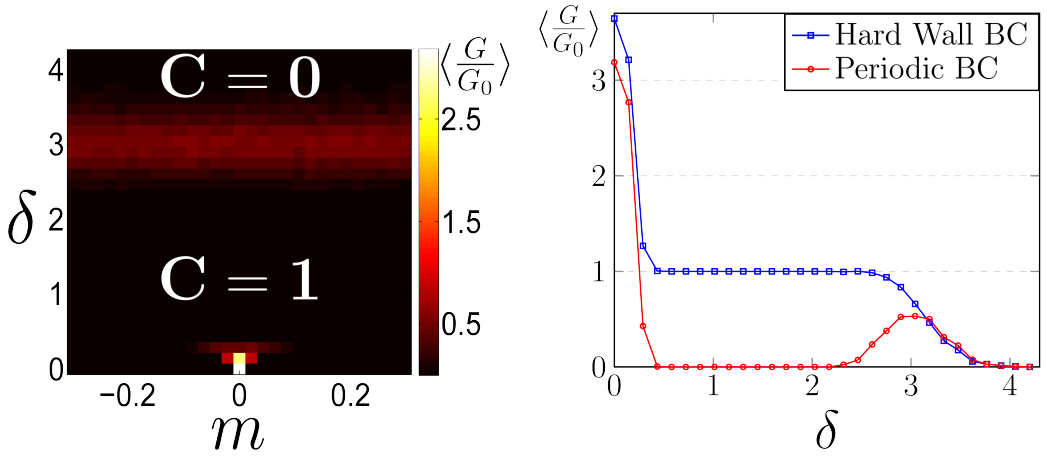

Figure 7.2.: **(a)** Disorder averaged bulk conductance of *model I* as a function of the disorder strength δ and the gap-opening parameter m. Chern numbers of the two phases are shown. **(b)** Average conductance G/G_0, for $m = 0$, as a function of δ, for periodic (red) and hard wall (blue) boundary conditions. The difference between the two curves is due to edge state conductance. The lattice size is $L \times W = 80 \times 80$, and the Hamiltonian parameters are $\mu = v_1 = 1$, $t_1 = 0$, $v_2 = 0.2$, and $t = 0.1$. Each point is obtained by averaging over 100 independent realizations of disorder. Figure reprinted with permission from *Baum et al. [2015a]*. Copyright (2015) by the American Physical Society.

which is also topologically trivial in two spatial dimensions. The full Hamiltonian, for $v_1 \neq v_2$, is then a class A Chern insulator with a non-zero Chern number that is independent of the sign of m, so it belongs to the first class of models mentioned in the introduction. Therefore, the system has to have chiral gapless edge states as well as a gapped bulk, independent of the orientation of the edge. The weak edge states must therefore be stabilized by the appearance of a small mass term. In fact, the same holds for disorder – the full Hamiltonian belongs to class A *[Kitaev, 2009; Schnyder et al., 2008]*, in which the bulk states become localized. Due to the non-zero Chern number, the edge states cannot disappear, and must therefore be stabilized by disorder.

To confirm this expectation, we numerically analyze the two-terminal transport in the system. All transport simulations are performed using the Kwant code *[Groth et al., 2014]*. We discretize the Hamiltonian on a square lattice of $L \times W$ sites, and attach ideal leads in the x-direction. This enables us to compute the scattering

matrix

$$S = \begin{pmatrix} r & t \\ t' & r' \end{pmatrix}, \tag{7.3}$$

which we use to determine the conductance $G/G_0 = \mathrm{Tr}\, t^\dagger t$, $G_0 = e^2/h$, in the low bias voltage, low temperature limit. In the y-direction, we use either hard-wall boundary conditions, or apply periodic boundary conditions to the states, $\psi(x, 0) = \psi(x, W)$, to access only the bulk contribution to transport. Here and in all other models, disorder is introduced as a random variation of the Fermi energy, drawn independently for each lattice site from the uniform distribution $[-\delta, \delta]$. As seen in Fig. 7.2b, when the disorder strength δ increases, the conducting bulk states originating from H_2 localize, leaving behind only the quantized conductance of the edge. The phase diagram is obtained by performing transport simulations with periodic boundary conditions and in the presence of a mass term (Fig. 7.2a). Starting from the gapless point, $m = \delta = 0$, both the addition of a mass term or disorder drive the system into a Chern insulating phase with $C = 1$.

7.1.2. *Model II*: Gapped Chern insulator coupled to a Chern insulator at its critical point

In this model, we keep H_1 as before, but replace H_2 by a Hamiltonian of a quantum Hall state at the transition between two Chern numbers. I.e.,

$$H_{\mathrm{II}} = \begin{pmatrix} H_1 & t(\sigma_0 + \sigma_x) \\ t(\sigma_0 + \sigma_x) & H_2 \end{pmatrix}, \tag{7.4}$$

where

$$H_{1,2} = \epsilon(\mathbf{k}) \pm (\mu_{1,2} - \cos k_x - \cos k_y)\sigma_z + v_1(\sigma_x \sin k_x + \sigma_y \sin k_y), \tag{7.5}$$

and $\epsilon(k) = t_1(1 - \cos k_x - \cos k_y)\sigma_0$. We choose $\mu_1 = 1$ such that H_1 is in a non-trivial phase with a Chern number $C = 1$. For $\mu_2 = 2$, H_2 is at a transition between two Chern insulating phases with $C = -1$ for $\mu_2 < 2$, and $C = 0$ for $\mu_2 > 2$. As such, the combined system is trivial for $\mu_2 < 2$ and has $C = -1$ for $\mu_2 > 2$.

This Hamiltonian is nothing but the Hamiltonian appearing in Eq. (7.2) with $\sigma_z \to -\sigma_z$ and with $\mu = 2$. Here, the gapped H_2 belongs to class A with either Chern number of zero or of -1. Therefore, the full Hamiltonian is a class A Chern insulator with a Chern number changing from $C = 0$ to $C = 1$.

Similar to the other models, the Hamiltonian (7.4) was discretized on a square lattice of $L \times W$ sites (lattice constant $a = 1$), and disorder was introduced as a random change of the on site Fermi energy, chosen independently for each lattice site from the uniform distribution $[-\delta, \delta]$. We have used $L \times W = 80 \times 80$, $t_1 = t = 0.2$, and $v_1 = 1$.

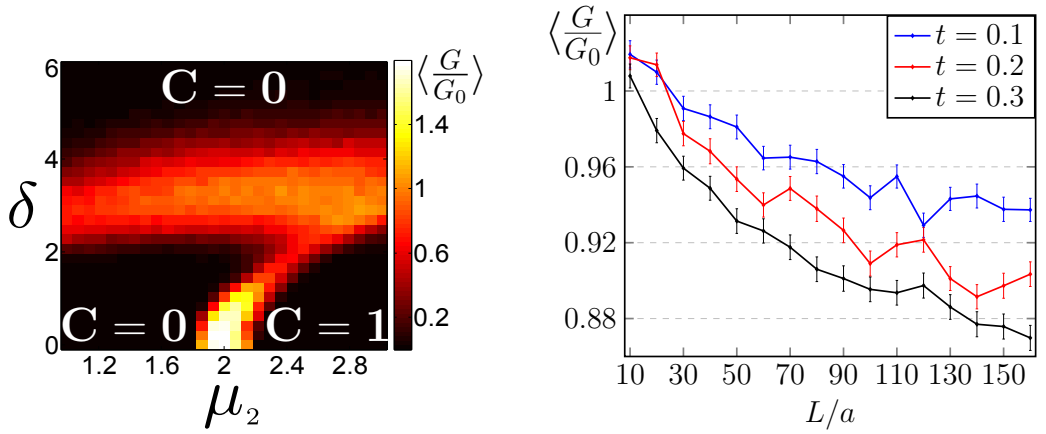

(a) Bulk conductance as a function of the disorder strength δ and μ_2. Each point was obtained by averaging over 100 disorder realizations.

(b) Average bulk conductance for $\mu_2 = 2$ and $\delta = 3.1$, as a function of the system size L for different coupling strengths t.

Figure 7.3.: Average bulk conductance of *model II*, Eq. (7.4). Figure reprinted with permission from *Baum et al. [2015a]* (supplemental material). Copyright (2015) by the American Physical Society.

The phase diagram as a function of the disorder strength δ and μ_2 is shown in Fig. 7.3a. The bulk insulating phases are separated by a critical line across which the edge states localize when the topological invariant changes from $C = 1$ to $C = 0$. In addition, there is a conducting region close to $\delta = 3$ that spreads throughout the plotted μ_2 range and is similar to the one in Fig. 7.2. This feature is a finite-size effect which appears due to the different gaps of H_1 and H_2. As we will also observe in *model III*, which is introduced below, the gap of H_1 is kept constant while the one of H_2 is closed and reopened when it undergoes a topological phase transition. Therefore, increasing the strength of disorder causes H_1 and H_2 to Anderson localize at different values of δ, leading to a finite-size effect which is more pronounced for a larger difference between their gaps. The scaling analysis of Fig. 7.3b confirms the nature of this conducting region, showing that the bulk conductance decreases with increasing system size. In the limit of an infinite system size, starting from the critical point of the clean system, $\mu_2 = \delta = 0$, both the bulk and the edge conductance vanish for $\mu_2 = 0$ and any $\delta > 0$.

7.1.3. *Model III*: Gapped Chern insulator coupled to a quantum spin Hall state at its critical point

In the previous models, both the gapped and the gapless Hamiltonian were subjected to localization by disorder. Now, we choose an H_2 that does not get localized by

weak disorder. Interestingly, we find that its coupling to the gapped Chern insulator makes it amenable to localization. We set H_2 to be the Bernevig-Hughes-Zhang (BHZ) model for the quantum spin Hall effect *[Bernevig et al., 2006]*,

$$H_2 = \begin{pmatrix} h(\mathbf{k}) & \Gamma(\mathbf{k}) \\ \Gamma^\dagger(\mathbf{k}) & h^*(\text{-}\mathbf{k}) \end{pmatrix}, \tag{7.6}$$

with

$$\begin{aligned} h(\mathbf{k}) =& \left(M_0 + 2M_2(1 - \cos k_x - \cos k_y)\right)\sigma_z + A\sigma_x \sin k_x \\ &+ \left(C_0 + 2C_2(1 - \cos k_x - \cos k_y)\right)\sigma_0 - A\sigma_y \sin k_y, \\ \Gamma(\mathbf{k}) =& \Delta\left(\sigma_0 \sin k_x + i\sigma_z \sin k_y\right) - i\Delta_0\sigma_y, \end{aligned} \tag{7.7}$$

where the σ_i's act in the subspace of the E and H orbitals of the BHZ model. We choose M_0 such that H_2 is in a metallic region between two non-trivial quantum spin Hall phases (symmetry class AII). For the full model, we take H_1 as in Eq. (7.2), and a simple coupling Hamiltonian,

$$H_c = t \begin{pmatrix} 1 & i & 1 & i \\ 1 & i & 1 & i \end{pmatrix}. \tag{7.8}$$

Similar to Figs. 7.1a-d, in the absence of disorder, bulk and edge states coexist at the Fermi level and overlap in momentum, causing them to hybridize, cf. Fig. 7.5. Even though they no longer decay exponentially into the bulk, their wave functions are still visibly peaked at the edges of the system. For the figure, we take $M_0 = -0.49$ and $t = 0.1$, keeping all other parameters unchanged.

While H_2 is time-reversal symmetric, allowing the existence of metallic phases in the presence of disorder, the coupled model belongs to class A, where weak disorder leads to localization. Seemingly, the phase diagram in the space of M_0 and disorder strength δ, depicted in Fig. 7.4a, shows a metallic phase at finite disorder strength (close to $\delta = 1$), reminiscent of that present in the BHZ model. However, a conductance scaling analysis (Fig. 7.4b) shows that it is only metallic in the decoupled case. When the coupling is turned on, the conductance decreases with system size, showing that the presence of the conducting region is caused by the finite-size of the system. In accordance with Fig. 7.2a, as the disorder strength is increased, the bulk states localize leaving behind only the quantized contribution of the edge states to the thermal conductance. This exemplifies the fact that both the topological and the localization properties depend on the symmetry class of the full Hamiltonian. In the thermodynamic limit, the phase diagram of this model should be identical to that of *model I*.

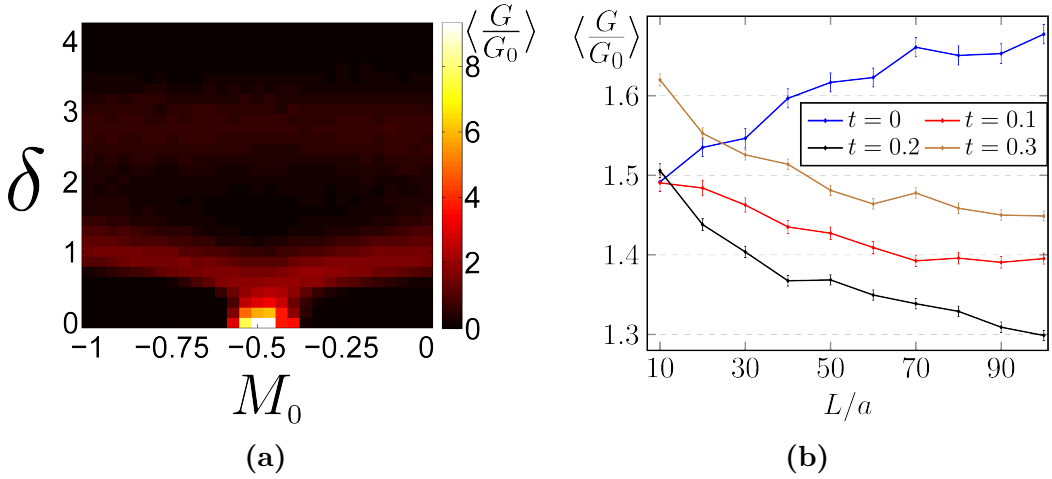

Figure 7.4.: **(a)** Disorder averaged bulk conductance of *model III* as a function of M_0 and disorder strength δ. **(b)** Average bulk conductance for $M_0 = -1$ and $\delta = 0.95$, as a function of the system size L for different coupling strengths. The conducting region around $\delta = 1$ becomes localized as the system size is increased. The lattice size in (a) is $L \times W = 80 \times 80$, and Hamiltonian parameters are $\mu = v_1 = 1$, $t_1 = 0.4$, $t = 0.2$, $A = M_2 = 1/4$, $\Delta_1 = 0.1$, $\Delta_0 = 0.05$, $C_0 = -0.02$ and $C_2 = 0$. Each point is obtained by averaging over 50 independent realizations of disorder. In (b), the aspect ratio is fixed to $L/W = 1$ and 2000 disorder realizations are considered. Figure reprinted with permission from *Baum et al. [2015a]*. Copyright (2015) by the American Physical Society.

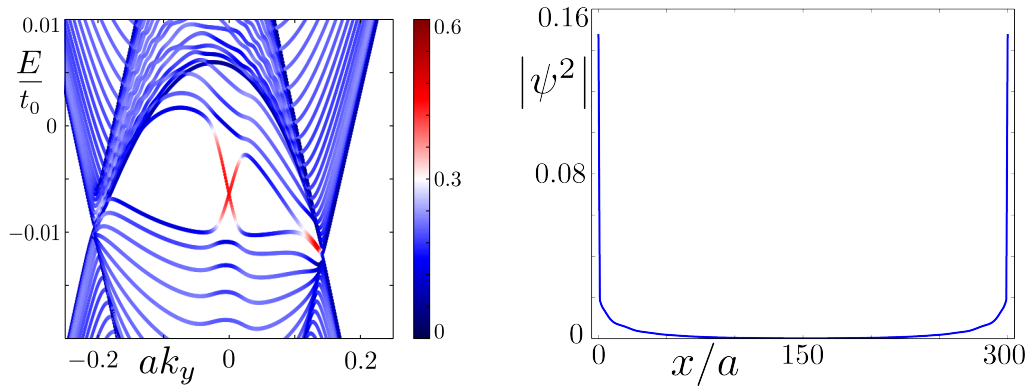

(a) Band structure of *model III* with open boundary conditions in the x-direction. The color scale shows the weight of the state on the first and last 10% of lattice sites.

(b) Intensity as a function of position for the edge states at $k_y = 0$ in the left panel.

Figure 7.5.: Figure reprinted with permission from *Baum et al. [2015a]* (supplemental material). Copyright (2015) by the American Physical Society.

7.1.4. *Model IV*: Gapped quantum spin Hall phase coupled to a quantum spin Hall phase at its critical point

We now consider both H_1 and H_2 to be BHZ models, as described in Eq. (7.6) and Eq. (7.7), with different mass terms, $M_{0,1}$ and $M_{0,2}$, respectively. We set H_1 to be in a topological phase and H_2 in a metallic region. This model can be directly implemented experimentally, for example by two coupled Hg(Cd)Te quantum wells as proposed by *Michetti et al. [2012]*. Most directly, this model may be realized in such systems when one of the quantum wells is grown with a critical thickness *[Buttner et al., 2011]* while the other well is chosen to be in a topologically non-trivial phase. Remarkably, the system may be driven to the gapless point by the application of voltage on front and back gates even when the thickness of the two wells does not conform to this requirement.

We choose the coupling term $H_c = t\,(\sigma_0 + \sigma_z)\,\tau_0$ of *Michetti et al. [2012]* to describe the experimentally accessible parameter regime. The Pauli matrices σ describe the space of the E and H orbitals, and the Pauli matrices τ act on the spin degree of freedom. As in the other models, Fermi level bulk and edge states can coexist in two coupled BHZ Hamiltonians. For some energies, edge and bulk states overlap, and therefore hybridize. Nevertheless, the spatial profile of the hybridized wave functions shows clear peaks at the edges of the system. We illustrate this observation in Fig. 7.6, using $M_{0,1} = -1$, $M_{0,2} = -1.45$, and keeping all other parameters as before. Additionally, like in *model III*, the bulk becomes insulating

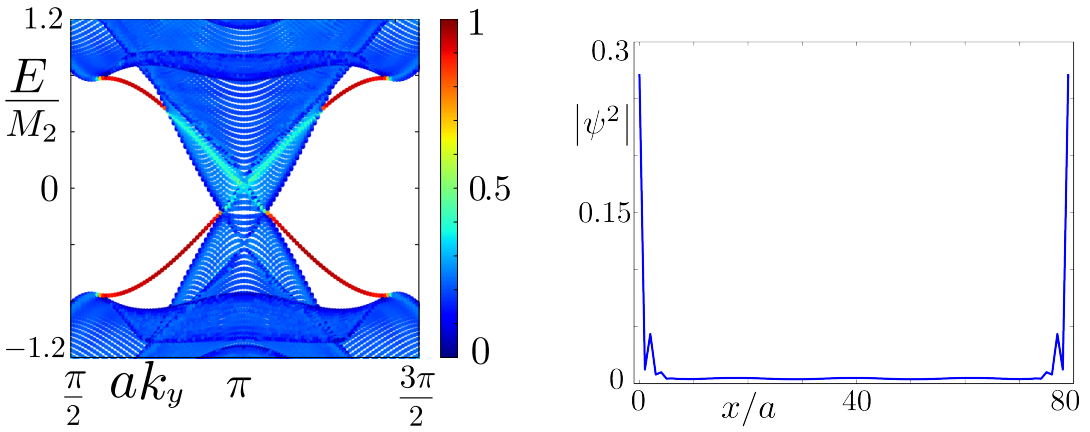

(a) Band structure of *model IV* with open boundary conditions in the x-direction, showing hybridized bulk and edge states. The color scale shows the relative intensity of each state on the first and last 10% of lattice sites.

(b) Intensity as a function of position for the edge states located at $k_y = \pi$ in the left panel.

Figure 7.6.: Figure reprinted with permission from *Baum et al. [2015a]* (supplemental material). Copyright (2015) by the American Physical Society.

when $M_{0,2}$ is changed. However, this time, the phase is characterized by a different invariant, belonging to $\mathbb{Z}_2$ instead of the $\mathbb{Z}$ valued Chern number.

At zero disorder, the experimental signature of this phase is the coexistence of helical edge modes together with a conducting bulk. This coexistence can be verified experimentally by performing conductance measurements in three-terminal devices with polarized leads as discussed below in Section 7.1.4.1.

The disordered case also shows a behavior different to the one of the previous models. Since the full Hamiltonian belongs to class *AII*, weak anti-localization leads to the formation of a metallic phase at finite disorder strength, see Fig. 7.7a. This is confirmed by the scaling analysis of Fig. 7.7b, showing that the conductance increases with system size

The reader may wonder why we employ a different set of topological masses $M_{0,1}$ and $M_{0,2}$ for Fig. 7.6 and Fig. 7.7. This illustrates, and anticipates, that the specific choice of the topological masses is not very important as long as one mass is close to a point of gap closure. The experimentally more relevant scenarios, however, are almost vanishing topological masses. We will elaborate on these in the following Section 7.1.4.1.

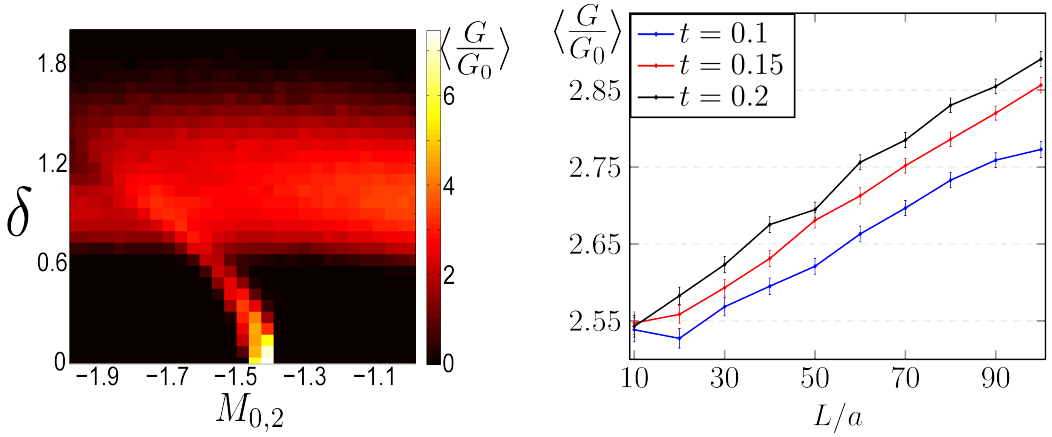

Figure 7.7.: **(a)** Disorder averaged bulk conductance of two coupled BHZ models as a function of disorder strength δ and $M_{0,2}$. **(b)** Average bulk conductance for $\delta = 1$ and $M_{0,2} = -1.47$, as a function of the system size L for different couplings t. All parameters of the two BHZ models are the same as in model *III*, except for $M_{0,1} = -0.8$. The coupling strength is $t = 0.15$. In (a), we averaged over 50 realizations, while 2000 are used in (b). The phase diagram is computed for a lattice of $L \times W = 80 \times 80$ sites, while the conductance scaling is done at a constant aspect ratio $L/W = 1$. Figure reprinted with permission from *Baum et al. [2015a]*. Copyright (2015) by the American Physical Society.

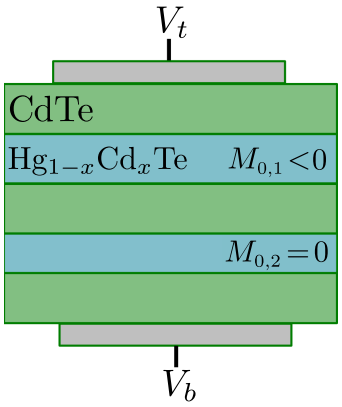

Figure 7.8.: Schematic setup of a double quantum well structure in Hg(Cd)Te, realizing a gapless topological phase. Figure reprinted with permission from *Baum et al. [2015a]* (supplemental material). Copyright (2015) by the American Physical Society.

thickness	A/eV	M_2/eV	C_0/eV	C_2/eV	$-M_0$/eV
7.0 nm	$0.365/a_c$	$-0.706/a_c^2$	0	$-0.532/a_c^2$	0.01009
6.3 nm	$-0.373/a_c$	$-0.857/a_c^2$	0	$-0.682/a_c^2$	0

Table 7.1.: Parameters used for the non-trivial quantum well (top row) from *Rothe et al. [2010]*, and the gapless one (bottom row) from *Buttner et al. [2011]*. We choose an effective lattice constant $a_c = 0.64$nm, and absorb the chemical potentials, parametrized by C_0, into the gate voltages, setting them to zero (see text).

7.1.4.1. Experimental realization of model IV

Model IV is realizable in a double HgTe quantum well structure in a CdTe matrix, a setup proposed in *Michetti et al. [2012]*. One of the quantum wells should be grown with the critical thickness of 6.3nm, which has been experimentally realized in *Buttner et al. [2011]*, while the other one is chosen to be topologically non-trivial, with a width of, e.g., 7nm, which is exemplified in Fig. 7.8. Both quantum wells themselves are described by the BHZ model, where the parameters are adjusted to the thickness of the respective quantum well. For our calculations, we use the experimentally relevant estimates of the parameters of *Rothe et al. [2010]* and *Buttner et al. [2011]*, summarized in Tab. 7.1.

For clarity, we neglect off-diagonal terms in the BHZ models, such as bulk and structural inversion asymmetry *[Bernevig et al., 2006; Liu et al., 2008; Rothe et al., 2010]* since they vanish at the Γ point where the bulk gap closes. The two quantum wells are coupled by the term introduced in *Michetti et al. [2012]*, which fulfills the following properties:

1. the overlap between the $E1$ states of the quantum wells is much stronger than the overlap between the $H1$ states[1], and

2. at the Γ point, the overlap between the $E1$ and $H1$ states of different quantum wells vanishes due to rotational symmetry along the axis of crystal growth [2].

These properties guarantee a simple structure of the inter layer coupling Hamiltonian at the Γ point,

$$H_c(0) = t\,(\sigma_0 + \sigma_z)\,\tau_0\rho_x, \tag{7.9}$$

where σ, τ and ρ are Pauli matrices describing the band-index, time-reversal and layer degree of freedom, respectively.

The value of $M_{0,2}$ at which the topological phase transition occurs changes as a function of the coupling strength t, such that the well of critical thickness becomes a gapped, topologically trivial system when $t > 0$. However, for any coupling Hamiltonian that preserves time-reversal symmetry there exists a value of $M_{0,2}$ at which the combined system is a gapless topological insulator.

Rather than tuning the width of the quantum wells to reach this point, the bulk gap may be closed by shifting the chemical potentials of the quantum wells relative to each other. This can be achieved by applying different gate voltages on top and bottom gates, V_t and V_b, as shown in Fig. 7.8. The combined system then becomes gapless when the top of the valence band in one well and the bottom of the conduction band in the second well touch each other.

Due to the coupling between the layers, a gap is reopened when the two bands overlap, with both gapped phases being topologically non-trivial Z_2 insulators. For the coupling in Eq. (7.9), there is a critical voltage difference, $\Delta V \equiv V_c$, at which the bulk gap closes. Generally, the critical voltage, V_c, depends on the bulk gaps and chemical potentials of the uncoupled wells, and also on the coupling between the layers. However, for the experimentally accessible case, where $|M_{0,1} - M_{0,2}| \ll t$, the critical voltage is $V_c = (M_{0,1} - M_{0,2}) - (C_{0,1} - C_{0,2})$, independent of t. Experimentally, the bulk gap closing should have the signature of an increased conductance through the sample, which helps to determine the necessary voltages V_t and V_b. We show the band structure of such a system for three different gate voltages in Fig. 7.9. Here, $M_{0,1}$ and $M_{0,2}$ are chosen such that the top layer is in a topological insulating phase while the bottom layer is in a trivial insulating phase.

Our main prediction is that helical edge channels coexist with a conducting bulk. Measurements of the two-terminal conductance contain contributions both from the

[1] The underlying reason is the interfacial character of the $E1$ quantum well bands opposed to the intra well character of the $H1$ bands.

[2] The introduction of a boundary and the lattice structure of the material system in fact break this symmetry. However, the former symmetry violation is a finite size effect and the latter becomes irrelevant close to the Γ point.

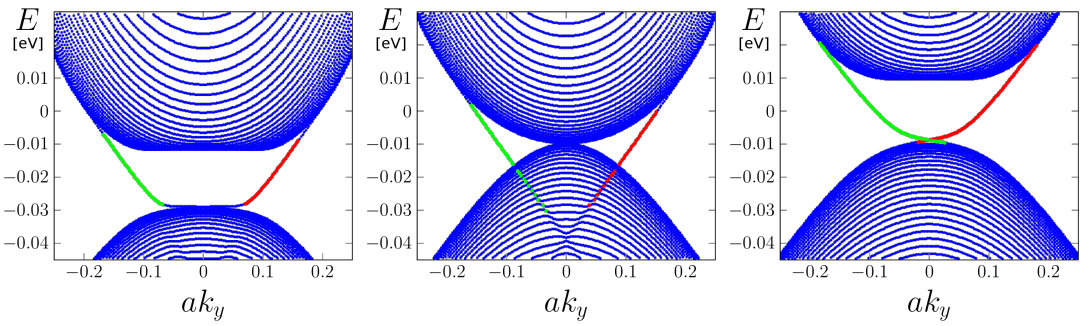

Figure 7.9.: Band structure of *model IV* with open boundary conditions in the x direction. $M_{0,1} = -M_{0,2} = 0.01$eV and the coupling between the layers is $t = 0.1$. Other parameters are as in Tab. 7.1. The band structure is calculated for three different configurations of the gate voltage such that (a) $\Delta V = V_c - 0.02$V (b) $\Delta V = V_c$ (c) $\Delta V = V_c + 0.02$V. The red and green points denote left/right moving edge states, while the blue points denote bulk states. Figure reprinted with permission from *Baum et al. [2015a]* (supplemental material). Copyright (2015) by the American Physical Society.

bulk states and from the helical edge modes. In order to separate these bulk and edge contributions, the conductance could be measured in a three-terminal setup as depicted in Fig. 7.10a. By subtracting the conductance between any two leads from the one of the reverse direction (for instance $G_{\mathrm{LR}} - G_{\mathrm{RL}}$), we obtain the chiral contribution to transport G_{chiral}. Here, the edge channels are helical, and therefore, G_{chiral} is zero. However, this is not the case if the leads are spin-polarized. We define the lead polarization as $P_{\mathrm{leads}} = (n_\uparrow - n_\downarrow)/(n_\uparrow + n_\downarrow)$, where $n_\uparrow$ and $n_\downarrow$ is the density of spin up and spin down particles in the leads, respectively. The value of G_{chiral} (in units of e^2/h) should change continuously from -1 to 1 as P_{leads} is smoothly changed from -1 to 1. Such a spin dependent chiral contribution along with a large two terminal conductance is a clear evidence for the existence of helical channels that coexist with a conducting bulk. To confirm this expectation, we employed a numerical simulation of the proposed three-terminal setup in the presence of finite disorder and with perfectly polarized leads. The two-terminal conductance from right to left, G_{RL}, the one from left to right, G_{LR}, and their difference are depicted in Fig. 7.10b as a function of the applied gate voltage. In these simulations, the disorder strength is twice the topological gap of the uncoupled wells.

Away from the critical voltage, the bulk is gapped and the only contribution to the two-terminal conductance stems from a single edge channel. As the voltage reaches the critical value, the bulk becomes conducting, hence both G_{LR} and G_{RL} get an equal contribution from the bulk. Nonetheless, their difference, i.e., the edge

contribution, remains close to its quantized value, one unit of conductance.

7.1.5. Summary

We provide a general scheme for realizing unusual two-dimensional topological phases that simultaneously host gapless modes in the bulk and on the edges. We find that the modes on the edge exhibit a peculiar structure that depends on the boundary orientation. Additionally, we find that the behavior of these phases in the presence of disorder can be extracted from the clean limit by analyzing their topological properties in the presence of an infinitesimal bulk gap. Finally, we propose a concrete physical realization of one such model, based on double Hg(Cd)Te quantum wells.

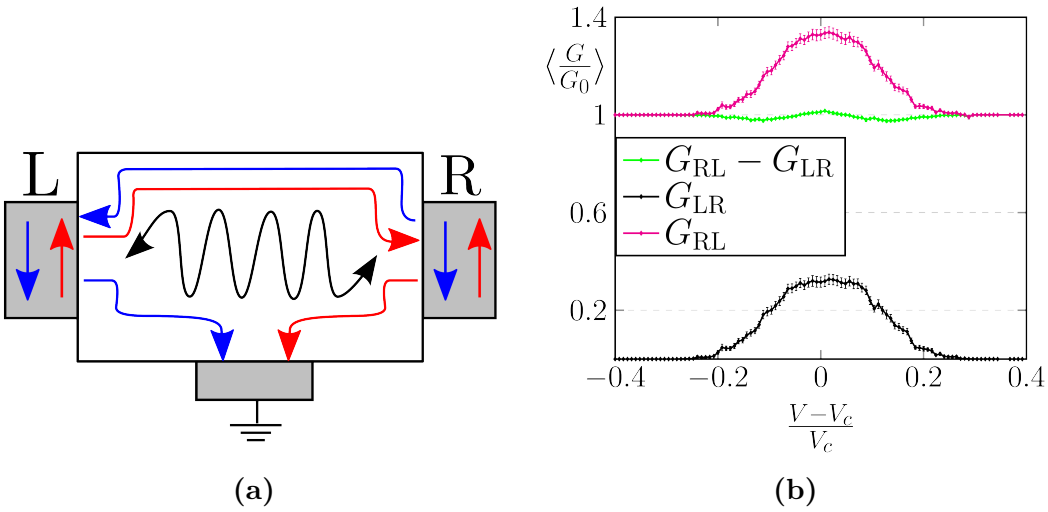

(a) **(b)**

Figure 7.10.: **(a)** Sketch of the three-terminal setup. The chiral contribution to transport is obtained by subtracting the conductance between any two leads from the one of the reverse direction, for instance, $G_{\mathrm{LR}} - G_{\mathrm{RL}}$. The helical edge modes can be probed by polarizing the leads. **(b)** Numerical simulation of the three-terminal setup with perfectly polarized leads. We depict the two-terminal conductances, G_{RL} and G_{LR}, as well as their difference, as a function of the applied gate voltage. As the gate voltage reaches the critical value, the bulk becomes conducting but the edge contribution remains almost quantized, despite the large strength of disorder (see text). The parameters are $M_{0,1} = -M_{0,2} = 0.01$, the coupling between the layers is $t = 0.1$, the lattice constant is 4, and all remaining parameters are as described in Tab. 7.1. The disorder strength is taken to be twice the topological gap, i.e., $\delta = 0.02$. The conductance is computed for a lattice of $L \times W = 80 \times 80$ sites and each point was obtained by averaging over 100 realizations of disorder. Figure reprinted with permission from *Baum et al. [2015a]* (supplemental material). Copyright (2015) by the American Physical Society.

8. Conclusion & outlook

This thesis is a brick in the wall of a building. The building is the vast field of topological insulators and the wall represents the combinations of topological insulators with well-known electronic phases and effects[1]. As such a brick, we have contributed to the analysis of the interaction of a topological insulator with a Rashba impurity, a Kondo dot, magnetic adatoms, proximity-induced superconductivity, and semimetals.

Most of the unique behaviors that we encounter are caused by the peculiarities of the edge liquids. The first example that we describe is the unexpected insensitivity of transport properties to the strength of the Rashba coupling at the refermionizable point in the Rashba setup. This is particularly interesting in view of the usual time-reversal-protected insensitivity to backscattering of the helical liquid. Furthermore, we discover an exact correspondence in the two channel Kondo model between time-resolved current correlations and the long sought-after Kondo cloud. This correspondence is essentially based on the spin-momentum locking of the helical liquid. Additionally, we discover the analytic structure of the Kondo cloud for the Toulouse points in form of the Hurwitz-Lerch transcendent, which could – speculatively – prove to be more generally valid. Continuing to investigate the effect of magnetic impurities on topological insulators, we find the stable spiral magnetic ground state order of adatoms at the surface of a three-dimensional strong topological insulator. The spiral order is generated by the hexagonal warping of the Fermi surface for a certain regime of chemical potentials but it does, above a critical threshold for the density of the magnetic adatoms, not seem to depend on the spatial order of the adatoms. We employ this spiral magnetic field to generate a peculiar class of two-dimensional gapless topological insulators, which host one dimensional Majorana edge channels that change their chirality if they are affected by disorder. Finally, we abstract the conditions that lead to gapless topological phases and combine gapped topological systems with gapless semimetals.

The research conducted and presented in this thesis has uncovered numerous interesting paths for further research. We want to present some of the ideas here, concluding the thesis. They should be taken as hints where exciting physics may be discoverable. In this regard, many of the ideas are guided by intuition and, in fact, it could be that some of them have been found independently or even have been addressed in publications that we are not aware of.

[1] The whole construct is far from completion.

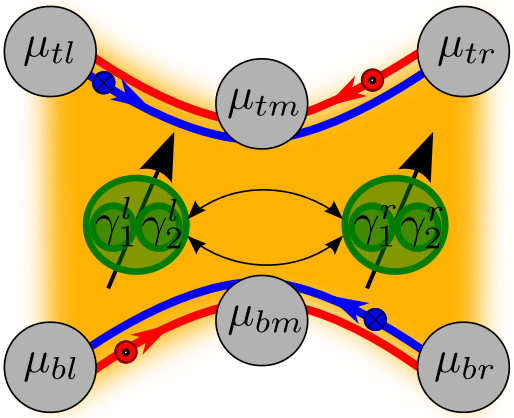

Figure 8.1.: A possible setup that could apply Kondo physics to realize the exchange of Majorana fermions and therefore quantum computation. Two Kondo dots in the two channel regime are coupled to two helical liquids. Each of the dots amounts to two differently coupled Majorana modes. The interaction between the Majorana modes can be engineered by time-dependent biases applied at the terminals.

Majorana braiding in the helical Kondo effect

The refermionized Hamiltonian of the two channel Kondo model, as analyzed in Section 5.1, utilizes the local fermion c, which basically represents the spin degree of freedom on the Kondo dot. If we decompose c into two Majorana modes, remarkably, these modes couple distinctly to the leads. In fact, at the Toulouse point, one of the Majorana modes completely decouples from the system. Therefore, under these circumstances, a single Kondo dot effectively amounts to one Majorana fermion. It is therefore possible to conceive of a double dot setup that could be employed to engineer an interaction between two Majorana modes mediated by the Kondo cloud, which effectively allows to exchange the Majorana excitations. A possible schematic setup is depicted in Fig. 8.1. The necessary time dependent variation of the coupling strength between the Majorana modes could, as indicated by the voltage dependence of the Kondo cloud in Section 5.1, be realized by time-dependent voltages in a multi-terminal setup. The idea could be a step towards the realization of topological quantum computation *[Fulga et al., 2013; Halperin et al., 2012; Stern & Lindner, 2013]*. However, there is a disadvantage that we do not want to conceal. The quantum bit of interest would be formed by two Majorana modes, each of which stemming from a different quantum dot. In the prevalent theoretical example of Majorana modes, *Kitaev [2001]*, and the possible experimental realizations, *Das et al. [2012]; Mourik et al. [2012]*, the quantum bit is separated from the states of the environment by an energy gap. In our scenario, instead, the density of states

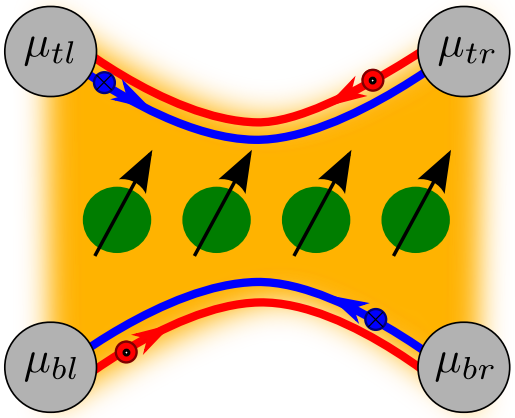

Figure 8.2.: A chain of Kondo dots that interact with each other via two helical liquid leads. By bringing the leads out of equilibrium, the sign of the interaction between neighboring dots can be tuned to be positive or negative, resulting in a global antiferromagnetic or ferromagnetic state, respectively.

of the leads is constant in energy. The isolated read-out of the quantum bit can therefore probably not be achieved without additional effort. A possible resource in this regard could be the temporal application of a Zeeman field, which gaps out the helical leads. It has to be kept in mind, although, that a Zeeman field also competes with the Kondo effect itself.

Helical Kondo chain

A quintessence of the nonequilibrium studies on the Kondo cloud in Section 5.1 is that the sign of the Kondo cloud switches in dependence on the applied voltage. We therefore expect the effective interaction between two spins that is mediated by the Kondo cloud – similar to the effective RKKY interaction of Section 6.1.1 – to change signs in dependence on the voltage as well *[Maciejko, 2012; Sodano et al., 2010]*. A setup where the effect could be exploited is depicted in Fig. 8.2 representing a chain of Kondo dots that interact with each other using the itinerant particles of two attached helical liquids. We expect to obtain two main scenarios. Either the interaction between adjacent dots is positive, then the ground state is antiferromagnetic, or the interaction is negative, which results in a ferromagnetic ground state. Most notably, the sign of the interaction is tunable by the voltage such that we get a completely electrically induced transition between both types of ground states. Such a system could serve as a useful device for spintronics and information storage, again, also in combination with quantum computational aspects.

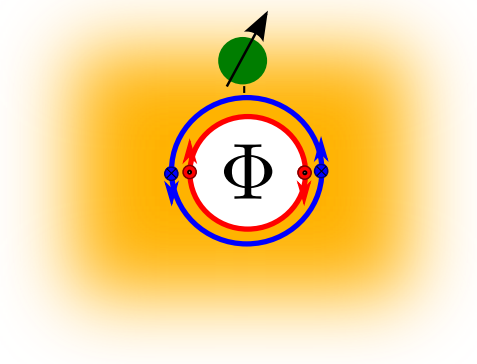

Figure 8.3.: A helical liquid in form of a ring is coupled to a Kondo dot. The circle is realized as the edges of an anti-dot. A flux Φ is threaded through the ring.

Helical Kondo ring

The intrinsic spin-momentum locking of the helical liquid in combination with a Kondo dot results in another unique behavior – apart from the ones described in Chapter 5 – if we consider the helical liquid being bent to the form of a circle. In particular, this may be achieved by an anti-dot in the proximity of a magnetic impurity as depicted in Fig. 8.3, which additionally has the advantage of a magnetic flux being threadable through the ring. If we consider the strong coupling, single particle limit, we observe a peculiar bound state. To demonstrate this, we consider that the particle and the dot initially have oppositely aligned spins and apply the classical picture that the particle behaves as a localized entity. Each time the particle arrives at the Kondo dot it scatters, inducing a simultaneous spin flip of the dot and itself. Therefore, the particle inverses its direction and travels around the whole circumference before it is flipped again at the Kondo dot. The loop continues ad infinitum. We therefore expect a bound state with interesting and unique properties that, by the introduction of the flux Φ can obtain an anyonic character *[Altland & Simons, 2006b]*.

Reaction of the electronic surface states of the three-dimensional topological insulator to the magnetization of the adatoms

In Chapter 6, we have calculated that the RKKY interactions result in a spiral magnetic order of the magnetic dopants. This spiral order, in turn, can effect the electrons such that their spectrum is altered, which, again, can alter the magnetization of the magnetic dopants, etc.. The effect of this back-action is of a higher

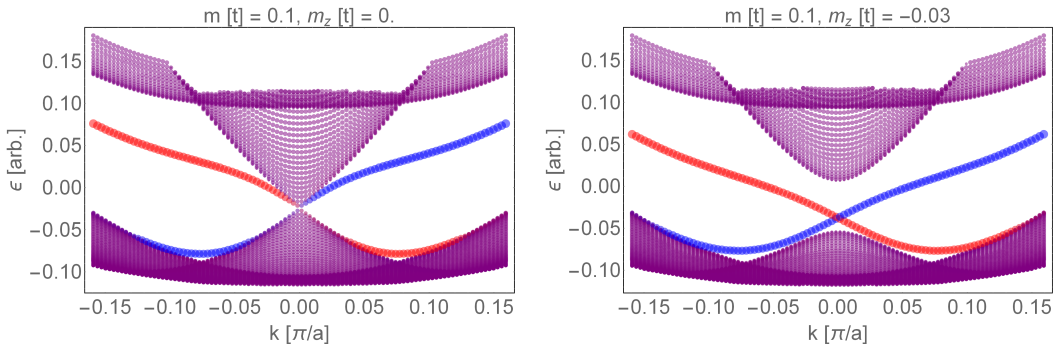

(a) Without Zeeman field. **(b)** With correctly chosen Zeeman field.

Figure 8.4.: The two-dimensional Rashba model, Eq. (6.12), with periodic magnetization m and a Zeeman field m_z exhibits edge channels (red and blue) for certain model parameters, which we expect to be one-dimensional, dispersing Jackiw-Rebbi states.

order in the coupling between the adatoms and the surface electrons. Therefore, we have considered it to be vanishingly small throughout Chapter 6. However, there are examples of one-dimensional systems, cf. *Braunecker et al. [2009a,b]*, where the inclusion of the back-action significantly enhances the stability of the magnetic order. It would be interesting to account for this effect, for instance, by a self-consistent mean field analysis as in the above references and determine whether the stability of our two-dimensional spiral is enhanced as well. This is especially interesting if we keep in mind that the stability of the spiral wave already reaches up into the Kelvin regime without the consideration of this effect.

Jackiw-Rebbi state for the non-superconducting, magnetically doped surface of a three-dimensional topological insulator

The Rashba toy model that is employed in Section 6.2 to exemplify the general mechanism behind the formation of our gapless topological insulators also exhibits edge states in the absence of superconductivity. The only ingredients present in this case is the Rashba toy model of Eq. (6.12) for a two-dimensional electron gas with Rashba spin orbit coupling and a periodic magnetization that opens a partial gap at the outer Fermi surface. If we additionally apply a Zeeman field, the inner Fermi surface is gapped out. A typical spectrum for this scenario is depicted in Fig. 8.4. The system in this case very much resembles the two-dimensional counterpart of the one dimensional system described in *Rainis et al. [2014]*, which is a one-dimensional wire exhibiting Rashba spin orbit coupling in the presence of a periodic magnetization and a Zeeman field. The zero-dimensional edge states that develop in this model are fractionally charged, so-called Jackiw-Rebbi states *[Jackiw & Rebbi, 1976]*. There-

fore, we expect that the edge states in our two-dimensional Rashba model are one-dimensional, dispersing Jackiw-Rebbi states. In fact, already Jackiw considered a two-dimensional extension *[Jackiw, 1984]*. In contrast to their zero dimensional counterparts, excitations in a one-dimensional channel can move. This seems to be particular interesting regarding the possibly non-abelian statistics of the excitations *[Klinovaja & Loss, 2013]*. It is also interesting how the character of the one-dimensional Jackiw-Rebbi channels is changed by the increase of superconductivity in the model. As we know from our studies in Section 6.2, the edge channels are Majorana edge channels in the absence of a Zeeman field. Therefore, a crossover from Jackiw-Rebbi properties to Majorana properties should be observable, which we expect at an equal strength of the Zeeman field and the superconducting gap function.

Determination of a global topological invariant for the presented gapless topological phases

The edge states of the gapless topological hybrid systems that are constructed in Chapter 7 have almost identical physical characteristics to the ones of the gapped topological phase the system was created from. As the edge states of gapped topological systems are well classified by global topological invariants, cf. Section 2.1, the described situation seems to indicate that gapless topological systems possess an equivalent to the topological invariant of the gapped case. Being able to construct such a global invariant also for gapless systems would enrich the set of methods that are used to classify such systems.

Bibliography

Affleck, I. (2010). "The Kondo screening cloud: what it is and how to observe it". In A. Aharony, Y. Imry, & O. Entin-Wohlman (Eds.), *Perspectives of Mesoscopic Physics: Dedicated to Yoseph Imry's 70th Birthday*, pp. 1–44. World Scientific. ISBN: 9789814299435. Also: Affleck, I. (2009). *ArXiv e-prints*, arXiv:0911.2209 [cond-mat.mes-hall]. (pp. 21, 22)

Affleck, I. and Simon, P. (2001). "Detecting the Kondo Screening Cloud Around a Quantum Dot". *Phys. Rev. Lett.*, Vol. **86**, Iss. 13, pp. 2854–2857. (pp. 21, 22)

Altland, A. and Simons, B. (2006a). *Condensed Matter Field Theory*. Cambridge University Press. ISBN: 9780521845083. (pp. 33, 36, 47)

Altland, A. and Simons, B. (2006b). *Condensed Matter Field Theory*, Section "Example: particle on a ring", p. 512 ff. Cambridge University Press. ISBN: 9780521845083. (p. 145)

Altland, A. and Zirnbauer, M. R. (1997). "Nonstandard symmetry classes in mesoscopic normal-superconducting hybrid structures". *Phys. Rev. B*, Vol. **55**, Iss. 2, pp. 1142–1161. (pp. 11, 13)

Amaricci, A.; Budich, J. C.; Capone, M.; Trauzettel, B.; and Sangiovanni, G. (2015). "First-Order Character and Observable Signatures of Topological Quantum Phase Transitions". *Phys. Rev. Lett.*, Vol. **114**, Iss. 18, p. 185701. (p. 14)

Andergassen, S.; Pletyukhov, M.; Schuricht, D.; Schoeller, H.; and Borda, L. (2011). "Renormalization group analysis of the interacting resonant-level model at finite bias: Generic analytic study of static properties and quench dynamics". *Phys. Rev. B*, Vol. **83**, Iss. 20, p. 205103. (p. 92)

Andrei, N. (1980). "Diagonalization of the Kondo Hamiltonian". *Phys. Rev. Lett.*, Vol. **45**, Iss. 5, pp. 379–382. (p. 20)

Araki, H. (1968). "On the Diagonalization of a Bilinear Hamiltonian by a Bogoliubov Transformation". *Publications of the Research Institute for Mathematical Sciences*, Vol. **4**, Iss. 2, pp. 387–412. (p. 28)

Bárðason, J. H. (2008). *Effects of Spin-Orbit Coupling on Quantum Transport*. PhD thesis, University of Leiden. Section "Spin-Orbit Coupling from the Dirac Equation", pp. 6-8. (p. 18)

Bardeen, J.; Cooper, L. N.; and Schrieffer, J. R. (1957). "Theory of Superconductivity". *Phys. Rev.*, Vol. **108**, Iss. 5, pp. 1175–1204. (p. 27)

Bardyn, C.-E.; Baranov, M. A.; Kraus, C. V.; Rico, E.; İmamoğlu, A.; Zoller, P.; and Diehl, S. (2013). "Topology by dissipation". *New Journal of Physics*, Vol. **15**(8), p. 085001. (p. 27)

Baum, Y.; Posske, T.; Cosma Fulga, I.; Trauzettel, B.; and Stern, A. (2015a). "Coexisting Edge States and Gapless Bulk in Topological States of Matter". *Phys. Rev. Lett.*, Vol. **114**, Iss. 13, p. 136801. (pp. 3, 56, 57, 124, 128, 129, 131, 133, 134, 135, 136, 137, 139, 141)

Baum, Y.; Posske, T.; Cosma Fulga, I.; Trauzettel, B.; and Stern, A. (2015b). "Gapless Topological Superconductors - Model Hamiltonian and Realization". *ArXiv e-prints*, arXiv:1503.04845 [cond-mat.supr-con]. (pp. 3, 17, 100, 105, 106, 108, 109, 114, 116, 117, 119, 120, 122)

Baum, Y. and Stern, A. (2012a). "Density-waves instability and a skyrmion lattice on the surface of strong topological insulators". *Phys. Rev. B*, Vol. **86**, Iss. 19, p. 195116. (p. 101)

Baum, Y. and Stern, A. (2012b). "Magnetic instability on the surface of topological insulators". *Phys. Rev. B*, Vol. **85**, Iss. 12, p. 121105. (pp. 17, 101, 103, 104)

Béri, B. and Cooper, N. R. (2012). "Topological Kondo Effect with Majorana Fermions". *Phys. Rev. Lett.*, Vol. **109**, Iss. 15, p. 156803. (p. 20)

Bernevig, B. A.; Hughes, T. L.; and Zhang, S.-C. (2006). "Quantum Spin Hall Effect and Topological Phase Transition in HgTe Quantum Wells". *Science*, Vol. **314**(5806), pp. 1757–1761. (pp. 2, 4, 15, 22, 125, 127, 132, 137, 167)

Berry, M. V. (1984). "Quantal Phase Factors Accompanying Adiabatic Changes". *Proceedings of the Royal Society of London A: Mathematical, Physical and Engineering Sciences*, Vol. **392**(1802), pp. 45–57. (p. 12)

Bethe, H. A. (1931). "Zur Theorie der Metalle; 1, Eigenwerte und Eigenfunktionen der linearen Atomkette". *Zeitschrift für Physik*, Vol. **71**, Iss. 3–4, pp. 205–226. (p. 20)

Bloch, F. (1933). "Bremsvermögen von Atomen mit mehreren Elektronen". *Zeitschrift für Physik*, Vol. **81**, Iss. 5–6, pp. 363–376. (p. 34)

Bloch, F. (1934). "Inkoheränte Röntgenstreuung und Dichteschwankungen eines entarteten Fermigases". *Helvetica Physica Acta*, Vol. **7**(IV), p. 385. (p. 34)

Borda, L. (2007). "Kondo screening cloud in a one-dimensional wire: Numerical renormalization group study". *Phys. Rev. B*, Vol. **75**, Iss. 4, p. 041307. (pp. 21, 79, 84)

Boulat, E. and Saleur, H. (2008). "Exact low-temperature results for transport properties of the interacting resonant level model". *Phys. Rev. B*, Vol. **77**, Iss. 3, p. 033409. (p. 92)

Braunecker, B.; Simon, P.; and Loss, D. (2009a). "Nuclear magnetism and electron order in interacting one-dimensional conductors". *Phys. Rev. B*, Vol. **80**, Iss. 16, p. 165119. (p. 146)

Braunecker, B.; Simon, P.; and Loss, D. (2009b). "Nuclear Magnetism and Electronic Order in ^{13}C Nanotubes". *Phys. Rev. Lett.*, Vol. **102**, Iss. 11, p. 116403. (p. 146)

Brüne, C.; Liu, C. X.; Novik, E. G.; Hankiewicz, E. M.; Buhmann, H.; Chen, Y. L.; Qi, X. L.; Shen, Z. X.; Zhang, S. C.; and Molenkamp, L. W. (2011). "Quantum Hall Effect from the Topological Surface States of Strained Bulk HgTe". *Phys. Rev. Lett.*, Vol. **106**, Iss. 12, p. 126803. (pp. 2, 16, 167)

Budich, J. C.; Dolcini, F.; Recher, P.; and Trauzettel, B. (2012). "Phonon-Induced Backscattering in Helical Edge States". *Phys. Rev. Lett.*, Vol. **108**, Iss. 8, p. 086602. (pp. 16, 60)

Budich, J. C. and Trauzettel, B. (2013). "From the adiabatic theorem of quantum mechanics to topological states of matter". *physica status solidi (RRL) – Rapid Research Letters*, Vol. **7**, Iss. 1–2, pp. 109–129. (pp. 11, 13, 14)

Budich, J. C.; Zoller, P.; and Diehl, S. (2015). "Dissipative preparation of Chern insulators". *Phys. Rev. A*, Vol. **91**, Iss. 4, p. 042117. (p. 27)

Buttner, B.; Liu, C. X.; Tkachov, G.; Novik, E. G.; Brune, C.; Buhmann, H.; Hankiewicz, E. M.; Recher, P.; Trauzettel, B.; Zhang, S. C.; and Molenkamp, L. W. (2011). "Single valley Dirac fermions in zero-gap HgTe quantum wells". *Nature Phys.*, Vol. **7**, p. 418. (pp. 134, 137)

Bychkov, Y. A. and Rashba, E. I. (1984). "Oscillatory effects and the magnetic susceptibility of carriers in inversion layers". *Journal of Physics C: Solid State Physics*, Vol. **17**(33), p. 6039. (p. 19)

Caprara, S.; Tugushev, V. V.; Echenique, P. M.; and Chulkov, E. V. (2012). "Spin-polarized states of matter on the surface of a three-dimensional topological insulator with implanted magnetic atoms". *Phys. Rev. B*, Vol. **85**, Iss. 12, p. 121304. (p. 101)

Cartan, E. (1926). "Sur une classe remarquable d'espaces de Riemann". *Bulletin de la Société Mathématique de France*, Vol. **54**, pp. 214–264. The article is continued in *Cartan [1927]*. (pp. 13, 151)

Cartan, E. (1927). "Sur une classe remarquable d'espaces de Riemann. II". *Bulletin de la Société Mathématique de France*, Vol. **55**, pp. 114–134. The article has been started in *Cartan [1926]*. (pp. 13, 151)

Cayssol, J.; Dóra, B.; Simon, F.; and Moessner, R. (2013). "Floquet topological insulators". *physica status solidi (RRL) – Rapid Research Letters*, Vol. **7**, Iss. 1–2, pp. 101–108. (p. 27)

Chalker, J. T.; Read, N.; Kagalovsky, V.; Horovitz, B.; Avishai, Y.; and Ludwig, A. W. W. (2001). "Thermal metal in network models of a disordered two-dimensional superconductor". *Phys. Rev. B*, Vol. **65**, Iss. 1, p. 012506. (p. 114)

Chen, G. and Goddard, W. A. (1988). "The Magnon Pairing Mechanism of Superconductivity in Cuprate Ceramics". *Science*, Vol. **239**(4842), pp. 899–902. (p. 27)

Chen, Y. L.; Analytis, J. G.; Chu, J.-H.; Liu, Z. K.; Mo, S.-K.; Qi, X. L.; Zhang, H. J.; Lu, D. H.; Dai, X.; Fang, Z.; Zhang, S. C.; Fisher, I. R.; Hussain, Z.; and Shen, Z.-X. (2009). "Experimental Realization of a Three-Dimensional Topological Insulator, Bi2Te3". *Science*, Vol. **325**(5937), pp. 178–181. (pp. 4, 125)

Chern, S.-S. and Chevalley, C. O. (1952). "Elie Cartan and his mathematical work". *Bull. Amer. Math. Soc.*, Vol. **58**, pp. 217–250. (p. 15)

Chiu, C.-K.; Teo, J. C. Y.; Schnyder, A. P.; and Ryu, S. (2015). "Classification of topological quantum matter with symmetries". *ArXiv e-prints*, arXiv:1505.03535 [cond-mat.mes-hall]. (pp. 11, 14)

Coleman, P. (2007). "Heavy Fermions: Electrons at the Edge of Magnetism". In *Handbook of Magnetism and Advanced Magnetic Materials*. John Wiley & Sons, Ltd. ISBN: 9780470022184. (p. 19)

Crépin, F.; Budich, J. C.; Dolcini, F.; Recher, P.; and Trauzettel, B. (2012). "Renormalization group approach for the scattering off a single Rashba impurity in a helical liquid". *Phys. Rev. B*, Vol. **86**, Iss. 12, p. 121106. (pp. 60, 62)

Dahlhaus, J. P.; Béri, B.; and Beenakker, C. W. J. (2010). "Random-matrix theory of thermal conduction in superconducting quantum dots". *Phys. Rev. B*, Vol. **82**, Iss. 1, p. 014536. (p. 56)

Das, A.; Ronen, Y.; Most, Y.; Oreg, Y.; Heiblum, M.; and Shtrikman, H. (2012). "Zero-bias peaks and splitting in an Al-InAs nanowire topological superconductor as a signature of Majorana fermions". *Nature Physics*, Vol. **8**, pp. 887–895. (p. 143)

De Gennes, P. (1999). *Superconductivity Of Metals And Alloys*. Advanced Books Classics Series. Westview Press. ISBN: 9780813345840. (p. 27)

de Haas, W.; de Boer, J.; and van den Berg, G. (1934). "The electrical resistance of gold, copper and lead at low temperatures". *Physica*, Vol. **1**(7-12), pp. 1115–1124. (p. 20)

Dehghani, H.; Oka, T.; and Mitra, A. (2014). "Dissipative Floquet topological systems". *Phys. Rev. B*, Vol. **90**, Iss. 19, p. 195429. (p. 27)

Delplace, P.; Li, J.; and Büttiker, M. (2012). "Magnetic-Field-Induced Localization in 2D Topological Insulators". *Phys. Rev. Lett.*, Vol. **109**, Iss. 24, p. 246803. (p. 60)

Deng, S.; Ortiz, G.; Poudel, A.; and Viola, L. (2014). "Majorana flat bands in s-wave gapless topological superconductors". *Phys. Rev. B*, Vol. **89**, Iss. 14, p. 140507. (p. 100)

Dowker, J. S. (1972). "Quantum mechanics and field theory on multiply connected and on homogeneous spaces". *Journal of Physics A: General Physics*, Vol. **5**(7), p. 936. (p. 4)

Doyon, B. (2007). "New Method for Studying Steady States in Quantum Impurity Problems: The Interacting Resonant Level Model". *Phys. Rev. Lett.*, Vol. **99**, Iss. 7, p. 076806. (p. 92)

Dresselhaus, S.; Dresselhaus, G.; and Jorio, A. (2008). *Group Theory: Application to the Physics of Condensed Matter*. SpringerLink: Springer e-Books. Springer. ISBN: 9783540328971. Section 3.4 "Reducible Representations". (p. 54)

Dzero, M.; Sun, K.; Galitski, V.; and Coleman, P. (2010). "Topological Kondo Insulators". *Phys. Rev. Lett.*, Vol. **104**, Iss. 10, p. 106408. (pp. 14, 27)

Emery, V. J. and Kivelson, S. (1992). "Mapping of the 2-channel Kondo problem to a resonant-level model". *Phys. Rev. B*, Vol. **46**(17), pp. 10812–10817. (pp. 20, 30, 38, 40, 79, 81, 82, 88, 92)

Essert, S.; Krueckl, V.; and Richter, K. (2015). "Two-dimensional topological insulator edge state backscattering by dephasing". *ArXiv e-prints*, arXiv:1507.00928 [cond-mat.mes-hall]. (p. 60)

Essert, S. and Richter, K. (2015). "Magnetotransport in disordered two-dimensional topological insulators: signatures of charge puddles". *2D Materials*, Vol. **2**(2), p. 024005. (p. 60)

Fabrizio, M. and Gogolin, A. O. (1995). "Interacting one-dimensional electron gas with open boundaries". *Phys. Rev. B*, Vol. **51**, Iss. 24, pp. 17827–17841. (p. 20)

Fu, L. (2009). "Hexagonal Warping Effects in the Surface States of the Topological Insulator Bi2Te3". *Phys. Rev. Lett.*, Vol. **103**, Iss. 26, p. 266801. (p. 16)

Fu, L. and Kane, C. L. (2008). "Superconducting Proximity Effect and Majorana Fermions at the Surface of a Topological Insulator". *Phys. Rev. Lett.*, Vol. **100**, Iss. 9, p. 096407. (pp. 2, 4, 27, 113, 115, 167)

Fu, L.; Kane, C. L.; and Mele, E. J. (2007). "Topological Insulators in Three Dimensions". *Phys. Rev. Lett.*, Vol. **98**, Iss. 10, p. 106803. (p. 4)

Fulga, I. C.; Haim, A.; Akhmerov, A. R.; and Oreg, Y. (2013). "Adaptive tuning of Majorana fermions in a quantum dot chain". *New Journal of Physics*, Vol. **15**(4), p. 045020. (p. 143)

Furusaki, A. and Nagaosa, N. (1994). "Kondo effect in a Tomonaga-Luttinger liquid". *Phys. Rev. Lett.*, Vol. **72**, Iss. 6, pp. 892–895. (p. 20)

Geim, A. K. and Novoselov, K. S. (2007). "The rise of graphene". *Nature materials*, Vol. **6**(3), pp. 183–191. (p. 15)

Geissler, F.; Crépin, F.; and Trauzettel, B. (2014). "Random Rashba spin-orbit coupling at the quantum spin Hall edge". *Phys. Rev. B*, Vol. **89**(23), p. 235136. (p. 60)

Giamarchi, T. (2003). *Quantum Physics in One Dimension*. International Series of Monographs on Physics. Clarendon Press. ISBN: 9780198525004. (p. 35)

Groth, C. W.; Wimmer, M.; Akhmerov, A. R.; and Waintal, X. (2014). "Kwant: a software package for quantum transport". *New Journal of Physics*, Vol. **16**(6), p. 063065. (pp. 56, 129)

Guinea, F. (1985). "Dynamics of a particle in an external potential interacting with a dissipative environment". *Phys. Rev. B*, Vol. **32**, Iss. 11, pp. 7518–7523. (p. 66)

Haldane, F. D. M. (1981). "'Luttinger liquid theory' of one-dimensional quantum fluids. I. Properties of the Luttinger model and their extension to the general 1D interacting spinless Fermi gas". *Journal of Physics C: Solid State Physics*, Vol. **14**(19), p. 2585. (p. 35)

Haldane, F. D. M. (1988). "Model for a Quantum Hall Effect without Landau Levels: Condensed-Matter Realization of the "Parity Anomaly"". *Phys. Rev. Lett.*, Vol. **61**, Iss. 18, pp. 2015–2018. (pp. 4, 11, 100)

Halperin, B. I.; Oreg, Y.; Stern, A.; Refael, G.; Alicea, J.; and von Oppen, F. (2012). "Adiabatic manipulations of Majorana fermions in a three-dimensional network of quantum wires". *Phys. Rev. B*, Vol. **85**, Iss. 14, p. 144501. (p. 143)

Hasan, M. Z. and Kane, C. L. (2010). "Colloquium: Topological insulators". *Rev. Mod. Phys.*, Vol. **82**, Iss. 4, pp. 3045–3067. (pp. 2, 4, 5, 8, 11, 12, 13, 16, 125, 167)

Hasan, M. Z.; Xu, S.-Y.; Hsieh, D.; Wray, L. A.; and Xia, Y. (2014). "Experimental Discovery of Topological Surface States - A New Type of 2D Electron Systems (Review Article)". *ArXiv e-prints*, arXiv:1401.0848 [cond-mat.mes-hall]. (pp. 2, 16, 105, 167)

Hewson, A. (1997). *The Kondo Problem to Heavy Fermions*. Cambridge Studies in Magnetism. Cambridge University Press. ISBN: 9780521599474. (pp. 19, 20, 21, 30, 86)

Hohenadler, M. and Assaad, F. F. (2012). "Luttinger liquid physics and spin-flip scattering on helical edges". *Phys. Rev. B*, Vol. **85**, Iss. 8, p. 081106. (p. 16)

Holm, R. and Meissner, W. (1932). "Messungen mit Hilfe von flüssigem Helium. XIII". *Zeitschrift für Physik*, Vol. **74**, Iss. 11–12, pp. 715–735. (p. 27)

Hsieh, D.; Xia, Y.; Qian, D.; Wray, L.; Dil, J. H.; Meier, F.; Osterwalder, J.; Patthey, L.; Checkelsky, J. G.; Ong, N. P.; Fedorov, A. V.; Lin, H.; Bansil, A.; Grauer, D.; Hor, Y. S.; Cava, R. J.; and Hasan, M. Z. (2009a). "A tunable topological insulator in the spin helical Dirac transport regime". *Nature*, Vol. **460**(7259), pp. 1101–1105. (pp. 4, 125)

Hsieh, D.; Xia, Y.; Wray, L.; Qian, D.; Pal, A.; Dil, J. H.; Osterwalder, J.; Meier, F.; Bihlmayer, G.; Kane, C. L.; Hor, Y. S.; Cava, R. J.; and Hasan, M. Z. (2009b). "Observation of Unconventional Quantum Spin Textures in Topological Insulators". *Science*, Vol. **323**(5916), pp. 919–922. (pp. 4, 125)

Jackiw, R. (1984). "Fractional charge and zero modes for planar systems in a magnetic field". *Phys. Rev. D*, Vol. **29**, Iss. 10, pp. 2375–2377. (p. 147)

Jackiw, R. and Rebbi, C. (1976). "Solitons with fermion number 1/2". *Phys. Rev. D*, Vol. **13**, Iss. 12, pp. 3398–3409. (p. 146)

Jänich, K. (2006). *Topologie*. Springer-Lehrbuch. Springer Berlin Heidelberg. ISBN: 9783540268284. There is an English version of this book available. We are, however, not familiar with the English version. (p. 7)

Jiang, J.-H. and Wu, S. (2011). "Spin susceptibility and helical magnetic order at the edges/surfaces of topological insulators due to Fermi surface nesting". *Phys. Rev. B*, Vol. **83**, Iss. 20, p. 205124. (pp. 102, 103, 104, 110)

Kane, C. L. and Fisher, M. P. A. (1996). "Thermal Transport in a Luttinger Liquid". *Phys. Rev. Lett.*, Vol. **76**, Iss. 17, pp. 3192–3195. (p. 56)

Kane, C. L. and Mele, E. J. (2005a). "Quantum spin Hall effect in graphene". *Phys. Rev. Lett.*, Vol. **95**(22). (pp. 2, 4, 11, 15, 22, 100, 167)

Kane, C. L. and Mele, E. J. (2005b). "Z_2 Topological Order and the Quantum Spin Hall Effect". *Phys. Rev. Lett.*, Vol. **95**, Iss. 14, p. 146802. (p. 4)

Karbach, M. and Muller, G. (1998). "Introduction to the Bethe ansatz I". *eprint arXiv:cond-mat/9809162*, cond-mat/9809162. (p. 20)

Kasuya, T. (1956). "A Theory of Metallic Ferro- and Antiferromagnetism on Zener's Model". *Progress of Theoretical Physics*, Vol. **16**(1), pp. 45–57. (pp. 23, 101)

Kato, T. (1950). "On the Adiabatic Theorem of Quantum Mechanics". *Journal of the Physical Society of Japan*, Vol. **5**(6), pp. 435–439. (pp. 4, 12)

Keselman, A. and Berg, E. (2015). "Gapless symmetry-protected topological phase of fermions in one dimension". *Phys. Rev. B*, Vol. **91**, Iss. 23, p. 235309. (p. 100)

Kimme, L.; Rosenow, B.; and Brataas, A. (2015). "Backscattering in helical edge states from a magnetic impurity and Rashba disorder". *ArXiv e-prints*, arXiv:1502.07927 [cond-mat.mes-hall]. (p. 60)

Kitaev, A. (2009). "Periodic table for topological insulators and superconductors". In V. Lebedev & M. Feigel'man (Eds.), *American Institute of Physics Conference Series*, volume 1134 of *American Institute of Physics Conference Series* pp. 22–30. (pp. 4, 113, 127, 129)

Kitaev, A. Y. (2001). "Unpaired Majorana fermions in quantum wires". *Physics-Uspekhi*, Vol. **44**(10S), p. 131. (pp. 9, 11, 100, 143)

Klinovaja, J. and Loss, D. (2013). "Fractional Fermions with Non-Abelian Statistics". *Phys. Rev. Lett.*, Vol. **110**, Iss. 12, p. 126402. (p. 147)

Klinovaja, J.; Stano, P.; Yazdani, A.; and Loss, D. (2013). "Topological Superconductivity and Majorana Fermions in RKKY Systems". *Phys. Rev. Lett.*, Vol. **111**, Iss. 18, p. 186805. (p. 102)

Kohmoto, M. (1985). "Topological invariant and the quantization of the Hall conductance". *Annals of Physics*, Vol. **160**(2), pp. 343–354. (p. 5)

Kondo, J. (1964). "Resistance minimum in dilute magnetic alloys". *Progress of Theoretical Physics*, Vol. **32**(1), p. 37 ff. (pp. 19, 20)

König, M. (2008). *Spin-related transport phenomena in HgTe-based quantum well structures*. PhD thesis, Julius-Maximilians-Universität Würzburg. Section 3.2. (p. 60)

König, M.; Wiedmann, S.; Brüne, C.; Roth, A.; Buhmann, H.; Molenkamp, L. W.; Qi, X.-L.; and Zhang, S.-C. (2007). "Quantum Spin Hall Insulator State in HgTe Quantum Wells". *Science*, Vol. **318**(5851), pp. 766–770. (pp. 2, 4, 15, 22, 125, 127, 167)

Kouwenhoven, L. and Glazman, L. (2001). "Revival of the Kondo effect". *Physics World*, Vol. **14**(1), pp. 33–38. (pp. 20, 21)

Kruschke, J. K. (2011). *Doing Bayesian Data Analysis : a tutorial with R and BUGS*. Burlington, MA: Academic Press. ISBN: 9780123814852. (pp. 52, 54)

Laidlaw, M. G. G. and DeWitt, C. M. (1971). "Feynman Functional Integrals for Systems of Indistinguishable Particles". *Phys. Rev. D*, Vol. **3**, Iss. 6, pp. 1375–1378. (p. 4)

Law, K. T.; Seng, C. Y.; Lee, P. A.; and Ng, T. K. (2010). "Quantum dot in a two-dimensional topological insulator: The two-channel Kondo fixed point". *Phys. Rev. B*, Vol. **81**(4). (pp. 2, 16, 20, 22, 80, 86, 87, 88, 89, 167)

Leggett, A. J.; Chakravarty, S.; Dorsey, A. T.; Fisher, M. P. A.; Garg, A.; and Zwerger, W. (1987). "Dynamics of the dissipative two-state system". *Rev. Mod. Phys.*, Vol. **59**, Iss. 1, pp. 1–85. (pp. 20, 30)

Leinaas, J. and Myrheim, J. (1977). "On the theory of identical particles". *Il Nuovo Cimento B Series 11*, Vol. **37**(1), pp. 1–23. (p. 4)

Lemaréchal, C. (2001). "Lagrangian Relaxation". In M. Jünger & D. Naddef (Eds.), *Computational Combinatorial Optimization*, volume 2241 of *Lecture Notes in Computer Science*, pp. 112–156. Springer Berlin Heidelberg. ISBN: 9783540428770. (p. 52)

Lindner, N. H.; Berg, E.; Refael, G.; and Stern, A. (2012). "Fractionalizing Majorana Fermions: Non-Abelian Statistics on the Edges of Abelian Quantum Hall States". *Phys. Rev. X*, Vol. **2**, Iss. 4, p. 041002. (pp. 2, 167)

Liu, C.; Hughes, T. L.; Qi, X.-L.; Wang, K.; and Zhang, S.-C. (2008). "Quantum Spin Hall Effect in Inverted Type-II Semiconductors". *Phys. Rev. Lett.*, Vol. **100**, Iss. 23, p. 236601. (p. 137)

Liu, Q.; Liu, C.-X.; Xu, C.; Qi, X.-L.; and Zhang, S.-C. (2009). "Magnetic Impurities on the Surface of a Topological Insulator". *Phys. Rev. Lett.*, Vol. **102**, Iss. 15, p. 156603. (pp. 2, 101, 167)

Lloyd, P. (1967). "Wave propagation through an assembly of spheres: II. The density of single-particle eigenstates". *Proceedings of the Physical Society*, Vol. **90**(1), p. 207. (p. 23)

Lowen, R. (2015). *Index Analysis: Approach Theory at Work*, Chapter "Approach Theory Meets Topology", p. 249. Springer Monographs in Mathematics. Springer London. ISBN: 9781447164852. The original source seems to be an interview of Nova with Edward Witten conducted in 2003 as part of the interview series "Viewpoints on String Theory". The interview was available at `http://www.pbs.org/wgbh/nova/elegant/view-witten.html` on July 19, 2015. (p. 4)

Luttinger, J. M. (1963). "An Exactly Soluble Model of a Many-Fermion System". *Journal of Mathematical Physics*, Vol. **4**(9), pp. 1154–1162. (pp. 31, 32, 34)

Maciejko, J. (2012). "Kondo lattice on the edge of a two-dimensional topological insulator". *Phys. Rev. B*, Vol. **85**, Iss. 24, p. 245108. (pp. 22, 40, 144)

Maciejko, J.; Liu, C.; Oreg, Y.; Qi, X.-L.; Wu, C.; and Zhang, S.-C. (2009). "Kondo Effect in the Helical Edge Liquid of the Quantum Spin Hall State". *Phys. Rev. Lett.*, Vol. **102**, Iss. 25, p. 256803. (pp. 16, 20, 22, 60, 78)

Mahan, G. (2000). *Many-Particle Physics*, Section "Friedel's Theorem", pp. 195–199. Physics of Solids and Liquids. Springer. ISBN: 9780306463389. (p. 21)

Martinek, J.; Utsumi, Y.; Imamura, H.; Barnaś, J.; Maekawa, S.; König, J.; and Schön, G. (2003). "Kondo Effect in Quantum Dots Coupled to Ferromagnetic Leads". *Phys. Rev. Lett.*, Vol. **91**, Iss. 12, p. 127203. (p. 20)

Matsuura, S.; Chang, P.-Y.; Schnyder, A. P.; and Ryu, S. (2013). "Protected boundary states in gapless topological phases". *New Journal of Physics*, Vol. **15**(6), p. 065001. (pp. 14, 100, 125)

Mattis, D. C. and Lieb, E. H. (1965). "Exact Solution of a Many-Fermion System and Its Associated Boson Field". *Journal of Mathematical Physics*, Vol. **6**(2), pp. 304–312. (pp. 31, 32, 34)

Matveev, K. A. (1995). "Coulomb blockade at almost perfect transmission". *Phys. Rev. B*, Vol. **51**, Iss. 3, pp. 1743–1751. (pp. 31, 66)

Mehta, P. and Andrei, N. (2006). "Nonequilibrium Transport in Quantum Impurity Models: The Bethe Ansatz for Open Systems". *Phys. Rev. Lett.*, Vol. **96**, Iss. 21, p. 216802. (p. 92)

Metropolis, N.; Rosenbluth, A. W.; Rosenbluth, M. N.; Teller, A. H.; and Teller, E. (1953). "Equation of State Calculations by Fast Computing Machines". *The Journal of Chemical Physics*, Vol. **21**(6), pp. 1087–1092. (pp. 52, 107)

Michetti, P.; Budich, J. C.; Novik, E. G.; and Recher, P. (2012). "Tunable quantum spin Hall effect in double quantum wells". *Phys. Rev. B*, Vol. **85**, Iss. 12, p. 125309. (pp. 127, 134, 137)

Miyamoto, K.; Kimura, A.; Okuda, T.; Miyahara, H.; Kuroda, K.; Namatame, H.; Taniguchi, M.; Eremeev, S. V.; Menshchikova, T. V.; Chulkov, E. V.; Kokh, K. A.; and Tereshchenko, O. E. (2012). "Topological Surface States with Persistent High Spin Polarization across the Dirac Point in Bi_2Te_2Se and Bi_2Se_2Te". *Phys. Rev. Lett.*, Vol. **109**, Iss. 16, p. 166802. (pp. 16, 105)

Moore, J. E. and Balents, L. (2007). "Topological invariants of time-reversal-invariant band structures". *Phys. Rev. B*, Vol. **75**, Iss. 12, p. 121306. (p. 4)

Mourik, V.; Zuo, K.; Frolov, S. M.; Plissard, S. R.; Bakkers, E. P. A. M.; and Kouwenhoven, L. P. (2012). "Signatures of Majorana Fermions in Hybrid Superconductor-Semiconductor Nanowire Devices". *Science*, Vol. **336**(6084), pp. 1003–1007. (p. 143)

Müller-Gronbach, T.; Novak, E.; and Ritter, K. (2012). *Monte Carlo-Algorithmen*, Chapter "Die Markov Chain Monte Carlo-Methode", pp. 179–244. Springer-Lehrbuch. Springer Berlin Heidelberg. ISBN: 9783540891406. (p. 52)

Müller-Hartmann, E. (1969). "Spin correlation in dilute magnetic alloys". *Zeitschrift für Physik A Hadrons and Nuclei*, Vol. **223**, Iss. 3, pp. 277–288. (p. 21)

Müller-Hartmann, E. and Zittartz, J. (1971). "Kondo Effect in Superconductors". *Phys. Rev. Lett.*, Vol. **26**, Iss. 8, pp. 428–432. (p. 20)

Nadj-Perge, S.; Drozdov, I. K.; Li, J.; Chen, H.; Jeon, S.; Seo, J.; MacDonald, A. H.; Bernevig, B. A.; and Yazdani, A. (2014). "Observation of Majorana fermions in

ferromagnetic atomic chains on a superconductor". *Science*, Vol. **346**(6209), pp. 602–607. (p. 110)

Nagaoka, Y. (1965). "Self-Consistent Treatment of Kondo's Effect in Dilute Alloys". *Phys. Rev.*, Vol. **138**, Iss. 4A, pp. A1112–A1120. (p. 21)

Nakamura, K.; Nakahara, Y.; Ohtomi, K.; and Sugano, S. (1985). "A mechanism of 7x7 reconstruction on Si(111) and Ge(111)Sn surfaces". *Surface Science*, Vol. **152-153,** Part 2, pp. 1020–1026. (p. 101)

Nash, C. (1999). "Topology and physics – a historical essay". In I. James (Ed.), *History of Topology*, pp. 359–416. Elsevier Science. ISBN: 9780080534077. Also: Nash, C. (1997). *ArXiv High Energy Physics – Theory e-prints*, hep-th/9709135. (p. 4)

Neupane, M.; Xu, S.-Y.; Wray, L. A.; Petersen, A.; Shankar, R.; Alidoust, N.; Liu, C.; Fedorov, A.; Ji, H.; Allred, J. M.; Hor, Y. S.; Chang, T.-R.; Jeng, H.-T.; Lin, H.; Bansil, A.; Cava, R. J.; and Hasan, M. Z. (2012). "Topological surface states and Dirac point tuning in ternary topological insulators". *Phys. Rev. B*, Vol. **85**, Iss. 23, p. 235406. (pp. 16, 105)

Nocedal, J. and Wright, S. J. (2006). *Numerical Optimization*. Springer Series in Operations Research and Financial Engineering. Springer New York. ISBN: 9780387303031. (p. 52)

Nozieres, P. and Blandin, A. (1980). "Kondo effect in real metals". *Journal de Physique*, Vol. **41**(3), pp. 193–211. (pp. 20, 79, 86)

Oreg, Y. and Goldhaber-Gordon, D. (2004). "Two-Channel Kondo Effect in a Modified Single Electron Transistor". In A. Alexandrov, J. Demsar, & I. Yanson (Eds.), *Molecular Nanowires and Other Quantum Objects*, volume 148 of *NATO Science Series*, pp. 67–76. Springer Netherlands. ISBN: 9781402020698. (p. 20)

Park, J.; Lee, S.-S. B.; Oreg, Y.; and Sim, H.-S. (2013). "How to Directly Measure a Kondo Cloud's Length". *Phys. Rev. Lett.*, Vol. **110**, Iss. 24, p. 246603. (pp. 21, 22)

Patton, K. R.; Hafermann, H.; Brener, S.; Lichtenstein, A. I.; and Katsnelson, M. I. (2009). "Probing the Kondo screening cloud via tunneling-current conductance fluctuations". *Phys. Rev. B*, Vol. **80**, Iss. 21, p. 212403. (p. 22)

Pereira, R. G.; Laflorencie, N.; Affleck, I.; and Halperin, B. I. (2008). "Kondo screening cloud and charge staircase in one-dimensional mesoscopic devices". *Phys. Rev. B*, Vol. **77**, Iss. 12, p. 125327. (p. 22)

Polini, M.; Guinea, F.; Lewenstein, M.; Manoharan, H. C.; and Pellegrini, V. (2013). "Artificial honeycomb lattices for electrons, atoms and photons". *Nat. Nanotechnol.*, Vol. **8**, Iss. 9, pp. 625–633. (p. 110)

Posske, T. (2012). "Kondo Tunneling between non-interacting Helical Edge Liquids: Analytical Examinations in the Toulouse Limit". Master's thesis, Julius-Maximilians-Univerität Würzburg. (p. 83)

Posske, T.; Liu, C.-X.; Budich, J. C.; and Trauzettel, B. (2013). "Exact Results for the Kondo Screening Cloud of Two Helical Liquids". *Phys. Rev. Lett.*, Vol. **110**, Iss. 1, p. 016602. (pp. 3, 22, 30, 40, 79, 80, 84, 85, 92, 95, 96)

Posske, T. and Trauzettel, B. (2014). "Direct proportionality between the Kondo cloud and current cross correlations in helical liquids". *Phys. Rev. B*, Vol. **89**, Iss. 7, p. 075108. (pp. 3, 22, 45, 89, 92, 97)

Potok, R. M.; Rau, I. G.; Shtrikman, H.; Oreg, Y.; and Goldhaber-Gordon, D. (2007). "Observation of the two-channel Kondo effect". *Nature*, Vol. **446**, pp. 167–171. (p. 20)

Potok, R. M.; Rau, I. G.; Shtrikman, H.; Oreg, Y.; and Goldhaber-Gordon, D. (2007). "Observation of the two-channel Kondo effect". *Nature*, Vol. **446**(7132), pp. 167–171. (p. 79)

Qi, X.-L.; Wu, Y.-S.; and Zhang, S.-C. (2006). "Topological quantization of the spin Hall effect in two-dimensional paramagnetic semiconductors". *Phys. Rev. B*, Vol. **74**, Iss. 8, p. 085308. (pp. 11, 100, 127)

Qi, X.-L. and Zhang, S.-C. (2011). "Topological insulators and superconductors". *Rev. Mod. Phys.*, Vol. **83**, Iss. 4, pp. 1057–1110. (pp. 4, 125)

Queiroz, R. and Schnyder, A. P. (2014). "Stability of flat-band edge states in topological superconductors without inversion center". *Phys. Rev. B*, Vol. **89**, Iss. 5, p. 054501. (pp. 14, 100, 125)

Rainis, D.; Saha, A.; Klinovaja, J.; Trifunovic, L.; and Loss, D. (2014). "Transport Signatures of Fractional Fermions in Rashba Nanowires". *Phys. Rev. Lett.*, Vol. **112**, Iss. 19, p. 196803. (p. 146)

Rammer, J. (2007). *Quantum field theory of non-equilibrium states*. Cambridge University Press. ISBN: 9780521874991. (pp. 24, 33)

Rego, L. G. C. and Kirczenow, G. (1999). "Fractional exclusion statistics and the universal quantum of thermal conductance: A unifying approach". *Phys. Rev. B*, Vol. **59**, Iss. 20, pp. 13080–13086. (p. 56)

Reinthaler, R. W.; Tkachov, G.; and Hankiewicz, E. M. (2015). "Superconducting quantum spin-Hall systems with giant orbital g-factors". *ArXiv e-prints*, arXiv:1502.07521 [cond-mat.mes-hall]. (p. 18)

Rosenberg, G. and Franz, M. (2012). "Surface magnetic ordering in topological insulators with bulk magnetic dopants". *Phys. Rev. B*, Vol. **85**, Iss. 19, p. 195119. (p. 101)

Roth, L. M.; Zeiger, H. J.; and Kaplan, T. A. (1966). "Generalization of the Ruderman-Kittel-Kasuya-Yosida Interaction for Nonspherical Fermi Surfaces". *Phys. Rev.*, Vol. **149**, Iss. 2, pp. 519–525. (p. 101)

Rothe, D. G. (2015). *Spin transport in topological insulators and geometrical spin control*. PhD thesis, Julius-Maximilians-Universität Würzburg. Section "Quantization of the Hall conductivity", in particular page 74. (p. 12)

Rothe, D. G.; Reinthaler, R. W.; Liu, C.-X.; Molenkamp, L. W.; Zhang, S.-C.; and Hankiewicz, E. M. (2010). "Fingerprint of different spin-orbit terms for spin transport in HgTe quantum wells". *New Journal of Physics*, Vol. **12**(6), p. 065012. (pp. 19, 137)

Ruderman, M. A. and Kittel, C. (1954). "Indirect Exchange Coupling of Nuclear Magnetic Moments by Conduction Electrons". *Phys. Rev.*, Vol. **96**, Iss. 1, pp. 99–102. (pp. 23, 25, 26, 101)

Ryu, S.; Schnyder, A. P.; Furusaki, A.; and Ludwig, A. W. W. (2010). "Topological insulators and superconductors: tenfold way and dimensional hierarchy". *New Journal of Physics*, Vol. **12**(6), p. 065010. (pp. 11, 14)

Sato, T.; Segawa, K.; Guo, H.; Sugawara, K.; Souma, S.; Takahashi, T.; and Ando, Y. (2010). "Direct Evidence for the Dirac-Cone Topological Surface States in the Ternary Chalcogenide $TlBiSe_2$". *Phys. Rev. Lett.*, Vol. **105**, Iss. 13, p. 136802. (pp. 16, 105)

Sau, J. D.; Lutchyn, R. M.; Tewari, S.; and Das Sarma, S. (2010). "Generic New Platform for Topological Quantum Computation Using Semiconductor Heterostructures". *Phys. Rev. Lett.*, Vol. **104**, Iss. 4, p. 040502. (pp. 120, 122)

Schiller, A. and Hershfield, S. (1998). "Toulouse limit for the nonequilibrium Kondo impurity: Currents, noise spectra, and magnetic properties". *Phys. Rev. B*, Vol. **58**, Iss. 22, pp. 14978–15010. (pp. 20, 80, 81, 83, 84, 92, 94, 95)

Schmidt, T. M.; Miwa, R. H.; and Fazzio, A. (2011). "Spin texture and magnetic anisotropy of Co impurities in Bi_2Se_3 topological insulators". *Phys. Rev. B*, Vol. **84**, Iss. 24, p. 245418. (p. 101)

Schnyder, A. P.; Ryu, S.; Furusaki, A.; and Ludwig, A. W. W. (2008). "Classification of topological insulators and superconductors in three spatial dimensions". *Phys. Rev. B*, Vol. **78**, Iss. 19, p. 195125. (pp. 4, 11, 13, 14, 113, 117, 126, 127, 129)

Schönhammer, K. (1997). "Interacting fermions in one dimension: The Tomonaga-Luttinger model". *eprint arXiv:cond-mat/9710330*, cond-mat/9710330. (pp. 35, 80)

Schrieffer, J. (1983). *Theory of Superconductivity*. Advanced Book Program Series. Advanced Book Program, Perseus Books. ISBN: 9780738201207. Remarks on the Nambu notation can be found in Section 7-2. (pp. 27, 28)

Schrieffer, J. R. and Wolff, P. A. (1966). "Relation between the Anderson and Kondo Hamiltonians". *Phys. Rev.*, Vol. **149**, Iss. 2, pp. 491–492. (p. 86)

Schwab, K.; Henriksen, E. A.; Worlock, J. M.; and Roukes, M. L. (2000). "Measurement of the quantum of thermal conductance". *Nature*, Vol. **404**, Iss. 6781, pp. 974–977. (p. 56)

Simonin, J. (2007). "Looking for the Kondo cloud". *ArXiv e-prints*, arXiv:0708.3604. (p. 21)

Sodano, P.; Bayat, A.; and Bose, S. (2010). "Kondo cloud mediated long-range entanglement after local quench in a spin chain". *Phys. Rev. B*, Vol. **81**, Iss. 10, p. 100412. (p. 144)

Stern, A. (2010). "Non-Abelian states of matter". *Nature*, Vol. **464**, Iss. 7286, pp. 187–193. (p. 4)

Stern, A. and Lindner, N. H. (2013). "Topological Quantum Computation-From Basic Concepts to First Experiments". *Science*, Vol. **339**(6124), pp. 1179–1184. (pp. 2, 12, 143, 167)

Ström, A.; Johannesson, H.; and Japaridze, G. I. (2010). "Edge Dynamics in a Quantum Spin Hall State: Effects from Rashba Spin-Orbit Interaction". *Phys. Rev. Lett.*, Vol. **104**, Iss. 25, p. 256804. (pp. 2, 60, 167)

Tanaka, Y.; Furusaki, A.; and Matveev, K. A. (2011). "Conductance of a Helical Edge Liquid Coupled to a Magnetic Impurity". *Phys. Rev. Lett.*, Vol. **106**, Iss. 23, p. 236402. (pp. 16, 60, 78, 79, 81, 82, 84)

Thouless, D. J.; Kohmoto, M.; Nightingale, M. P.; and den Nijs, M. (1982). "Quantized Hall Conductance in a Two-Dimensional Periodic Potential". *Phys. Rev. Lett.*, Vol. **49**, Iss. 6, pp. 405–408. (pp. 5, 12)

Tinkham, M. (2004). *Introduction to Superconductivity: Second Edition*. Dover Books on Physics. Dover Publications. ISBN: 9780486435039. For the treatment of the pairing Hamiltonian, we refer to Sections 3.4 and 3.5. (p. 27)

Tomonaga, S.-i. (1950). "Remarks on Bloch's Method of Sound Waves applied to Many-Fermion Problems". *Progress of Theoretical Physics*, Vol. **5**(4), pp. 544–569. (p. 34)

Toulouse, G. (1969). "Exact Expression of energy of Kondo Hamiltonian base state for a particular J(z)-value". *C. R. Acad. Sci. Ser. B*, Vol. **268**(18), p. 1200. (pp. 20, 30, 40, 92)

Tsunetsugu, H.; Sigrist, M.; and Ueda, K. (1997). "The ground-state phase diagram of the one-dimensional Kondo lattice model". *Rev. Mod. Phys.*, Vol. **69**, Iss. 3, pp. 809–864. (p. 19)

van Delft, D. and Kes, P. (2010). "The discovery of superconductivity". *Physics today*, Vol. **63**, Iss. 9, pp. 38–43. (pp. 20, 27)

Väyrynen, J. I.; Goldstein, M.; and Glazman, L. I. (2013). "Helical Edge Resistance Introduced by Charge Puddles". *Phys. Rev. Lett.*, Vol. **110**, Iss. 21, p. 216402. (p. 60)

von Delft, J. and Schoeller, H. (1998). "Bosonization for beginners — refermionization for experts". *Annalen der Physik*, Vol. **7**(4), pp. 225–305. (pp. 15, 28, 30, 31, 32, 33, 34, 35, 36, 37, 38, 40, 61, 64, 66, 69, 80, 82)

von Delft, J.; Zaránd, G.; and Fabrizio, M. (1998). "Finite-Size Bosonization of 2-Channel Kondo Model: A Bridge between Numerical Renormalization Group and Conformal Field Theory". *Phys. Rev. Lett.*, Vol. **81**, Iss. 1, pp. 196–199. (pp. 20, 30)

Weinberg, S. (1996). *The quantum theory of fields – Volume I, Foundations*. The Quantum Theory of Fields. Cambridge University Press. ISBN: 9780521550017. Section 1.1, p. 14. (p. 32)

Weisstein, E. W. (2013). *Lerch Transcendent*, MathWorld – A Wolfram Web Resource, http://mathworld.wolfram.com/LerchTranscendent.html. Last visited on July 8, 2015. (p. 95)

Wiegmann, P. B. (1981). "Exact solution of the s-d exchange model (Kondo problem)". *Journal of Physics C: Solid State Physics*, Vol. **14**(10), p. 1463. (p. 20)

Winkler, R. (2003a). *Spin–Orbit Coupling Effects in Two-Dimensional Electron and Hole Systems*, volume 191 of *Springer Tracts in Modern Physics*, Chapter "Origin

of Spin–Orbit Coupling Effects", pp. 61–68. Springer Berlin Heidelberg. ISBN: 9783540011873. (pp. 18, 19)

Winkler, R. (2003b). *Spin–Orbit Coupling Effects in Two-Dimensional Electron and Hole Systems*, volume 191 of *Springer Tracts in Modern Physics*. Springer Berlin Heidelberg. ISBN: 9783540011873. (p. 19)

Winkler, R. (2003c). *Spin–Orbit Coupling Effects in Two-Dimensional Electron and Hole Systems*, volume 191 of *Springer Tracts in Modern Physics*, Chapter "Inversion-Asymmetry-Induced Spin Splitting", pp. 69–130. Springer Berlin Heidelberg. ISBN: 9783540011873. (p. 19)

Wolfram Research, Inc. (2015). "Mathematica". Versions 8-10.1, Champaign, Illinois. (p. vi)

Wu, C.; Bernevig, B. A.; and Zhang, S.-C. (2006). "Helical Liquid and the Edge of Quantum Spin Hall Systems". *Phys. Rev. Lett.*, Vol. **96**, Iss. 10, p. 106401. (pp. 4, 15)

Ye, F.; Ding, G. H.; Zhai, H.; and Su, Z. B. (2010). "Spin helix of magnetic impurities in two-dimensional helical metal". *EPL (Europhysics Letters)*, Vol. **90**, p. 47001. (p. 102)

Yosida, K. (1957). "Magnetic Properties of Cu-Mn Alloys". *Phys. Rev.*, Vol. **106**, Iss. 5, pp. 893–898. (pp. 23, 101)

Zaránd, G. and von Delft, J. (2000). "Analytical calculation of the finite-size crossover spectrum of the anisotropic two-channel Kondo model". *Phys. Rev. B*, Vol. **61**, Iss. 10, pp. 6918–6933. (pp. 20, 40, 69, 79, 82, 83)

Zeeman, P. (1897). "The Effect of Magnetisation on the Nature of Light Emitted by a Substance". *Nature*, Vol. **55**(1424), p. 347. (p. 18)

Zhu, J.-J.; Yao, D.-X.; Zhang, S.-C.; and Chang, K. (2011). "Electrically Controllable Surface Magnetism on the Surface of Topological Insulators". *Phys. Rev. Lett.*, Vol. **106**, Iss. 9, p. 097201. (p. 101)

Zyuzin, A. A. and Loss, D. (2014). "RKKY interaction on surfaces of topological insulators with superconducting proximity effect". *Phys. Rev. B*, Vol. **90**, Iss. 12, p. 125443. (p. 102)

Part III.

Appendix

A. Deutsche Zusammenfassung und Motivation

A.1. Kurze Zusammenfassung

Topologische Isolatoren sind elektronische Phasen, welche im Inneren isolieren, jedoch auf ihren Oberflächen über besondere, metallische Randkanäle mit einer spinabhängigen Dispersion verfügen. Diesen Phasen wird eine große Bedeutung hinsichtlich zukünftiger Realisationen von Spintronik und topologischem Quantenrechnen zugeordnet. Neben der Bestimmung intrinsischer Eigenschaften dieser neuartigen Systeme kann die Betrachtung von Kombinationen mit wohlbekannten physikalischen Systemen originelle, neue Physik generieren. Diese Dissertation befasst sich mit eben solchen Kombinationen. Insbesondere werden die folgenden Systeme analysiert: Ein lokaler Rashba-Rückstreuer, ein Kondo-Quantenpunkt im Zweikanalregime, im Gitter geordnete, magnetische Adatome auf einem starken, dreidimensionalen topologischen Isolator, die näheinduzierte Supraleitung in letzteren Systemen und Hybridverbindungen bestehend aus einem topologischen Isolator und einem Halbmetall. Die primären Resultate sind die analytische Beschreibung der Kondowolke und die Beschreibung ihrer möglichen Detektion in Stromkorrelationen weit entfernt von der Kondo-Region. Dabei wird die Methode der refermionisierbaren Parameterkonfigurationen verwendet und erweitert. Des Weiteren wird die Entdeckung einer Klasse von bandlückenfreien topologischen Phasen beschrieben, deren Randkanäle sich fast wie die von konventionellen topologischen Isolatoren verhalten. Die dargestellte Forschung wird voraussichtlich in der zukünftigen Klassifizierung und Anwendung von Systemen, die als Komponente mindestens einen topologischen Isolator enthalten, hilfreich sein. Dafür werden einige Beispiele gegeben.

A.2. Deutsche Einführung und Motivation

Das elektronische Verhalten kondensierter Materie wird, wie aus dem Schulunterricht bekannt, in zwei Hauptklassen eingeteilt, die nach der elektrischen Leitfähigkeit unterschieden werden: Leiter und Nichtleiter[1]. Typische Leiter sind Metalle. Die Leitfähigkeit von Metallen ist allein durch ihre Leitungsbandelektronen bestimmt, welche

[1] Häufig wird aus praktischen Gründen zusätzlich die Klasse der Halbleiter eingeführt.

sich nahezu frei bewegen können. Diese Elektronen formen damit ein elementares Beispiel für eine elektronische Phase, die Fermiflüssigkeit. Fermiflüssigkeiten sind die häufigsten in natürlichen Materialien vorkommenden elektronischen Phasen. Jedoch haben uns die letzten hundert Jahre die Entdeckung einer Vielzahl elektronischer Phänomene beschert, die von selteneren elektronischen Phasen herrühren. Beispiele sind Supraleiter, Mott-Isolatoren, Wigner-Kristalle, nematische Phasen und die Familie der Quanten-Hall-Effekte. Letztere beinhalten die ersten Beispiele für topologisch klassifizierte elektronische Phasen. Dieses Klassifikationsschema erweitert das bisherige Verständnis davon, was eine Phase ausmacht erheblich *[Hasan & Kane, 2010]*. In naher Vergangenheit wurde eine ganze Klasse von topologischen Isolatoren entdeckt *[Bernevig et al., 2006; Brüne et al., 2011; Hasan & Kane, 2010; Hasan et al., 2014; Kane & Mele, 2005a; König et al., 2007]*. Diese zeichnen sich dadurch aus, dass sie in ihrem Inneren elektrisch isolieren, jedoch an Ihrer Oberfläche (im Fall von dreidimensionalen Strukturen) elektrisch leiten. Die leitenden Oberflächen werden, in Anlehnung an die Fermiflüssigkeit, auch Randflüssigkeiten genannt. Sie leiten den elektrischen Strom auf sehr spezifische Weise, die vom Spin der geleiteten Teilchen abhängt. Diese einmalige Eigenschaft macht topologische Isolatoren interessant für Anwendungen in der Spintronik, die es sich zum Ziel gesetzt hat, die klassische Elektronik im Bereich der Computer, also der maschinellen Berechnung, abzulösen. Spintronik kann aufgrund elementarer physikalischer Eigenschaften schneller und hitzeverlustärmer arbeiten als Elektronik. Außerdem öffnen topologische Isolatoren im Bereich des topologischen Quantenrechnens neue Pforten *[Stern & Lindner, 2013]*.

Nach der Entdeckung der topologischen Isolatoren wurden zunächst ihre intrinsischen Eigenschaften bestimmt und die Qualität der Systeme verbessert *[Brüne et al., 2011; Hasan et al., 2014]*. Dieser Vorgang hält weiter an. Interessant ist es allerdings, im nächsten Schritt die vielfältigen Kombinationsmöglichkeiten topologischer Isolatoren mit altbekannten physikalischen Systemen zu explorieren. Nicht zuletzt wurden in der Vergangenheit durch einen solchen Kombinationsansatz interessante Effekte entdeckt. Zu diesen zählen der Josephson-Kontakt, die Diode, der Transistor und das zweidimensionale Elektronengas im magnetischen Feld (d. h. die Quanten Hall Effekte). Diese Dissertation trägt einen Teil zu der Erforschung solcher Effekte bei, die durch Kombination eines topologischen Isolators mit Bekanntem entstehen. Beispiele bisheriger Ergebnisse in diese Richtung können in *Fu & Kane [2008]; Law et al. [2010]; Lindner et al. [2012]; Liu et al. [2009]; Ström et al. [2010]* gefunden werden. Natürlich ist der Konfigurationsraum aller möglichen Kombinationen viel zu umfangreich, um hier dargestellt werden zu können. Diese Dissertation konzentriert sich deshalb auf einige wenige elementare Systeme mit denen topologische Isolatoren kombiniert werden. Die grundlegende Physik wird in Kapitel 2 eingeführt. Es wird erklärt, was ein topologischer Isolator ist (Abschnitt 2.1) und auf elektromagnetische Störungen, dargestellt durch den Zeeman Effekt und den Rashba Effekt, den Kondo Effekt (Abschnitt 2.2.3), die Ruderman-Kittel-Kasuya-Yosida-Wechselwirkung (Ab-

schnitt 2.2.4) sowie Supraleitung (Abschnitt 2.3), eingegangen wird. Nachfolgend, in Kapitel 3, werden die verwendeten theoretischen Methoden vorgestellt. Darunter befinden sich: Die Theorie der refermionisierbaren Parameterkonfigurationen (Section 3.1), welche Bosonisierung und Refermionisierung beinhaltet, eine spezielle Methode, um Divergenzen zu behandeln, die von einer lokalen Störstelle herrühren (Section 3.2), der Metropolis Algorithmus (Section 3.3) und Informationen über die durchgeführten Transportsimulationen (Section 3.5).

In Abschnitt II wird die Analyse der kombinierten topologischen Isolatoren präsentiert. Zunächst handelt dieser Abschnitt von einem lokalen Rashba-Rückstreuer an den Rändern eines Quanten-Spin-Hall-Isolators mit repulsiver Elektronenabstoßung, der sogenannten helikalen Flüssigkeit, und analysiert dessen refermionisierbare Parameterkonfiguration, welche eine interessante Ähnlichkeit zum wechselwirkungsfreien System aufweist (Kapitel 4). Als nächstes wird ein lokaler Kondo-Quantenpunkt betrachtet, der an zwei helikale Flüssigkeiten gekoppelt ist (Kapitel 5). Insbesondere wird dabei die Kondowolke für bestimmte Parameterkonfigurationen exakt aufgelöst und ein Weg vorgeschlagen, wie sie experimentell in bestimmten Stromkorrelationen nachgewiesen werden kann. Danach werden magnetische Momente betrachtet, die in Gitterform auf einem dreidimensionalen topologischen Isolator angebracht werden, der über eine hexagonal verformte Fermi-Fläche verfügt (Kapitel 6). Das Hinzufügen von Supraleitung generiert einen speziellen, zweidimensionalen bandlückenfreien Supraleiter, dessen Entstehung auf einen generalisierbaren Mechanismus zurückführt werden kann (Kapitel 6.2). In Kapitel 7 wird der Versuch unternommen ähnliche Supraleiter durch die künstliche Kopplung zweidimensionaler Systeme zu erstellen, wobei eine reiche Phänomenologie in der Gegenwart von Fehlstellen aufgefunden wird.

Die Darstellung wird in Kapitel 8 dadurch abgerundet, dass mögliche zukünftige Projekte beschrieben werden, deren Fragestellungen sich aus den hier präsentierten Resultaten ergeben. Diese reichen von Kondo-Majorana-Vertauschung bis zu eindimensionalen, dispergierenden Jackiw-Rebbi-Flüssigkeiten.

B. Officially required appendices

B.1. List of publications

- Yuval Baum, Thore Posske, Ion Cosma Fulga, Björn Trauzettel, and Ady Stern (2015). "Gapless topological superconductors: Model Hamiltonian and realization". *Physical Review B*, Vol **92**, Iss. 4, p. 045128.
- Yuval Baum, Thore Posske, Ion Cosma Fulga, Björn Trauzettel, and Ady Stern (2015). "Coexisting edge states and gapless bulk in topological states of matter". *Physical Review Letters*, Vol **114**, Iss. 13, p. 136801.
- Thore Posske and Björn Trauzettel (2014). "Measuring the Kondo Cloud by Current Cross Correlations in Helical Liquids". *Physical Review B* Vol. **89**, Iss. 7,p. 075108.
- Thore Posske, Chao-Xing Liu, Jan Carl Budich and Björn Trauzettel (2013). "Exact Results for the Kondo Screening Cloud of Two Helical Liquids". *Physical Review Letters*, Vol. **110**, Iss. 1, p. 016602.